/THE JOURNAL OF

PHYSICAL

CHEMISTRY

THE JOURNAL OF
PHYSICAL CHEMISTRY

COMMUNICATIONS TO THE EDITOR

■ Supplementary material for this paper is available separately, in photocopy or microfiche form. Ordering information is given in the paper.

* In papers with more than one author, the asterisk indicates the name of the author to whom inquiries about the paper should be addressed.

AUTHOR INDEX

Chemical Kinetic Effects of Walls on Active Species. Results for Hydrogen Atoms

Jorge J. Ahumada and J. V. Michael*

Department of Chemistry, Carnegie-Mellon University, Pittsburgh, Pennsylvania 15213   (Received August 10, 1973)

Publication costs assisted by the U. S. Atomic Energy Commission

This paper presents a model for active species in a contained cylindrical system which considers first-order homogeneous reaction, diffusion, and heterogeneous reaction at the walls. Predictions of the time dependence of atomic or radical concentrations are made in their approach to steady state, in the steady state, and the decay from steady state when the species is produced from an external source which can be extinguished. Four cases are presented and the model is tested with hydrogen atoms which are produced photochemically at various temperatures and pressures in a real time experiment. The atomic concentration is monitored by means of Lyman α photometry. Only one parameter is used, ϵ, the wall recombination coefficient, and the mechanism for wall recombination is found to be of the Rideal type in agreement with previous results which are obtained with a completely different technique. Results at five temperatures which range from 298 to 470°K are presented, and for exact agreement with the data, a slight ϵ variation as a function of pressure is indicated at the lower temperatures. This is interpreted as a physical adsorption inhibiting effect of heat bath molecules. Such ϵ variation becomes less important at higher temperatures where model and experiment agree well with a constant ϵ value which is pressure independent.

Introduction

In recent years there have been an increasing number of time-dependent radiation chemical, photochemical, and chemical kinetic studies of radicals and atoms in contained gaseous systems. The importance of wall termination was recognized several years ago in the kinetics of branching chain reactions,[1] and it has been considered in nonchain studies but only in the steady state.[2,3] Approximate time-dependent solutions have also been given.[4]

The usual assumption is that uniform and homogeneous concentrations of highly reactive species are present throughout a contained volume. In photochemical experiments nonlinear injection of energy into reactive systems always occurs when absorption is governed by the Beer-Lambert law. This gives rise to spacial nonuniformities in active species concentration. However, this effect can usually be controlled by working at low absorption coefficients so that energy injection is linear with distance. Thus, the energy injected per unit volume can be made to be uniform in such a system. Even if this condition holds, nonuniformities in concentration both in steady state and in time-resolved experiments can exist in chemically reactive systems due to the coupling of homogeneous first- and second-order reactions, diffusion, and heterogeneous reaction at the walls.

It is the purpose of this paper to examine and test several cases where these processes are important. The energy injection is assumed to be uniform in all cases, and, for the sake of simplification, is assumed to be a step function in time. It is not necessary to make this assumption but the solutions become more difficult.

Model.[5] The model which is chosen is that of an infinite cylinder even though most studies are performed in finite cylinders. However, if concentrations are observed radially in the center of a finite cylinder and the axial distance is a few times the radius of the cylinder the perturbations due to end walls are negligible compared to that of the cylinder walls. For such a model the basic differential equation which couples first- and second-order homogeneous reaction, diffusion, and heterogeneous wall reaction is the well-known diffusion equation

$$\partial n / \partial t = D\nabla^2 n - kn - k'n^2 + n_0 \qquad (1)$$

where n is the active species concentration and D is the binary diffusion coefficient of the active species through heat bath molecules. k is the first-order volume reaction rate constant for removal of n from the system in the case where a reactant is purposely added. This first-order rate constant is equal to $k_b[R]_0$ for a bimolecular reaction of n with R if $[R]_0$ is very much greater than n. k' represents

the second-order volume termination constant and is generally proportional to the total gas concentration if n is atomic. The term, n_0, represents the rate of n production from an external source and is assumed to be independent of time and space coordinates. It may, for example, be the rate of light absorption times a quantum yield for n production. ∇^2 is the Laplacian operator.

Equation 1 is nonlinear and is difficult to solve, but if the sensitivity for detection of n is high and k' is small (e.g., low pressures) the second-order volume termination process is negligible and eq 1 may be simplified. With this approximation and writing eq 1 in cylindrical coordinates, eq 2 is obtained.

$$\frac{\partial^2 n}{\partial r^2} + \frac{1}{r}\frac{\partial n}{\partial r} - \frac{kn}{D} + \frac{n_0}{D} = \frac{1}{D}\frac{\partial n}{\partial t} \qquad (2)$$

The solution of eq 2 is well known under a variety of boundary conditions.[5] For the present cases the first boundary condition is that n must be finite at the center of the cylinder ($r = 0$), and the second boundary condition is

$$(\partial n/\partial r) + hn = 0 \qquad \text{at } r = a \qquad (3)$$

where a is the radius of the cylinder measured from the center. h is taken from the derivation of Semenoff[1] to be $\bar{c}\epsilon/4D$, where $\bar{c}$ is the average velocity of the atomic or radical species and ϵ is the wall recombination coefficient, defined as the probability of destruction of the species upon its collision with the wall of the vessel. If ϵ is less than 0.1 this is an adequate expression for h.[1,6]

Case I. Constant Irradiation with No Volume Termination (i.e., $k = 0$). In this case eq 2 becomes

$$\frac{\partial^2 n}{\partial r^2} + \frac{1}{r}\frac{\partial n}{\partial r} + \frac{n_0}{D} = \frac{1}{D}\frac{\partial n}{\partial t} \qquad (4)$$

A third boundary condition is that $n = 0$ at $t = 0$. This differential equation may be solved with the three mentioned boundary conditions. The result is

$$n = \frac{n_0 a}{2hD} + \frac{n_0}{4D}(a^2 - r^2) - \frac{2n_0 h}{aD}\sum_{n=1}^{\infty} e^{-D\alpha_n^2 t}\frac{J_0(\alpha_n r)}{\alpha_n^2[\alpha_n^2 + h^2]J_0(\alpha_n a)} \qquad (5)$$

J_0 being the Bessel function of the first kind of order zero of the appropriate arguments. The boundary condition, eq 3, implies the choices of α_n according to the roots of $\alpha_n J_1(\alpha_n a) = hJ_0(\alpha_n a)$.[5a] Equation 5 is consistent with the first two boundary conditions. In order to recover the third, the solution of eq 4 at small times[5a] has to be found. This solution does show that as t approaches zero, n also goes to zero. An interesting feature of eq 5 is that as time approaches infinity (steady state) the concentration distribution becomes

$$n_\infty = \frac{n_0 a}{2hD} + \frac{n_0}{4D}(a^2 - r^2) \qquad (6)$$

and the concentration distribution is parabolic across the cylinder with a maximum in the center. The severity of this distribution is dependent on the magnitudes of h and D. Thus, if h is very small (i.e., ϵ is small), the first term in eq 6 may always be large in comparison to the second at even large values of pressure. D is inversely proportional to pressure and becomes smaller at pressure increases. On the other hand, if ϵ is even moderately large the steady-state solution (eq 6) shows that radial gradients can be very severe, particularly at high pressure where D is smaller. Equation 6 can be derived directly from eq 4 with the first two boundary conditions and $\partial n/\partial t = 0$.

The radially averaged concentration implied by eq 5 is

$$\bar{n} = \frac{2}{a^2}\int_0^a nr\,dr = \frac{n_0 a}{2hD} + \frac{n_0 a^2}{8D} - \frac{4n_0 h^2}{a^2 D}\sum_{n=1}^{\infty} e^{-D\alpha_n^2 t}\frac{1}{\alpha_n^4[\alpha_n^2 + h^2]} \qquad (7)$$

the first two terms of which represent the steady-state ($t = \infty$) average concentration, $\bar{n}_\infty$.

Case II. No Irradiation ($n_0 = 0$) with No Volume Termination ($k = 0$). In this case eq 2 becomes

$$\frac{\partial^2 n}{\partial r^2} + \frac{1}{r}\frac{\partial n}{\partial r} = \frac{1}{D}\frac{\partial n}{\partial t} \qquad (8)$$

The solution to this equation is straightforward if boundary conditions are again specified. In order to obtain a complementary solution which is continuous with case I, the three boundary conditions are as follows: n is finite at $r = 0$, eq 3, and eq 6 at $t = 0$. The solution with these three boundary conditions is

$$n = \frac{2n_0 h}{aD}\sum_{n=1}^{\infty} e^{-D\alpha_n^2 t}\frac{J_0(\alpha_n r)}{\alpha_n^2[\alpha_n^2 + h^2]J_0(\alpha_n a)} \qquad (9)$$

where eq 3 again implies the choices for α_n from the roots of $\alpha_n J_1(\alpha_n a) = hJ_0(\alpha_n a)$. The solution at small times gives eq 6 at $t = 0$, as it should. Also eq 9 is consistent with the other two boundary conditions.

A comparison of eq 9, the decay from steady state, with eq 5, the buildup to steady state, shows that the time dependence for buildup is exactly complementary to the decay. Similarly the radially averaged concentration is

$$\bar{n} = \frac{4n_0 h^2}{a^2 D}\sum_{n=1}^{\infty} e^{-D\alpha_n^2 t}\frac{1}{\alpha_n^4[\alpha_n^2 + h^2]} \qquad (10)$$

Case III. Constant Irradiation with Volume Termination ($k \neq 0$) in the Steady State ($\partial n/\partial t = 0$). In this case eq 2 becomes

$$\frac{\partial^2 n_\infty}{\partial r^2} + \frac{1}{r}\frac{\partial n_\infty}{\partial r} - \frac{kn_\infty}{D} = -\frac{n_0}{D} \qquad (11)$$

If eq 3 is taken as the first boundary condition, n is taken to be finite at $r = 0$ as the second boundary condition, the solution of eq 11 is

$$n_\infty = \frac{n_0}{k}\left[1 - \frac{hI_0(qr)}{qI_1(qa) + hI_0(qa)}\right] \qquad (12)$$

where $q = (k/D)^{1/2}$, and I_0 and I_1, represent the modified Bessel functions of the first kind of order zero and one, respectively, of the appropriate arguments. Equation 12 predicts a radial concentration distribution just as does eq 6 where no reactant is present. However, for the same values of h and D the presence of a reactant (eq 12) considerably depresses the radial distribution over that predicted by the no reactant case (eq 6).

The radially averaged concentration may be calculated as in eq 7 for this case, and the result is

$$\bar{n}_\infty = \frac{n_0}{k}\left[\frac{\left(q - \dfrac{2h}{aq}\right)I_1(qa) + hI_0(qa)}{qI_1(qa) + hI_0(qa)}\right] \qquad (13)$$

Case IV. No Irradiation ($n_0 = 0$) with Volume Termination ($k \neq 0$). In this case eq 2 becomes

$$\frac{\partial^2 n}{\partial r^2} + \frac{1}{r}\frac{\partial n}{\partial r} - \frac{kn}{D} = \frac{1}{D}\frac{\partial n}{\partial t} \qquad (14)$$

The three boundary conditions are chosen so as to be

complementary with the other three cases which have been considered. Thus, n is finite at $r = 0$, eq 3 holds, and at $t = 0$ the condition of the system is given by eq 12. The solution of eq 14 is then

$$n = \frac{2n_0 h}{a} \sum_{n=1}^{\infty} e^{-(D\alpha_n^2 + k)t} \frac{J_0(\alpha_n r)}{[D\alpha_n^2 + k][\alpha_n^2 + h^2]J_0(\alpha_n a)} \quad (15)$$

where eq 3 implies the same choices for α_n as in cases I and II, namely, α_n are the roots of $\alpha_n J_1(\alpha_n a) = h J_0(\alpha_n a)$. A comparison of eq 9 (no reactant) and eq 15 (with reactant) shows that the time-dependent part of the solutions changes by the additive factor of k in the exponent. Also the amplitude factor is decreased in eq 15 by the additive factor, k, to $D\alpha_n^2$ in the denominator.

The radially averaged concentration for this case may also be computed, and the result is

$$\bar{n} = \frac{4n_0 h^2}{a^2} \sum_{n=1}^{\infty} e^{-(D\alpha_n^2 + k)t} \frac{1}{\alpha_n^2[D\alpha_n^2 + k][\alpha_n^2 + h^2]} \quad (16)$$

In preparation to use these solutions for analysis of some experimental data obtained with hydrogen atoms, some features can be pointed out immediately. In cases I, II, and IV the choices for α_n are the same and inspection of the roots of $\alpha_n J_1(\alpha_n a) = h J_0(\alpha_n a)$[5a] shows that regardless of the values of h or a the only important root is the first one in which case only one term needs to be retained in the infinite summations. This fact considerably simplifies the predicted time dependence of the radially averaged concentrations. Thus, the buildup constant predicted with eq 7 from $\ln (\bar{n}_\infty - \bar{n})$ vs. time will be $D\alpha_1^2$. Similarly the decay constant predicted with eq 10 from $\ln \bar{n}$ vs. time will also give $D\alpha_1^2$. Also, the decay constant predicted when reactant is present (eq 16) from $\ln \bar{n}$ vs. time will be $D\alpha_1^2 + k$. This result shows that the effects of homogeneous first-order reaction can easily be separated from that due to diffusion and reaction with the wall from a time-dependent analysis with and without reactant. The result is also independent of any radial distribution. This is exactly the assumption which many authors have made in atomic and radical reaction studies.[7-10] It also means that there is no necessity to design experimental apparatus which has no wall. In fact, the best configuration is when walls are present and are highly poisoned so that ϵ and subsequently h is very small. In this event diffusion is no longer an important removal process because α_1^2 approaches $2h/a = \bar{c}\epsilon/2aD$ for small ϵ and is zero when ϵ is zero. Under these unattainable conditions (second-order homogeneous termination eventually becomes competitive) the model predicts that no decay in the absence of reactant results, i.e., one starts with a bottle of the "active" species, and any decay that results in the presence of reactant is entirely due to homogeneous reaction with reactant. On the other hand, if ϵ is very large, such that h is essentially infinity at all values of D, the model predicts a maximum value of $\alpha_1 a$ of 2.4048.[5a] This means that the time constant for wall destruction will always be $D(2.4048)^2/a^2$ in which case active species removal is always completely controlled by diffusion. In the event the pressure is low (very high D) the experimental apparatus must necessarily have a fast time response and also reactant concentrations will have to be increased so that k is comparable in magnitude to $D(2.4048)^2/a^2$ before the effects of added reactant can be time resolved.

Experiments have been reported[11,12] in which steady-state concentrations of active species (hydrogen atoms in these cases) are measured under steady irradiation in the presence of reactant (eq 13) and in the absence of reactant (eq 7 at $t = \infty$). The observation in studies of this type is $\bar{n}_\infty$ as a function of n_0 both with and without a reactant. If n_0 is controlled to be the same in both experiments (i.e., if, for instance, light is absorbed and quantum yields for n production is unaffected by the addition of small concentrations of reactant), and if ϵ is unaffected by small amounts of reactant at a given pressure, then the model predicts

$$\frac{[\bar{n}_\infty/n_0]_0}{[\bar{n}_\infty/n_0]_r} = \frac{k\left(\dfrac{a^2}{8D} + \dfrac{a}{2hD}\right)(qI_1(qa) + hI_0(qa))}{\left[\left(q - \dfrac{2h}{qa}\right)I_1(qa) + hI_0(qa)\right]} \quad (17)$$

where $[\bar{n}_\infty/n_0]_0$ represents the case with no reactant and $[\bar{n}_\infty/n_0]_r$ is the case with added reactant. Expansion of the modified Bessel functions in eq 17, collection of terms in q^2, and division shows the first two terms give

$$\frac{[\bar{n}_\infty/n_0]_0}{[\bar{n}_\infty/n_0]_r} = 1 + k\left(\frac{a^2}{8D} + \frac{a}{2hD}\right) = 1 + k[\bar{n}_\infty/n_0]_0 \quad (18)$$

an equation which is identical with eq 8 of ref 11.

Experimental Section

In order to test the predictions of the model, experiments have been performed in which hydrogen atom concentrations have been measured in their approach to steady state and in their subsequent decay from steady state after the initiating source has been turned off. The atoms are produced from the $Hg(^3P_1)$ sensitization of molecular hydrogen. Two apparatuses have been used and these are subsequently referred to as experiment A and experiment B.

Experiment A. This apparatus has been described previously[7,13] and therefore, no detailed description will be given here. However, two changes in procedure have been incorporated in the present experiments in an attempt to regulate and reproduce the amount of absorbed mercury radiation in an experiment. First the lamp was operated under controlled dc power and temperature conditions, and second a variable time shutter of diameter equal to that of the resonance lamp and photolysis cell was used to vary the exposure time per experiment. The turn on and off buildup and decay time constants for the shutter has been measured oscilloscopically to be 3 msec.

The photocurrent attenuation with and without mercury in the photolysis cell was measured with an RCA 935 ultraviolet sensitive phototube coupled to a Keithley 610B electrometer. In preparation for an experiment research grade molecular hydrogen (from Airco) was introduced through a liquid nitrogen cooled trap that contained mercury. The observation of no mercury light attenuation and no production of hydrogen atoms by Lyman α photometry confirmed the absence of mercury in the photolysis system. The trap was then allowed to warm up, and mercury was allowed to diffuse into the system until a desired level of attenuation was reached. Then an experiment was performed. Thus, the absorbed intensity (measured by the attenuation) could be varied by the variation of mercury concentration.

The atom concentrations were measured by time-resolved Lyman α photometry as described previously. New photometer calibrations (i.e., transmittance as a function of [H]) with both nitric oxide ionization and solar blind photomultiplier detectors on a flow system apparatus coupled to a time-of-flight mass spectrometer[13] have been
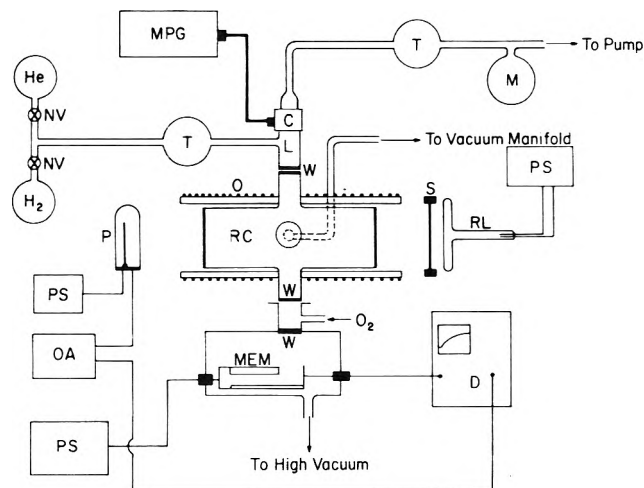
Figure 1. Block diagram of experimental apparatus: MPG, microwave power generator; C, Evenson cavity; L, Lyman α source; W, LiF windows; O, oven; RC, reaction cell; MEM, magnetic electron multiplier; NV, needle valve; T, liquid nitrogen trap; P, phototube; PS, power supply; OA, operational amplifier; D, oscilloscope or multichannel analyzer; S, shutter; RL, mercury resonance lamp; M, manometer.

carried out. One of the photometer configurations which was calibrated is that used in the present experiment. For the sake of internal consistency, a configuration which has been used and calibrated previously[14] was also checked with this apparatus. The new calibration agrees within 25% of that reported previously. This consistency then gives confidence to the procedure and allows a growth curve (*i.e.*, absorbance against [H]) to be constructed for the present apparatus. Thus, absolute [H] is reported in this paper for experiment A.

Experiment B. The apparatus is similar in principle to that of experiment A except for some modifications which make it more useful in reaction studies. A block diagram is given in Figure 1.

As in experiment A the hydrogen atoms are generated from the $Hg(^3P_1)$ photosensitization of research grade molecular hydrogen. The exposure time can be varied with a mechanical camera shutter of diameter equal to that of the reaction cell and resonance lamp. The turn on turn off half-times for the shutter are 3 msec. The mercury resonance radiation is detected by an RCA 935 phototube which can be operated in either the steady illumination or pulsed modes. The level of attenuation can be adjusted by the variation of mercury concentration with the former mode, and the pulsed mode is then used for synchronization in the pulse experiment. This pulse is amplified and triggers either a Tektronix 547 oscilloscope with a 1A1 preamplifier or a Nuclear Data 2400 multichannel analyzer.

The Lyman α absorption photometer system consists of a 2450-MHz microwave-driven flowing He (2 Torr) discharge lamp (Raytheon Model PGM-10X-1 with an Evenson cavity from Ophthos Instruments Co.)[8,15,16] and a Bendix M306 magnetic electron multiplier which can be operated in steady illumination (electrometer), analog (oscilloscope), or single photon (multichannel analyzer) modes. The Lyman α radiation is filtered by 2.2 cm of flowing O_2 at 1 atm. The windows are 0.5-in. blanks of LiF from Harshaw Chemical Co. and are glued onto the lamp, cell, and photomultiplier assemblies with high-temperature epoxy cement. It is a routine experiment to obtain relative growth curves for this apparatus as a func-

tion of microwave power (temperature in the lamp) and added H_2 in the He flow of the lamp at a constant level of absorbed mercury radiation. For most sensitive operation the lamp is operated with no added H_2, and the He stream is passed through a liquid N_2 cooled trap. Apparently the H_2 impurity in tank He or a small H_2O concentration which outgasses from the delivery lines serves as the source of Lyman α in the discharge. Even very small amounts of added H_2 systematically destroys the growth curves for detection. Even though the photon flux increases and the signal to noise is better, the loss in sensitivity for detection counterbalances the increased signal-to-noise gain. The effect of microwave power is much less important. Sensitivity is only slightly greater at low power (15%) than at high (60%). The measured temperature (with thermocouples) at 15% is 235 ± 10° and that at 60% is 525 ± 20°. Both of these effects are consistent with the known behavior of resonance lamps with regard to reversal and Doppler line broadening.[14,17] Thus, the lamp is operated with no added H_2 and at low microwave power. The limit of hydrogen atom sensitivity is 1×10^{10} atoms/cm^3.

The photolysis cell is a 6.7-cm quartz cylinder. The inside radius is 1.70 cm. It is surrounded by a ceramic furnace which is twice the length of the cell. The heating element is nichrome wire, and chromel–alumel thermocouples placed at various positions on the outside of the cell are used to measure the temperature. Since thermal gradients always exist, these thermocouples were calibrated at various pressures against a movable thermocouple placed on the inside of the cell. The measurements indicate that temperature gradients exist but are not severe either axially or radially up to 400°, and temperatures can be accurately reported to ±1% of the temperature expressed in °C.

The data can be collected either oscilloscopically in single-shot experiments or repetitively by means of photon counting in the multiscaling mode with a multichannel analyzer.[16] The results are independent of which mode of analysis is used. The present experiments were obtained in the single-shot mode.

Results and Discussion

In order to test the complementary nature of eq 7 and 10 experiments have been performed under low levels of absorbed mercury radiation in experiment A. A typical result at room temperature is shown in Figure 2 where absolute [H] is plotted against time. The decay constant in the dark period for this experiment is 35.0 sec^{-1}. According to eq 10 this value is equal to $D_{H,H_2}\alpha_1^2$ and since D_{H,H_2} is known at 298°K to be 1900 cm^2 sec^{-1}/P(torr),[18,19] a value for α_1 of 0.445 cm^{-1} is implied. Through the boundary condition implied by eq 35a a value of 0.208 cm^{-1} for h is obtained (a = 1.90 cm for this apparatus). Since $h = \bar{c}\epsilon/4D_{H,H_2}$, a value of ϵ = 6 × 10^{-4} for this experiment is derived. All of the quantities necessary to calculate $\bar{n}/n_0$ in the light period are then specified, and these values are shown also in Figure 2 along with similar values during the dark period. The scale is chosen so as to coincide with absolute [H] in the steady state. The continuous nature of eq 7 followed by eq 10 is then demonstrated. If the quantum yield for atom production is near unity a value for absorbed intensity, n_0 of ~4 × 10^{12} quanta/cc sec for this experiment is indicated. Thus, if ϵ is known the complete description of the system is specified in both the approach to steady state, the steady state, and decay from the steady state.
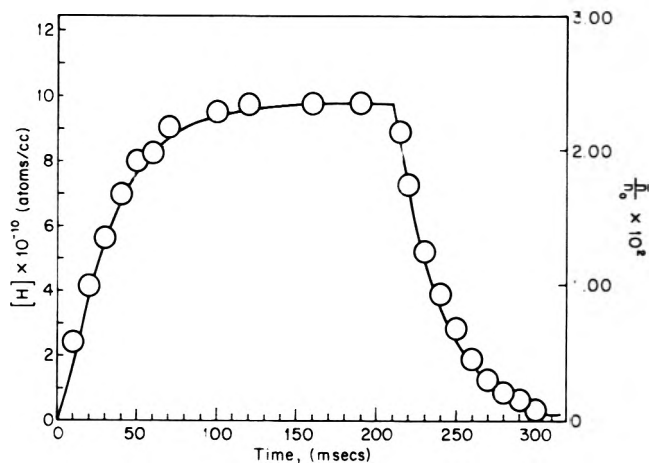
Figure 2. Growth and decay of hydrogen atom concentration at $P_{H_2} = 10$ Torr. The calculated line for $\bar{n}/n_0$ is obtained with $\epsilon = 6 \times 10^{-4}$ and $D\alpha_1^2 = 35.0 \sec^{-1}$.

Figure 3. k_d as a function of P_{H_2}. The calculated line is obtained with $\epsilon = 1 \times 10^{-4}$. Data points are from ref 4.

Figure 4. k_d as a function of P_{H_2} at $T = 298°K$. The solid line is calculated with $\epsilon = 1.2 \times 10^{-3}$; the dashed line is obtained by varying ϵ (see Table I).

Equation 3 presupposes that the frequency of wall collision, $\bar{c}n/4$, is much faster than atom removal by wall recombination, i.e., the surface condition is constant. When active species concentration is small the frequency may not be sufficient for eq 3 to hold in which case time dependence has to be introduced in eq 3.[5] Under these conditions surface sites may not be filled by adatoms and time will be required to establish eq 3. There are presumably 1.35×10^{15} sites/cm^2 to be filled for complete coverage on clean glass.[20] and the average velocity for H is 2.52×10^5 cm/sec. Adsorption is generally chemisorption which is highly exothermic. If the reasonable assumption is made that initial coverage is very efficient and occurs on every collision, the time for saturation of the [H] (1×10^{11} atoms/cc) indicated in Figure 2 would be 0.21 sec. This is not consistent with the results of Figure 2 and leads to the conclusion that either the available sites have been over-estimated by a factor of at least 100 or the surface is always permanently reduced. Either conclusion tends to justify use of eq 3 without time dependence.

In ref 4 decay constants for several different pressures (variable diffusion coefficients) of H_2 were constant within a specified error of $\pm15\%$. This behavior can be understood in terms of the present model. This system represents a highly poisoned one where ϵ is small. For example, if ϵ is taken to be 1×10^{-4} the behavior predicted by eq 10 with the boundary condition implied by eq 3 is shown in Figure 3 as the solid line. The data of ref 4 are also shown with estimated errors.

This behavior (small ϵ) may be contrasted with data obtained in experiment B where the wall surface is clean quartz. Typical decay constants are shown in Table I and Figure 4 at room temperature as a function of pressure. It is obvious that there is a strong pressure dependence to the decay constant. Also shown in the table and figure are values for $D_{H,H_2}\alpha_1^2$ which are calculated for $\epsilon = 1.2 \times 10^{-3}$. Comparison of predicted with observed values shows that the general features of the pressure dependence are confirmed even though exact quantitative agreement is not obtained. However, this value for ϵ does reproduce the low-pressure ($\sim$1-10 Torr) behavior within experimental error. It ought to be pointed out that this estimate for ϵ is consistent with a value of 2.8×10^{-3} by Wood and Wise[21] at 27° with a completely different technique. These workers have estimated their accuracy to be 50%.

Quantitative agreement between predictions and mea-

surements can be obtained from 1 to 350 Torr if ϵ is allowed to vary smoothly downward from 1.5×10^{-3} to 5.3×10^{-4} for the room temperature experiments of Table I. Even though this is a fairly minor change in ϵ, it is not expected. The only explanation for this behavior which may be consistent with heterogeneous kinetics is that the heat bath molecules act as a surface site inhibitor.[22] If this is the case the effect for molecular hydrogen or monatomic gases should not be a strong function of pressure and this would agree with the minor effect observed here. We know of no other work which has a sensitivity sufficient to confirm this behavior.
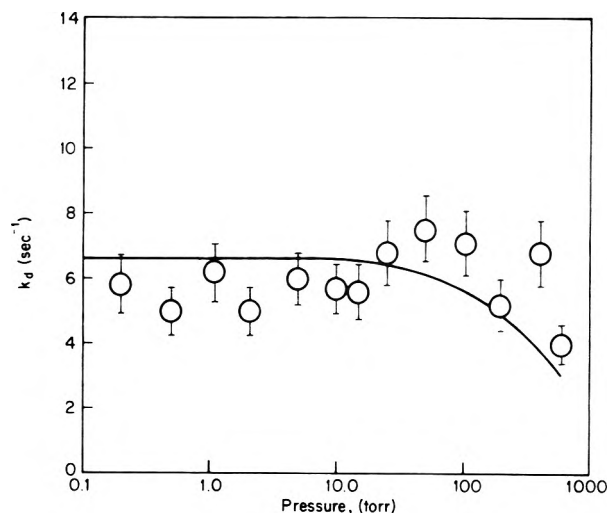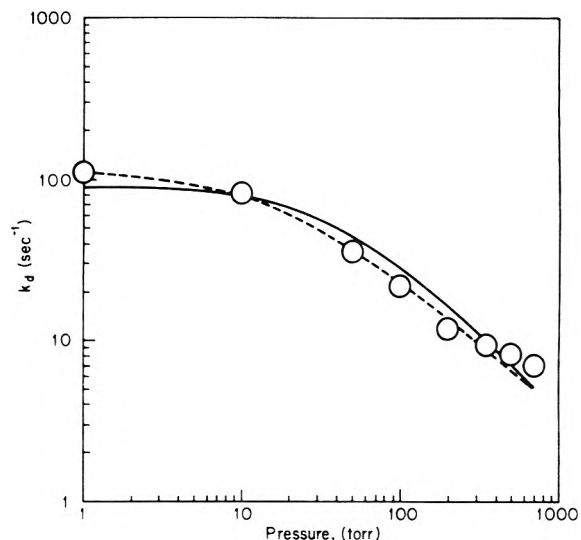
No reasonable value of ϵ can predict the behavior at pressures greater than 350 Torr. The measured decay constants are always greater than the predictions by about 30%. This would mean physically that the atoms are being removed faster than they can diffuse. The explanation for this effect may lie in the inapplicability of the present model. Equation 1 was written with both first- and second-order volume termination terms, but, in the model, only the first-order term was considered to be important. However, it is probable that at pressures in ex-

TABLE I: Decay Constants on Quartz in H_2

P, Torr	k_d, sec^{-1}	$D\alpha_1^2$, sec^{-1a}	$D\alpha_1^2$, sec^{-1}	$\epsilon \times 10^3$
		$T = 298°K$		
		$\epsilon = 1.2 \times 10^{-3}$		
700	7.1 ± 0.4	5.2	5.0	0.53
500	8.3 ± 0.7	7.2	6.5	0.53
350	9.6 ± 0.8	10.0	9.0	0.53
200	12 ± 1	16.4	14.0	0.56
100	22 ± 2	28.6	22.5	0.80
50	36 ± 4	44.6	36.0	0.97
10	83 ± 11	78.1	78.1	1.2
1	113 ± 15	87.0	109.5	1.5
		$T = 333°K$		
		$\epsilon = 1.8 \times 10^{-3}$		
700	$7.5 = 0.4$	6.4	6.2	0.82
500	8.7 ± 0.7	8.9	8.3	0.82
350	12 ± 1	12.5	11.7	0.82
200	17.5 ± 1.5	20.8	19.0	0.94
100	30 ± 3	37.1	31.5	1.1
50	55 ± 6	60.6	54.0	1.4
10	105 ± 15	104.0	104.0	1.8
		$T = 369°K$		
		$\epsilon = 2.3 \times 10^{-3}$		
700	8.0 ± 0.4	7.4		
500	11 ± 1	10.3		
350	$14 = 1$	14.4		
200	22 ± 2	24.3		
100	$40 = 4$	43.0		
50	74 ± 7	74.0		
10	150 ± 30	147.0		
		$T = 420°K$		
		$\epsilon = 3.2 \times 10^{-3}$		
700	12 ± 1	9.4		
500	13.5 ± 1.0	13.0		
350	17.0 ± 1.5	18.2		
200	29 ± 3	30.8		
100	54 ± 5	56.6		
50	90 ± 9	97.5		
		$T = 470°K$		
		$\epsilon = 4.5 \times 10^{-3}$		
700	21 ± 2	11.3		
500	26 ± 2	15.7		
350	28 ± 3	22.2		
200	44 ± 4	37.2		
100	57 ± 6	70.7		
50	130 ± 15	125.0		

^{a} The values for $D_{H,H}$ are taken from ref 18 and 19: 298°K $- 1900/P$; 333°K $- 2326/P$; 369°K $- 2675/P$; 420°K $- 3350/P$; and 470°K $- 4035/P$. D_{H,H_2} has units of cm^2 sec^{-1} and P is in Torr.

Figure 5. k_d as a function of P_{H_2} for $T = 333°K$. The solid line is calculated with $\epsilon = 1.8 \times 10^{-3}$. The dashed line is calculated by varying ϵ (see Table I).
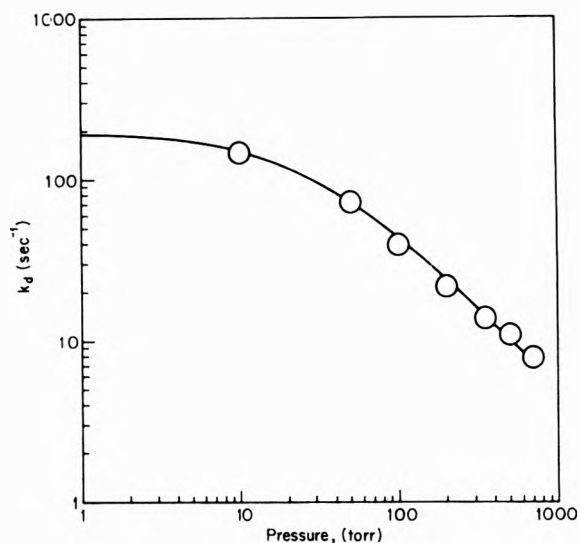
Figure 6. k_d as a function of P_{H_2} for $T = 369°K$. The calculated line is obtained with $\epsilon = 2.3 \times 10^{-3}$.

cess of 350 Torr second-order volume termination accounts for some of the decay. The third-order rate constant for atom recombination is known to be 8.3×10^{-33} cc^2/molecule^2 sec.[23] Typical steady-state hydrogen atom concentrations for these high-pressure experiments are 5×10^{12} molecule/cc, and this yields a decay constant for second-order decay at 700 Torr of 1 sec^{-1}. Since the second-order component is small compared to the first-order wall component it is impossible with the present accuracy to dissect the effect with a time analysis.

Termination constants have also been obtained at four higher temperatures, the maximum being 470°K. These results are also shown in Table I and Figures 5–8. The values of ϵ which specify the best low-pressure fits to the data are also indicated in Table I at each temperature, and these are proportional to, but lie consistently slightly

lower than, those of Wood and Wise.[21] An Arrhenius plot of the ϵ values, however, indicates an activation energy for H atom recombination on quartz of 2.1 ± 0.2 kcal/mol. Thus, the results are in agreement with the strongly bound Rideal type mechanism which exhibits a theoretically estimated activation energy of 2.2 kcal/mol and is most important from 120 to 500°K according to Wood and Wise[21] and Gelb and Kim.[20]

Exact fits to the 333°K temperature data can again be obtained by the smooth downward variation of ϵ. The range of variation becomes much less pronounced, however, and as temperature increases (369 and 420°K) it is not necessary to change ϵ at all to exactly recover the data within experimental error. Again this behavior is consistent with a weak physical adsorption poisoning effect of the heat bath molecules acting as an inhibitor. It is known that such equilibrium processes show negative enthalpies of reaction[24] so that as temperature increases the equilibrium constant should decrease.

The decay constants at 470°K are not predicted well, and the decay constants at any temperature can never be
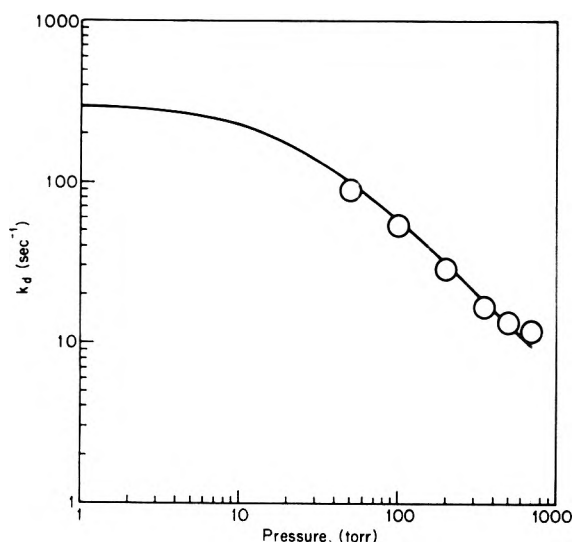
Figure 7. k_d as a function of P_{H_2} for $T = 420°K$. The calculated line is obtained with $\epsilon = 3.2 \times 10^{-3}$.
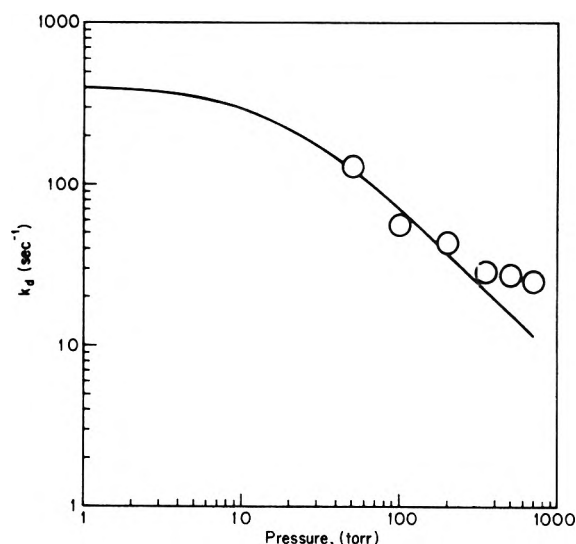
Figure 8. k_d as a function of P_{H_2} for $T = 470°K$. The calculated line is obtained with $\epsilon = 4.5 \times 10^{-3}$.

TABLE II: Decay Constants on Quartz in Kr at 298°K

P, Torr	k_d, sec^{-1}	$D a_1^2$, sec^{-1} ($\epsilon = 1.0 \times 10^{-3}$)
700	4.7 ± 0.4	2.4
500	4.5 ± 0.4	3.4
350	6.2 ± 0.6	4.8
250	6.7 ± 0.6	8.0
150	9.7 ± 1.0	10.5
50	19.8 ± 2.0	25.4
10	49 ± 5	55.3

predicted at 700 Torr for any reasonable value of ϵ. The measured values are consistently higher than the predictions. This may again be due to second-order volume termination and, at 470°K, the onset of a second-order heterogeneous termination process.[20,21] Neither of these processes have been considered in the present model and, therefore, the model may break down for these conditions.

Results have also been obtained at room temperature for hydrogen atom decay with Kr being the third body. These results are presented in Table II. The Lennard-Jones potential parameters for H atoms can be obtained[18,19] and can be combined with the known parameters for Kr.[25] Thus the binary diffusion coefficient at 298°K for hydrogen atoms in Kr is 875 cm^2 sec^{-1}/P(Torr). Calculations for predicted decays are also presented in Table II for an ϵ value of 1.0×10^{-3}. This is nearly identical with the value used at the same temperature for molecular hydrogen (Table I). As in the molecular hydrogen case, the features of the behavior are predicted and can be accommodated by slight ϵ variation except for the highest pressures where the predictions are only about one-half of the observed decays. This may indicate a substantially larger termolecular rate constant for H atom recombination than in molecular hydrogen.

In summary, a model has been developed which considers the coupling between homogeneous first-order reaction, diffusion, and heterogeneous reaction at the walls of an active species in a cylindrical system. Four cases are presented. The model is tested with hydrogen atoms produced photochemically at various temperatures. Since diffusion coefficients are known the model can be used with only one variable parameter, ϵ, the wall recombina-

tion coefficient. The wall recombination occurs by a strongly bound Rideal type mechanism in complete agreement with earlier workers who used an entirely different technique.

The model also shows how time analysis can be used to extract rate constants for volume processes if the order with which the active species is removed is one. In atomic reaction studies the first-order volume termination constant is generally $k_b[R]_0$ where k_b is the second-order rate constant for n with R, and $[R]_0$ is large so that its concentration does not change during an experiment. It is almost always true that the products of the reaction of n with R is also an active species (e.g., Rn) which might also be capable of undergoing a similar fate as n itself; i.e., diffusion with wall termination. If this does occur then a separate treatment of its concentration distribution has to be performed with n_0 in eq 1 replaced by its rate formation, kn. Obviously this becomes a very complicated problem since the new species may itself have a volume termination process of the type Rn + R or Rn + n which also has to be included in eq 1. Second-order volume termination for Rn may also have to be included. These processes may set up a series of consecutive processes which may introduce several other active species, each of which have to be considered separately in the same way.

Fortunately, the reason the usual assumptions of chemical kinetic analysis are of value in such a system is that most active species are large and have small diffusion coefficients (except for H and D) in which case the spacial term in the diffusion equation (eq 1) becomes negligible compared to the others. Then the usual chemical kinetic equations are exactly recovered.

Also, if the initially formed species has a large diffusion coefficient so that a spacial distribution can be established for it, and all other active species which may be formed in consecutive reactions have small diffusion coefficients, all of the active species will have predictable spacial distributions from the initially formed one. The most important case is the steady state ($t = \infty$) case. If, for example, Rn reacts with n then eq 1 (with the assumption of negligible second-order reaction for n) must be modified to be

$$\partial n / \partial t = 0 = D_1 \nabla^2 n_\infty - k_1 n_\infty - k_2 (Rn)_x n_x + n_0 \quad (19)$$

A similar equation can be written for Rn but D_2 is small and the spacial term is considered negligible.

$$\partial Rn / \partial t = 0 = -k_2(Rn)_x n_x + k_1 n_x \tag{20}$$

Thus, eq 19 reduces to eq 11 and the solution is eq 12 with k replaced by $2k$. Equation 20 shows that $(Rn)_\infty$ is constant and exhibits no spacial distribution even though n_∞ might (eq 12). The development of the equations, for time-dependent solutions with the assumption of small diffusion coefficients for secondary active species, is obvious even though the solutions may not be possible in closed form.

The important point to realize is that these considerations with regard to the approach to steady state, in the steady state, and the decay from steady state can be experimentally minimized if the spacial distribution of the initially formed species is eliminated. This can be accomplished in three ways: poisoning the walls, working at low pressure (high diffusion coefficients), or working at high reactant concentrations so that the volume termination always dominates the diffusional term. The first two are designed to eliminate the effect through minimization of h, and the last, through maximization of k/D.

References and Notes

(1) N. N. Semenoff, *Acta Physicochim., URSS.* **28**, 93 (1943).
(2) T. L. Hill, *J. Chem. Phys.,* **17**, 1125 (1949).
(3) R. M. Noyes, *J. Amer. Chem. Soc.,* **73**, 3039 (1951).
(4) D. A. Frank-Kamenetskii, "Diffusion and Heat Exchange in Chemical Kinetics," Princeton University Press, Princeton, N. J., 1955.
(5) The mathematics required for this model is discussed in detail in (a) H. S. Carslaw and J. C. Jaeger, "Conduction of Heat in Solids," Oxford University Press, London, 1959; (b) J. Crank, "The Mathematics of Diffusion," Oxford University Press, London, 1956; (c) N. W. McLachlan, "Bessel Functions for Engineers," Oxford University Press, London, 1955.
(6) H. Motz and H. Wise, *J. Chem. Phys.,* **32**, 1893 (1960).
(7) J. V. Michael and D. T. Osborne, *Chem. Phys. Lett.,* **3**, 402 (1969).
(8) W. Braun and M. Lenzi, *Discuss. Faraday Soc.,* **44**, 252 (1967).
(9) F. S. Uhl and H. Niki, *J. Chem. Phys.,* **57**, 3671 (1972).
(10) J. A. Eyre, T. Hikida, and L. M. Dorfman, *J. Chem. Phys.,* **53**, 1281 (1970).
(11) J. A. Cowfer, D. G. Keil, J. V. Michael, and C. Yeh, *J. Phys. Chem.,* **75**, 1584 (1971).
(12) J.-H. Hong, Ph.D. Thesis, University of Detroit, 1972.
(13) J. F. Barker, D. G. Keil, J. V. Michael, and D. T. Osborne, *J. Chem. Phys.,* **52**, 2079 (1970).
(14) J. F. Barker and J. V. Michael, *J. Opt. Soc. Amer.,* **58**, 1615 (1968).
(15) D. Davis and W. Braun, *Appl. Opt.,* **7**, 2071 (1968).
(16) M. J. Kurylo, N. C. Peterson, and W. Braun, *J. Chem. Phys.,* **53**, 2776 (1970).
(17) W. Braun, A. M. Bass, and D. D. Davis, *J. Opt. Soc. Amer.,* **60**, 166 (1970).
(18) B. Khouw, J. E. Morgan, and H. I. Schiff, *J. Chem. Phys.,* **50**, 66 (1969).
(19) Dah Yu Cheng and P. L. Blackshear, Jr., *J. Chem. Phys.,* **56**, 213 (1972).
(20) A. Gelb and S. K. Kim, *J. Chem. Phys.,* **55**, 4935 (1971).
(21) B. J. Wood and H. Wise, *J. Phys. Chem.,* **66**, 1049 (1962).
(22) K. J. Laidler, "Chemical Kinetics," McGraw-Hill, New York, N. Y., 1965, Chapter 6.
(23) D. C. Ham, D. W. Trainor, and F. Kaufman, *J. Chem. Phys.,* **53**, 4395 (1970).
(24) S. Cushman and J. M. Lafferty, Ed., "Scientific Foundations of Vacuum Technique," Wiley, New York, N. Y., 1962, Chapter 6.
(25) J. C. Hirschfelder, C. F. Curtiss, and R. B. Byrd, "Molecular Theory of Gases and Liquids," Wiley, New York, N. Y., 1954.

Kinetics of the Shock-Induced Competitive Dehydrofluorinations of 1,1,2-Trifluoroethane[1a]

M. V. C. Sekhar[1b] and E. Tschuikow-Roux*

Department of Chemistry, University of Calgary, Calgary, Alberta, Canada, T2N 1N4   (Received August 23, 1973)

The thermal decomposition of 1,1,2-trifluoroethane between 1100 and 1250°K gives three isomeric difluoroethylenes as the major carbon-containing products. The rate constants for the three molecular elimination processes $CH_2FCHF_2 \rightarrow CH_2CF_2 + HF$ (k_1), $CH_2FCHF_2 \rightarrow trans\text{-}CHFCHF + HF$ (k_2), and $CH_2FCHF_2 \rightarrow cis\text{-}CHFCHF + HF$ (k_3) have been evaluated to be log $(k_1/\text{sec}^{-1}) = 13.0 \pm 0.5 - (65.4 \pm 2.6)/2.303RT$, log $(k_2/\text{sec}^{-1}) = 14.1 \pm 0.5 - (69.1 \pm 2.9)/2.303RT$, and log $(k_3/\text{sec}^{-1}) = 13.5 \pm 0.5 - (64.5 \pm 2.6)/2.303RT$ where R is in kcal mol^{-1}. The experimental Arrhenius parameters were found to be in good agreement with those predicted theoretically using a *modified* semiion pair model. The observed differences in the three rate constants can be explained in terms of intramolecular interactions of the fluorine atoms.

Introduction

In recent years the shock-tube technique has been successfully employed for studying the thermal decompositions of several fluorinated hydrocarbons.[2-4] In these studies, it has been shown that the molecular elimination of hydrogen fluoride is the predominant reaction, the side reactions involving C–C bond rupture becoming more important with increase in temperature. Molecular dehydrofluorination in several fluoroethanes has also been observed in chemical activation studies.[3-8]

Among the fluoroethanes, 1,1,2-trifluoroethane is unique in that it is the only member of the series that undergoes dehydrofluorination giving more than one olefin. This was confirmed in two independent chemical acti-

vation studies[7,8] on CH_2FCHF_2 which decomposed to three isomeric difluoroethylenes: 1,1-difluoroethylene and *cis*- and *trans*-1,2-difluoroethylenes. Of these the two geometric isomers, *cis*- and *trans*-CHFCHF are formed through transition states that are diasterioisomers and hence provide the advantage of making a comparison of two reactions in which the same bonds are made and broken. The 1,1-difluoroethylene, CF_2CH_2, is also formed in the decomposition of 1,1,1-trifluoroethane.[9] Thus the isomeric trifluoroethanes CH_3CF_3 and CH_2FCHF_2 constitute an interesting pair to study the influence of the position of the fluorine atom on the dehydrofluorination reaction.

The present work deals with the hitherto unreported pyrolitic decomposition of 1,1,2-trifluoroethane.

Experimental Section

The reactant CH_2FCHF_2 (Phillips Petroleum Co.) and the product gases, CH_2CF_2, and *cis*- and *trans*-CHFCHF (Peninsular Chem Research Inc.) were purified by bulb-to-bulb distillation using methanol and *n*-pentane slush baths. The purity of these gases was determined by gc analysis to be better than 99.5%. Reaction mixtures of ~0.5 and ~1% trifluoroethane in argon (Matheson, 99.998% stated purity) were used for quantitative kinetic data runs. In the case of exploratory runs above 1300°K a 5% CH_2FCHF_2-Ar mixture was used for total product analysis. The reaction mixtures were prepared in large stainless steel tanks and were allowed to mix thoroughly before use.

The modified single pulse shock tube, the recording devices, and the operating procedure were the same as described in previous communications.[10,11]

After initiation of the shock, the ball valve was closed, isolating the reaction mixture in the end section. Samples of the fully mixed gases were then withdrawn and analyzed in two ways: qualitative product identification was carried out by means of a gc-coupled mass spectrometer (Finnigan Model 3000) and the results were verified using authentic samples; quantitative analyses by means of a Varian 1740 gas chromatograph equipped with a flame ionization detector were carried out using a 12-ft Porapak Q column and temperature programming (45–150°). Standard calibration mixtures were used to correct for the sensitivity of the flame ionization detector. Hydrogen fluoride was not identified quantitatively because of its reactivity with the shock tube walls.

Data Reduction and Results. The reflected shock conditions were calculated from measured incident and reflected shock velocities.[12] The reaction dwell time and the cooling corrections were evaluated by a previously described method.[10,13]

Between 1100 and 1250°K the three isomeric difluoroethylenes were the major reaction products. However, above 1300°K, as many as 15 products were formed. Some of these were identified as CH_3F, CH_2F_2, CHF_3, CH_2CHF, CF_2CHF, CH_2FCH_2F, CHF_2CHF_2, CH_3CHF_2, and CF_3CH_2F. Unfortunately, the formation of these compounds could not be studied in detail but it does indicate the presence of a reaction channel involving C–C bond scission (see Discussion).

Below 1250°K, the three difluoroethylenes constitute nearly 93% of the total products formed. The rest of the reacted mixture consisted primarily of vinyl fluoride and trifluoroethylene. By analogy with the behavior of the rest of the fluoroethanes and coupled with the fact that the difluoroethylenes were the predominant products, it is con-

cluded that the following reactions represent the principal mechanism of decomposition of CH_2FCHF_2 below 1250°K.

$$CH_2FCHF_2 \xrightarrow{\begin{subarray}{l} k_1 \\ k_2 \\ k_3 \end{subarray}} \begin{array}{ll} CH_2CF_2 + HF & (1) \\ \textit{trans-}CHFCHF + HF & (2) \\ \textit{cis-}CHFCHF + HF & (3) \end{array}$$
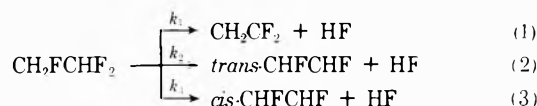
Using the theoretical mass balance

$$[CH_2FCHF_2]_0 = [CH_2FCHF_2]_t + [CH_2CF_2]_t + [t\text{-}CHFCHF]_t + [c\text{-}CHFCHF]_t \quad (I)$$

the three first-order rate constants are given as

$$k_1 = [R_1/(t\Sigma R_i)] \ln [1 + \Sigma R_i] \quad (II)$$

$$k_2 = [R_2/(t\Sigma R_i)] \ln [1 + \Sigma R_i] \quad (III)$$

$$k_3 = [R_3/(t\Sigma R_i)] \ln [1 + \Sigma R_i] \quad (IV)$$

where the R_i are product/reactant ratios at time t

$$R_1 = [CH_2CF_2]_t/[CH_2FCHF_2]_t$$

$$R_2 = [\textit{trans-}CHFCHF]_t/[CH_2FCHF_2]_t$$

$$R_3 = [\textit{cis-}CHFCHF]_t/[CH_2FCHF_2]_t$$

The rate constants and various shock parameters are listed in Table I.

Discussion

The unimolecular character of the hydrogen fluoride eliminations from fluoroethanes has been demonstrated by several workers.[14,15] Among the other possible primary processes, the homolytic bond scissions of the CF and CH bonds are energetically unfavorable. By analogy to the thermochemical data on other fluoroethanes[16,17] the bond energies of the C–F and C–H bonds in CH_2FCHF_2 are estimated to be 110 and 103 kcal mol^{-1}, respectively. Homolytic initiation followed by radical chain reactions could, of course, lead to an apparent overall activation energy considerably lower than the bond dissociation energies. However, the presence of such chain reactions would be indicated by the formation of other fluorohydrocarbon products in addition to the fluoroethylenes, and these were not observed at temperatures below 1250°K. As for the C–C bond scission reaction channel, it has been shown[4,18,19] that this reaction becomes competitive with HF eliminations only at temperatures above 1300°K. The presence of small amounts of vinyl fluoride and trifluoroethylene below 1300°K indicates the onset of this process and as expected at higher temperatures the C–C bond rupture does become important as evidenced by the large number of products. The radical chain reaction can therefore be excluded in the temperature range below ~1250°K and the formation of the $C_2H_2F_2$ isomers explained through reactions 1–3. The rate constants listed in Table I were obtained by neglecting the two side products C_2H_3F and C_2F_3H. In order to test whether this exclusion would affect the results, the calculations were repeated using a new mass balance equation

$$[CH_2FCHF_2]_0 = [CH_2FCHF_2]_t + [CH_2CF_2]_t + [t\text{-}CHFCHF]_t + [c\text{-}CHFCHF]_t + [C_2H_3F]_t + [C_2HF_3]_t \quad (V)$$

and it was found that the rate constants were affected only in their last digits.

Another possible side reaction that need be considered is the consecutive HF elimination from the product difluoroethylenes. However, earlier studies on fluoroethylenes[20,21] and specifically 1,1-difluoroethylene[20] have shown that these reactions require much higher activation ener-

Table I: Experimental Results

| Mach no.[a] | | P_b,[a] Torr | T_b,[a] °K | t, μsec | Product ratios[b] | | | k,[c] sec^{-1} | k_1, sec^{-1} | k_2, sec$^-$ | k_3, sec$^-$ |
W_{1i}	W_{2i}				R_1	R_2	R_3				
2.10	1.24	3321	1101	409	0.0098[d]	0.00230	0.00461	9.98	1.24	2.98	5.76
2.13	1.25	4318	1127	377	0.00060[d]	0.00195	0.00451	12.8	1.08	3.58	8.10
2.13	1.26	4370	1130	379	0.00105[d]	0.00254	0.00517	15.7	1.88	4.64	9.21
2.16	1.25	2715	1139	544	0.00422	0.0126	0.0229	31.9	3.37	10.4	18.1
2.15	1.26	4465	1157	402	0.00229[d]	0.00609	0.0123	30.5	3.36	9.17	18.0
2.20	1.24	2772	1163	141	0.00233[d]	0.00554	0.0125	44.4	5.05	12.5	26.8
2.18	1.26	2779	1167	457	0.00330[d]	0.0105	0.0212	49.8	4.68	15.2	29.9
2.19	1.27	2822	1169	552	0.00675	0.0210	0.0408	64.0	6.27	20.0	37.7
2.19	1.26	2796	1172	188	0.00281[d]	0.00835	0.0164	68.9	7.00	21.4	40.5
2.20	1.28	2862	1179	511	0.00684	0.0149	0.0299	67.7	8.93	19.9	38.9
2.20	1.26	2853	1182	130	0.00262[d]	0.00696	0.0142	69.1	7.59	20.9	40.7
2.20	1.26	2837	1182	309	0.00412[d]	0.0120	0.0216	82.8	9.04	26.7	47.0
2.20	1.27	2856	1182	405	0.00515[d]	0.0144	0.0275	63.7	6.95	19.9	36.8
2.20	1.29	2884	1188	183	0.00365[d]	0.0109	0.0201	98.0	10.3	31.6	56.1
2.22	1.27	2931	1189	571	0.0131	0.0390	0.0747	109	11.2	34.2	63.2
2.22	1.27	2907	1190	555	0.00918	0.0315	0.0555	94.9	9.01	31.7	54.1
2.20	1.27	2871	1190	220	0.00534[d]	0.0156	0.0278	103	11	33.9	58.1
2.21	1.28	2911	1192	655	0.0137	0.0457	0.0833	128	12.3	41.9	74.3
2.20	1.28	2881	1192	185	0.00422[d]	0.0117	0.0239	85.3	9.00	25.9	50.5
2.21	1.27	2897	1196	572	0.00890[d]	0.0226	0.0406	81.8	10.1	26.7	45.6
2.22	1.28	2941	1199	589	0.0143	0.0449	0.0812	134	13.7	43.8	76.8
2.23	1.28	2978	1202	554	0.0130	0.0341	0.0595	111	13.5	36.2	61.3
2.23	1.29	2705	1214	562	0.0151	0.0533	0.0950	170	15.7	56.6	98.2
2.23	1.30	3022	1218	549	0.0194	0.0601	0.1071	197	20.4	64.7	112
2.23	1.28	2995	1219	456	0.0142[d]	0.0397	0.0692	144	16.6	47.4	79.9
2.23	1.28	2992	1220	479	0.0176[d]	0.0524	0.0957	158	16.7	51.3	90.2
2.25	1.27	3022	1220	565	0.0176	0.0548	0.0957	156	16.3	52.0	87.9
2.24	1.28	2820	1223	564	0.0174	0.0580	0.100	209	20.6	69.8	118
2.25	1.29	3075	1228	547	0.0162	0.0475	0.0828	168	18.5	55.4	94.2
2.24	1.30	3052	1234	555	0.0182[d]	0.0510	0.0903	192	21.9	62.4	108
2.25	1.30	3095	1236	555	0.0218	0.0665	0.110	225	24.7	76.6	124
2.27	1.29	2820	1246	473	0.0234	0.0761	0.132	300	30.2	100	169

[a] W_{1i} and W_{2i} denote, respectively, incident and reflected shock Mach numbers relative to laboratory coordinates (reference speed of sound: argon at 298° K). P_b and T_b refer to pressure and temperature in the reflected shock zone. [b] R_1 = [CH_2CF_2]/[CH_2FCHF_2]; R_2 = [$trans$-CHFCHF]/[CH_2FCHF_2]; R_3 = [cis-CHFCHF]/[CH_2FCHF_2]. [c] Overall rate constant, k = k_1 + k_2 + k_3. 1 $\sim$1% CH_2FCHF_2 in Ar. Rest of the runs were made with $\sim$0.5% CH_2FCHF_2 in Ar.

gies than their saturated analogs and occur only at temperatures above the range of this study. Yet another possible side reaction is the cis–trans isomerization of the 1,2-difluoroethylenes. The rate constants[22a] and the activation energies for these reactions are of the same order of magnitude as those of reactions 1–3. However, when the rate constants k_1, k_2, and k_3 were recalculated taking into account the cis–trans isomerization reactions, it was found again that this affected the k values only in their last digits.[22b] Thus the three reactions 1–3 represent the only main processes that occur in the decomposition of 1,1,2-trifluoroethane below 1250°K.

The temperature dependence of the three rate constants is shown in Figure 1 and a least-squares analysis of the data gives log (k_1/sec^{-1}) = 13.0 ± 0.5 − (65.4 ± 2.6)/2.303RT, log (k_2/sec^{-1}) = 14.1 ± 0.5 − (69.1 ± 2.9)/2.303RT, and log (k_3/sec^{-1}) = 13.5 ± 0.5 − (64.5 ± 2.6)/2.303RT where R is in kcal mol^{-1} and the error limits are standard deviations.

α,β vs. α,α Eliminations. Recent experiments on vibrationally excited haloethanes produced by chemical activation have indicated[23,24] the occurence of three-center (α,α) HX eliminations in competition with the more common four-center (α,α) eliminations. This type of three-center elimination is, in principle, possible with CH_2FCHF_2

$$CH_2FCHF_2 \xrightarrow{(\alpha,\alpha)} \begin{cases} CH_2F\ddot{C}F + HF & (4) \\ \ddot{C}HCHF_2 + HF & (5) \end{cases}$$
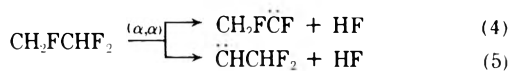
The α,α elimination is followed by rapid rearrangement of the carbene to give the olefin.

TABLE II: Ratios of $C_2H_2X_2$ Isomers Produced in the Decompositions of CH_2XCHX_2 Molecules

X	Temp, °K	Asym:trans:cis	Ref
F	393–597	1:1.06:3.12	8
F	293	1:3.8:6	7
F	1100–1250	1:2.7:4.6	This work
F		1:2:6	Free rotation[a]
Cl	298	1:2.1:3.2	24

[a] Based on the assumption that the three conformers d, e, and f have equal probability of decomposition which implies roughly equal energies for HF elimination and free rotation about the C–C bond, the probability of decomposition of anyone conformer is $^1/_3$. Since $trans$-CHFCHF can only be formed from the e form, and since two of the three ways in which this conformer eliminates lead to $trans$-CHFCHF the probability of its formation $(^2/_3)$ $(^1/_3)$ = $^2/_9$. Similarly the probability of formation of CH_2CF_2 which can be formed only from the e conformer is $^1/_9$. Finally, since the d and f conformers can decompose in only one way giving rise to cis-CHFCHF, the cis isomer has a probability of formation of $2(^1/_3)$ = $^2/_3$. Hence the ratio asym:trans:cis = 1:2:6.

$$\begin{matrix} CH_2F\ddot{C}F \\ \text{or} \\ \ddot{C}HCHF_2 \end{matrix} \longrightarrow \begin{cases} CH_2CF_2 \\ trans\text{-CHFCHF} \\ cis\text{-CHFCHF} \end{cases} \quad (6)$$
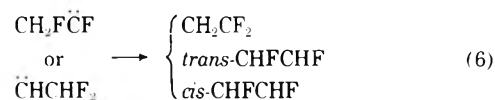
It has been argued[24] that carbenes such as $CH_2F\ddot{C}F$ are thermodynamically more stable than CHF_2CH due to π bonding between the halogen and the vacant p orbital of the carbene,[25] and hence reaction 4 is more likely to occur than reaction 5. Thus with CD_3CH_2F only four-center eliminations have been observed.[26] In the present case, it is not possible to distinguish between three- and four-center eliminations. However, Kim, et al.,[26] have shown that

the three-center process in the case of CD_3CHF_2 is 18% of the total rate. After correction for the intramolecular isotope effects, an estimate for the α,α contribution of 10% was obtained in the case of CH_3CHF_2. By inference, we therefore conclude that the experimental Arrhenius parameters for CH_2FCHF_2 obtained in this study are a close estimate for the α,β process.

The Effect of Rotational Isomerism. The product distribution observed in this investigation is compared with other related systems in Table II. Unlike the rest of the fluoroethanes, CH_2FCHF_2 undergoes HF elimination to give three different products depending upon the rotational conformation of the reacting molecule. Microwave spectral studies[27] on CH_2FCHF_2 indicate that there are three stable forms of the molecule represented by the following Newman projection formulae.

a   b   c
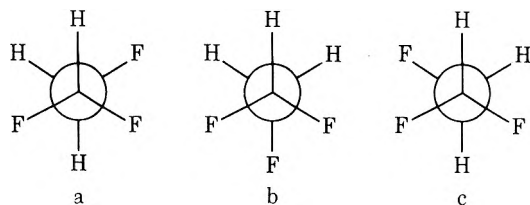
Based on calculations the two conformations a and c which are enantiomorphic are suggested to be more stable that the form b in contrast to the 1,2-difluoroethane rotational isomers. The three conformations d, e, and f correspond to the three maxima in the potential for internal rotation with the lower maximum corresponding to the e form. The planar four-center cyclic transition state requires that the H and F atoms forming hydrogen fluoride depart from the same side of the incipient double bond and such a transition state can be formed only with the three conformations d, e, and f. Of these the optically ac-

d   e   f
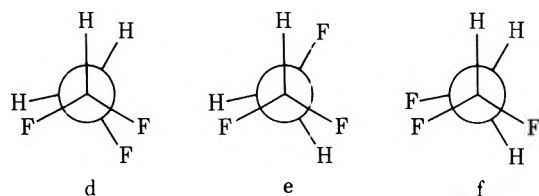
tive d and f forms eliminate HF to give *cis*-1,2-difluoroethylene, whereas the conformer e dehydrofluorinates to give either *trans*-1,2-difluoroethylene or 1,1-difluoroethylene. However, since the activation energies for the elimination reactions are large compared to the potential barrier for internal rotation, the relative populations of the ground state conformations are not reflected in the proportion of the final products.[28] If there were free rotation about the C–C bond *and* if the activation energies for the eliminations were about equal, then one would expect a product ratio of asymmetric:trans:cis equals 1:2:6. The experimental ratio is 1:2.7:4.6 and shows the effects of the hindered rotation and the small differences in the activation energies for the three eliminations. As seen from Table II, the agreement between the three studies on the observed product ratios is only qualitative which is probably due to the wide difference in the temperature ranges of these studies.

A Factor Calculations. The preexponential factor A is related to the entropy of activation ΔS^* by the relation

$$A = (ekT/h) \exp(\Delta S^*/R) \quad \text{(VI)}$$

and a rigorous evaluation of ΔS^* would require a normal coordinate analysis on the transition state and the reac-
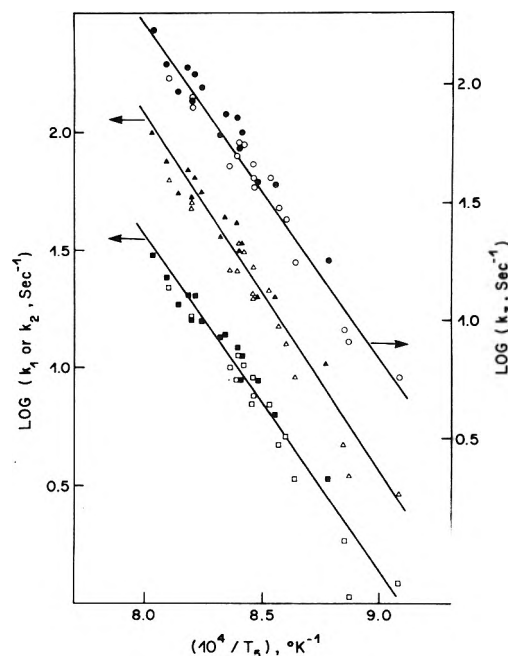
Figure 1. Temperature dependence of the rate constants for HF elimination from CH_2FCHF_2: squares, k_1; triangles, k_3; circles, k_3. Filled symbols refer to runs with 1% reactant in Ar; open symbols refer to runs with 0.5% reactant in Ar.

TABLE III: Evaluation of Entropies of Activation, ΔS^* (gibbs mol^{-1}) at 1200°K

| | HF elimination products from CH_2FCHF_2 | | |
	CH$_2$CF$_2$	*trans*-CHFCHF	*cis*-CHFCHF
C–C torsional frequency, cm^{-1}	357[a]	165[b]	248[b]
S_{tors}^*	3.7	5.2	4.4
S_{bir}	7.5	7.5	7.5
ΔS_{int}^*	~0	~0	~0
ΔS_{sym}^{*c}	0	2.8	1.4
ΔS_{total}^*	−3.8	0.5	−1.7
Log A_{calcd}, sec^{-1}		13.9	13.5
Log A_{expt}, sec^{-1}	13.0	14.1	13.5

[a] S. Brodersen and A. Langseth, *J. Mol. Spectrosc.*, **3**, 114 (1959). [b] N. C. Craig and J. Overend, *J. Chem. Phys.*, **51**, 1127 (1969). [c] The transition state leading to CH_2CF_2 does not have any optical isomers, $n^* = n = 1$ and also $(\sigma/\sigma^*) = 1$. For the formation of *trans*-CHFCHF, $n^* = 2, r = 1$, and $(\sigma/\sigma^*) = 2$, while the *cis*-CHFCHF, $n^* = n = 2$ and $(\sigma/\sigma^*) = 2$.

TABLE IV: Thermochemical Values^a (kcal mol^{-1})

Fluoroethane	$\Delta H_f^{\circ 211}$	Fluoroethylene	$\Delta H_f^{\circ 211}$
CH$_3$CHF	−62.5	C$_2$H$_4$	12.5[d]
CH$_3$CHF$_2$	−118.0 ± 1	C$_2$H$_3$F	−31.6[d]
CH$_2$FCH$_2$F	−103.7 ± 2[b]	CH$_2$CF$_2$	−82.5 ± 2.4
CH$_3$CF$_3$	−170.6 ± 1[c]	CHFCHF	−75.2[e]
CH$_2$FCHF$_2$	−158.9 ± 1	C$_2$HF$_2$	−118.5 ± 0.7
CH$_2$FCF$_3$	−211.8 ± 2[b]		
CHF$_2$CHF$_2$	−201.1 ± 2[b]	HF	−64.8[d]

^{a} All values taken from J. R. Lacher and H. A. Skinner, *J. Chem. Soc. A*, 1034 (1968), unless specified otherwise. ^{b} Derived from thermochemical calculations. ^{c} Based on group additivity contributions derived from $\Delta H_f^{\circ}{}_{298}$ values for C$_2$H$_6$ (−20.2) and C$_2$F$_6$ (−321.0 ± 1). ^{d} Reference 34. ^{e} Based on group additivity tables of Benson.[34]

tant. In view of the uncertain geometry of the activated complex, the much simpler group frequency method of Benson and O'Neal[29] was adopted to compute the entropies of activation. According to this method ΔS^* is given by

TABLE V: Arrhenius Parameters for HF Eliminations from Fluoroethanes

		Activation energy, kcal mol^{-1}				
Fluoroethane	C products	E_{caled}	E_{exptl}	Log A, sec^{-1}	Method[c]	Ref
CH_3CH_2F	C_2H_4	60.5	62.6	14.4	FS	14
			58.2	13.3	SP	3
			59.9	13.4	ST	3
CH_3CHF_2	C_2H_3F	61.3	61.9	13.3	FS	14
			65.0	13.5	ST	3
			61.9 ± 1.8	13.9 ± 0.3	SPST	a
CH_2FCH_2F	C_2H_3F	56.9	62.9	13.4	SP	15
CH_3CF_3	CH_2CF_2	67.7	61.4	12.1	FS	14
			73.6	13.8	ST	3
			68.7 ± 2.4	14.0 ± 0.4	SPST	9
CH_2FCHF_2	$C_2H_2F_2$[b]		65.9 ± 2.6	14.0 ± 0.5	SPST	This work
	CH_2CF_2	67.5	65.4 ± 2.6	13.0 ± 0.5	SPST	This work
	trans-CHFCHF	69.1	69.1 ± 2.9	14.1 ± 0.5	SPST	This work
	cis-CHFCHF		64.5 ± 2.6	13.5 ± 0.5	SPST	This work
CH_2FCF_3	C_2HF_3	73.0	70.7 ± 1.7	13.4 ± 0.3	SPST	4
CHF_2CHF_2	C_2HF_3	77.9	69.4 ± 3.1	13.3 ± 0.3	SPST	18

^{a} E. Tschuikow-Roux, W. J. Quiring, and J. M. Simmie, *J. Phys. Chem.*, **75**, 3195 (1971). ^{b} Overall rate constant for the formation of $C_2H_2F_2$ isomers. ^{c} FS = flow system; SP = static pyrolysis; ST = comparative shocktube; SPST = single pulse shock tube.

$$\Delta S^* = (S_{tors}{}^* - S_{hir}) + \Delta S_{int} + R \ln (n^*\sigma/n\sigma^*) \quad (VII)$$

where $(S_{tors}{}^* - S_{hir})$ is the entropy change in going from the hindered internal rotation of the ground state to the torsional mode of the complex, $\Delta S_{int}{}^*$ is the intrinsic entropy change of the vibrational modes in going from the ground state to the transition state, and the last term is the contribution due to symmetry changes. In the above equation, σ and σ^* are the overall symmetry numbers and n and n^* are the number of optical isomers of the ground and transition states, respectively. $\Delta S_{int}{}^*$ was calculated using the equation

$$\Delta S_{int}{}^* = \sum_i^{3N-8} S_i{}^* - \sum_i^{3N-7} S_i \quad (VIII)$$

where the vibrational frequency assignments were made by comparison with other fluoroethanes.[19] $S_{tors}{}^*$ was computed using torsion frequencies of $\frac{3}{2}$-order bonds which were taken as half the torsion frequency of the corresponding olefin.[29] The calculation of S_{hir} is involved due to the presence of more than one minimum in the potential function for internal rotation and hence an indirect method was adopted for its computation. Using the experimental entropy of activation for reaction 1 S_{hir} was evaluated from eq VII and VIII to be 7.5 eu at 1200°K. This value was then used in the subsequent calculations for reactions 2 and 3. The details of the calculations are given in Table III. The predicted values for the preexponential factors agree very well with the experiment.

Activation Energy Calculations. Maltman and Tschuikow-Roux[30] have proposed a modification to the semiion pair model of Benson and Bose[31] for the calculation of activation energies for addition reactions of olefins including halo-substituted polar olefins. The major aspect of this modification lies in the fact that the partial formal charge separation is treated as a variable of the system rather than being held constant and that true generalized bond order conservation is invoked. The necessary input parameters are the bond energies and bond lengths of the bonds undergoing change in the reaction. The partial formal charge separation was calculated from parameters related to these quantities. This method has been found to be very successful with the addition reactions of hydrogen halides to various olefins.

According to the method, the activation energy for the addition reaction, E_{ad}, is given by

$$E_{ad} = \sum_{i=1}^{4} E_i + E_{dip}$$

where the E_i represent the bond energies of the four partial bonds and E_{dip} is the energy contribution due to the interaction of the two induced dipoles. The bond energies for the partial bonds were calculated using a bond-energy–bond-order relationship similar to that of Johnston.[32] The dipole–dipole interaction was approximated to the interaction of two point dipoles of the same magnitude and orientation situated at the center of the two breaking bonds.

The activation energy for the elimination reaction, E_{el}, was then calculated from E_{ad} and the heat of reaction

$$E_{el} = E_{ad} + \Delta H°_{298} - RT$$

The heats of reaction for the elimination processes were calculated using either known values[33] of heats of formation or values derived from the group additivity method of Benson.[34] The various $\Delta H_f°$ values used are listed in Table IV and the calculated activation energies are given in Table V. Unfortunately the calculations could not be carried out for all the reactions in Table V, as reliable structural parameters for some of the fluoroethylenes are not available.

The experimentally observed activation energy difference of 4.6 kcal mol^{-1} between trans- and cis-CHFCHF is at first surprising. The two transition states are diastereoisomers and both reactions involve the breaking and the formation of the same bonds. However, the transition state for reaction 3 can be stabilized through p-p interaction[35] between the unshared electron pairs of the fluorine substituents, whereas such interaction is not possible with the transition state for reaction 2. Additional support that the reaction path leading to the cis olefin is one of lower energy is suggested by the fact that the cis-CHFCHF is more stable than the trans isomer. The increased stability of the cis isomer has been explained[36] in terms of resonance contributions from the ionic forms
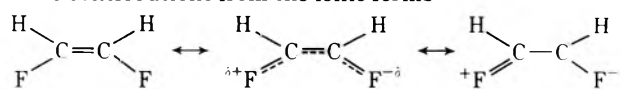
where the interaction between the two dipoles is energetically more favorable in the cis than in the trans isomer.

TABLE VI: Dehydrofluorination Rate Constant Ratios for α- and β-Fluorine Substitutions at 1200°K

CH_3CF_3	CH_3CHF_2	CH_2FCHF_2
0.07	1	0.24
CH_2FCF_3	CH_2FCHF_2	CHF_2CHF_2
0.03	1	0.05

Comparison with Other Systems Table V summarizes the rate constants for the thermal elimination reactions of fluoroethanes. As may be seen, the position of the fluorine atom does not significantly change the activation energy for HF elimination. Thus between the isomeric di- and tetrafluoroethanes the difference in the activation energies is only about 1 kcal mol^{-1}, which is well within the experimental uncertainty. Between the isomeric trifluoroethanes, the difference is somewhat larger, ~ 3 kcal mol^{-1}.

The effects of α- and β-fluoro substitutions are illustrated in Table VI, where the rate constant ratios correspond to a mean temperature of 1200°K. Unlike in the case of chloro- and bromoethanes, in fluoroethanes both α and β fluorinations decrease the rate of elimination. The following sequence shows the percentage increases in activation energy for α- and β-fluorine substitutions.

$$CH_3CF_3 \xleftarrow{11\%} CH_3CHF_2 \xrightarrow{3\%} CH_2FCHF_2$$

$$CH_2FCF_3 \xleftarrow{7\%} CH_2FCHF_2 \xrightarrow{5\%} CHF_2CHF_2$$
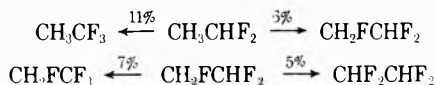
The more pronounced effect with the first series can be attributed to the larger change in the atomic charge densities in the rearrangement of the fluorine atoms in $C_2H_3F_3$ than in $C_2H_2F_4$. Based on microwave spectra, the C–F bond length in CH_3CF_3 has been reported[37] to be 1.335 ± 0.005 Å whereas in CH_2FCHF_2. the C–F bonds are 1.37 ± 0.01 Å and 1.35 ± 0.01 Å in the CH_2F and the CHF_2 groups, respectively.[38] In analogy with the fluorinated methanes, the shorter C–F bonds reflect an increase in the positive charge on the carbon atom and a strengthening of the C–F bond. Also the polarization along the C–C bond in CH_2FCHF_2 is expected to be smaller than in CH_3CF_3 which would tend to lower the C–C bond dissociation energy.

References and Notes

(1) (a) Work supported by the National Research Council of Canada. (b) Abstracted, in part, from Ph.D. Thesis of M. V. C. Sekhar, University of Calgary. 1973.
(2) D. C. Montagne and R. Walsh, *Ann. Rep. A, Chem. Soc. (London),* 175 (1971).
(3) P. Cadman, M. Day, A. W. Kirk, and A. F. Trotman-Dickenson, *Chem. Commun.,* 203 (1970).
(4) G. E. Millward and E. Tschuikow-Roux, *J. Phys. Chem.,* **76,** 292 (1972).
(5) J. A. Kerr, A. W. Kirk, B. V. O'Grady, D. C. Phillips, and A. F. Trotman-Dickenson, *Discuss. Faraday Soc.,* **44,** 263 (1967).
(6) H. W. Chang and D. W. Setser, *J. Amer. Chem. Soc.,* **91,** 7648 (1969).
(7) (a) J. T. Bryant, B. Kirtman, and G. O. Pritchard, *J. Phys. Chem.,* **71,** 1960 (1967); (b) G. O. Pritchard and J. T. Bryant, *ibid.,* **72,** 1603 (1968).
(8) D. C. Phillips and A. F. Trotman-Dickenson, *J. Chem. Soc. A,* 1144 (1968).
(9) E. Tschuikow-Roux and W. J. Quiring, *J. Phys. Chem.,* **75,** 295 (1971).
(10) E. Tschuikow-Roux, *Phys. Fluids,* **8,** 821 (1965).
(11) J. M. Simmie, W. J. Quiring, and E. Tschuikow-Roux, *J. Phys. Chem.,* **73,** 3830 (1969).
(12) E. Tschuikow-Roux, J. M. Simmie, and W. J. Quiring, *Astronaut. Acta,* **15,** 511 (1970).
(13) G. E. Millward and E. Tschuikow-Roux, *Int. J. Chem. Kinet.,* **4,** 559 (1972).
(14) D. Sianesi, G. Nelli, and R. Fontanelli, *Chem. Ind. (Milan),* **50,** 619 (1968).
(15) J. A. Kerr and D. M. Timlin, *Int. J. Chem. Kinet.,* **3,** 427 (1971).
(16) B. de B. Darwent, *Nat. Stand. Ref. Data Ser., Nat. Bur. Stand.,* 31 (1970).
(17) J. A. Kerr, *Chem. Rev.,* **66,** 465 (1966).
(18) G. E. Millward, R. Hartig, and E. Tschuikow-Roux, *J. Phys. Chem.,* **75,** 3195 (1971).
(19) E. Tschuikow-Roux, G. E. Millward, and W. J. Quiring, *J. Phys. Chem.,* **75,** 3493 (1971).
(20) J. M. Simmie and E. Tschuikow-Roux, *J. Phys. Chem.,* **74,** 4075 (1970).
(21) J. M. Simmie, W. J. Quiring, and E. Tschuikow-Roux, *J. Phys. Chem.,* **74,** 992 (1970).
(22) (a) P. M. Jeffers and W. Shaub, *J. Amer. Chem. Soc.,* **91,** 7706 (1969). (b) In this treatment we have not taken into account the possibility of HF-promoted isomerization of the 1 2-difluoroethylenes, as noted by one of the reviewers. It is felt that our mode of product analysis does not provide enough information to estimate this possible effect.
(23) M. J. Perona, J. T. Bryant, and G. O. Pritchard, *J. Amer. Chem. Soc.,* **90,** 4782 (1968).
(24) K. C. Kim and D. W. Setser, *J. Phys. Chem.,* **76,** 283 (1972).
(25) J. F. Harrison, *J. Amer. Chem. Soc.,* **93,** 4112 (1971).
(26) K. C. Kim, D. W. Setser, and B. E. Holmes, *J. Phys. Chem.,* **77,** 725 (1973).
(27) (a) I. A. Mukhtarov and R. I. Mukhtarov, *Opt. Spectrosk.,* **19,** 979 (1965); (b) I. A. Mukhtarov, *ibid.,* **20,** 352 (1966); (c) *Dokl. Akad. Nauk SSSR,* **151,** 1076 (1963); (d) I. A. Mukharov and R. I. Mukhtarov, *ibid.,* **180,** 150 (1968).
(28) D. Y. Curtin, *Rec. Chem. Progr.,* **15,** 111 (1954).
(29) H. E. O'Neal and S. W. Benson, *J. Phys. Chem.,* **71,** 2903 (1967).
(30) (a) K. R. Maltman and E. Tschuikow-Roux, to be submitted for publication; (b) K. R. Maltman, M.Sc. Thesis, University of Calgary, 1973.
(31) S. W. Benson and A. N. Bose, *J. Chem. Phys.,* **39,** 3463 (1963).
(32) H. S. Johnston, "Gas Phase Reaction Rate Theory," Ronald Press, New York, N. Y., 1966.
(33) J. R. Lacher and H. A. Skinner, *J. Chem. Soc. A,* 1034 (1968).
(34) S. W. Benson, "Thermochemical Kinetics," Wiley, New York, N. Y., 1968.
(35) W. A. Sheppard and C. M. Sharts, "Organic Fluorine Chemistry," W. A. Benjamin, New York, N. Y., 1969.
(36) (a) N. C. Craig and E. A. Entemann, *J. Amer. Chem. Soc.,* **83,** 3047 (1961); (b) H. G. Viehe, J. Dale, and E. Franchimont, *Chem. Ber.,* **97,** 244 (1964).
(37) W. F. Edgell, G. B. Miller, and J. W. Amy, *J. Amer. Chem. Soc.,* **79,** 2391 (1957).
(38) I. A. Mukhtarov, R. I. Mukhtarov, and E. I. Mukhtarov, *Izv. Akad. Nauk Azerb. SSR, Ser. Fiz.-Tekh. Mat. Nauk,* 74 (1967).

The Effect of Iron Impurities on the Thermal Decomposition of α-Lead Azide

Richard W. Hutchinson*

Explosives Division, Picatinny Arsenal, Dover, New Jersey 07801

and Fred P. Stein

Chemical Engineering Department, Lehigh University, Bethlehem, Pennsylvania 18015   *(Received October 11, 1973)*

Samples of pure α-lead azide and α-lead azide doped with known quantities of Fe^{2+} and $(FeN_3)^{2+}$ impurities were thermally decomposed. It was determined through the use of a mathematical model which compensated for the differences in particle size on the rate of decomposition that the Fe^{2+} impurity at 0.191 mol % increased the rate of penetration of the reaction front by 97% and decreased the length of the induction period by 68% relative to pure α-lead azide. The $(FeN_3)^{2+}$ impurity at a level of 0.0615 mol % increased the penetration rate by 12% and decreased the induction period by 48% relative to the pure material. At equal concentrations the Fe^{2+} impurity had a greater effect on increasing the penetration rate and a smaller effect on decreasing the induction period than did the $(FeN_3)^{2+}$ impurity. Neither impurity affected the Arrhenius temperature coefficient of the reaction or the percentage of total conversion.

Introduction

Fair and Forsyth[1] observed that doping lead azide with 0.05 to 0.5 mol % of Fe resulted in absorption and photoconductivity peaks at 6250 Å which were lacking in the pure material and, thus, demonstrated that small amounts of iron impurities significantly affect the energy levels within lead azide. If it is assumed that a relationship exists between the energy levels of a crystal and its thermal decomposition properties, then it is to be expected that the incorporation of Fe impurity in lead azide would alter its decomposition properties. The purpose of this work was to observe accurately the effects of iron impurities on the thermal decomposition of α-lead azide and, thereby, to provide an experimental basis for relating changes in crystalline energy levels to changes in thermal decomposition properties. It is inherently required that the impurities be incorporated in the azide at a low level such that the weight fraction of the impurity if considered in isolation would have a negligible effect (less than experimental error) on the measured decomposition properties.

The influences of Ag^+, Cu^{2+},[2] and $(BiN_3)^{2+}$[3] impurities on the thermal decomposition of lead azide have been investigated. Ag^+ and Cu^{2+} impurities were observed to have no effect on the Arrhenius temperature coefficient of penetration, whereas $(BiN_3)^{2+}$ was observed to reduce the temperature coefficient of penetration. Neither work took into account the possibility of a difference in particle size between the pure and doped azides. Pai Verneker and Forsyth[4] investigated the effects of iron impurities on the thermal sensitivity of lead azide but did not measure quantitatively the effects of iron impurities on the kinetics of lead azide decomposition.

Previous studies[5-7] of the thermal decomposition of lead azide mentioned qualitative observations of the effect of particle size on the rate of decomposition. The state of the art does not permit the preparation of different batches of α-lead azide powder with well controlled, identical particle-size distributions. Thus, preliminary to a quantitative study of the effects of impurities on the thermal decompo-

sition of α-lead azide it was necessary to characterize the effects of particle size on the decomposition. The results of that study[8] indicated that the effects of particle size could be of even greater magnitude than the effects of selected impurities. The model developed accounted in a quantitative way for the effects of particle size distribution, thereby permitting thermal decomposition data for α-lead azide powder of a given particle-size distribution to be transformed to another size and distribution. Using the model the effects of added impurities may be observed independent of particle-size effects. Furthermore, it was demonstrated that one of the derived parameters of the model had the physical significance of the rate of penetration of the reaction front into the crystal.

In this work, samples of pure, Fe^{2+}-doped and $(FeN_3)^{2+}$-doped α-lead azide were thermally decomposed *in vacuo.* The percentage of decomposition was monitored continuously throughout each run, and the percentage of total conversion was measured. These data were correlated with the model mentioned previously, and the model parameters generated for each type of lead azide were compared to observe the quantitative effects of the impurities independently of particle size.

Experimental Section

Apparatus and Technique. The apparatus and experimental technique used in this work have been described in detail elsewhere.[9] Decomposition of α-lead azide was monitored by collecting the released nitrogen, at pressures of less than 5×10^{-4} Torr, on activated charcoal which was maintained at the temperature of liquid nitrogen and by continuously recording the weight of the charcoal with an electrobalance. Decomposition of the approximately 10-mg samples was carried out in a constant-temperature furnace which was controlled to within $\pm 0.05°$. The furnace was designed such that the decomposing sample could "see" only surfaces that were at the controlled temperature.

Materials. Two batches of lead azide, designated batch I and II, were prepared by bubbling HN_3 through an

aqueous solution of lead nitrite. The lead nitrite solution was prepared by bubbling 99.995% pure $NO-NO_2$ gas mixture through triple-distilled, deionized water which contained Johnson, Matthey, and Co., Ltd., Specpure lead oxide (<10 ppm impurity). Batch I was pure α-lead azide, and batch II contained 0.191 mol % Fe^{2+} which was introduced in the following manner.

The iron impurity was prepared by the reaction of high-purity metallic iron with a 5% water solution of HN_3 to form a solution of iron-azide complex, $(FeN_3)^{2+}$.[10] A quantitative amount of the iron azide solution was mixed with the lead nitrite solution prior to the precipitation of the lead azide. In this medium the Fe^{3+} was reduced by the nitrite ions to Fe^{2+} and the solution turned from red to yellow. Addition of HN_3 to the system precipitated lead azide doped with iron. It was speculated that the iron existed as Fe^{2+} at lead sites.

The particles in both batches varied greatly in size from small needle-shaped particles approximately 60 μ long to the largest particles which appeared in the shapes of both needles and platelets with a length of 400 to 600 μ. Both batches were classified according to particle size by a hydraulic settling technique.[11] Three particle-size fractions were obtained for each of the two batches. The volume particle-size distribution of each sample was measured with a Coulter counter. The quantitative description of the size distributions is available in Table I of ref 8.

Three additional batches of α-lead azide, two of which contained the iron impurity as the $(FeN_3)^{2+}$ complex, were prepared by the reaction of an aqueous 5% solution of spectroscopic grade lead acetate, 99.999% pure, and an aqueous 5% solution of HN_3. Batch III contained 0.0615 mol % $(FeN_3)^{2+}$, batch IV was pure, and batch V contained 0.0124 mol % $(FeN_3)^{2+}$.

In preparing the $(FeN_3)^{2+}$-doped lead azide, a portion of the $(FeN_3)^{2+}$ solution previously described was mixed with the lead acetate solution prior to precipitation of the lead azide. Reduction of the iron did not occur under these conditions. HN_3 solution was then added to the lead acetate-$(FeN_3)^{2+}$ solution to precipitate iron-doped α-lead azide.

Electron spin resonance measurements indicated that the electronic state of the iron was a strongly perturbed $^6S_{5/2}$ state both within the $(FeN_3)^{2+}$-doped lead azide and within the initial iron-azide solution.[12] Based on this observation, it was hypothesized that the iron existed in batches III and V as $(FeN_3)^{2+}$ located at Pb^{2+} sites.

The particles of batches III, IV, and V were agglomerates of spherical crystallites with diameters of 1-2 μ. Both the size distribution of the agglomerates, as indicated by Coulter counter measurements, and the size of the crystallites, based on photomicrographs, appeared identical for the three batches—an unusual occurance for different batches of lead azide. Attempts to classify this material hydraulically failed due to the agglomerative structure of the particles.

X-Ray analysis showed that the lead azide in each of the five batches was entirely of the α form. Elemental analysis by spark-source mass spectrograph showed overall undesired impurities to be approximately 270 ppm by weight. Analysis of another batch of lead azide prepared by an identical procedure from the same ingredients as discussed herein, but not subjected to the hydraulic classification, had total undesirable impurities at a level of 150 ppm by weight. It is felt that a substantial part of the undesired impurities resulted from the handling of the

TABLE I: Model Parameters for Pure and Iron-Doped α-Lead Azide

Temp, °C	Sample	$k/\rho \times 1000$, μ/min	A, min/$\mu^{1/3}$
230	Batch I, pure	8.9 ± 0.2	69 ± 2
230	Batch II, 0.191 mol % Fe^{2+}	17.5 ± 0.4	22 ± 0.6
220	Batch IV, pure	5.0 ± 0.1	143 ± 4
220	Batch V, 0.0124 mol % $(FeN_3)^{2+}$	4.9 ± 0.1	109 ± 3
220	Batch III, 0.0615 mol % $(FeN_3)^{2+}$	5.6 ± 0.1	75 ± 2

material after preparation and that these impurities adhered superficially to the surface of the lead azide rather than being incorporated within the lattice.

There was no evidence that the iron impurities incorporated within the lead azide affected the particle-size distribution or morphology of the crystals. Indeed, photomicrographs of the three batches of lead azide prepared by the lead acetate technique appeared identical. Likewise, the shape of the crystals in batches I and II was very similar, and the difference between the particle-size distributions for these was no greater than the difference normally observed between batches of lead azide prepared by identical procedures.

The samples of lead azide were stored under vacuum and in the dark. These precautions were taken to avoid buildup of surface contaminants and photodecomposition which could interfere with experimental results. Photographic darkroom lights were used when handling the lead azide.

Results

Isothermal decomposition data were obtained as the weight of released nitrogen vs. time. These data were recast in the form of weight per cent decomposed vs. time.

Isothermal decomposition curves for the fine samples of pure batch I and the fine samples of Fe^{2+}-doped batch II at 230° are presented in Figure 1. A similar set of data for the coarse particles in batches I and II is presented in Figure 2 for the temperature of 230°. These decomposition data cannot be directly compared quantitatively because of the complicating influence of particle size. However, a qualitative comparison in Figure 1 shows that the fine sample of Fe^{2+}-doped α-lead azide began to decompose sooner and decomposed at a higher rate (greater slope) than did the fine sample of pure material. The hump in the initial portion of the decomposition curve for the coarse particles of pure α-lead azide, Figure 2, has been attributed to the fracturing of the very largest particles in the sample at the onset of the decomposition.[8] This hump complicates comparison between the decomposition data for the coarse particles of batches I and II; however, it can be observed, qualitatively, in Figure 2 that the Fe^{2+}-doped material did decompose at a faster rate than did the pure α-lead azide.

Isothermal decomposition data for pure batch IV and $(FeN_3)^{2+}$-doped batches III and V are presented in Figures 3 and 4 for temperatures of 220 and 210°, respectively. The three curves in each figure can be directly compared because the particle size distribution of these three batches was identical. Inspection of Figures 3 and 4 shows that the rate of decomposition was similar for the three batches, but the decomposition curves for the $(FeN_3)^{2+}$-doped material were shifted toward shorter times.
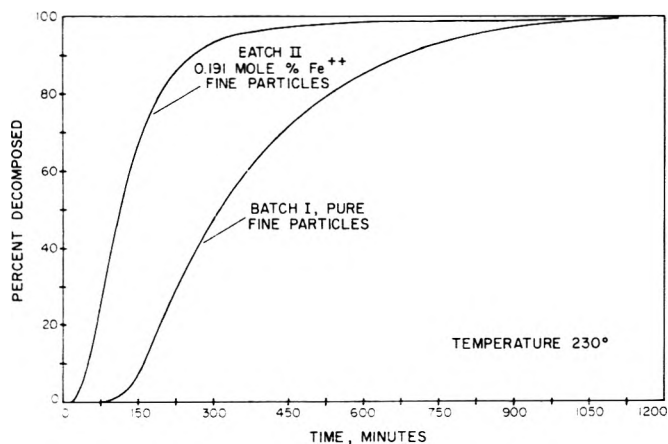
Figure 1. Isothermal decomposition of pure and Fe^{2+}-doped α-lead azide at 230°—fine particles.
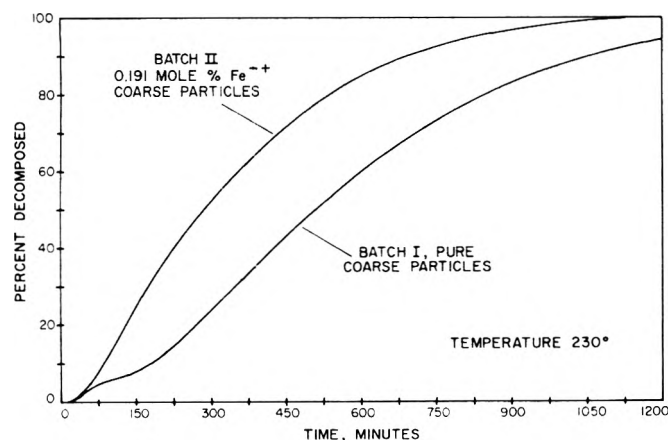
Figure 2. Isothermal decomposition of pure and Fe^{2+}-doped α-lead azide at 230°—coarse particles.
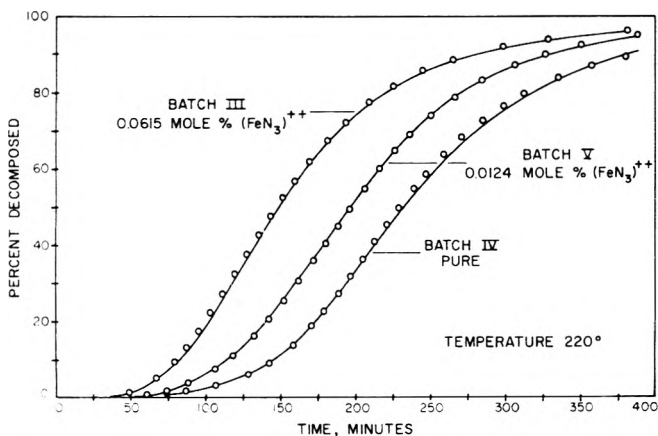
Figure 3. Isothermal decomposition of pure and $(FeN_3)^{2+}$ doped α-lead azide at 220°.

Isothermal decomposition data were collected at various temperatures to determine the effect of temperature on decomposition rate. Arrhenius temperature coefficients of the reaction were obtained and are discussed in a later section. Temperature was observed to have no influence on the relative effects of the impurities on decomposition.

Reproducibility of the decomposition data can be assessed by comparing the circles to the solid lines in Figure 3. The circles are from one run, whereas the solid lines are from another run performed under identical conditions but on a different day. Average reproducibility of the de-
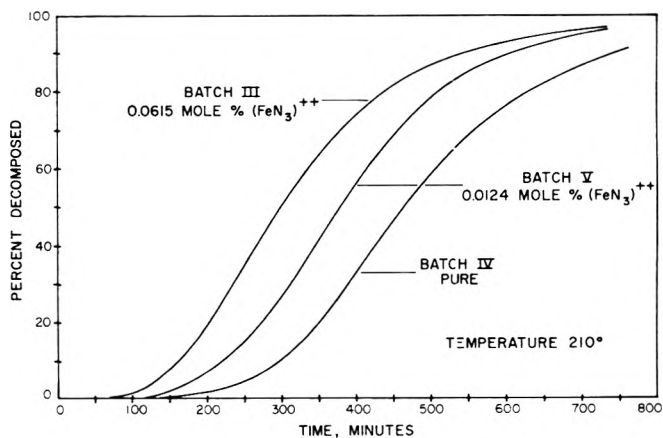
Figure 4. Isothermal decomposition of pure and $(FeN_3)^{2+}$-doped α-lead azide at 210°.

composition data was ±0.5% decomposed at any given time.

Analysis of Data and Discussion

A single-equation mathematical model[8] was developed which approximated the sigmoid-shaped thermal decomposition data for the various samples of lead azide to within ±1% decomposed at any given time. The model incorporated the independently measured particle-size distribution of the sample and contained two parameters, called the penetration-rate and the induction-period constants, which were independent of particle size. The accuracy of the model in discerning the effects of particle size on the rate of decomposition, that is to say, the independence of the model parameters on particle size, was on the order of ±10%. The penetration-rate constant, given the symbol k/ρ, was shown to have the physical significance of the rate of penetration of the reaction front into a single crystal of α-lead azide, as measured directly by Fox,[13] and to have an Arrhenius temperature coefficient within the range of values usually reported for α-lead azide.[8] The induction period constant, given the symbol A, reflected when the particles started to decompose. The model was fit to the experimental data from the five batches of α-lead azide over temperatures ranging from 210 to 250°. By comparing the numerical values of the model parameters generated for the different batches of lead azide, the effects of the iron impurities on decomposition were quantitatively observed independently of particle size effects. The model parameters for the five batches of α-lead azide at 220 and 230° are listed in Table I.

The Fe^{2+} impurity at a level of 0.191 mol % effected an increase of the penetration-rate constant by 97% and a decrease of the induction period constant by 68%. Thus, the Fe^{2+}-doped α-lead azide decomposed at a rate of nearly double that of the pure lead azide and started to decompose in approximately one-third of the time required by the pure material.

Lead azide containing 0.0615 mol % $(FeN_3)^{2+}$ had a penetration rate 12% greater than pure batch IV and an induction period constant 48% less than that of the pure material. The $(FeN_3)^{2+}$ impurity at the lower level of 0.0124 mol % did not have an observable effect on penetration rate but did reduce the induction period constant by 24%. Thus, the impurity $(FeN_3)^{2+}$ had a weak effect on increasing the rate of reaction but had a strong effect on reducing the induction period.

Batch V contained only one-fifth the concentration of

TABLE II: Temperature Coefficients for Pure and Iron-Doped α-Lead Azide

Sample	ΔE_{mr}, kcal/ mol	$\Delta E_{k/\rho}$, kcal/ mol	ΔE_A, kcal/ mol
Batch I, pure	35	35	35
Batch II, 0.191 mol % Fe^{2+}	36	37	37
Batch IV, pure	30	28	35
Batch V, 0.0124 mol % $(FeN_3)^{2+}$	30	29	32
Batch III, 0.0615 mol % $(FeN_3)^{2+}$	33	31	33

$(FeN_3)^{2+}$ impurity contained in batch III, but the lower amount of $(FeN_3)^{2+}$ impurity had one-half the effect on reducing the induction-period constant as did the larger amount. The following equation relates the induction period constant to the concentration of $(FeN_3)^{2+}$ for batches III, IV, and V

$$A(\text{doped}) = A(\text{pure}) - 274(\text{mol } \% \, (FeN_3)^{2+})^{1/2} \quad (1)$$

A linear relationship was used to relate penetration rate to the level of $(FeN_3)^{2+}$ impurity

$$(k/\rho)[\text{doped}] = (k/\rho)[\text{pure}] + 9.75 \times 10^{-3}(\text{mol } \% \, FeN_3{}^{2+}) \quad (2)$$

Equation 2 gives the effect of $(FeN_3)^{2+}$ impurity at the low level of 0.0124 mol % to be of the same magnitude as the reproducibility of the data, consistent with the experimental observation.

Equations 1 and 2 were used to predict k/ρ and A for α-lead azide containing $(FeN_3)^{2+}$ at the same concentration as the Fe^{2+} impurity in batch II, 0.191 mol %. The predicted values of $k/\rho \times 1000$ and A for α-lead azide containing 0.191 mol % $(FeN_3)^{2+}$ are 6.8 μ/min and 25 min/$\mu^{1/3}$, respectively. These values correspond to a 36% increase in penetration rate and a 83% decrease in induction period relative to the values for pure batch IV. Fe^{2+} at this same level increased k/ρ by 97% and decreased A by 68%. These effects can be directly compared to observe the relative effects of the Fe^{2+} and the $(FeN_3)^{2+}$ impurities on the thermal decomposition of α-lead azide: the Fe^{2+} impurity had approximately three times the effect of increasing the reaction penetration rate as did the $(FeN_3)^{2+}$ impurity; the $(FeN_3)^{2-}$ impurity effected a decrease of the induction period constant 1.2 times greater than did the Fe^{2+} impurity.

The percentage of total conversion was obtained for each decomposition run by comparing the weight of nitrogen collected to the weight of lead azide introduced into the reaction chamber. The percentages of total conversion for the various batches of lead azide were close to 96% for thermal decomposition. When samples from each batch were exploded, the percentages of total conversion were greater than 99%. There was no measurable effect of the iron impurities on total conversion.

Temperature coefficients of the experimental maximum rates of decomposition, ΔE_{mr}, of the penetration-rate constants, $\Delta E_{k/\rho}$, and of the induction-period constants, ΔE_A, were determined for each batch of lead azide and are listed in Table II. The average fit of the Arrhenius equation to the data was ±1 kcal/mol.

It is expected that ΔE_{mr} and $\Delta E_{k/\rho}$ should be related to the mechanism controlling penetration of the reaction interface into the crystal, while the temperature coefficient of the induction period, ΔE_A, should be related to the mechanism controlling the onset of reaction. The data

presented in Table II do not show a significant difference between the temperature coefficients related to induction period and those related to penetration rate. This observation supports the theory that there is but one mechanism controlling both the start and the advance of thermal decomposition in α-lead azide. Furthermore, the equality of induction and penetration temperature coefficients precludes the possibility of a surface contaminate decomposition as the controlling mechanism during the induction period. Past work with lead azide coated with carbonates has shown that the temperature coefficient for carbonate decomposition is approximately 15 kcal/mol.[7]

The apparent 1-3 kcal/mol increase in the various temperature coefficients for the Fe^{2+} doped material (compare batches I and II) and for the $(FeN_3)^{2+}$ doped material compare batches III and IV) is of the same order of magnitude as is the accuracy of the fit of the Arrhenius equation to the data. Neither of the iron impurities had any real effect on the temperature coefficients. This result is in contrast to the findings of Singh,[3] who observed that the $(BiN_3)^{2+}$ (0.24 wt %) impurity reduced the temperature coefficient of penetration for thermally decomposing lead azide by 12 kcal/mol but is similar to the findings with Ag^+ and Cu^{2+} impurities.[2]

The negligible effect of both Fe^{2+} and $(FeN_3)^{2-}$ impurities on the temperature coefficients of induction and penetration is an indication that the impurities did not significantly alter the magnitude of the rate-controlling energy barrier. In all likelihood, the impurities did not alter the mechanism of the rate-controlling step either, since it would be an unlikely coincidence for an alternate mechanism to have the same ΔE as did the original mechanism. The iron impurities did strongly affect both the induction and decomposition properties of the α-lead azide. Hence, the Fe^{2+} and $(FeN_3)^{2+}$ impurities must have affected the kinetics of decomposition but left the mechanism of decomposition unchanged.

The effects of particle size were clearly distinguished from the effects of doping on the thermal decomposition of α-lead azide. Iron impurities in concentrations of approximately 0.1% were observed to alter the kinetics of thermal decomposition of α-lead azide significantly.

References and Notes

(1) H. D. Fair, Jr., and A. C. Forsyth, "Reactivity of Solids." Wiley-Interscience, New York, N. Y., 1969, p 83.
(2) G. G. Savel'yev, Yu. A. Zakharov, G. T. Shechkow, and R. A. Vasyutkova, *Izv. Tomskogo Politekhn. In-ta*, **151**, 40 (1966).
(3) K. Singh, *Indian J. Chem.*, **7**, 694 (1969).
(4) V. R. Pai Verneker and A. C. Forsyth, *J. Phys. Chem.*, **72**, 111 (1968).
(5) W. E. Garner and A. S. Gomm, *J. Chem. Soc.*, 2123 (1931).
(6) F. P. Bowden and K. Singh, *Proc. Roy. Soc. Ser. A.* **227**, 22 (1954).
(7) P. J. F. Griffiths and J. M. Groocock, *J. Chem. Soc.*, 3380 (1957).
(8) R. W. Hutchinson, S. Kleinberg, and F. P. Stein, *J. Phy. Chem.*, **77**, 870 (1973).
(9) S. Kleinberg and F. P. Stein, *Ind. Eng. Chem., Fundam.*, **11**, 134 (1972).
(10) R. M. Wallace and E. K. Dukes, *J. Phys. Chem.*, **65**, 2094 (1961).
(11) R. W. Hutchinson and F. P. Stein, *Ind. Eng. Chem., Fundam.*, **10**, 635 (1971).
(12) D. S. Downs, A. C. Forsyth, H. D. Fair, Jr., submitted for publication.
(13) P. G. Fox, *J. Solid State Chem.*, **2**, 491 (1970).

Absolute Quenching Cross Sections of Hg(^{3}P$_1$) with Various Molecules

J. V. Michael* and G. N. Suess

Department of Chemistry, Carnegie-Mellon University, Pittsburgh, Pennsylvania 15213 (Received July 30, 1973)

The absolute quenching cross sections for Hg(^{3}P$_1$) with a number of quenching gases have been obtained in a steady-state photolytic experiment. The intensity of 2537-Å emission has been followed as a function of absorbed intensity, and also pressure of the quenching gas. Low Hg concentrations are maintained in order to avoid the complication of radiation imprisonment. Quenching rate constants are determined from modified Stern–Volmer plots. The results are compared to cross sections from Zemansky type experiments on a relative basis and in several cases to the absolute results of Yarwood, Strausz, and Gunning who applied Holstein theory to Zemansky type experimental results. Comparison is also made to other low opacity studies and, where possible, to the relative cross sections determined from chemical methods. Generally, good agreement is obtained. NO provides the only gross disagreement in these comparisons of the nine molecules studied.

Introduction

The quenching of the ^{3}P$_1$ state of mercury by a foreign gas represents probably the most extensively investigated and most useful primary photochemical system. The fundamental photophysical processes in this system are indicated in the following mechanism

$$Hg(^1S_0) + h\nu_{2537} \longrightarrow Hg(^3P_1) \tag{1}$$

$$Hg(^3P_1) \longrightarrow Hg(^1S_0) + h\nu_{2537} \tag{2}$$

$$Hg(^3P_1) + Q \longrightarrow Hg(^1S_0) + Q^* \tag{3}$$

$$\longrightarrow Hg(^3P_0) + Q^{**} \tag{4}$$
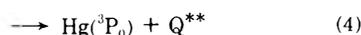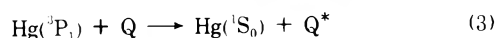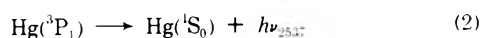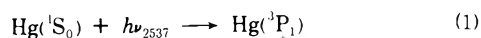
Deactivation of Hg(^{3}P$_1$) to the ground state by chemical quenching has not been included in this mechanism. Even though such a process may be important with a particular molecule, this experiment measures the total or overall reaction rate of Hg(^{3}P$_1$) with various acceptor molecules. Therefore dissection of the nature of the quenching process is not the goal of this research.

Mercury photosensitization has been the subject of thorough reviews.[1-3] Several experimental methods have been developed to obtain the total bimolecular quenching rate constant, k_Q. Traditionally, the efficiency for this energy transfer has been reported as an effective cross section, σ_Q^2, computed with the simple collision theory expression

$$\sigma_Q^2 = k_Q \left[8\pi RT \frac{M_{Hg} + M_Q}{M_{Hg} M_Q} \right]^{-1/2} \tag{I}$$

M_{Hg} and M_Q are the atomic and molecular weights of mercury and the quencher species, respectively. In the microfilm edition we present a review of the various experimental methods.[4]

In spite of advances in experimental techniques, many studies continue to be plagued by radiation imprisonment. Many workers have attempted to assess its effects theoretically as did the early workers. Only a few have tried to minimize or eliminate the phenomenon experimentally. Investigation of quenching as a function of Hg concentration has been reported.[22,28] Alternatively, sufficiently low Hg concentrations have been obtained[16,17,23-25] so as to make imprisonment nearly negligible. Of these, only the cross section of C$_2$H$_4$ reported by Yang[28] has

been determined by measurement of the 2537-Å emission intensity as a function of quencher pressure.

In this study, the quenching of Hg(^{3}P$_1$) by a variety of gases has been investigated. The quenching molecules include H$_2$, O$_2$, CO, NO, N$_2$O, C$_2$H$_4$, C$_3$H$_6$, *cis*-2-C$_4$H$_8$ and *n*-C$_4$H$_{10}$. The total quenching rate constants have been extracted from Stern–Volmer plots which were obtained from a measurement of the intensity of 2537-Å emission as a function of absorbed intensity and pressure of the quenching gas in a steady-state photolysis at sufficiently low H$_2$ concentrations to minimize the effects of imprisonment. This work represents an attempt to remove ambiguities which exist in cross sections due to this effect.

Experimental Section

A schematic diagram of the experimental apparatus is presented in Figure 1. A 6-W low-pressure mercury resonance lamp serves as the source of the resonance radiation. This lamp consists of a flat spiral about 5 cm in diameter constructed from 7-mm quartz tubing. Cooling of the lamp by a flow of compressed air maintained a low mercury vapor pressure in the lamp and minimized the reversal of the 2537-Å line.

Radiation from the mercury resonance lamp passed through a Baird Atomic interference filter which had a peak transmittance of 5% at 2600 Å and a width at half-maximum of 350 Å. A quartz lens collimated the beam which then passed through the photolysis cell. The T-shaped cell, fabricated from quartz, is 6.3 cm long and 3.8 cm in diameter. An observation window, 1.9 cm in diameter, midway between the end windows facilitates detection of the light emitted at right angles to the incident beam. The cell is joined through a stopcock and cold trap, which contains a drop of mercury, to a conventional Pyrex vacuum line.

The light transmitted from the cell is focused by another quartz lens onto an RCA 935 phototube. Any light through the observation port is filtered by a broadband uv filter with a peak transmittance of 83% at 3300 Å and approximately 30% transmittance at 2537 Å. An RCA 1P28 photomultiplier tube then receives the light through the filter. The currents from the two photosensitive devices are measured with and amplified by Keithley 610B electrometers for simultaneous recording on two potentiometric recorders.
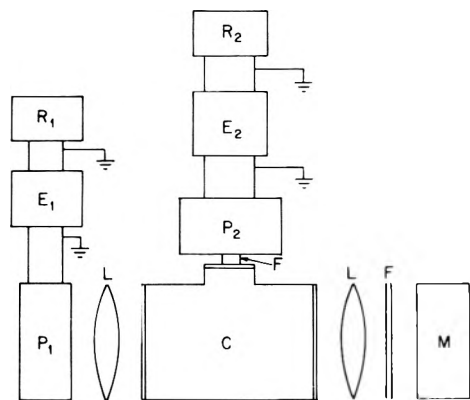
Figure 1. Schematic diagram of the apparatus: M, low-pressure mercury lamp; C, reaction cell; P$_1$ and P$_2$, phototubes; E$_1$ and E$_2$, electrometers; R$_1$ and R$_2$, potentiometric recorders; F. filters; L, quartz lenses.

The mercury atom concentration in the cell was regulated by the temperature of the trap adjacent to the cell. Calibration of the transmittance (I/I_0) to the mercury atom concentration was accomplished by the use of slush baths at different temperatures which were measured with a chromel–alumel thermocouple with ice water as a reference. The atom concentration was calculated from the vapor pressure of Hg at these temperatures.[29] I_0 was measured with a liquid nitrogen bath on the trap.

The effect of desorption of mercury from the walls of the initially well-cleaned photolysis cell was examined by closing off the cell after evacuation of the mercury with liquid nitrogen. After 15 min the transmitted intensity showed no change. The emission intensity had increased only slightly. The increase in this signal was approximately that which would result if the trap temperature were changed from −196 (liquid nitrogen bath) to −77° (Dry Ice–acetone slush bath). At these temperatures, the vapor pressure of mercury is less than 10^{-6} Torr. As a result, the effect of desorption from the walls on the regulation of atom concentration was considered to be negligible.

Initially, mercury vapor is removed from the cell by cooling the adjacent trap with liquid nitrogen. The liquid nitrogen bath is replaced by a Dry Ice–acetone slush in order to avoid condensation of the quenching gas and still maintain low mercury concentration. The quenching gas is admitted to the cell and the pressure is measured to within 10 μ with a previously calibrated tilting McCleod gauge. Initial output from the photosensitive devices is measured, and then the bath is removed. As the trap warms, mercury diffuses into the cell and the photocurrents are recorded with continuous variation in the mercury concentration. Typically, mercury was admitted until the intensity fell to approximately 75% of the initial value. Occasionally the pressure was measured during a run to examine the effect of the changing temperature of the trap. At no time was the pressure increase greater than the uncertainty in the initial measurement. Measurement in this manner requires only several minutes for a run and permits repetition for improved statistical data analysis.

Under these conditions, perturbation of the quenching rate because of product accumulation is negligible. Estimates[30] of absorbed intensities have been made from the H$_2$ yields in the photosensitized decompositions of propane and butane. On the extreme assumption of unit conversion efficiency to products for the molecules considered

in this work, a product concentration of 2.5 × 10^{13} molecules/cc results from a typical run time of 120 sec. If the quencher concentration is typically taken to be 1.6 × 10^{16} molecules/cc (0.5 Torr), this is only 0.15% conversion. For most of the quenching species in this study, the quenching rate constant of the product is less than or equal to that of the quencher. For quenching by butane however, the quenching rate constant of the product butene is about 10 times greater than that of butane. In this case, the quenching rate by product at these concentrations is only 1.5% of the rate by the quenching gas. After three runs, this fraction would be about 4.5% which is still less than the experimental error of 5–15%. For these estimates, the actual conditions of the experiment have been exaggerated for a maximum estimate of the product concentration. Therefore, no complication due to competitive quenching by reaction products is indicated.

Research grade H$_2$ (99.99%) from Air Products, Inc., CO (99.99%), and O$_2$ (99.99%) from Linde Division, Union Carbide Corp., were all used without further purification.

Technical grade NO and N$_2$O from Matheson Compressed Gases, Inc., and Air Products, respectively, CP grade C$_2$H$_4$ and C$_3$H$_6$ and instrument grade n-C$_4$H$_{10}$ from Matheson, and research grade cis-2-C$_4$H$_8$ from Phillips Petroleum were all purified by bulb-to-bulb vacuum distillation.

Results

In the steady-state photolysis of a mixture of mercury and added quencher the concentration of Hg(^{3}P$_1$) may be obtained from the mechanism of reactions 1–4, and the resulting Stern–Volmer equation can be derived

$$\frac{I_a}{I_f} = 1 + \frac{k_Q}{k_f}[Q] \tag{II}$$

I_a/I_f is the ratio of the absorbed intensity of 2537-Å light to the emitted intensity. A plot of I_a/I_f against the concentration of quencher should result in a straight line with the slope k_Q/k_f from this equation. The quenching rate constant is readily extracted if k_f is known. If radiation imprisonment is negligible, k_f becomes the inverse of the natural lifetime of Hg(^{3}P$_1$). The most recent experimental determinations have led to an average of 1.14 × 10^{-7} sec for this lifetime.[31]

In this experiment, the photocurrent outputs are proportional to the transmitted and emitted light intensities. The results of an experiment in the absence of added gas is presented in Figure 2 where the transmitted photocurrent, i_t, is plotted against the emission photocurrent, i_f. As the transmittance decreases, the emission intensity increases. The plot is linear at high transmittance (low [Hg]) and becomes curved with decreasing transmittance. The curvature results from radiation imprisonment and also an end-on effect. With increasing Hg concentration, absorption of the incident light occurs in a region closer to the front window of the cell. As this becomes more pronounced, less of the emitted light is received by the photomultiplier. The effect of quenching by H$_2$ is also illustrated in Figure 2. Competitive collisional quenching of Hg(^{3}P$_1$) results in a decreased emission intensity for a given absorbed intensity, hence a more negative slope.

Measurement of the slope in the linear region yields the negative of the ratio of photocurrents, i_a/i_f, which is proportional to the ratio of absorbed and emitted intensities. Thus, a modified Stern–Volmer plot is obtained in this experiment
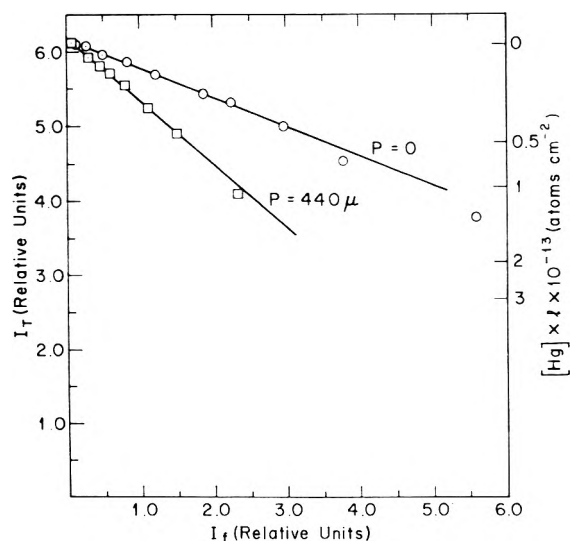
Figure 2. Plot of transmitted intensity against the emission intensity. The right-hand ordinate gives the equivalent [Hg] × l (l = 3 cm) which corresponds to the per cent transmittance on the left-hand ordinate.

$$\frac{i_a}{i_f} = C\left(1 + \frac{k_Q}{k_f}[Q]\right) \qquad \text{(III)}$$

where C is a proportionality constant. The ratio of k_Q/k_f is obtained as the slope-to-intercept ratio of the linear plot of i_a/i_f against $[Q]$.

Quenching cross sections determined in this manner may be in error if band emission from mercury-quencher excimers is appreciable. This has been recognized previously by Gunning and coworkers.[32] Of the molecules examined in the present study, band emission has been observed for quenching by CO and n-C_4H_{10}.[33,34] The CO emission spectrum[34] exhibits weak and broad band emission. The most intense emission occurs in the visible region and is outside the bandpass of the uv filter between the cell and the photomultiplier tube. In the case of n-C_4H_{10}, very weak emission has been reported by Penzes, Strausz, and Gunning.[33] The apparently low intensity of this emission and the lack of quantitative evidence to the contrary lead us to assume a negligible contribution to the observed emission intensity.

By consideration of only the linear region in Figure 2 where the Hg concentration is very low, the complication of radiation imprisonment is avoided. Generally only the region above 85% transmittance was used although linearity extended to well below 80% transmittance. Michael and Yeh[24] and Yang[35] examined imprisonment lifetimes at low atom concentrations. The results of Michael and Yeh indicate that the Milne theory of radiation diffusion reproduces the experimental apparent lifetime if Samson's equivalent opacity is used. The opacity may be readily calculated if the Hg concentration and the thickness of the absorbing layer are known. The mercury concentration at 85% transmittance is 10^{12} atoms cc^{-1} with this apparatus. If the thickness of the absorbing layer is assumed to be the distance from the center of the cell to the observation window ($\sim$3 cm) then this theory estimates a maximum increase in the apparent lifetime by a factor of 1.25. This agrees with the value of 1.20 obtained with the use of Yang's[35] empirical expression. Since the experimental points, used to determine i_a/i_f, are restricted to the transmittance range of 100–85%, these calculations indicate that the lifetime increase due to imprisonment varies
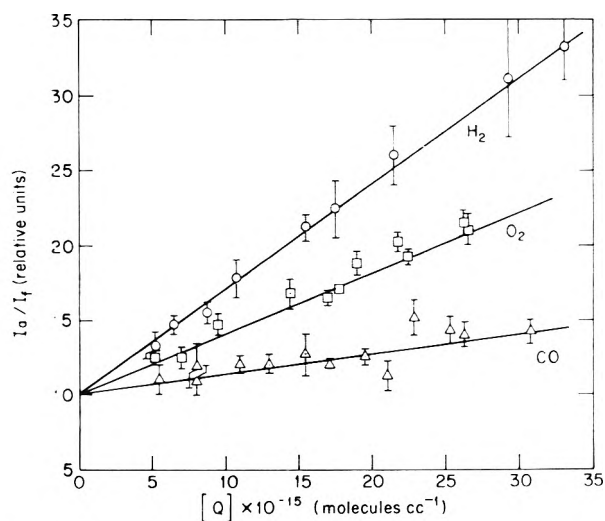
Figure 3. Stern–Volmer plots for H_2, O_2, and CO.

TABLE I: Photocurrent Ratio (i_a/i_f) as a Function of Pressure of Hydrogen Gas

P_Q, Torr	i_a/i_f × 10^4	P_Q, Torr	i_a/i_f × 10^4
0	4.23 ± 0.48	0.48	8.72 ± 0.39
0	4.20 ± 0.29	0.54	9.19 ± 0.80
0.16	5.47 ± 0.35	0.66	10.7 ± 0.8
0.20	6.06 ± 0.24	0.90	12.8 ± 1.6
0.27	6.37 ± 0.30	1.02	13.7 ± 0.9
0.33	7.33 ± 0.52		

from a factor of 1.0 to 1.2. Thus, radiation imprisonment is assumed to be negligible because of the strong criterion of linearity in plots such as Figure 2. Also this uncertainty of ±10% in the lifetime is equal to or less than the statistically propagated error which results from a given determination of a quenching rate constant.

The assumption of a homogeneous mercury atom distribution in the cell during a run is implicit in this discussion. The time for diffusion of an atom across the cell has been roughly estimated from Einstein's diffusion equation[36]

$$t_d = \bar{x}^2/6D_{12} = \bar{x}^2 P_Q/6D_{12}' \qquad \text{(IV)}$$

where $\bar{x}^2$ represents the mean square displacement and D_{12} is the binary diffusion coefficient of mercury atoms through pressure, P_Q of a quencher. These diffusion coefficients have been calculated from the Chapman–Enskog expression with Lennard-Jones potential parameters obtained from viscosity data.[37] The value of D_{12}' ranges from 757 cm^2 Torr sec^{-1} for diffusion through H_2 to 46.7 cm^2 Torr sec^{-1} for diffusion through n-butane. For a mean square displacement of 9 cm^2 (from the diameter of the cell), the diffusion time at 1 Torr of n-C_4H_{10} is about 0.03 sec. Since Hg atoms diffuse faster through the other quenching species and since all experiments were performed at pressures below 1 Torr, the diffusion time is instantaneous in comparison with the run time of several minutes. Thus, at all times during a run the Hg concentration is distributed homogeneously throughout the cell.

The results of a quenching experiment for H_2 are presented in Table I. The results for the other molecules are available.[4] The i_a/i_f value for a single run has been obtained from plots such as Figure 2 as the negative of the least-squares slope in the linear region. All i_a/i_f values
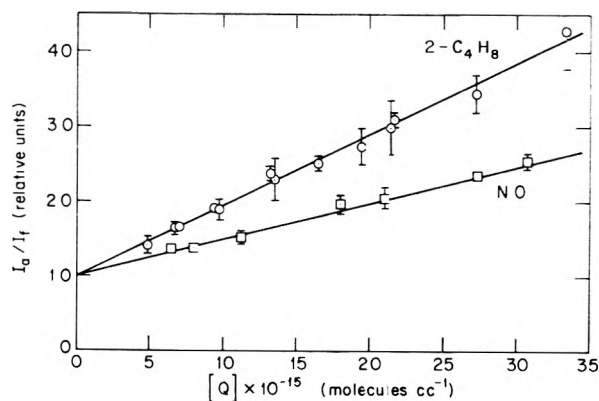
Figure 4. Stern–Volmer plots for 2-C$_4$H$_8$ and NO.
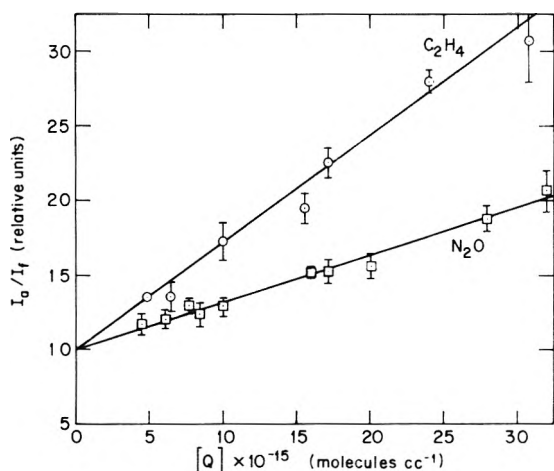
Figure 5. Stern–Volmer plots for C$_2$H$_4$ and N$_2$O.

Figure 6. Stern–Volmer plots for C$_3$H$_6$ and n-C$_4$H$_{10}$.

TABLE II: Quenching Rate Constants and Cross Sections

Q	$k_Q \times 10^{10}$, cc molecule^{-1} sec^{-1}	σ_Q^2, Å^2
H$_2$	6.15 ± 0.20	11.1 ± 0.4
O$_2$	3.57 ± 0.22	23.9 ± 1.5
CO	1.17 ± 0.15	7.4 ± 1.0
NO	4.36 ± 0.12	28.3 ± 0.8
N$_2$O	2.77 ± 0.15	21.2 ± 1.1
C$_2$H$_4$	6.27 ± 0.33	39.6 ± 2.1
C$_3$H$_6$	6.49 ± 0.59	48.5 ± 4.4
cis-2-C$_4$H$_8$	8.28 ± 0.24	69.7 ± 2.0
n-C$_4$H$_{10}$	0.80 ± 0.24	6.9 ± 2.0

such as those shown in Table I have been averaged over three to four runs at a given pressure of quencher. The uncertainty represents the standard deviation obtained from the residuals from the mean.

The photocurrent ratios (i_a/i_f) are then least-squares fitted to a straight line as a function of [Q] with each point weighted by the inverse of the square of the standard deviation. These Stern–Volmer plots for the nine molecules are presented in Figures 3–6. The ratio of the slope-to-intercept from these fits yields the ratio k_Q/k_f. A value of 1.14 × 10^{-7} sec was used for the lifetime of Hg(^{3}P$_1$) to obtain the quenching rate constant from the ratio. The quenching cross section was calculated from eq I. The experimental quenching rate constants and cross sections are tabulated in Table II. The uncertainty represents the standard deviation obtained from the estimated standard deviation in the slope and intercept from the least-squares fits.

Discussion

The quenching cross sections for Hg(^{3}P$_1$) with the various foreign gases from this experiment are listed with those from previous physical measurements in Table III. Zemansky I values represent those obtained from a Zemansky type experiment with imprisonment ratios which are calculated by Milne theory. For the Zemansky II values, Samson's equivalent opacity has been used in Milne's theory to assess imprisonment. Since the difference between the cross sections from a Zemansky type experiment and those from this study can be attributed only to imprisonment (which is constant for both experiments),

comparison on a relative basis should show agreement. In Table IV, the cross sections are presented relative to that for CO. Excellent agreement between the values for H$_2$. O$_2$. n-C$_4$H$_{10}$, and C$_4$H$_8$ is obtained. Also the relative values for C$_2$H$_4$ and C$_3$H$_6$ may be considered to agree within the limits of experimental uncertainty. NO provides the only inconsistency in this comparison.

The absolute cross sections (Table III) for H$_2$, O$_2$, N$_2$O, C$_2$H$_4$, and n-C$_4$H$_{10}$ compare favorable with the values reported by Yarwood, Strausz, and Gunning[14] from a Zemansky type experiment. Holstein theory has been used to account for imprisonment in this data. These workers and also Michael and Yeh[24] have indicated that at the conditions of a typical Zemansky experiment, $i.e.$, [Hg] ∼ 4-5 × 10^{13} atoms cc^{-1} and a cell thickness of ∼8 mm, Holstein theory adequately accounts for imprisonment. The experimental results of this study support this conclusion.

Table III also indicates good agreement with other studies at conditions of negligible imprisonment. Quenching of Hg(^{3}P$_1$) by H$_2$ has been the subject of numerous investigations. Thomas and Gwinn[22] observed the quenching by H$_2$ at various Hg concentrations and extrapolated to zero concentration to obtain a value 11.4 Å^2. This compares well with that of 11.1 Å^2 of the present study as do 10.8 and 10.0 Å^2 by Michael and Yeh[24] and Hong and Mains,[25] respectively. London, Vikis, and LeRoy[23] observed the depletion of H$_2$ in a flow system and were able to extract the apparent lifetime of Hg(^{3}P$_1$) from their data. A quenching cross section of 9.2 Å^2 was reported. The cross sections for O$_2$ and CO from the depolarization studies of Barrat, et $al.$,[16] and Deech, et $al.$,[17] show reasonable agreement with those of the present study. These workers have reported a cross section of 8 Å^2 for H$_2$ which is low in comparison with 11.1 Å^2 from this study. Also, Yang's investigation[28] of quenching by C$_2$H$_4$ as a function of Hg concentration led to a value of 45.7 Å^2 which is reasonably close to that of 39.6 Å^2 obtained here.

TABLE III: Summary of Experimental Quenching Cross Sections[a,b]

	H₂	O₂	CO	NO	N₂O	C₂H₄	C₃H₆	2-C₄H₈	n-C₄H₁₀
This work	11.1 ± 0.4	23.9 ± 2.1	7.4 ± 1.0	28.3 ± 0.8	21.2 ± 1.1	39.6 ± 2.1	48.5 ± 4.4	69.7 ± 2.0	6.9 ± 2.0
Zemansky I	5.3[c]	12.3[c]	3.6[c]	21.7[d]		23[e]	28[e]	34[e]	3.5[e]
Zemansky II	7.6	17.6	5.1	31.0		32	40	49	5.0
Reference 14	9.3	21.8				39.8			8.4
Reference 17	7.8 ± 0.4	19.2 ± 1.0	6.9 ± 0.4						
Reference 16	8 ± 1	20 ± 2	6.5 ± 1.0						
Others	11.4 ± 1.7[f]		5.9 ± 0.1[g]	22[k]	24.6	45.7 ± 1.4[l]			7.1[m]
	9.2[g]		2.4[k]						
	10.8 ± 0.4[h]								
	10.0 ± 0.4[i]								
	7.3[j]								
	11.9[m]								

[a] Quenching cross sections have been adjusted to a natural lifetime at 1.14×10^{-7} sec, where appropriate. [b] All numbers in units of Å². [c] Reference 6. [d] Reference 7. [e] Reference 13. [f] Reference 22. [g] Reference 23. [h] Reference 24. [i] Reference 25. [j] Reference 26. [k] Reference 27. [l] Reference 28. [m] Reference 38.

TABLE IV: Comparison of Quenching Cross Sections Relative to σ_{CO}^2

Q	This work	Zemansky-type experiment
H₂	1.5	1.5
O₂	3.2	3.4
NO	3.8	6.0
C₂H₄	5.4	6.4
C₃H₆	6.6	7.4
2-C₄H₈	9.5	9.5
n-C₄H₁₀	0.97	0.93

Finally, Gunning and coworkers[38] have recently reported rate constants for the reactions of $Hg(^3P_1)$ with H_2 and various paraffins. Cross sections of 11.9 Å² and 7.1 Å² for H_2 and $n-C_4H_{10}$, respectively, compare well with the values from this study.

The chemical method of Cvetanovic[18] produces quenching cross sections relative to that for N_2O. Previously a value of 12.6 Å² for the cross section of N_2O has been used to calculate absolute cross sections from these ratios. However, a cross section of 21.2 Å² has been observed in this study. The absolute cross sections for H_2, C_2H_4, C_3H_6, and C_4H_{10} which are derived from the relative ratios of the chemical method are presented in Table V. The results obtained with the present value of $\sigma_{N_2O}^2 = 21.2$ Å² agree quite well with the experimental cross sections for C_2H_4, C_3H_6, and $n-C_4H_{10}$. However, the cross section for H_2 from Yang's chemical data is slightly lower than the 11.1 Å² value of this study.

The chemical method proposed by Cundall and Palmer[21] is based on the cis-trans isomerization of cis-2-butene. This method has received only limited application, but the relative cross section for NO has been obtained by these workers. Darwent's[13] value for $cis-2-C_4H_8$ of 39 Å² had been used previously to obtain an absolute cross section of 23 Å² for NO. If the 69.7-Å² value from this study is used for $cis-2-C_4H_8$, an absolute cross section of 41.1 Å² results from Cundall and Palmer's ratio. This does not agree with the 28.3-Å² cross section from the present experiment.

In summary, the quenching of $Hg(^3P_1)$ by various molecules has been examined. Generally good agreement is obtained in comparisons with the values from previous physical determinations at conditions of negligible imprisonment as well as with cross sections from Zemansky type experiments when corrected by Holstein theory. Furthermore the cross sections relative to that of N_2O in this study exhibit good agreement with the experimentally determined values. Since a large number of these relative chemical cross sections have been measured, the value of $\sigma_{N_2O}^2 = 21.2$ Å² obtained in this work will allow accurate specification of many more cross sections than have been measured here. Although the N_2O chemical method provides cross sections for quenching only to the ground state as indicated in the analysis of Vikis, Torrie, and LeRoy,[20] accurate specification of these parameters requires an accurate value for the total cross section for N_2O.

The availability of accurate kinetic parameters for the quenching reactions of $Hg(^3P_1)$ is of importance for several reasons. The reactions of transient species in mercury photosensitization other than $Hg(^3P_1)$ have been the subject of active research interest. Recent examples include studies of metastable $Hg(^3P_0)$[19,39,40] and Hg_2 excimers.[40] In order to obtain rate constants for reactions of these species from proposed reaction mechanisms, it is necessary to specify quenching rate constants for $Hg(^3P_1)$

TABLE V: Comparison with Cross Sections Derived from Relative Ratios[a]

	H_2	C_2H_4	C_3H_6	$n\text{-}C_4H_{10}$		NO
This work Relative to N_2O	11.1 ± 0.4 (ref 35)	39.6 ± 2.1 (ref 18)	48.5 ± 4.4 (ref 19)	6.9 ± 2.0 (ref 18)	This work Relative to $2\text{-}C_4H_8$	28.3 ± 0.8 (ref 21)
$\sigma_{N_2O}{}^2 = 12.6 \text{ Å}^2$	5.3	22	29.8	3.6	$\sigma_{C_4H_8}{}^2 = 39 \text{ Å}^2$	23
$\sigma_{N_2O}{}^2 = 21.2 \text{ Å}^2$	8.9	37	50.1	6.1	$\sigma_{C_4H_8}{}^2 = 69.7 \text{ Å}^2$	41.1

[a] All numbers in units of Å^2.

reactions. Also the accurate measurement of total absolute cross sections is essential to theoretical and mechanistic interpretation of this energy transfer process. Theoretical work has progressed slowly, primarily because of the difficulty in calculation of pertinent potential energy surfaces. A summary of early work is presented by Mitchell and Zemansky.[10] A discussion of theoretical efforts concerning Hg(³P₁) quenching is included in a recent review on electronic energy transfer by Cundall.[41] The recent paper by Gunning, et al.,[38] includes a review of work on the mechanism of quenching by the alkanes. The authors hope that the results of this study will contribute to further elucidation of these interactions.

Supplementary Material Available. A review of earlier work[5-27] which is appropriate to the present work and further experimental results will appear following these pages in the microfilm edition of this volume of the journal. Photocopies of the supplementary material from this paper only or microfiche (105 × 148 mm, 24× reduction, negatives) containing all of the supplementary material for the papers in this issue may be obtained from the Journals Department, American Chemical Society, 1155 16th St., N.W., Washington, D. C. 20036. Remit check or money order for $3.00 for photocopy or $2.00 for microfiche, referring to code number JPC-74-482.

References and Notes

(1) R. J. Cvetanovic, *Progr. React. Kinet.*, **2**, 39 (1964).
(2) H. E. Gunning and O. P. Strausz, *Advan. Photochem.*, **1**, 209 (1963).
(3) J. G. Calvert and J. N. Pitts, Jr., "Photochemistry," Wiley, New York, N. Y., 1966.
(4) See paragraph at end of text regarding supplementary material.
(5) O. Stern and M. Volmer, *Phys. Z.*, **20**, 183 (1919).
(6) M. W. Zemansky, *Phys. Rev.*, **36**, 919 (1930).
(7) J. R. Bates, *J. Amer. Chem. Soc.*, **52**, 3825 (1930); **54**, 569 (1932).
(8) E. A. Milne, *J. London Math Soc.*, **1**, 1 (1926).
(9) E. W. Samson, *Phys. Rev.*, **40**, 940 (1932).
(10) A. C. G. Mitchell and M. W. Zemansky, "Resonance Radiation and Excited Atoms," Cambridge University Press, New York, N. Y., 1971.
(11) T. Holstein, *Phys. Rev.*, **72**, 1212 (1947).
(12) L. M. Biberman, *Zh. Eksp. Teor. Fiz.*, **17**, 416 (1947).
(13) B. deB. Darwent, *J. Chem. Phys.*, **18**, 1532 (1950); B. deB. Darwent and M. K. Phibbs, *ibid.*, **22**, 110 (1954); B. deB. Darwent, M. K. Phibbs, and F. G. Hurtubise, *ibid.*, **22**, 859 (1954).
(14) A. J. Yarwood, O. P. Strausz, and H. E. Gunning, *J. Chem. Phys.*, **41**, 1705 (1964).
(15) C. G. Matland, *Phys. Rev.*, **92**, 637 (1953).
(16) J. P. Barrat, D. Casalta, J. L. Cojan, and J. Hamel, *J. Phys.*, **27**, 608 (1966).
(17) J. S. Deech, J. Pitre, and L. Krause, *Can. J. Phys.*, **49**, 1976 (1971).
(18) R. J. Cvetanovic, *J. Chem. Phys.*, **23**, 1203, 1208 (1955).
(19) Y. Rousseau and H. E. Gunning, *Can. J. Chem.*, **41**, 465 (1963); M. G. Bellas, Y. Rousseau, O. P. Strausz, and H. E. Gunning, *J. Chem. Phys.*, **41**, 768 (1964).
(20) A. C. Vikis, G. Torrie, and D. J. LeRoy, *Can. J. Chem.*, **50**, 176 (1972).
(21) R. B. Cundall and T. F. Palmer, *Trans. Faraday Soc.*, **56**, 1211 (1960).
(22) L. B. Thomas and W. D. Gwinn, *J. Amer. Chem. Soc.*, **70**, 2643 (1948).
(23) G. London, A. C. Vikis, and D. J. LeRoy, *Can. J. Chem.*, **48**, 1420 (1970).
(24) J. V. Michael and C. Yeh, *J. Chem. Phys.*, **53**, 59 (1970).
(25) J. Hong and G. J. Mains, private communication.
(26) H. B. Farmer and K. Shimokoshi, *Bull. Chem. Soc. Jap.*, **45**, 2269 (1972).
(27) H. Horiguchi and S. Tsuchiya, *Bull. Chem. Soc. Jap.*, **44**, 1213, 3221 (1971).
(28) K. Yang, *J. Amer. Chem. Soc.*, **88**, 4575 (1966).
(29) "CRC Handbook of Chemistry and Physics," Chemical Rubber Publishing Co., Cleveland, Ohio, 1948.
(30) G. N. Suess, Ph.D. Thesis, Carnegie-Mellon University, 1973.
(31) Experimental lifetimes compiled by A. Lurio, *Phys Rev.*, **140**, A1505 (1965).
(32) H. E. Gunning, S. Penzes, H. S. Sandhu, and O. P. Strausz, *J. Amer. Chem. Soc.*, **91**, 7684 (1969).
(33) S. Penzes, O. P. Strausz, and H. E. Gunning, *J. Chem. Phys.*, **45**, 2322 (1966).
(34) O. P. Strausz, J. M. Campbell, S. DePaoli, H. S. Sandhu, and H. E. Gunning, *J. Amer. Chem. Soc.*, **95**, 732 (1973).
(35) K. Yang, *J. Amer. Chem. Soc.*, **87**, 5294 (1965).
(36) D. F. Eggers, Jr., N. W. Gregory, G. D. Halsey, Jr., and B. S. Rabinovitch, "Physical Chemistry," Wiley, New York, N. Y., 1964, p 397.
(37) J. O. Hirschfelder, C. F. Curtiss, and R. B. Bird, "Molecular Theory of Gases and Liquids," Wiley, New York, N. Y., 1964.
(38) H. E. Gunning, J. M. Campbell, H. S. Sandhu, and O. P. Strausz, *J. Amer. Chem. Soc.*, **95**, 746 (1973).
(39) J. M. Campbell, S. Penzes, H. S. Sandhu, and O. P. Strausz, *Int. J. Chem. Kinet.*, **3**, 175 (1971).
(40) S. Penzes, H. S. Sandhu, and O. P. Strausz, *Int. J. Chem. Kinet.*, **4**, 449 (1972).
(41) R. B. Cundall, "Transfer and Storage of Energy by Molecules," Vol I, G. M. Burnett and A. M. North, Ed., Wiley, London, 1969, p 1.

A Pulse Radiolysis Study of Thallium(II) in Aqueous Perchloric Acid Solutions

H. A. Schwarz,* D. Comstock, J. K. Yandell,[1] and R. W. Dodson

Chemistry Department, Brookhaven National Laboratory, Upton, New York 11973 (Received October 1, 1973)

Publication costs assisted by Brookhaven National Laboratory

Thallium(II) was produced by pulse radiolysis of Tl^+ and Tl^{3+} solutions in 1 M $HClO_4$. The absorption spectrum of Tl^{2+} rises continuously from 380 to 225 nm, with a shoulder around 280 nm. Rate constants were measured for the following reactions at 23°: $OH + Tl^+ \rightarrow Tl^{2+} + OH^-$, $k = 1.0 \times 10^{10}$ M^{-1} sec^{-1}; $H + Tl^{3+} \rightarrow Tl^{2+} + H^+$, $k = 3.9 \times 10^7$; $2Tl^{2+} \rightarrow Tl^+ + Tl^{3+}$, $k = 1.9 \times 10^8$; $Tl^{2-} + Fe^{2+} \rightarrow Tl^+ + Fe^{3+}$, $k = 6.7 \times 10^6$. The last rate constant was combined with rate data from the thermal oxidation of Fe^{2+} by Tl^{3+} to give $Tl^{3+} + Fe^{2+} \rightleftharpoons Tl^{2+} + Fe^{3+}$, $k_f = 0.0139$ M^{-1} sec^{-1}, $k_r = 3.4 \times 10^5$. Thus the equilibrium constant for this reaction is 4.1×10^{-8} and the free energy of formation of Tl^{2+} is 42 kcal/mol. It is shown that Tl^{2+} plays no role in the exchange reaction between Tl^+ and Tl^{3+}.

Thallium(II) is often suggested as an intermediate in oxidation–reduction reactions of thallium(I) and thallium(III). In several cases persuasive evidence for thallium(II) reactions has been obtained. Of particular interest in connection with the present work are the reduction of thallium(III) by iron(II);[2] the oxidation of thallium(I) to thallium(II) by OH radicals in aqueous solution during γ-radiation,[3] pulse radiolysis,[4] and flash photolysis;[5] the acceleration of the thallium(I)–thallium(III) electron exchange by X-rays,[6] and by ultraviolet light;[7] and the induction of this exchange by iron(II).[8]

Ashurst and Higginson[2] showed that the oxidation of iron(II) by thallium(III) is retarded by iron(III) and that the kinetics of the overall reaction is in accord with the rate law deduced from the mechanism

$$Tl^{3+} + Fe^{2+} \rightleftharpoons Tl^{2+} + Fe^{3+} \quad (k_1, k_{-1}) \quad (1)$$

$$Tl^{2+} + Fe^{2+} \longrightarrow Tl^+ + Fe^{3+} \quad (k_2) \quad (2)$$
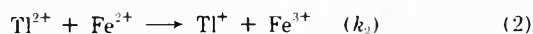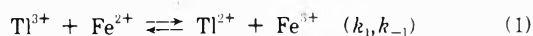
Measurements of the extent of the overall reaction as a function of time led to estimates of k_1 and of k_{-1}/k_2. Stranks and Yandell[7] found that the thallium(I)–thallium(III) electron exchange is accelerated by ultraviolet light. The results are in accord with a mechanism in which Tl^{2+} is formed photochemically, disappears by disproportionation, and, in addition, undergoes the rapid exchange reactions

$$Tl^{2+} + {}^*Tl^+ \rightleftharpoons Tl^+ + {}^*Tl^{2+} \quad (k_1) \quad (3)$$

$${}^*Tl^{2+} + Tl^{3+} \rightleftharpoons {}^*Tl^{3+} + Tl^{2+} \quad (k_{III}) \quad (4)$$
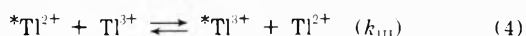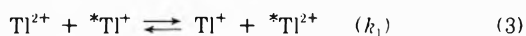
From the dependence of the quantum yield of the electron exchange on the ratio $(Tl^+)/(Tl^{3+})$ they evaluated the ratio of exchange rate constants k_{III}/k_I. They also give relations between these rate constants and the rate constant for the disproportionation of Tl^{2+}

$$2Tl^{2+} \longrightarrow Tl^+ + Tl^{3+} \quad (k_5) \quad (5)$$
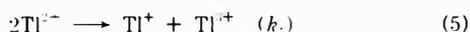
Using a value of k_5 determined by Cercek, Ebert, and Swallow[4] from pulse radiolysis experiments on dilute solutions of thallous sulfate they calculated k_I and k_{III}. On the basis of the photochemical results, Warnqvist and Dodson[8] looked for chemical induction of the thallium(I)–thallium(III) electron exchange by iron(II). Acceleration of the exchange in the presence of ferrous ion was observed, although the effect was not quantitatively consistent with expectations based on the earlier work.

The present study was undertaken with the aim of mea-

suring the disproportionation rate constant, k_5, in the same medium (1 M $HClO_4$) as that used in the photochemical exchange studies, so that a more reliable calculation of k_I and k_{III} could be made. In connection with measurements on the rate of disappearance of Tl^{2+}, the specific rates of its formation by $OH + Tl^+$, and by $H + Tl^{3+}$ were determined. Finally it proved feasible to follow the disappearance of Tl^{2+} in the presence of Fe^{2+} and thereby to make a direct measurement of k_2, the specific rate of reduction of Tl^{2+} by Fe^{2+}. A kinetic determination of the equilibrium constant of reaction 1 is thereby obtained. The result allows a choice between two earlier estimates of the standard free energy of Tl_{aq}^{2+} and to a refinement of the more reliable of these estimates. The equilibrium and kinetic results lead to a firm conclusion that reaction 5, considered as a reversible equilibrium, plays no significant role in the thermal exchange reaction between thallium(I) and thallium(III) in perchloric acid solution.

Experimental Section

Baker Analyzed 72% perchloric acid was used, in most cases without further purification. In a few runs redistilled perchloric acid was used instead, with no perceptible difference in the results. Thallous perchlorate was prepared from A. D. MacKay thallium metal. The metal was dissolved in nitric acid, and thallous perchlorate was precipitated by adding concentrated perchloric acid. The product was dissolved in distilled water, and thallous perchlorate was again precipitated by adding concentrated perchloric acid. The thallous perchlorate was recrystallized twice from triply distilled water. Solutions of the final product were neutral to pH paper, gave no test for chloride with silver nitrate, or for nitrate with brucine. Solutions of thallic perchlorate were prepared by anodic oxidation of the thallous perchlorate in perchloric acid solution.[9] Stock solutions of thallous perchlorate and of thallic perchlorate were analyzed for thallium(I) by bromate titration and for total thallium by bromate titration after reduction with formaldehyde in alkaline solution. The perchloric acid content of thallic stock solutions was determined by titration with standard sodium hydroxide after the addition of sodium bromide. G. F. Smith iron(II) perchlorate was dissolved in distilled water, and the solution was filtered. Iron(II) perchlorate was precipitated by addition of concentrated perchloric acid, was again dissolved, and repre-

cipitated. The product was dissolved in air-free argon-saturated aqueous perchloric acid and stored under argon. More dilute stock solutions were prepared and also stored under argon.

Solutions for kinetic experiments were deaerated by bubbling with nitrogen or with argon. Some measurements of the absorption spectrum of Tl^{2+} were made with solutions saturated with 4% oxygen-96% nitrogen. All measurements were made at room temperature (23°).

Two electron accelerators were used in this study: a 2-MeV Van de Graaff and a 1.9-MeV Febetron. The latter machine, with its short intense pulse (less than 10^{-7} sec), was used to measure the reaction of hydroxyl radicals with Tl^+ and hydrogen atoms with Tl^{3+}.

It is well known that scattered light from the analyzing lamp presents serious problems in pulse radiolysis studies in the ultraviolet region. This problem was minimized by the use of a pulsed deuterium lamp for the slower studies. A pulsed xenon arc was used for the Febetron work, but a 30° quartz prism was placed in the light train 25 cm before the monochromator, allowing only light in the neighborhood of the desired wavelength to enter. The rest of the pulse radiolysis equipment was standard.

The thermal oxidation of iron(II) by thallium(III) in 1 M perchloric acid was measured with a Cary 16K recording spectrophotometer. The reaction was followed for several half-lives so that retardation by the accumulated iron-(III) product could be measured. Thallium(III) was at all times in large excess over total iron. A series of runs was also made in which iron(III) was present initially in large excess over the iron(II).

Results

Absorption Spectrum of Tl^{2+}. The absorption spectrum of Tl^{2+} in 1 M $HClO_4$ is given in Figure 1. Thallium(I) and (III) absorb light strongly below 225 nm preventing work at shorter wavelength. Our spectrum is in disagreement with those in the literature,[4,5] and so it was checked by several methods.

(A) The most precise data were obtained in 10^{-3} M Tl^+ solutions saturated with 4% O_2, 96% N_2 (5 × 10^{-5} M O_2). The oxygen was present to provide a known fate for hydrogen atoms. The good precision of these data was made possible by the use of electrical shielding around the pulse radiolysis cell which allowed integration of the electron beam current with greater accuracy than in our other measurements (0.5% $vs.$ 3%). The decay of Tl^{2+} was followed for 5 × 10^{-4} sec after the pulse. The product of yield and extinction coefficient ($G\epsilon$) was determined from the initial absorbance after the pulse, A_0, by

$$G\epsilon = A_0/Dl$$

where l is the optical path length (6.1 cm) and D is the dose, in appropriate units, determined by ferrous sulfate dosimetry. The observed $G\epsilon$ is related to $\epsilon(Tl^{2+})$ by

$$G\epsilon = G(Tl^{2+})[\epsilon(Tl^{2+}) - \epsilon(Tl^+)] + G(HO_2)\epsilon(HO_2)$$

$G(Tl^{2+})$ is equal to G_{OH} (2.95 radicals per 100 eV) and $G(HO_2)$ was taken as G_H (3.65 radicals per 100 eV). The other extinction coefficients ($\epsilon(Tl^+)$ and $\epsilon(HO_2)$) are known[10,11] and so $\epsilon(Tl^{2+})$ can be calculated.

(B) The decay of Tl^{2+} absorption at 270 nm was followed for 5 × 10^{-4} sec following the pulse in solutions of Tl^+ with no O_2, from which

$$G\epsilon = G(Tl^{2+})[\epsilon(Tl^{2+}) - \epsilon(Tl^+)] + G_H\epsilon(H)$$
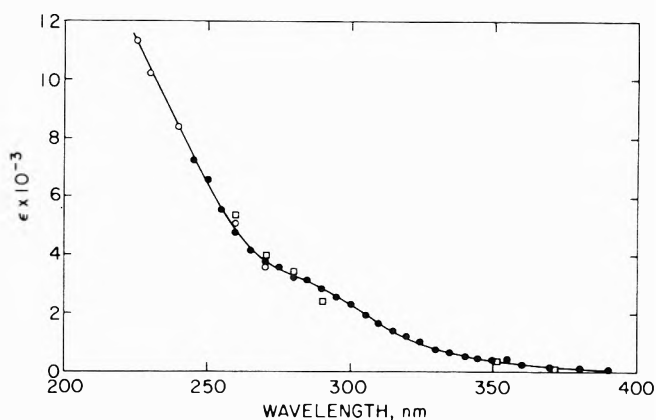
Figure 1. Absorption spectrum of Tl^{2+}: ●, method A; O, method C; □, method D.

The extinction coefficients of Tl^+ and H are negligible at 270 nm.[10,12] The extinction coefficient obtained from 10^{-3} M Tl^+ was 1.5% higher than that of method A. From 10^{-4} M Tl^+ it was 5% lower, possibly because of incomplete scavenging of OH.

(C) The buildup of Tl^{2+} absorption due to reaction 6

$$OH + Tl^+ \xrightarrow{H^+} H_2O + Tl^{2+} \tag{6}$$
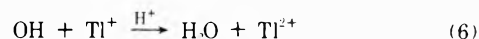
was followed in deaerated Tl^+ solutions. The observed absorbances were fit to first-order growth, and the change in absorbance due to reaction 6 was determined. The observed values of $G\epsilon$ are related to $\epsilon(Tl^{2+})$ by

$$G\epsilon = G(Tl^{2+})[\epsilon(Tl^{2+}) - \epsilon(OH) - \epsilon(Tl^+)]$$

The absorption spectrum of the hydroxyl radical is given by Pagsberg, et al.[12] Only relative values of $G\epsilon$ at different wavelengths were determined by this method. The results were normalized to the absolute values of method A.

(D) The decay of Tl^{2+} absorption produced in deaerated 10^{-3} M Tl^+, 5 × 10^{-3} M Tl^{3+} solutions was followed for two-four half-lives. The decay followed second-order kinetics and was assumed to be due to reaction 5. The hydrogen atoms should produce Tl^{2+} by

$$H + Tl^{3+} \longrightarrow H^+ + Tl^{2+} \tag{7}$$
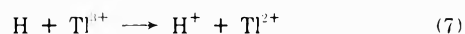
The observed values of $G\epsilon$ are related to $\epsilon(Tl^{2+})$ by

$$G\epsilon = G(Tl^{2+})\{\epsilon(Tl^{2+}) - (1/2)[\epsilon(Tl^+) + \epsilon(Tl^{3+})]\}$$

Again, $\epsilon(Tl^+)$ and $\epsilon(Tl^{3+})$ are known;[10] and $G(Tl^{2+})$ should be given by $G_H + G_{OH}$ (6.6 radicals per 100 eV). The shape of the spectrum is the same as that from method A. The absolute values were 11% lower, presumably because of incomplete reaction of H with Tl^{3+}. The data were normalized to the values of method A for presentation in Figure 1.

Reaction of OH with Tl^+. The rate constant of reaction 6 was measured by following the buildup of Tl^{2+} absorption in dilute solutions of Tl^+ in 1 M $HClO_4$. If the buildup were strictly first order the absorbance, A. would follow the equation

$$A_\infty - A = (A_\infty - A_0)e^{-k_{obsd}t}$$

where A_∞ and A_0 are the absorbances at infinite and zero time. The buildup is not strictly first order, however, because Tl^{2+} is reacting with H atoms. This effect can be represented by a linear approximation, βt

$$A_\infty - A = (A_\infty - A_0)e^{-k_{obsd}t} + \beta t$$

The maximum value of A is less than A_∞ because of the
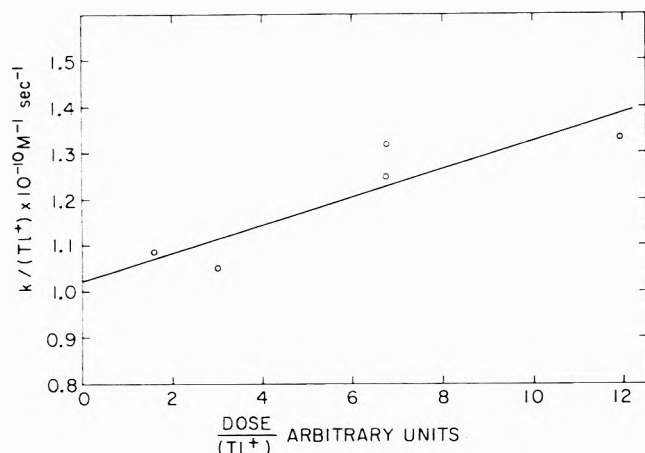
Figure 2. Dependence of pseudo-first-order rate constant for Tl^{2+} buildup in Tl^+ solutions on Tl^+ concentration and dose. The intercept is k_6.

Figure 3. Dependence of pseudo-first-order rate constant for Tl^{2+} buildup in Tl^+-Tl^{3+} solutions on Tl^{3+} concentration and dose. The buildup corresponds to the slow component (due to reaction 7) and the intercept is k_7.

reactions of Tl^{2+}, and so both A, and k_{obsd} are found from the best fit to the data. The value of β was determined by decay studies on a time scale ten times that used in the buildup experiments. Rate constants determined by this method were 5–10% smaller than values determined by the expedient of ignoring the decay.

Sufficiently high doses were used that some OH disappeared by reaction with radiation-produced products, for instance

$$OH + H \longrightarrow H_2O$$

$$OH + Tl^{2+} \xrightarrow{H^+} H_2O + Tl^{3+}$$
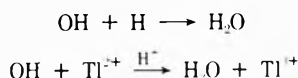
The observed rate constants would include contributions from the above reactions, but these contributions would be independent of (Tl^+) and approximately proportional to dose so that

$$k_{obsd} = k_6(Tl^+) + \alpha(\text{dose}) \qquad (8)$$

$$\frac{k_{obsd}}{[Tl^+]} = k_6 + \alpha\frac{\text{dose}}{[Tl^+]} \qquad (9)$$

Experiments were performed at two total doses (equivalent to approximately 3×10^{-6} and 7×10^{-6} M in H atoms) and two Tl^+ concentrations (2.52×10^{-5} and 1.00×10^{-4} M). The resulting pseudo-first-order constants are plotted according to eq 9 in Figure 2, from which k_6 is found to be $(1.0 \pm 0.1) \times 10^{10}$ M^{-1} sec^{-1}.

Reaction of H with Tl^{3+}. The rate constant for reaction 7 was determined by irradiating solutions containing Tl^+ (to remove OH radicals) and from 3×10^{-4} to 1×10^{-2} M Tl^{3+}. A 10:1 ratio of Tl^{3+} to Tl^+ was employed, in which case reaction 6 is 25 times faster than reaction 7 and is complete before measurements of reaction 7 begin. Again, following the buildup there is a relatively slow decay due to reaction 5; and at the doses used some H atoms recombine or react with Tl^{2+}. The treatment of the buildup is analogous to that of Tl^{2+} from OH radicals and the pseudo-first-order constants are shown in Figure 3, plotted according to

$$\frac{k_{obsd}}{[Tl^{3+}]} = k_7 + \frac{\alpha'}{[Tl^{3+}]} \qquad (10)$$

from which k_7 is $(3.9 \pm 0.5) \times 10^7$ M^{-1} sec^{-1}.

The Disproportionation of Tl^{2+}. The decay of the Tl^{2+} absorption of pulsed solutions of Tl^+ and Tl^{3+} is due solely to reaction 5. The second-order nature of the decay is shown in Figure 4 (constant slope is maintained over a
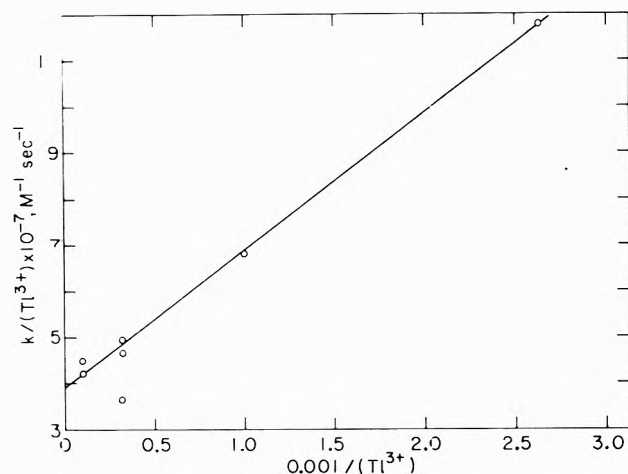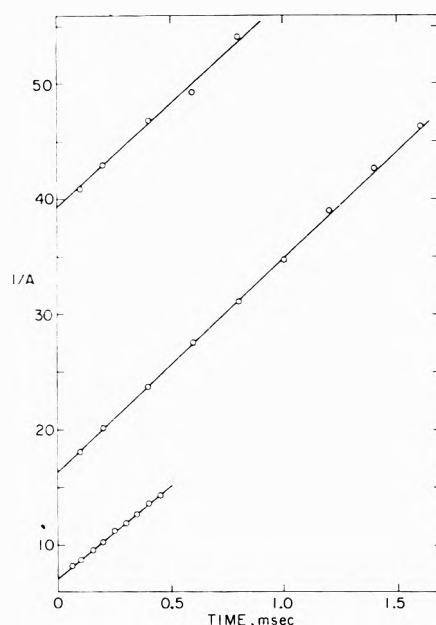
Figure 4. Three second-order tests for the decay of absorbance at 280 nm in solutions containing 1 M $HClO_4$, 10^{-3} M Tl^+, 10^{-2} M Tl^{3+}. The slopes of the lines are $2k_5/l\epsilon$ ($l = 6.1$ cm).

factor of 5 in initial concentration). The slopes of the curves are $2k_5/l\epsilon$ where l is the light path length (6.1 cm). Values of k_5 were found using extinction coefficients from Figure 1. Rate constants were determined on 4 days with an average of 10 samples per day. The daily averages were 2.13×10^8, 1.88×10^8, 1.50×10^8, and 1.91×10^8 M^{-1} sec^{-1}. On any day the rate constants were independent of wavelength in the range 260–290 nm. The standard deviation of the daily averages is about twice the standard deviation of the measurements on a given day (7%), indicating a systematic error. We are unable to specify what the error is and consequently average all the values to give k_5 as $(1.8 \pm 0.3) \times 10^8$ M^{-1} sec^{-1}.

Reaction of Tl^{2+} with Fe^{2+}. The rate constant for reaction 2 was measured in 1 M $HClO_4$ solutions containing 10^{-3} M Tl^+ and 10^{-2} M Tl^{3+} to ensure that all radicals are converted to Tl^{2+} within a few microseconds. Two Fe^{2+} concentrations, 1×10^{-3} and 2×10^{-3} M, were used, the higher limit being set by the rate of the thermal

reaction

$$Tl^{2+} + 2Fe^{2+} \longrightarrow Tl^+ + 2Fe^{3+}$$

which causes the solutions to become opaque in the ultraviolet range due to the Fe^{3+}. The experiments were carried out by adding 0.5 or 1 cc of Fe^{2+} stock solution to 25 cc of deaerated Tl^+–Tl^{3+} solution and deaerating with N_2 a further 2 min. The actual ferrous concentration when pulsed was computed from the known rate law for the reaction.[2] At the wavelength used, 290 nm, Tl^{2-} absorbs more strongly than Fe^{3+} so there is a decay of the absorbance. This decay is nearly pseudo-first order but there is a small second-order contribution due to reaction 5. A sufficiently accurate rate expression is

$$y \equiv (A - A_r)/\left\{1 + \frac{2k_5(A - A_\infty)}{k_2 l[\epsilon(Tl^{2+}) - \epsilon(Fe^{3+})][Fe^{2+}]}\right\} =$$

$$y_0 e^{-k_2[Fe^{2+}]t} \quad (11)$$

where A and A_∞ are the absorbances at time t and infinity. (Equation 11 may be derived assuming

$$A - A_\infty = [Tl^{2+}]l[\epsilon(Tl^{2+}) - \epsilon(Fe^{3+})]$$

which is rigorously true only if all Tl^{2+} reacts with Fe^{2+}. Trial calculations show the effect of this approximation on the estimate of k_2 to be negligible.) The denominator in eq 11 is only slightly greater than one (1.2 at the most) and all quantities are known to compute the term except k_2. Consequently an approximate value of k_2 was found from the slope of $\ln (A - A_\infty)$ vs. time (i.e., ignoring reaction 5, see dashed lines of Figure 5) and this value used to compute y for each point. Typical dependence of y on time is shown in Figure 5. As may be seen, the difference between a simple exponential and eq 11 is small, amounting to about 8% in slope. Five runs using 10^{-3} M Fe^{2+} gave $k_2 = 6.4 \times 10^6$ and five runs using 2×10^{-3} M Fe^{2+} gave 7.0×10^6; the average is $k_2 = (6.7 \pm 0.7) \times 10^6$ M^{-1} sec^{-1}.

The Overall Reaction $2Fe^{2+} + Tl^{3+} = 2Fe^{3+} + Tl^+$. The medium employed in the present work was somewhat different from that employed by Ashurst and Higginson[2] and so we studied the thermal reaction between Tl^{3+} and Fe^{2+} in 1 M HClO$_4$ solution. Two initial concentrations of Tl^{3+} were used: 9.93×10^{-3} and 15.2×10^{-3} M. Initial Fe^{2+} concentrations ranged from 0.044×10^{-3} to 0.64×10^{-3} M. Under these conditions the integrated form of the rate law expected from reactions 1 and 2 is

$$kt = (1 - k_{-1}/k_2) \ln (c_0/c) + (k_{-1}/k_2)(1 + d/c_0)[(c_0/c) - 1] \quad (12)$$

where c is the concentration of Fe^{2+}, d the initial concentration of Fe^{3+}, and $k = 2k_1(Tl^{3+})$. The Tl^{3+} concentration was taken as constant during each run, and given by $[Tl(III)]_0 - \frac{1}{4}Fe(II)]_0$. c_0/c was taken as the absorbance ratio $(A_\infty - A_0)/(A_\infty - A)$, where the A is the absorbance of the reaction mixture. A_0 was estimated by extrapolation of observed A values to time zero. Direct observation of A_∞ proved unreliable, possibly because of experimental artifacts during the several-day time scale. Therefore it was estimated from the kinetic data with the aid of eq 12. A trial value of $A_\infty - A_0$ was calculated from c_0 and the extinction coefficient of Fe^{3+}. A trial value of k_{-1}/k_2 was chosen from the data of Ashurst and Higginson.[2] A preliminary value of k was then computed from the data covering the first half-life of the reaction. This value of k was used to compute a new value of k_{-1}/k_2 from the
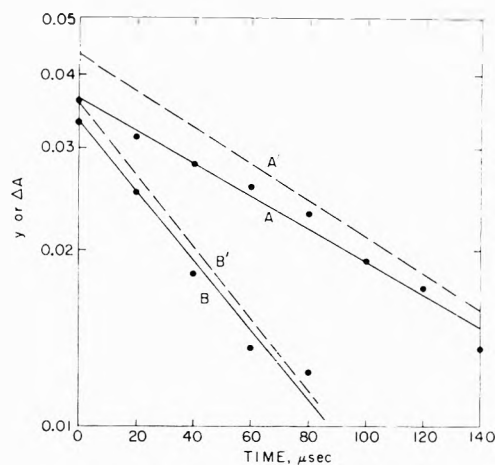
Figure 5. The reaction of Tl^{2+} with Fe^{2+}. The dashed line A' is the absorbance decay at 290 nm in 1 M HClO$_4$, 1 × 10^{-3} M Tl$^+$, 1 × 10^{-2} M Tl^{3+}, and 1 × 10^{-3} M Fe^{2+}. The dashed line B' is the same except the Fe^{2+} concentration is 2 × 10^{-3} M. The points and solid curves A and B are the same results corrected for reaction 5 by use of eq 12.

TABLE I: Oxidation of Iron(II) by Thallium(III) in 1.1 M Perchloric Acid at 25°

$10^3[Tl(III)]_0$, M	$10^3[Fe(II)]_0$, M	10^3 [Fe(III)]$_0$, M	$10^2 k_1$, M^{-1} sec^{-1}	k_{-1}/k_2
9.93	0.640	a	1.37	0.055
15.23	0.446		1.40	0.045
15.23	0.446		1.41	0.046
15.23	0.0445		1.38	0.050
15.23	0.0445		1.42	0.055
9.14	0.0393		1.38	0.055
9.14	0.0393	0.204	1.38^b	0.054
9.14	0.0393	0.408	1.38^b	0.052
9.14	0.0393	0.612	1.38^b	0.048

^{a} In the first five entries the initial iron(III) was only that present as impurity in the ferrous stock solution, about 1% of the total iron. ^{b} Assumed value, input for the calculation of k_{-1}/k_2 when iron(III) was added initially.

data late in the reaction. This process was repeated until input and output values converged. Minor adjustments were made in A_∞ and the calculation repeated until point-by-point values of k and k_{-1}/k_2 showed no drift with time. The final values of A_∞ agreed within a few per cent with the trial value. The results are given in Table I, from which $k_1 = (1.39 \pm 0.02) \times 10^{-2}$ M^{-1} sec^{-1}, and $k_{-1}/k_2 = 0.051 \pm 0.005$.

Discussion

Spectrum and Disproportionation of Tl^{2+}. Comparison of our results with those of Cercek, Ebert, and Swallow[4] is complicated by the difference in media (dilute thallous sulfate vs. 1 M perchloric acid). They found a peak in the Tl^{2+} spectrum between 250 and 260 nm which we do not find. We made some measurements at higher pH and found no peak in the spectrum for either neutral, N_2O-saturated, 5 × 10^{-4} M Tl$_2$SO$_4$ solutions or 10^{-4} M TlClO$_4$ in 0.01 M H$_2$SO$_4$. We noted that the neutral samples tended to be photolyzed on continuing exposure to the analyzing light, with the formation of a brown precipitate. We can offer no persuasive explanation of the discrepancy. The agreement between their extinction coefficient at 260 nm (5400) and ours (4900) is adequate.

Two of the reaction rates they measured in neutral solution were measured by us in 1 M acid. They found k_6 to be 7.6 × 10^9 M^{-1} sec^{-1}, in satisfactory agreement with

our value of 1.0×10^{10}, but reported k_5 to be 2.3×10^9 M^{-1} sec^{-1}, an order of magnitude greater than our 1.9×10^8. We found the decay of the absorption in N_2O saturated 5×10^{-4} M Tl_2SO_4 gave a second-order rate constant of 1.7×10^9 M^{-1} sec^{-1}, in agreement with their value. Use of $TlClO_4$ instead of Tl_2SO_4 made no difference. A rate constant of this magnitude cannot be attributed to the reaction between two doubly charged ions of like sign. The diffusion-limited rate constant for such a reaction assuming a reaction radius of 4 Å (corresponding to one water molecule between the two ions) would be 4×10^7. A reaction radius of 10 Å would be required to explain a rate constant of 2.3×10^9. The rate constant should be higher in 1 M acid than in infinitely dilute solution, although exact prediction is not possible. The initial product of reaction 6 is likely to be the singly charged $TlOH^+$. If the stability constant of $TlOH^+$ is greater than 10^7 M^{-1}, then the lifetime of $TlOH^+$ (with respect to dissociation into Tl^{2+} and OH^-) in neutral solution would be greater than 10^{-3} sec (since the reverse rate constant cannot be greater than 10^{10} M^{-1} sec^{-1}); and the neutral solution studies would pertain to the hydroxide complex. The stability constant of $TlOH^{2+}$ is 7×10^{12} M^{-1}, so a value of 10^7 M^{-1} for $TlOH^+$ is not unreasonable.

Burchill and Wolodarsky[5] found a peak at 270 nm in the Tl^{2+} spectrum produced by the flash photolysis of 5×10^{-3} M Tl^{3+} in 1 M $HClO_4$. The absorption of Tl^{3+} extends[10] to longer wavelengths than Tl^+ and a 5×10^{-3} M Tl^{3+} solution in a 10-cm cell becomes opaque below 260 nm. We believe their spectrum below 270 nm is heavily influenced by scattered light. They found k_5/ϵ to be 3.1×10^4 at 270 nm, from which k_5 would be 1.2×10^8 M^{-1} sec^{-1} in comparison with out 1.9×10^8.

The Reaction $2Fe^{2+} + Tl^{3+} = 2Fe^{3+} + Tl^+$. Our values of k_1 and k_{-1}/k_2 in 1 M perchloric acid are close to those $(0.93$ M^{-1} min^{-1} and $0.045)$ reported by Ashurst and Higginson[2] for $[H^+] = 1.00$ M, ionic strength 1.60. Our k_1 is, also, in excellent agreement with the value for 1 M perchloric acid 0.86 M^{-1} min^{-1}, read from a graph in the paper by Forchheimer and Epple.[13] For additional cross checks we followed the reaction in 2.9 M perchloric acid and found k_1 and k_{-1}/k_2 to be 0.83 M^{-1} min^{-1} and 0.018. Ashurst and Higginson[2] give 0.82 M^{-1} min^{-1} and 0.016 for 2.8 M $HClO_4$, ionic strength 3. We conclude that our procedure for studying the kinetics of the overall reaction gives results in good agreement with earlier investigations, which used different methods.

A significant feature of our data is that the rate law was confirmed down to initial iron(II) concentrations of 4×10^{-5} M (final concentrations about 1×10^{-5}) with no drift in the value of k_{-1}/k_2. It can therefore be concluded that reactions 1 and 2 adequately describe the mechanism over a range of at least 10^2 in $[Fe^{2+}]_0$. Under the experimental conditions the disproportionation reaction, (5), does not compete seriously with reaction 2 when $[Fe^{2+}]$ is of the order of 10^{-5} M. This fact sets a lower limit on k_2 of the order of 10^5 M^{-1} sec^{-1}. Our experimental value 6.7×10^6 M^{-1} sec^{-1} agrees with this conclusion.

It is of interest to calculate the equilibrium constant for the overall reaction in which iron(II) is oxidized by thallium(III). For the potential of the $Tl(I)|Tl(III)$ couple in 1 M $HClO_4$ we adopt 1.259 ± 0.001 V, the mean of values reported by Sherrill and Haas[14] and by Stonehill.[15] For the $Fe(II)|Fe(III)$ couple in the same medium we use the result of Magnusson and Huizenga,[16] 0.738 ± 0.001 V. The equilibrium constant is, then

$$K_{1,2} = \frac{[Fe^{3+}]^2[Tl^+]}{[Fe^{2+}]^2[Tl^{3+}]} = 4 \times 10^{17}$$

The Reaction $Tl^{3+} + Fe^{2+} = Tl^{2+} - Fe^{3+}$. Our values of k_{-1}/k_2 and k_2 give $k_{-1} = 3.4 \times 10^5$ M^{-1} sec^{-1}. The equilibrium constant of reaction 1 is therefore $K_1 = k_1/k_{-1} = 4.1 \times 10^{-8}$. The corresponding standard free-energy change is $\Delta G^\circ(1) = 10.1$ kcal/mol, in 1 M perchloric acid medium. Using tabulated G° values[17] we may now estimate the standard free energy of formation of Tl_{aq}^{2+}. It is not feasible to make detailed corrections for the difference between H_2O and 1 M $HClO_4$ in H_2O as media; this neglect may introduce an error of *ca.* 1 kcal/mol. The result is $G^\circ(Tl_{aq}^{2+}) = \Delta G^\circ(1) - G^\circ(Fe^{3+}) + G^\circ(Tl^{3+}) + G^\circ(Fe^{2+}) = 10.1 + 2.53 + 50.0 - 20.30 = 42$ kcal/mol.

There are two estimates of this quantity with which our result may be compared. Brewer and coworkers[18] reported a calculated value of the heat of formation of the aqueous ion as $\Delta H^\circ = 45 \pm 10$ kcal/mol. Dulz[19] repeated the calculation, with the same result, and estimated the entropy of the ion as zero from the equation of Powell and Latimer.[20] Dulz's conclusion[19] was therefore that $G^\circ(Tl_{aq}^{2+}) = 45 \pm 10$ kcal/mol. In spite of the unavoidably large uncertainty in this calculated value, the agreement with our result is gratifying. Hush[21] derived a value 23 kcal/mol, but his analysis was based on the assumption that the mechanism of the $Tl(I)-Tl(III)$ electron exchange reaction is $Tl^+ + Tl^{3+} \rightleftharpoons 2Tl^{2+}$. As we will discuss below, this mechanism can now be ruled out.

Using data only for reactions in 1 M $HClO_4$ we may calculate the potentials of the $Tl^{3+}|Tl^{2+}$ and $Tl^{2+}|Tl^+$ couples in this medium. From the equilibrium constant for reaction 1 and the potential of the $Fe^{3+}|Fe^{2+}$ couple, 0.738 V, it follows that $E^\circ(Tl^{3+}|Tl^{2+}) = 0.30$ V. Then, from the $Tl^{3+}|Tl^+$ potential, 1.259 V, it follows that $E^\circ(Tl^{2+}|Tl^+) = 2.22$ V. These potentials may be contrasted with those deduced by Hush: $Tl^{2+}|Tl^+$, 1.50 V; $Tl^{3+}|Tl^{2+}$, 1.00 V. Tl_{aq}^{2+} is a far more powerful oxidant, by 0.7 V, than indicated by the earlier calculation.

In a volt-ammetric study Catherino and Jordan[22] concluded that the electrooxidation of Tl_{aq}^+ and the electroreduction of Tl_{aq}^{3+} in 1 M perchloric acid proceed *via* a Tl^{2+} intermediate, and that the Tl^{2+} is a stronger oxidant than Tl^{3+}. The latter conclusion is, of course, consistent with either the potentials deduced by Hush, or those of the present work.

Implications for Certain Electron Exchange Reactions. In their calculation of k_{III} and k_I Stranks and Yandell[7] used a relation in which k_{III} (calculated) is proportional to k_5^{-2}. They used the k_5 obtained by Cercek, Ebert, and Swallow[4] from measurements on the disproportion of Tl^{2+} in a dilute solution of thallous sulfate extrapolated to zero ionic strength. Our measurement of k_5 in the appropriate medium (we neglect the difference between 1.0 and 1.1 M $HClO_4$) leads to values of k_{III} and k_I, lower by a factor of 0.3. The Stranks and Yandell data[7] now give $k_{III} = 3.0 \times 10^4$, and $k_I = 1.5 \times 10^4$ M^{-1} sec^{-1}.

It is of interest to examine the results in the light of the Marcus cross relation[23] $k_{AB} = [k_A k_B K_{AB} f]^{1/2}$. We take for k_B the specific rate of the iron(II)-iron(III) electron exchange reaction[24] 4.2 M^{-1} sec^{-1}. For reaction 1, taking $k_A = k_{III}$ we calculate $k_{AB} = k_1 = 2.9 \times 10^{-2}$, in good agreement with the measured value of 1.4×10^{-2} M^{-1} sec^{-1}. For reaction 2 the equilibrium constant calculated from K_1 and $K_{overall}$ is 1×10^{25}. Now k_A is k_I, and k_{AB} is k_2. The calculated value of k_2 is 2.3×10^{10}, or over three or-

ders of magnitude greater than the observed 6.7×10^6 M^{-1} sec^{-1}. We have no explanation for this discrepancy, but note that one in the same direction and of similar magnitude is found[25] for the cerium(IV)-iron(II) reaction in perchloric acid, which also has $K_{AB} \gg 1$, namely, ca. 10^{16}.

The results of the present work give, we believe, a forthright negative answer to the question whether the thermal thallium(I)-thallium(III) electron exchange involves to any significant degree the reversible disproportionation of Tl^{2+}. The question has been considered in a number of earlier publications. Gryder and Dorfman[26] noted that the Ce(IV)-Tl(I) reaction is unaffected by Tl(III). They argued that if Tl(II) is involved in both reactions, then the Ce(IV) reaction in the presence of Tl(III) could be no slower than the exchange. But it is much slower; hence either the Tl(I)-Tl(III) exchange or the Ce(IV)-Tl(I) reaction, or both, must involve a two electron transfer. Sykes[27] argued that the oxidation of V(IV) by Tl(III) involves Tl(II) but is unaffected by the addition of Tl(I), contrary to what would have been observed were Tl(II) an intermediate in the exchange reaction. Halpern[28] considered that the entropy correlations of Higginson, et al.,[29] favor the conclusion that a two-electron transfer occurs rather than the intermediate formation of Tl^{2+}. Sutin[30] presented considerations in favor of a two-step process involving Tl^{2+} as an intermediate. Stranks and Yandell[31] argued that the extreme sensitivity of the photochemically induced exchange to impurities, in contrast to the insensitivity of the thermal exchange, was evidence against a Tl^{2+} intermediate in the thermal exchange. They later[7] observed that this reasoning does not exclude the possibility of two successive one-electron transfers occurring in the same solvent cage. On the basis of the volume of activation (-13.2 ml mol^{-1}) determined by them Adamson and Stranks[32] expressed the opinion that the mechanism is a two-electron transfer.

We now may calculate what the rate of the Tl(III)-Tl(I) exchange would be under typical conditions if the mechanism were establishment of the equilibrium $Tl^{3+} + Tl^+ \rightleftharpoons 2Tl^{2+}$ supplemented by reactions 3 and 4. By combining K_1 and the equilibrium constant for the overall reaction 1 + 2 we find for the reaction (-5) $Tl^{3+} + Tl^+ \rightleftharpoons 2Tl^{2+}$

$$K_{-5} = \frac{k_{-5}}{k_5} = \frac{K_1^2}{K_{12}} = \frac{[Tl^{2+}]^2}{[Tl^{3+}][Tl^+]} = 4 \times 10^{-33}$$

and the specific rate of the forward reaction is $k_{-5} = 7.4 \times 10^{-25}$ M^{-1} sec^{-1}. In an exchange mixture in which $[Tl^{3+}] = [Tl^+] = 10^{-2}$ M, the equilibrium concentration of Tl^{2+} is 0.6×10^{-18} M. (The relaxation time of the equilibrium is 140 years!) A three-site exchange system a $\leftrightarrow$ c $\leftrightarrow$ b in which exchange between a and b occurs only via intermediate c will have an observed rate of exchange between a and b of

$$R_{ex} = R_{ac}R_{bc}/(R_{ac} + R_{bc})$$

provided the concentration of c is much less than that of a and of b. (This relation can be derived directly, or can be obtained from the general treatment of Abell, Bonner, and Goishi.[33] In the present example $R_{ac} = k_{-5}[Tl^+][Tl^{3+}] + k_{III}[Tl^{2+}][Tl^{3+}]$ and $R_{bc} = k_{-5}[Tl^+][Tl^{3+}] + k_I[Tl^{2+}][Tl^+]$. The calculated exchange rate is $R_{ex} = 0.58 \times 10^{-16}$ M sec^{-1}. The experimental rate under these conditions is 1.2×10^{-8} M sec^{-1}, i.e., faster by a factor of 2×10^8 than that calculated for the Tl^{2+} equilibrium mechanism. The latter mechanism therefore plays no role in the thermal exchange.

References and Notes

(1) On leave from Monash University, Clayton, Victoria, Australia 3168.
(2) K. G. Ashurst and W. C. E. Higginson, *J. Chem. Soc.*, 3044 (1953).
(3) T. J. Sworski, *J. Amer. Chem. Soc.*, 77, 4689 (1955).
(4) B. Cercek, M. Ebert, and A. J. Swallow, *J. Chem. Soc. A*, 612 (1966).
(5) C. E. Burchill and W. H. Wolodarsky, *Can. J. Chem.*, 48, 2955 (1970).
(6) G. E. Challenger and B. J. Masters, *J. Amer. Chem. Soc.*, 78, 3012 (1956).
(7) D. R. Stranks and J. K. Yandell, *J. Phys. Chem.*, 73, 840 (1969).
(8) B. Warnqvist and R. W. Dodson, *Inorg. Chem.*, 10, 2624 (1971).
(9) G. Biedermann, *Ark. Kemi.* 5, 441 (1953).
(10) T. E. Rogers and G. M. Waind, *Trans. Faraday Soc.*, 57, 1360 (1961).
(11) D. Behar, G. Czapski, J. Rabani, L. M. Dorfman, and H. A. Schwarz, *J. Phys. Chem.*, 74, 3209 (1970).
(12) P. Pagsberg, H. Christensen, J. Rabani, G. Nilsson, J. Fenger, and S. O. Nielsen, *J. Phys. Chem.*, 72, 1029 (1969).
(13) O. L. Forchheimer and R. P. Epple, *J. Amer. Chem. Soc.*, 74, 5772 (1952).
(14) M. S. Sherrill and A. J. Haas, Jr., *J. Amer. Chem. Soc.*, 58, 952 (1936).
(15) H. I. Stonehill, *Trans. Faraday Soc.*, 39, 72 (1943).
(16) L. B. Magnusson and J. R. Huizenga, *J. Amer. Chem. Soc.*, 75, 2242 (1953).
(17) W. M. Latimer, "Oxidation Potentials," Prentice-Hall, New York, N. Y., 1952.
(18) L. Brewer, L. A. Bromley, P. W. Gilles, and N. L. Lofgren, National Nuclear Energy Series IV-19B (Paper 6), 76 (1950).
(19) G. Dulz, private communication, 1959.
(20) R. Powell and W. M. Latimer, *J. Chem. Phys.*, 19, 1139 (1951).
(21) N. S. Hush, *Trans. Faraday Soc.*, 57, 557 (1961).
(22) H. A. Catherino and J. Jordan, *Talanta*, 11, 155 (1964).
(23) R. A. Marcus, *Ann. Rev. Phys. Chem.*, 15, 155 (1964).
(24) J. Silverman and R. W. Dodson, *J. Phys. Chem.*, 56, 846 (1952).
(25) M. G. Adamson, F. S. Dainton, and P. Glenworth, *Trans. Faraday Soc.*, 61, 689 (1965).
(26) J. W. Gryder and M. C. Dorfman, *J. Amer. Chem. Soc.*, 83, 1254 (1961).
(27) A. G. Sykes, *J. Chem. Soc.*, 5549 (1961).
(28) J. Halpern, *Quart. Rev., Chem. Soc.*, 15, 207 (1961).
(29) W. C. E. Higginson, D. R. Rosseinsky, J. B. Stead, and A. G. Sykes, *Discuss. Faraday Soc.*, 29, 49 (1960).
(30) N. Sutin, *Ann. Rev. Nucl. Sci.*, 12, 285 (1962).
(31) D. R. Stranks and J. K. Yandell, "Exchange Reactions," IAEA, Vienna, 1965, p 83.
(32) M. G. Adamson and D. R. Stranks, *Chem. Commun.*, 648 (1967).
(33) D. F. Abell, N. A. Bonner, and W. Goishi, *J. Chem. Phys.*, 27, 658 (1957).

Band-Shape Correlations in the Electronic Absorption Spectra of Para-(+M)-Substituted Nitrobenzene Derivatives

Richard R. Minesinger and Mortimer J. Kamlet*[1]

Chemistry Department. Andrews University. Berrien Springs. Michigan 49104. and Advanced Chemistry Division. U. S. Naval Ordnance Laboratory. White Oak. Silver Spring. Maryland 20910   (Received May 16. 1973: Revised Manuscript Received November 26. 1973)

The longer wavelength half-band-widths-at-half-height for the first intramolecular charge transfer band of a number of para-(+M)-substituted nitrobenzene derivatives are linearly related to frequencies of maximum absorption. A rationale involving relative equilibrium geometries of ground and electronic excited states is proposed.

Relationships between the structures of organic compounds and their electronic absorption spectra have occupied a significant proportion of the total literature in physical organic chemistry for almost 30 years. Of the thousands of correlation studies which have been published, an overwhelming majority have been based on inferences drawn from relative positions and/or intensities of absorption maxima. Primary emphasis has been on the effects of substituents. steric hindance to planarity. and molecular environment on ν_{max} (or λ_{max}) and ϵ_{max} values, and only infrequent attention has been devoted to details regarding the shapes of the spectral envelopes. We wish now to record some recent observations regarding band shapes in the electronic absorption spectra of para-(+M)-substituted nitrobenzene derivatives.[2] and to suggest that band-width variations for related compounds may also provide important information in the field of spectra-structure correlations.

Results

The electronic absorption spectra of para-(+M)-substituted nitrobenzenes, p-R-C_6H_4-NO_2, are dominated in the visible and near-ultraviolet by a moderately intense band (ϵ_{max} 8–20,000) which is found near 250 nm for R = H and near 400 nm for R = $(C_2H_5)_2$N. This band has been termed an "intramolecular charge-transfer band," and is considered to arise from a one-electron transition from the highest occupied perturbed molecular orbital of the R-C_6H_4- moiety to the lowest unoccupied perturbed molecular orbital of the nitro group.[3] Such a transition has as its terminus a highly polar electronic excited state, which is conveniently represented by 1. That this band

1
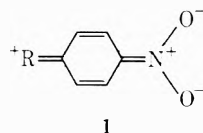
undergoes a bathochromic shift with increasing solvent polarity.[4] and with increasing electron-donor ability of the para substituent[5,6] is fully consistent with its designation as an intramolecular charge-transfer band involving ring → nitro electron promotion.

Band-shape and ν_{max} data for the [⁻R=C(4) → C(1)=NO_2⁻] bands of 25 para-complementary substituted nitrobenzene derivatives in cyclohexane, methanol, and water are assembled in Table I. Positions of the maxima cover a 16.5-kK (180 nm) range, which corresponds to a difference of about 46 kcal/mol in excitation energies.

Where the maxima for these bands fall below about 280 nm (35.7 kK), they are strongly overlapped on their shorter wavelength sides by the tails of high-intensity bands below 210 nm. To minimize the effects of such complications on the band shapes. we have confined our consideration to those portions of the spectral envelopes from ν_{max} to the red, the operating assumption being that corresponding transitions in structurally related compounds should lead to absorption bands of comparable symmetry. Also, to simplify and quantitate the comparisons, we have tabulated the band-shape data in terms of half-band-widths-at-half-height (HBW), this quantity being defined here as the difference (in kK) between ν_{max} and the frequency on the longer wavelength side (ν_{hh}) at which the absorption intensity is one-half of ϵ_{max}, i.e., HBW (in kK) = ν_{max} − ν_{hh}. Values of HBW in Table I range from ca. 1.5 to ca. 3.3 kK.

It is evident from the tabulated results that there are strong trends in the three solvents toward decreasing HBW with decreasing ν_{max}. These trends, plotted in Figure 1, appear to show fair linear regression as is confirmed by least-squares analysis. The least-squares equations are in C_6H_{12}

$$HBW = 0.095\nu_{max} - 0.99 \text{ kK} \tag{1}$$

r (the correlation coefficient) = 0.94, sd (the standard deviation) = 0.15 kK; in CH_3OH

$$HBW = 0.084\nu_{max} - 0.20 \text{ kK} \tag{2}$$

r = 0.96, sd = 0.13 kK; and in H_2O

$$HBW = 0.095\nu_{max} - 0.28 \text{ kK} \tag{3}$$

r = 0.95, sd = 0.17 kK. Considering the precision limits of the measurements.[7] these r and sd values must be considered to indicate fair-to-good correlation in the linear fits. Deviations of the individual data points from the correlation equations are also tabulated in Table I.

Discussion

A trend toward decreasing HBW with decreasing transition energy is best understood if we consider the respective ground and excited states of the molecules involved. The ground state of nitrobenzene has been calculated to

TABLE I: Spectral Data for Para-(+M)-Substituted Nitrobenzene Derivatives[a]

R in 4-R-C$_6$H$_4$-NO$_2$	Cyclohexane		Sd from eq 1	Methanol		Sd from eq 2	Water		Sd from eq 3
	ν_{max}	HBW		ν_{max}	HBW		ν_{max}	HBW	
H	39.53	2 56	(−0.20)	38.61	2.90	(−0.14)	37.31	3.00	(−0.26)
F	38.68	2 58	(−0.10)	37.74	2.96	(−0.01)	36.63	3.07	(−0.15)
ClCH$_2$	38.31	2 47	(−0.18)	37.52	2.80	(−0.15)	36.63	3.07	(−0.15)
CH$_3$COO	37.74	2 90	(+0.30)	37.03	3.36	(+0.45)	36.63	3.30	(+0.08)
CH$_3$	37.59	2 63	(+0.05)	36.43	2.88	(+0.02)	35.09	3.14	(+0.09)
Cl	37.52	2 56	(−0.01)	36.97	2.84	(−0.07)	35.87	3.05	(−0.07)
BrCH$_2$	37.52	2 62	(+0.05)	36.76	2.75	(−0.13)	35.50	3.06	(−0.03)
C$_2$H$_5$	37.52	2 68	(+0.11)	36.43	2.88	(+0.02)	34.96	3.06	(+0.02)
Br	36.90	2 48	(−0.03)	36.36	2.69	(−0.16)	35.15	3.00	(−0.06)
HO	35.21	2 53	(+0.18)	32.05	2.46	(−0.03)	31.45	2.88	(+0.17)
I	34.48	2 01	(−0.28)	34.31	2.56	(−0.12)	33.11	2.71	(−0.15)
CH$_3$O	34.01	2 06	(−0.18)	32.68	2.42	(−0.12)	31.55	2.86	(+0.10)
C$_6$H$_5$O	33.90	2 15	(−0.08)	33.11	2.53	(−0.05)	31.95	2.88	(+0.12)
C$_6$H$_5$	33.78	2 53	(+0.31)	32.68	2.68	(+0.14)	31.85	3.03	(+0.28)
CH$_3$CONH	32.57	2 13	(+0.03)	31.85	2.62	(+0.14)	31.55	3.10	(+0.38)
H$_2$N	31.01	2 07	(+0.11)	26.95	2.11	(+0.05)	26.28	2.36	(+0.14)
CH$_3$NH	29.11	1 64	(−0.14)	26.01	1.88	(−0.10)	24.54	1.97	(−0.08)
C$_2$H$_5$NH	28.98	1 70	(−0.06)	25.84	1.92	(−0.05)	24.33	1.88	(−0.15)
(CH$_3$)$_2$CHNH	28.82	1 65	(−0.10)	25.67	1.92	(−0.04)	24.24	1.92	(−0.11)
(CH$_3$)$_2$N	28.09	1 71	(+0.03)	25.64	1.89	(−0.06)	23.61	1.92	(−0.04)
O$^-$				25.58	1.97	(+0.02)	24.94	1.79	(−0.30)
(CH$_2$)$_3$N	28.05	1 80	(+0.12)	25.45	2.00	(+0.06)	23.64	2.04	(+0.07)
(CH$_2$)$_4$N	27.59	1 68	(+0.05)	25.22	1.84	(−0.08)	23.09	1.86	(−0.05)
(CH$_2$)$_5$N	27.70	1 64	Nil	25.58	2.00	(+0.05)	23.50	2.09	(+0.14)
(C$_2$H$_5$)$_2$N	27.40	1 46	(−0.15)	25.13	1.85	(−0.06)	23.26	1.85	(−0.08)

[a] All ν_{max}, HBW, and sd values are in kilokaysers (kK).

include a 6.6% contribution from an intramolecular charge-transfer state polarized parallel to the twofold axis of symmetry of the molecule (conveniently represented by **2**), while the electronic excited state which is reached by absorption of energy at the first charge-transfer band is calculated to include a 70.3% contribution from **2**.[3]

2
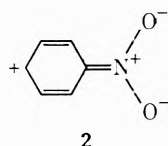
Hence, the ground state of nitrobenzene has much less polar character than the excited state for the first charge-transfer band, and the two states will have some degree of difference in preferential geometry.[8] For example, the preferential or equilibrium geometry for the excited state of nitrobenzene will reflect increased double bond character in the C(2)–C(3), C(5)–C(6), and C(1)–N bonds relative to the ground state.

It has been mentioned that the [$^+$R=C(4) → C(1)=NO$_2^-$] intramolecular charge-transfer band is shifted to longer wavelengths by +M substituents in the para position, absorption maxima for the N,N-dialkyl-4-nitroanilines being displaced bathochromically by about 150 nm relative to nitrobenzene. Classical resonance theory predicts fairly large contributions to the ground-state resonance hybrids for such compounds by quinoid structures such as **3**.

3
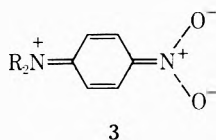
Dipole moment measurements provide support for such a view. For example, the so-called interaction moment

(the difference between the experimental dipole moment and that calculated from group moments) represents 21% of the experimental dipole moment for N,N-dimethyl-4-nitroaniline.[9] The contribution of **3** to the ground state is also evidenced by near coplanarity of the substituents and shortened (CH$_3$)$_2$N–C(4), C(2)–C(3), C(5)–C(6), and C(1)–NO$_2$ bonds in the crystal structure of N,N-dimethyl-4-nitroaniline.[10]

The electronic excited states for the N,N-dialkyl-4-nitroanilines are also identified with charge-separated quinoid structures such as **3**. Thus, as compared with the situation discussed earlier for nitrobenzene, the ground and electronic excited states will have much more closely similar preferential geometries.[8]

Indeed, it is reasonable to enunciate as a general rule that complementary conjugative disubstitution in aromatic compounds (i.e., mesomeric electron donor para to mesomeric electron acceptor) will lead to large contributions by dipolar quinoid structures to ground states, and hence toward increasing similarities of these ground states to preferential geometries of electronic excited states for the first charge-transfer transition. Since complementary conjugative disubstitution also leads to decreasing transition energies for these first charge-transfer bands,[5,11] it logically follows that we should expect a trend of increasingly similar preferential geometries of ground and electronic excited states with increasing λ_{max} (or decreasing ν_{max}).

From the Franck–Condon theory of band spectra has come the postulate that the greater the difference in preferential configuration of the ground and excited states of a molecule, the greater will be the extent of the vibrational progression associated with the electronic transition.[12] Although vibrational progressions cannot usually be resolved for spectra in condensed media, it is generally considered that they are largely responsible for the overall width of any given electronic absorption band.[13,14]

Figure 1. Half-band-width variations with ν_{max} for para-(+M)-substituted nitrobenzene derivatives.

bornanedione whose ground and excited states have very similar preferential geometries.

Out-of-Line Results. One important utility of correlation equations (1-3) is that nonconformance (*i.e.*, half-band widths differing from predicted by more than two standard deviations) could suggest the operation of other than usual factors contributing to abnormalities in band shape. For example, significantly higher than predicted HBW values are noted in the cases of 4-nitrophenyl acetate in cyclohexane and methanol, and N-(4-nitrophenyl)-acetamide in water (Table I). For these compounds we have the possibility of multiple conformational isomers, 4a and 4b, wherein the para substituent is coplanar with the ring, and it is not unreasonable that, depending on the solvents, such conformers should be of comparable free energies.

X = O. NH
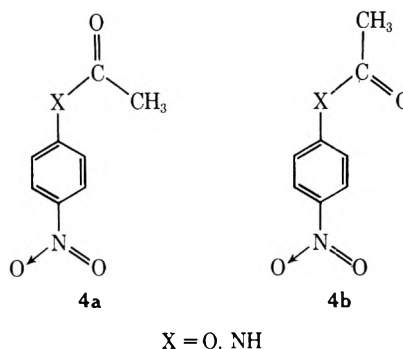
This might lead to **4a** and **4b** each being represented by separate zero-zero species whose dipole moments should be different and which would therefore be expected to absorb light of somewhat different frequencies. The factors discussed above regarding ground- and excited-state geometries and band shape could apply for each conformer, but in the summation the spectral envelope would show the same effect as results from the fusion of two closely spaced bands of comparable intensity, *i.e.*, a broadened band with ν_{max} midway between the individual ν values.[16] That ϵ_{max} values for 4-nitrophenyl acetate are significantly lower than those for the other 4-nitrophenol derivatives of Table I,[17] while half-band integrated intensities are about the same is consistent with such a rationale.

Solvent Effects on Band Widths. The trend of increasing HBW on going from cyclohexane to methanol to water (see Table I) deserves comment. It has recently been demonstrated[18] that weak hydrogen bonds are formed between protic solvents and nitro group oxygens of nitrobenzene derivatives, and that such hydrogen bonding leads to bathochromic displacements of first charge-transfer bands. Thus, a solution of a nitrobenzene derivative in R-OH could include non-hydrogen-bonded molecules, as well as molecules involved in hydrogen bonds with solvent monomer

$$X—C_6H_4—N{\overset{\displaystyle O\cdots H—O}{\underset{\displaystyle O}{\diagdown}}}\!\diagup^{R}$$
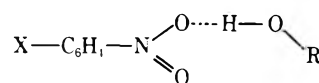
and solvent polymer

$$X—C_6H_4—N{\overset{\displaystyle O\cdots H—O\cdots(H—O)_n}{\underset{\displaystyle O}{\diagdown}}}\!\diagup_{R}\diagdown^{R}$$
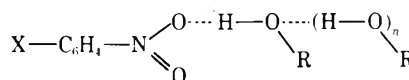
The spectral consequences of having molecules at three differing states of solvation would again be to broaden the spectral envelope. Each type of solvated molecule would give rise to its own slightly different absorption band, and

Thus, we believe the present correlations of HBW with ν_{max} for nitrobenzene derivatives to be consequences of fundamental properties of the ground and excited states associated with the $[^+R=C(4) \rightarrow C(1)=NO_2^-]$ electronic transition. Our reasoning is summarized as follows. (1) Positions of maximal absorption, ν_{max}, have been inversely related to strengths of mesomeric interaction,[5,11] *i.e.*, nitrobenzenes with stronger +M substituents in the para position absorb at smaller ν_{max} than those with weaker +M substituents. (2) Relative similarities of preferential geometries of ground *vs.* excited states for the first charge-transfer band of para-complementary substituted nitrobenzenes are directly related to strengths of mesomeric interactions, *i.e.*, strong +M substituents directly conjugated with a strong −M substituent such as nitro lead to similar preferential geometries. (3) The difference in preferential geometry of the ground *vs.* excited state affects the extent of the vibrational progression of the absorption bands;[12] consequently relatively narrow bands result when preferential geometries are similar. (4) Relatively narrow bands would thus be expected for nitrobenzenes with strong +M substituents. These same nitrobenzenes exhibit the smallest ν_{max} values, and hence arises the direct relationship which we have found between HBW and ν_{max}.

At least one example which accords with the above reasoning has been reported in the recent literature. Evans and Leermakers[15] have shown that the preferential geometries of the ground and excited states of pivalil differ significantly. They also noted that the absorption band for pivalil was very broad, in marked contrast to that of

the overlap of these bands would lead to the higher HBW values in the protic solvents.

Experimental Section

Compounds were obtained commercially or prepared by published procedures. Absorption spectra were determined using a Cary Model 14 recording spectrophotometer with matched 1-cm silica cells. Previously described precautions were taken to guard against photochemical transformations.[19]

References and Notes

(1) Permanent address, Advanced Chemistry Division, U. S. Naval Ordnance Laboratory.

(2) C. K. Ingold, "Structure and Mechanism in Organic Chemistry," 2nd ed, Cornell University Press, Ithaca, N. Y., 1969, Section II-7e.

(3) (a) S. Nagakura, M. Kojima, and Y. Murayama, *J. Mol. Spectrosc.*, **13**, 174 (1964); (b) H. Suzuki, "Electronic Absorption Spectra and Geometry of Organic Molecules," Academic Press, New York, N. Y., 1967, Section 22.1.

(4) W. M. Schubert, H. Steadly, and J. M. Craven, *J. Amer. Chem. Soc.*, **82**, 1253 (1960); W. M. Schubert, J. Robins, and J. L. Haun, *ibid.*, **79**, 910 (1957); K. Semba, *Bull. Chem. Soc. Jap.*, **34**, 722 (1961); J. H. P. Utley, *J. Chem. Soc.* 3252 (1963).

(5) L. Doub and J. M. Vandenbelt, *J. Amer. Chem. Soc.*, **69**, 2714 (1947).

(6) C. N. R. Rao, "Ultraviolet and Visible Spectroscopy, Chemical Applications," 2nd ed, Butterworths, London, 1967, pp 63–71.

(7) To provide a context within which to evaluate the magnitudes of the sd's a 1-nm combined error in estimates of λ_{max} and λ_{hh} leads to a 0.06-kK error in HBW at 400 nm, a 0.16-kK error at 250 nm.

(8) By *preferential* or *equilibrium geometry* of the excited state, we do not imply any violation of the Franck–Condon principle. Rather, we use the term *preferential geometry* to indicate that geometry which the molecule would prefer to assume in the excited state if the Franck–Condon principle were not operative, and which it probably does assume through here unspecified relaxation processes subsequent to the actual instant of excitation.

(9) V. I. Minkin, O. A. Osipov, and Y. A. Zhdanov, "Dipole Moments in Organic Chemistry," Plenum Press, New York, N. Y., 1970, p 211.

(10) T. C. W. Mak and J. Trotter, *Acta Crystallogr.*, **18**, 68 (1965).

(11) H. H. Jaffé and M. Orchin, "Theory and Applications of Ultraviolet Spectroscopy," Wiley, New York, N. Y., 1962, Section 12.3.

(12) E. U. Condon, *Phys. Rev.*, **32**, 858 (1928); a concise outline is given in ref 3, section 5.1.1.

(13) Reference 11, section 6.8.

(14) The difference in full-band widths (= 2 HBW) between nitrobenzene and N,N-diethyl-4-nitroaniline (ca. 2.2 kK, corresponding to 6.3 kcal/mol) is within the range usually associated with energy differences between vibrational levels of low quantum number; see ref. 3, section 1.1.1.

(15) T. R. Evans and P. A. Leermakers, *J. Amer. Chem. Soc.*, **89**, 4380 (1967).

(16) J. M. Vandenbelt and C. Heinrich, *Appl. Spectrosc.*, **7**, 173 (1953); ref 11, Section 6.1.

(17) For example, for R-O-C₆H₄-NO₂ in methanol, R-, and ϵ_{max} (× 10³) are as follows: H, 10.9; CH₃, 11.2; C₆H₅, 11.8; CH₃CO, 8.9.

(18) M. J. Kamlet, E. G. Kayser, J. W. Eastes, and W. H. Gilligan, *J. Amer. Chem. Soc.*, **95**, 5210 (1973).

(19) M. J. Kamlet and L. A. Kaplan, *J. Org. Chem.*, **22**, 576 (1957).

Rate Constant for CO + O₂ = CO₂ + O from 1500 to 2500 K. A Reevaluation of Induction Times in the Shock-Initiated Combustion of Hydrogen–Oxygen–Carbon Monoxide–Argon Mixtures

W. T. Rawlins and W. C. Gardiner, Jr.*

Department of Chemistry, The University of Texas, Austin, Texas 78712 (Received September 20, 1973)

Induction time data for shock-initiated combustion of H₂:O₂:Ar = 1:5:94 and H₂:O₂:CO:Ar = 1:5:3:91 mixtures were reanalyzed to provide the rate constant expression $k_{10} = 1.2 \times 10^{11} \exp(-35 \text{ kcal}/RT)$ cm³ mol⁻¹ sec⁻¹ for the reaction CO + O₂ = CO₂ + O from 1500 to 2500 K.

Introduction

The direct reaction between CO and O₂ is too slow, by many orders of magnitude, to lead to perceptible oxidation of CO at room temperature. At temperatures above 1000 K, however, it is fast enough to play an important role in many combustion processes. We reported a measurement of its rate based on a comparison of OH radical induction times in H₂:O₂:Ar = 1:5:94 and H₂:O₂:CO:Ar = 1:5:3:91 mixtures.[1] The data analysis employed in that work has several shortcomings: (1) the data points were not corrected for shock velocity attenuation; (2) the set of rate constant expressions used to describe the H₂–O₂ chemistry was not in accord with current experimental re-

sults[2,3] (3) the rate constant expression used for the reaction CO + OH = CO₂ + H was not in accord with the most recent measurements;[3] (4) the rate constant expression for CO + O₂ = CO₂ + O was derived using a higher temperature result[4] as a reference point, which implies that the activation energy was not determined from induction time data alone.

These shortcomings are alleviated in the revised data analysis presented here. The resulting rate constant expression $k_{10} = 1.2 \times 10^{11} \exp(-35 \text{ kcal}/RT)$ cm³ mol⁻¹ sec⁻¹ is about 20% less than the one previously reported over the 1500 to 2500 K temperature range of our experiments.

TABLE I: Mechanism and Rate Constant Expressions[a]

	Reaction	k	Ref
(01)	$H_2 + M = 2H + M$	$2.23 \times 10^{12}T^{1/2} \exp(-92,600/RT)$	b
(02)	$O_2 + M = 2O + M$	$1.85 \times 10^{11}T^{1/2} \exp(-95,700/RT)$	c
(03A)	$H_2 + M = H_2^* + M$	$4.11 \times 10^{12} \exp(-49,600/RT)$	d
(03B)	$H_2^* + O_2 = 2OH$	$5.0 \times 10^{10}T^{1/2}$	d
(1)	$H + O_2 = OH + O$	$4.0 \times 10^{13} \exp(-12,300/RT)$	e
(2)	$H_2 + O = OH + H$	$1.6 \times 10^{14} \exp(-13,500/RT)$	f
(3)	$H_2 + OH = H_2O + H$	$5.2 \times 10^{13} \exp(-6500/RT)$	g
(4)	$H + O_2 + M = HO_2 + M$	$2.0 \times 10^{15} \exp(870/RT)$	h
(5)	$H + O_2 + H_2O = HO_2 + H_2O$	$5.0 \times 10^{16} \exp(870/RT)$	h
(6)	$H + OH + M = H_2O + M$	$7.5 \times 10^{23}T^{-2.6}$	i
(7)	$H_2 + HO_2 = H_2O + OH$	$2.0 \times 10^{11} \exp(-24,000/RT)$	j
(8)	$OH + OH = H_2O + O$	$5.5 \times 10^{13} \exp(-7000/RT)$	f
(9)	$CO + OH = CO_2 + H$	$4.0 \times 10^{12} \exp(-8000/RT)$	k, g
(10)	$CO + O_2 = CO_2 + O$	$1.2 \times 10^{11} \exp(-35,000/RT)$	See text
(11)	$CO + O + M = CO_2 + M$	$3.4 \times 10^{11} \exp(-23,400/RT)$	l

[a] Concentration units are mol/cm^3. Energy units are cal/mol. [b] A. L. Myerson and W. S. Watt, *J. Chem. Phys.*, **49**, 425 (1968). [c] W. S. Watt and A. L. Myerson, *ibid.*, **51**, 1638 (1969). [d] Reference 8. The rate of reaction 03A was adapted for the composition of these mixtures from J. H. Kiefer and R. W. Lutz *J. Chem. Phys.*, **44**, 668 (1966). The rate of reaction 03B was adjusted for optimal fit of $H_2:O_2:Ar = 1:5:94$ induction times. It should be noted that the initiation mechanism of the H_2-O_2 explosion is not of importance for the purposes of the present paper. All that is necessary is a correct accounting for the length of the induction period in the one H_2-O_2 mixture with which we are comparing the H_2-O_2-CO mixture. Any other combination of elementary reactions and rate constants which would give the correct induction times would also be satisfactory. [e] Reference 9. [f] W. T. Rawlins and W. C. Gardiner, Jr., *J. Chem. Phys.*, submitted for publication. [g] W. C. Gardiner, Jr., W. G. Mallard, and J. H. Owen, *ibid.*, submitted for publication; reference 3. [h] D. Gutman, E. A. Hardwidge, F. A. Dougherty, and R. W. Lutz, *J. Chem. Phys.*, **47**, 4400 (1967). [i] J. B. Homer and I. R. Hurle, *Proc. Roy. Soc., Sec. A*, **314**, 585 (1970). [j] V. V. Voevodsky, *Symp. (Int.) Combust., [Proc.], 7th, 1958*, 34 (1959). [k] W. C. Gardiner, Jr., M. McFarland, K. Morinaga, W. T. Rawlins, T. Takeyama, and B. F. Walker, *J. Chem. Phys.*, submitted for publication. [l] M. C. Lin and S. H. Bauer, *ibid.*, **50**, 3377 (1969).

Experimental Section

The details of the laboratory procedures used to obtain OH radical induction times were given previously.[1]

One aspect of the experiments not taken into account before is velocity attenuation of the incident shock waves. Detailed analysis of the velocity records for a large number of runs with conditions similar to those reported here revealed that, in our shock tube, an average velocity attenuation of about 2% per meter underlies an irregular jitter in shock arrival times due to shock front wobble, inconsistent resistance gauge response, and counting error.[5] Although an exacting accounting for the consequences of this attenuation is only possible in terms of unsteady shock flow, an approximate correction appropriate for these experiments can be obtained as follows. The principal effect of attenuation here is that the gas which is observed at the onset of ignition (when $[OH] = 2.5 \times 10^{-7}$ M) was first compressed in a shock front that was typically 15 K hotter than the shock front which later passed the observation station. Since the computer-generated reaction profiles with which the experiments are to be compared assume steady shock flow, the experimental induction times should be assigned to no-reaction shock temperatures characteristic of the shock fronts which compressed the gas observed at the end, rather than at the beginning, of the induction period. Due to the irregularity of the arrival time measurements in a single experiment, the average attenuation value was used for this assignment. The laboratory time between shock passage and ignition was converted to distance behind the shock front using the measured shock velocity; the attenuation correction corresponding to this distance was multiplied by the shock density ratio and this product was then added to the measured velocity to give the velocity used to calculate no-reaction shock parameters.

The rate constant set used in numerical integrations is given in Table I. As described in our earlier paper, the final result for reaction 10 is slightly sensitive both to the expressions assumed for some of the other rate constants and to assumptions about the character of the shock flow
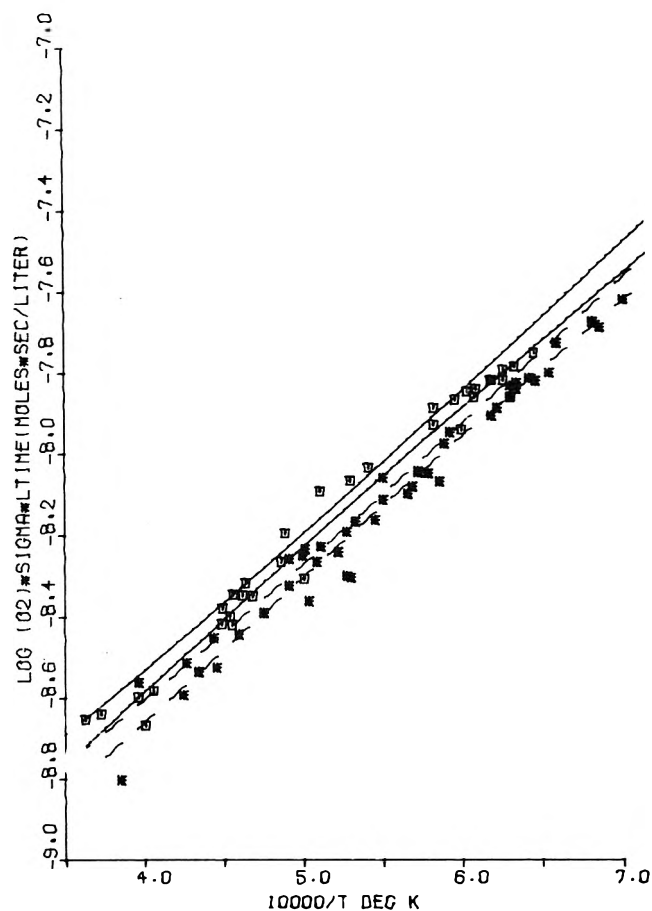
Figure 1. Experimental induction time data. The ordinate is log $(\sigma[O_2]_0 t_i)$, where σ = shock density ratio, $[O_2]_0$ = initial postshock O_2 concentration, t_i = laboratory time from shock passage to $OH] = 2.5 \times 10^{-7}$ M, $\square$ = $H_2:O_2:Ar = 1:5:94$ data,* $\ast$ = $H_2:O_2:CO:Ar = 1:5:3:91$ data. The curves represent 95% confidence limits on the least-squares line for each set of data.

resulting from boundary layer growth. In order to obtain a valid k_{10} expression, a consistent choice of rate constants and flow model must be made for both mixtures; in order
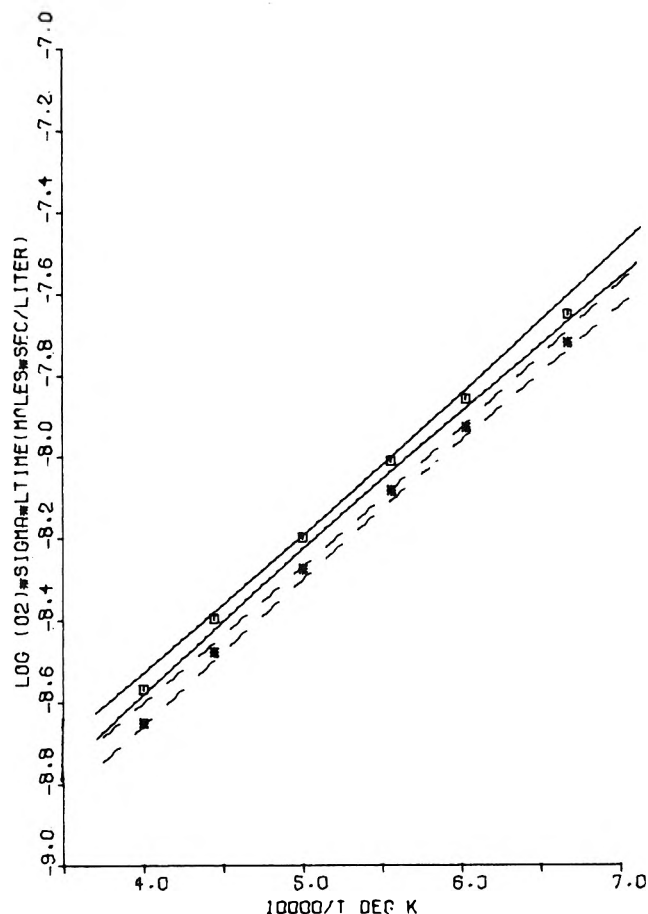
Figure 2. Computed induction times. The coordinates and the confidence limit lines are the same as in Figure 1. The symbols □ and * show induction times computed using the rate constant set of Table I.

Figure 3. Arrhenius graph for CO + O₂ = CO₂ + O. BARTLE-MYERS: unpublished work of E. R. Bartle and B. F. Myers. (B. F. Myers, private communication.) The upper expression is obtained from the O_3-CO_2-Ar results of these authors when the value of $k(CO_2 + M = CO + O + M)$ of E. S. Fishburne, K. R. Bilwakesh, and R. Edse, *J. Chem. Phys.*, **45**, 160 (1966), (FBE), is used in the data analysis, while the lower expression is obtained with $k(CO_2 + M = CO + O + M)$ from K. W. Michel, H. A. Olschewski, H. Richterling, and H. G. Wagner, *Z. Phys. Chem. (Frankfurt am Main)*, **39**, 129 (1963); *ibid.*, **44**, 160 (1965) (MORW). Both expressions were derived from k_{-10}. BBB: T. A. Brabbs, F. E. Belles, and R. S. Brokaw, *Symp. (Int.) Combust.*, [Proc.], *13th*, *1970*, 129 (1971). BROKAW: R. S. Brokaw, ref **4**. DK: A. M. Dean and G. B. Kistiakowsky, *J. Chem. Phys.*, **53**, 830 (1970). DRUMMOND: L. J. Drummond, *Aust. J. Chem.*, **21**, 2631 (1968). SLP: R. G. P. Sulzmann, L. L. Leibowitz, and S. S. Penner, *Symp. (Int.) Combust.*, [Proc.], *13th*, *1970*, 137 (1971). SMB: K. G. P. Sulzmann, B. F. Myers, and E. B. Bartle, *J. Chem. Phys.*, **42**, 3969 (1965); **43**, 1220 (1965). Two entries on the corresponding Arrhenius graph of our previous paper (ref 1) are deleted here, as the results were apparently affected by hydrocarbon impurities; cf. T. C. Clark, A. M. Dean, and G. B. Kistiakowsky, *J. Chem. Phys.*, **54**, 1726 (1971). A discussion of possible reasons for the discrepancy between the BBB line and the other data is given in ref 1. The apparent curvature of the consensus Arrhenius graph is in accord with experience for other bimolecular reactions studied over wide temperature ranges (cf. ref 3).

to obtain the most accurate possible result, the optimal set of other rate constant expressions is required. All rate constant expressions except for k_{03B} were obtained in independent experiments, as cited in Table I. An expression for k_{03B} was optimized for the H_2:O_2:Ar = 1:5:94 induction time data by requiring the calculated induction times to match the least-squares regression of the data at temperatures near the high and low ends of the experimental temperature range, and assuming Arrhenius temperature dependence over that range. The differential equations that were integrated were derived on the assumption of steady, limiting separation, incident shock flow with a laminar boundary layer. The equations of Mirels[3] were used to obtain the limiting separation l_m.

Results

The attenuation-corrected induction time data were subjected to a conventional regression analysis in the $x = 10^4/T$, $y = \log(\alpha[O_2]_0 t_i)$ plane. For 33 data points with H_2:O_2:Ar = 1:5:94, the regression gave

$$\log(\sigma[O_2]_0 t_i) = -8.150 \pm 0.0074 + (0.3453 \pm 0.0070)(10^4/T - 5.170)$$

with variance 0.0020. For 46 data points with H_2:O_2:CO:Ar = 1:5:3:91, the result was

$$\log(\sigma[O_2]_0 t_i) = -8.122 \pm 0.0066 + (0.3441 \pm 0.0076)(10^4/T - 5.475)$$

with variance 0.0019. The indicated errors are standard

deviations. An "F" test showed that there was not a significant difference between the two variances, so a common variance of 0.0017 was computed. A "t" test on the slopes of the two lines showed that their difference was not significant, so a common slope of 0.3446 and a new common variance of 0.0414 were computed. A second "t" test on the position of the lines gave $t = 8.02$, with 76 degrees of freedom, which indicated at the 99.9% confidence level that the two regression lines are for data points from different populations. Confidence intervals were computed from

$$\Delta y = t_{N-2}^{95\%}\left[\left(\frac{\sum_{i=1}^{N}(y_i - y)^2 - b\sum_{i=1}^{N}(x_i - \bar{x})(y_i - \bar{y})}{N(N-2)\sum_{i=1}^{N}(x_i - \bar{x})^2}\right) \times \left(\sum_{i=1}^{N}(x_i - \bar{x})^2 + N(x - \bar{x})^2\right)\right]^{1/2}$$

where $N = 33$, t_{N-2} 95% = 2.04 for the $H_2:O_2:Ar$ = 1:5:94 data and $N = 46$, t_{N-2} 95% = 2.015 for the $H_2:O_2:CO:Ar$ = 1:5:3:91 data.[7]

The data and the corresponding confidence intervals are displayed in Figure 1.

All rate constant expressions except for k_{10} having been fixed as described above, numerical integrations of the $H_2:O_2:CO:Ar$ = 1:5:3:91 kinetics were carried out for various k_{10} values until the calculated induction times fit the regression line at temperatures near 1500 and 2000 K. Fitting these two k_{10} values to an Arrhenius expression gave

$$k_{10} = 1.2 \times 10^{11} \exp(-35 \text{ kcal}/RT) \text{ cm}^3 \text{ mol}^{-1} \text{ sec}^{-1}$$

The degree to which numerical integrations with this k_{10} expression reproduce the experimental induction time data over the temperature range 1500–2500 K is shown in Figure 2. In Figure 3 our k_{10} result is compared to previous results.

It was found that calculated induction times depend on the choice of flow model.[8] However, the similar induction times and gas properties of the two mixtures compared here lead to a cancellation of the flow model effect, such that the rate constant expression eventually deduced for reaction 10 is unaffected by the flow model as long as a consistent choice is made for both mixtures.

Discussion

The tolerance in our k_{10} expression required to keep the calculated induction times within the 95% confidence limits is about ±20%. Systematic error, however, is possible from several sources. Since dissociation of impurities can generate chain centers, a significant difference in impurity concentration between the two mixtures would invalidate the data analysis. Against this interpretation are the facts that all the experiments were done with the same procedures and equipment, in part concurrently, and that several gas mixtures of each nominal composition, prepared at various times from different gas sources by different workers, were used for these experiments. Since the differences between the two sets of induction times are relatively small, typically about 20%, it is unlikely that errors could be introduced by anomalies in the gas flow. The mechanism given in Table I is generally thought to be complete; however, it cannot be excluded that there may be some peculiarities in the initiation mechanism of shock-heated CO-containing mixtures that are not encompassed by it.[9]

The role of vibrational relaxation of H_2, O_2, and CO, which occurs on the same or on a slower time scale than chain initiation in these mixtures, is difficult to assess. The translational temperature errors involved in assuming instantaneous vibrational relaxation of O_2 and CO in the numerical integrations are too small to influence the results appreciably, since the same assumption was also made in calculating the no-reaction shock temperature from the shock velocity. The vibrational state populations are changing during the course of chain initiation, however, and if this changes the rates of the initiation reactions, as appears likely on the basis of H_2-O_2 data above,[8] then the meaning of a rate law containing terms such as [CO] [O_2] becomes quite unclear. As suggested previously,[1] repeating these experiments with CO_2 or He catalysis of vibrational relaxation of O_2 and CO might shed light on this problem.

It can be seen that the consensus of the data shown in Figure 3 is that log k_{10} does not vary linearly with inverse temperature. The implications of this nonlinearity, which has been noted before for other reactions,[3] will be the subject of a forthcoming paper on the theory of bimolecular gas reaction rates.

References and Notes

(1) W. C. Gardiner, Jr., M. McFarland, K. Morinaga, T. Takeyama, and B. F. Walker, *J. Phys. Chem.*, **75**, 1504 (1971).
(2) G. L. Schott and R. W. Getzinger, "Shock Tube Studies of the Hydrogen-Oxygen Reaction System" in "Physical Chemistry of Fast Reactions," B. P. Levitt, Ed., Plenum Press, London, 1973.
(3) W. C. Gardiner, Jr., W. G. Mallard, M. McFarland, K. Morinaga, J. H. Owen, W. T. Rawlins, T. Takeyama, and B. F. Walker, *Symp. (Int.) Combust.. [Proc.]*, *14th, 1972*, 61 (1973).
(4) R. S. Brokaw. *Symp. (Int.) Combust.. [Proc.]*, *11th, 1966*, 1063 (1967).
(5) M. McFarland, unpublished results.
(6) H. Mirels, *AIAA J.*, **2**, 84 (1963); *Phys. Fluids*, **6**, 1201 (1963); 7, 1208 (1964); **9**, 1265, 1907 (1966).
(7) F. S. Acton. "Analysis of Straight Line Data," Dover, New York, N. Y., 1966.
(8) C. B. Wakefield. Ph.D. Dissertation, The University of Texas, 1969.
(9) G. L. Schott. *Symp. (Int.) Combust.. [Proc.]*, *12th, 1968*, 569 (1969).

Reactions of NO⁺ with Methanol

David L. Turner and Larry I. Bone*

Department of Chemistry, East Texas State University, Commerce, Texas 75428 (Received August 27, 1973)

Publication costs assisted by the Robert A. Welch Foundation

The reactions of NO⁺ with methanol have been studied in a photoionization mass spectrometer. NO⁺ is found to undergo consecutive clustering reactions until four molecules of CH_3OH are added. These reactions all require collisional stabilization. The clustering reactions are in competition with a series of second-order reactions producing the solvated proton and, presumably, methyl nitrite. Rate constants are calculated and the clustering of NO⁺ with methanol is compared to similar reactions with water. The rate constants for clustering with methanol are found to be large for small clusters but approach those of water for clusters containing three molecules.

Introduction

We have recently become interested in ion clustering reactions and have developed a photoionization quadrupole mass spectrometer which is particularly well suited to these types of investigations. Our first study involved an examination of the reactions of NO⁺ with water.[1]

Fehsenfeld, Mosesman, and Ferguson[2] and Howard, Rundle, and Kaufman[3] have previously reported the reactions of NO⁺ with water using a flowing afterglow system. Puckett and Teague[4] have also investigated the same system by sampling a stationary afterglow. Related studies involving hydration of O_2^+ have been carried out by Fehsenfeld, Mosesman, and Ferguson[5] and Good, Durden, and Kebarle.[6] These authors have reported the reaction mechanism and measured rate constants in the presence of various carrier or buffer gases. We have reported a mechanism for the ion clustering reactions of NO⁺ with water that is consistent with that reported by other authors.

$$NO^+ + H_2O + M \xrightarrow{k_1} NO(H_2O)^+ + M \quad (1)$$

$$NO(H_2O)^+ + H_2O + M \underset{k_{-2}}{\overset{k_2}{\rightleftharpoons}} NO(H_2O)_2^+ + M \quad (2)$$

$$NO(H_2O)_2^+ + H_2O + M \underset{k_{-3}}{\overset{k_3}{\rightleftharpoons}} NO(H_2O)_3^+ + M \quad (3)$$

$$NO(H_2O)_3^+ + H_2O \xrightarrow{k_4} HONO + H(H_2O)_3^+ \quad (4)$$

$$H(H_2O)_n^+ + H_2O \rightleftharpoons H(H_2O)_{n+1}^+ \quad (5)$$
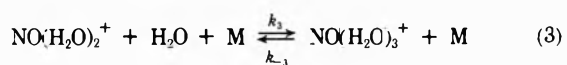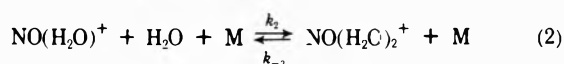
Here M is any third body. The values for the rate constants were measured along with the heats of formation of the various hydrates of NO⁺.

In a related study, Kerbale, Haynes, and Collins[7] investigated the competitive solvation of the proton by water and methanol. They found that methanol is preferentially added to small clusters with water becoming more favored as the cluster size increases. They have attributed this effect to the greater polarizability of methanol. We,[8] as well as a number of other authors,[9,10] have studied the relative acidities of the alcohols and find that the higher homologs are more acidic again because the more polarizable molecule can better stabilize the charge. With this background of data it was felt that quite a bit of information could be learned about clusters by studying the solvation of NO⁺ with methanol.

Experimental Section

A photoionization quadrupole mass spectrometer developed in this laboratory is used in this study. This instrument has been described previously.[1] The instrument can be used with electron impact, photoionization, or in a tandem mode; however, only the photoionization mode is used in this study. A schematic drawing of the instrument is shown in Figure 1.

Mixtures of nitric oxide with methanol mole fractions of 0.0625, 0.125, 0.25, 0.33, 0.50, and 0.66 at a total pressure of 20 to 100 Torr are prepared in a 2-l. expansion bulb in the gas inlet system. Pressure in the inlet is monitored using a Wallace and Tiernan gauge reading from 0 to 100 in. of water.

The reactant gases are bled through a Granville-Phillips variable leak into the ion–molecule source which also serves as the reaction chamber. The pressure in the source is measured with a Granville-Phillips capacitance manometer. The gauge was calibrated with static pressures from aqueous sulfuric acid solutions. The pressure calibration is periodically verified against the rate constant for the reaction of NO⁺ with water. The temperature in the source is measured with an iron–constantan thermocouple and is never found to deviate more than 2° from room temperature.

The photoionization source used is nearly cubical and is 1 cm³ in volume and is constructed of tobin bronze. There is a 0.25-in. o.d. copper gas inlet tube leading into the source. The photoionization source has 1-mm thick LiF windows both front and rear to allow photons to pass through the source without striking metal. All other metal surfaces on the source and analyzer are shielded from photons by a glass plate to prevent photoelectron production. No drawout or repeller potential is used in these experiments leaving the entire source field-free.

One of a series of interchangeable plates with a hole in the center is used as the back of the source. This hole serves as the ion exit for the mass spectrometer. Plates with ion exit holes of 0.040, 0.46, and 0.0625 in. diameter are available. The plate with the 0.0625-in. hole has a wire mesh screen to prevent field penetration into the source and can be used with the plate with the 0.040-in. hole if both a smaller hole and the screen are desired.

Rare gas resonance lamps similar to those described by Ausloos and Lias[11] are the source of ionization. In these studies a krypton resonance lamp with a 1-mm thick LiF
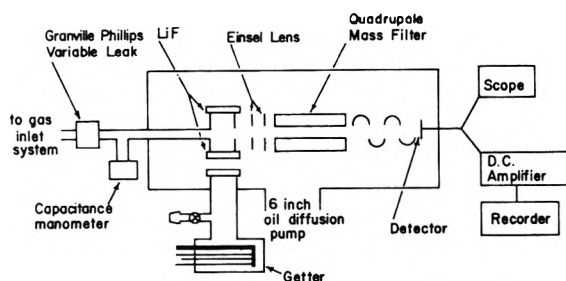
Figure 1. Schematic drawing of the mass spectrometer.

Figure 2. Typical ion spectrum *vs.* total pressure: ■, NO^+; ●, $NO(CH_3OH)^+$; ▲, $NO(CH_3OH)_2^+$; ◖, $NO(CH_3OH)_3^+$; ▼, $NO(CH_3OH)_4^+$; ○, $H(CH_3OH)^+$; △, $H(CH_3OH)_2^+$; ◓, $H(CH_3OH)_3^+$; ▽, $H(CH_3OH)_4^+$; □, $H(CH_3OH)_5^+$.

window is used. It emits two lines at 10.03 and 10.63 eV. A krypton resonance lamp with a 2-mm thick CaF_2 window has also been used with the same results. The CaF_2 window filters out the 10.63-eV line and also reduces the intensity of 10.03-eV line which has an adverse effect on the total ion intensity.

The quadrupole mass filter is an unmodified Du Pont Instruments 21-440 residual gas analyzer. The entire source, including the base plate, is operated at +20 V and the entrance plate to the quadrupole is at ground potential. The intermediate ion-focus plate is normally operated from −150 to −200 V. Experiments with the source at potentials as low as 3 V and the focus plate at much lower potentials yield the same data. An unmodified 13-stage Cu–Be electron multiplier and d.c. amplifier from the original Du Pont instrument are used. The resolution of the quadrupole is variable up to 300 amu. All experiments were conducted at a resolution below 100 to minimize mass discrimination against the higher mass ions. No corrections were made for the mass discrimination of the electron multiplier or the quadrupole.

The entire system is pumped by a Norton pumping station. The source can be operated at 5–8 Torr without exceeding 10^{-5} Torr in the remainder of the instrument. The reagents used were Matheson CP grade nitric oxide, Matheson reagent grade methanol, Stohler Chemicals perdeuteriomethanol, and distilled water which has been passed through two ion-exchange columns. All reagents were out gassed prior to use.

Experiments were conducted on binary mixtures of NO and CH_3OH with CH_3OH mole fractions of 0.0625, 0.125, 0.25, 0.33, 0.50, and 0.66. Also competitive solvation of nitric oxide between water and methanol was studied using ternary mixtures of NO, CH_3OH, and H_2O at mole fractions of H_2O and CH_3OH of 0.25 each. The chemical identity of the ions was established by duplicating experiments with CD_3OD.

Data were collected by mass analyzing the ion distribution diffusing from the source at constant source pressure. The premixed gases were irradiated continuously during the experiments producing the single primary ion NO^+. For a given mixture mass scans were repeated at a variety of source pressures between 0 and 1 Torr. The data are presented as the logarithm of the per cent of total ionization as a function of pressure.

Results and Discussion

In the nitric oxide–water system, which was reported previously, the largest solvate of nitric oxide occurs with three water molecules attached. As an attempt is made to attach the fourth water molecule to the cluster, a "crossover" reaction occurs in which a neutral species, presumably HONO, and the triply solvated proton are produced.

Figure 2 shows a typical plot of the logarithm of the per

cent ionization as a function of total pressure for a mixture of nitric oxide and methanol. In this instance the mixture is 0.66 mol fraction in methanol. Based on the appearance and disappearance of various species as shown in Figure 2, and other data at various mole fractions and on an analogy with the previous study,[1] the following mechanism for the ion clustering reactions of NO^+ with methanol is proposed

$$NO^+ + CH_3OH + M \xrightarrow{k_6} NO(CH_3OH)^+ + M \qquad (6)$$

$$NO(CH_3OH)^+ + CH_3OH + M \underset{k_{-7}}{\overset{k_7}{\rightleftharpoons}} NO(CH_3OH)_2^+ + M \qquad (7)$$

$$NO(CH_3OH)^+ + CH_3OH \xrightarrow{k_8} CH_3ONO + H(CH_3OH)^+ \qquad (8)$$

$$NO(CH_3OH)_2^+ + CH_3OH + M \underset{k_{-9}}{\overset{k_9}{\rightleftharpoons}} NO(CH_3OH)_3^+ + M \qquad (9)$$

$$NO(CH_3OH)_2^+ + CH_3OH \xrightarrow{k_{10}} CH_3ONO + H(CH_3OH)_2^+ \qquad (10)$$

$$NO(CH_3OH)_3^+ + CH_3OH + M \underset{k_{-11}}{\overset{k_{11}}{\rightleftharpoons}} NO(CH_3OH)_4^+ + M \qquad (11)$$

$$NO(CH_3OH)_3^+ + CH_3OH \xrightarrow{k_{12}} CH_3ONO + H(CH_3OH)_3^+ \qquad (12)$$

$$NO(CH_3OH)_4^+ + CH_3OH \xrightarrow{k_{13}} CH_3ONO + H(CH_3OH)_4^+ \qquad (13)$$

$$H(CH_3OH)_n^+ + CH_3OH \rightleftharpoons H(CH_3OH)_{n+1}^+ \qquad (14)$$
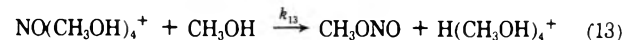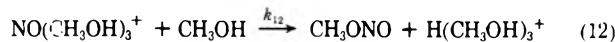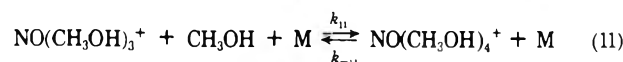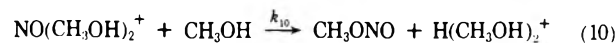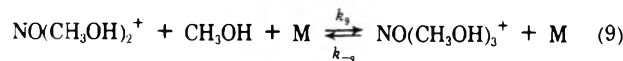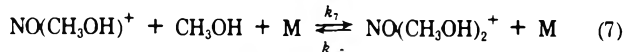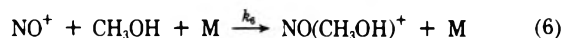
It can be observed that as NO^+ disappears, $NO(CH_3OH)^+$ appears; as its abundance grows $NO(CH_3OH)_2^+$ and $H(CH_3OH)^+$ begins to appear by reactions 7 and 8. The next ion to appear as the pressure is increased is $H(CH_3OH)_2^+$ which is produced both by reactions 10 and reaction 14. NO^+ clusters further with as many as four molecules of methanol but every step, except the first, is in competition with a "crossover" reaction which produces the solvated proton and, presumably, methyl nitrite. Each proton cluster also reacts further by reaction 14.

We have found in previously reported studies[1,12] and in others in progress that if the initial ion produced by the photolysis reacts by a second-order mechanism, a plot of the logarithm of the relative intensity of that ion *vs.* pressure is a straight line at low source pressures. If the initial ion reacts by a third-order mechanism, a plot of the inten-
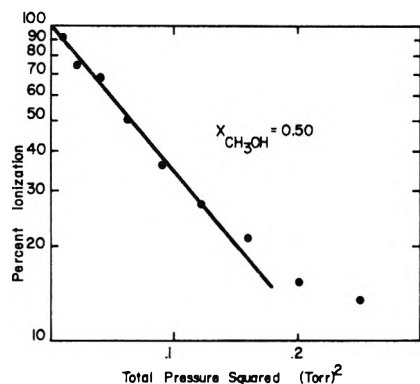
Figure 3. Relative intensity of NO$^+$ vs. total pressure squared.

Figure 4. Determination of k_7 and k_8.

sity of that ion vs. the pressure squared is similarly a straight line at the lowest pressures where we can observe sufficient intensity. Sieck, Searles, and Ausloos,[13] using a similar instrument, observe the same results and, as we do, find that this straight line behavior holds to approximately 0.4 Torr in the ion source. We have also investigated the dependence of ln NO$^+$ on the pressure cubed and find a straight line at pressures between 0.25 and 0.5 Torr. This suggests that the residence time of unreacted primary ions passing from the source is independent of pressure at low pressures and becomes proportional to pressure in the diffusion region. The pressure-independent resident time is expected when the mean free path is long compared to the source dimensions and the unreacted ions observed pass out of source without colliding. We find, however, that this relationship exists to somewhat higher pressures then would be expected.

Figure 3 shows a plot of the logarithm of the per cent ionization of NO$^+$ as a function of pressure squared. In the low-pressure limit a straight line is predicted by the following integrated rate expression

$$\ln \text{NO}^+ = -k_6 X_{CH_3OH} M^2 \tau + \text{constant}$$

where M is the total pressure, X is the mole fraction of methanol, and τ is the residence time of NO$^+$ in the source. The rate constant, k_6, can be calculated from the slope of the line by first computing the collision free residence time using the source dimensions and assuming the unreacted NO$^+$ ions are at thermal velocities. The rate constant, k_6, has also been verified by comparing the slope of the straight line with that obtained in an identical experiment involving NO$^+$ and water where the rate constant has also been measured by a number of other workers.[2-4] A value of $8.0 \pm 1.2 \times 10^{-28}$ cm^6 sec^{-1} is obtained for k_6.

If the reverse rate constant, k_{-7}, k_{-9}, and k_{-11}, can be assumed to be very small as they are in the NO$^+$ water clustering, it is possible to equate the sum of the rates of reactions 7 and 8 to the rate of reaction 6 at the pressure (0.27 Torr in Figure 2) where the concentration of NO-(CH$_3$OH)$^+$ is at a maximum. The following steady-state equation results.

$$k_6[\text{NO}^+][\text{CH}_3\text{OH}][\text{M}] = k_7[\text{NO(CH}_3\text{OH)}^+][\text{CH}_3\text{OH}][\text{M}] + k_8[\text{NO(CH}_3\text{OH)}^+][\text{CH}_3\text{OH}]$$

simplifying

$$k_7[\text{M}] + k_8 = k_6 \frac{[\text{NO}^+][\text{M}]}{[\text{NO(CH}_3\text{OH)}^+]} = k_7(\text{observed})$$
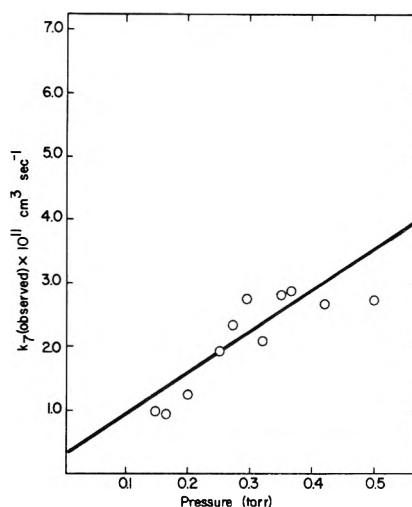
Figure 4 shows a plot of $k_6[\text{NO}^+][\text{M}]/[\text{NO(CH}_3\text{OH)}^+]$, which is called k_7(observed), vs. pressure [M]. The value of k_7 obtained from the slope is $1.9 \pm 0.4 \times 10^{-27}$ cm^6 sec^{-1} while the intercept yields a value of $3.6 \pm 4 \times 10^{-12}$ cm^3 sec^{-1} for k_8.

The same type of kinetic analysis may be applied to the competition between reactions 9 and 10. A value for k_9 of approximately 2×10^{-27} cm^6 sec^{-1} is obtained but the compounded uncertainty is very large since this calculation is based on all of the previous ones. Because of the uncertainty and the low intensity of the ions involved, rate constants for further clustering steps are not calculated.

Comparison of the reaction rate constants for addition of methanol to NO$^+$ and its solvates with those for the addition of water to NO$^+$ and its hydrates proves interesting. A value of $1.3 \pm 0.3 \times 10^{-28}$ cm^6 sec^{-1} is reported[1] for the rate constant for the addition of the first water molecule to NO$^+$. This value is somewhat smaller than $8.0 \pm 1.2 \times 10^{-28}$ cm^6 sec^{-1}, the corresponding rate constant in the methanol–NO$^+$ system. Addition of the second methanol molecule to NO$^+$ is again faster than the addition of the second water molecule to NO$^+$, their rate constants being $1.9 \pm 0.4 \times 10^{-27}$ and $1.2 \pm 0.3 \times 10^{-27}$ cm^6 sec^{-1}, respectively. The rate constant for the third solvation of methanol approaches the corresponding value for the solvation of water with NO$^+$. The rate constant for the third methanol, 2×10^{-27} cm^6 sec^{-1}, is within the experimental error of the corresponding NO$^+$ water rate constant, $3.6 \pm 1.3 \times 10^{-27}$ cm^6 sec^{-1}.

The higher polarizability of methanol (3.23 Å^3) as compared to water (1.48 Å^3) is probably the overriding factor in methanol reacting faster than water with NO$^+$. Kebarle and coworkers have studied the competitive solvation of the hydrogen ion with water and methanol molecules. These studies have shown that methanol molecules are clustered preferentially over those of water to the hydrogen ion in small clusters. As cluster size increases, water molecules are taken up preferentially. This is consistent with the idea that the potential energy of the ion-dipole interaction decreases with the square of the distance while that for the polarizability decreases with the fourth power. The greater polarizability will not only enhance the cross section for initial cluster formation but, coupled with the larger number of vibrational modes of methanol, should increase the stability of the cluster to

decomposition. This is of course consistent with the trend observed by both us and Kebarle.

References and Notes

(1) M. J. McAdams and L. I. Bone, *J. Chem. Phys.*, **57**, 2173 (1973).
(2) F. C. Fehsenfeld, M. Mosesman, and E. E. Ferguson, *J. Chem. Phys.*, **55**, 2120 (1971).
(3) C. J. Howard, H. W. Rundle, and F. Kaufman, *J. Chem. Phys.*, **55**, 4772 (1971).
(4) L. J. Puckett and M. W. Teague, *J. Chem. Phys.*, **54**, 2564 (1971).
(5) F. C. Fehsenfeld, M. Moseman, and E. E. Ferguson, *J. Chem. Phys.*, **55**, 2115 (1971).
(6) A. Good, D. A. Durden, and P. Kebarle, *J. Chem. Phys.*, **52**, 222 (1970).
(7) P. Kebarle, R. N. Haynes, and J. G. Collins, *J. Amer. Chem. Soc.*, **89**, 5753 (1967).
(8) M. J. McAdams and L. I. Bone, *J. Phys. Chem.*, **75**, 2226 (1971).
(9) (a) J. I. Brauman and L. K. Blair, *J. Amer. Chem. Soc.*, **92**, 5987 (1970); (b) *ibid.*, **90**, 6561 (1968).
(10) T. O. Tiernan and B. M. Hughes, Seventeenth Annual Conference on Mass Spectrometry and Allied Topics, 18-23, Dallas, Tex., May 1969.
(11) P. Ausloos and S. B. Lias, *Radiat. Res. Rev.*, **1**, 75 (1968).
(12) J. M. Hopkins and L. I. Bone, *J. Chem. Phys.*, **58**, 1473 (1973).
(13) L. W. Sieck, S. K. Searles, and P. J. Ausloos, *J. Amer. Chem. Soc.*, **91**, 7627 (1969).

Prompt Electron Scavenging by Benzene in Pulse-Irradiated Alcohols

Hajime Ogura[1] and William H. Hamill*

Department of Chemistry and the Radiation Laboratory,[2] University of Notre Dame, Notre Dame, Indiana 46556

(Received September 17, 1973)

The yield of solvated electrons in 1-propanol at the end of 5-15-nsec pulse irradiation was decreased by 0.5, 1.0, and 1.5 M benzene from 0.122 to 0.097, 0.073, and 0.058 at $t = 0$ in terms of the e_{sol}^- optical density at 700 nm. The spectrum from 500 to 800 nm was unaffected by benzene at $t = 0$ and at $t = 50$ nsec. For the slow reaction of the solvated electron $k(e_{sol}^- + C_6H_6) \cong 10^7 M^{-1} sec^{-1}$ and the decreased yield of e_{sol}^- at $t = 0$ cannot be attributed to it. On the other hand, the dry-electron attachment by benzene is a possible explanation. Comparable results were obtained for electron scavenging by benzene in ethanol at 0.5-2 M. Limited observations in 1,2-ethanediol gave comparable results. The efficiencies of the prompt scavenging of e^- in alcohols are similar to results for electron scavenging in alkanes, which indicates that in alcohols a quasi-free state of the electron precedes solvation and that the dry electron is chemically significant under some experimental conditions. For very fast electron scavenging the conventional rate laws are not valid because the uncertainty principle would require the energy of the dry electron to increase with the rate of scavenging, *i.e.*, with the scavenger concentration, and "k" is not a constant.

Introduction

The fate of the primary charge species in water and in various other liquids subjected to ionizing radiation has been under continued investigation for many years. The conclusion of Samuel and Magee[3] that the dry charge pair in water (and other liquids) always recombines prior to solvation proved to be incorrect, in part, because the bulk dielectric relaxation time is not applicable for electron-dipole nearest neighbor interactions.[4] Nevertheless, however short the solvation time, and it is $<10^{-11}$ sec,[5] it is still to be expected from first principles that all vertical excitations to the continuum will produce electrons which are dry initially, *i.e.*, quasi-free.

Previous attempts to investigate the very early ionic processes have usually been difficult to interpret because of transient kinetic phenomena.[6] Czapski and Peled,[7] for example, could not find evidence for electron scavenging that required the involvement of dry electrons when high concentrations of scavengers, known to react efficiently with e_{aq}^-, were used.

Both ionic strength and kinetic transient effects can be avoided by selecting reagents which are uncharged, unreactive with the solvated electron e_{sol}^-, and reactive with the dry electron e^- in a polar medium. One reagent which has been shown to meet these requirements is $(CH_3)_2SO$ in aqueous solutions.[8] Experience with electron scavenging in nonpolar solids[9] as well as in polar liquids[10] and solids[11] shows that benzene is comparatively efficient for scavenging dry electrons although $k(C_6H_6 + e_{aq}^-) < 7 \times 10^6 M^{-1} sec^{-1}$.[12] For electron scavenging in liquid alkanes, using efficiency reagents at low concentrations, and in terms of a classical description, $k \cong 10^{12} M^{-1} sec^{-1}$ when the mobility is $\mu \cong 1 cm^2 V^{-1} sec^{-1}$.[13]

Under pulse radiolytic conditions it should be possible to distinguish between the prompt and slow reactions of electrons with $\sim 1 M$ benzene in alcohols. It is to be expected that the dry electron in alcohols would be quasi-free and less solvated than an electron in, *e.g.*, cyclohexane for which the reaction rate constant with a scavenger S at very low concentration is $k(e^- + S) > 10^{12} M^{-1}$
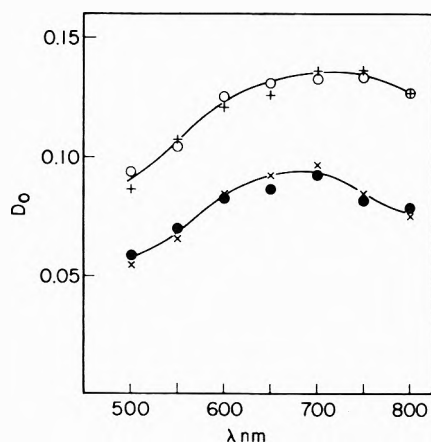
Figure 1. The spectra at $t = 0$ of e_{sol}^- in ethanol (O); with addition of 0.5 M C_6H_6 (+); with 10^{-2} M NaOH (●); with 10^{-2} M NaOH and 1.5 M C_6H_6 (×). Scaling factors are 1.37 (+) and 2.10 (×) for solutions containing C_6H_6.

sec^{-1}. The electron is assumed to spend most of its time in shallow potential wells and the high rate constants would be associated with the quasi-free high-conducting state.[14] In a polar solvent trapping appears to be thermally irreversible and the initial high-conducting state may have a lifetime less than 10^{-12} sec. Electronic processes would be nonclassical for this state and rate constants would not necessarily be applicable to fast transients. The preceding considerations have been applied to the experiments to be described.

Experimental Section

Some series of irradiations were performed with an ARCO LP-7 linear accelerator using 5-nsec pulses of 8-MeV electrons and ~2.7 A. The dose approximated 4.6 krads. Other series of irradiations were performed with 15-nsec pulses of 2-MeV electrons from a Van de Graaff accelerator, the dose approximating 3.5 krads. The analyzing light for measuring optical density, OD, was provided by a pulsed 450-W xenon arc and all OD's were measured at maximum absorption, 700 nm for ethanol and propanol, 550 nm for 1,2-propanediol. Samples were irradiated in Suprasil cells. The length of the light path was 1 cm. Solutions were purged with N_2. Ethanol (95%) was supplied by Commercial Solvents Corp.; certified grade 1-propanol, 1,2-ethanediol, and benzene were supplied by Fisher. Reagents were used as received.

The values of initial OD's used here are obtained by extrapolating to the beginning of the pulse. This procedure intentionally underestimates the difference between the OD of solvent and OD of solution which is attributed to prompt scavenging of electrons by benzene. The effects reported are therefore conservative estimates. The evaluation of initial OD's is based partly on pure empiricism, partly on kinetic guidelines, and partly on simple chemical kinetics.

Results

Ethanol. The absorption spectrum of e_{sol}^- in ethanol was measured in the range 500-800 nm. Since $1/OD$ was linear in time from 40 nsec (due to improper adjustment of the time constant) to 300 nsec it was possible to determine $OD(e_{sol}^-)$ empirically at $t = 0$, hereafter D_0. In solutions containing benzene an exponential dependence of $OD(e_{sol}^-)$ was obeyed and this was used to determine D_0 at each wavelength. The spectra for e_{sol}^- in 0 and 0.5 M
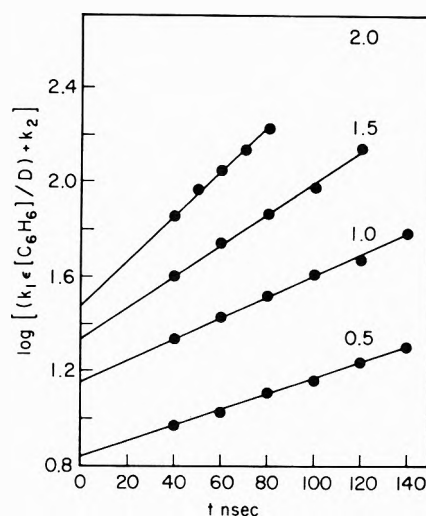
Figure 2. The decay of e_{sol}^- in 0.5, 1.0, 1.5, and 2.0 M C_6H_6 in ethanol in terms of eq 3.

benzene appear in Figure 1 at $t = 0$. The absorption spectrum of e_{sol}^- is not affected by benzene and the prompt yield of e_{sol}^- was decreased by 1/1.37. To facilitate the comparison of spectra, 1.37 D_0 for the benzene solution is used in Figure 1.

The half-life of e_{sol}^- in ethanol alone was 170 nsec and in 0.5 M benzene it was 75 nsec. Consequently the two processes compete for e_{sol}^- and the simple exponential decay of e_{sol}^- in benzene solutions is fortuitous. The kinetics of e_{sol}^- is of no direct concern in this study but it must be considered to the extent required to establish D_0. We try eq 1 as the simplest semi-empirical description.

$$d[e_{sol}^-]/dt = k_1[e_{sol}^-][S] + k_2[e_{sol}^-]^2 \qquad (1)$$

The term in $[e_{sol}^-]^2$ is not to be taken literally and may quite well be dominated by $[e_{sol}^-]$ [radicals] since $[e_{sol}^-]$ $\cong$ constant [radicals].

The integral rate equation is

$$\ln \frac{k_1[S] + k_2[e_{sol}^-]}{[e_{sol}^-]} = k_1[S]t + constant \qquad (2)$$

Replacing $[e_{sol}^-]$ in eq 2 by $D/\epsilon l$, where D is optical density, ϵ is the molar extinction coefficient, and l is 1 cm for these experiments, we have

$$\ln (k_1\epsilon[S]D^{-1} + k_2) = k_1[S]t + \ln (k_1\epsilon[S]D_0^- + k_2) \qquad (3)$$

Using the data for 2 M benzene and neglecting the small term $k_2[e_{sol}^-]^2$ it is found that $k_1\epsilon = 1.0 \times 10^{11}$ M^{-2} sec^{-1}. The value of k_2 from the empirically second-order decay of e_{sol}^- in ethanol is 3.5×10^{11} M^{-1} sec^{-1}, but no specific mechanism is implied here. For solutions containing benzene it is preferable to use a fitted rate constant k_2 since new free radical species may be involved in reactions with e_{sol}^-. The value $k_2 = 2.0 \times 10^{11}$ M^{-1} sec^{-1} was found to fit the results.

Plots of the left-hand side of eq 3 vs. time appear in Figure 2 for measurements at 700 nm of 0.5, 1.0, 1.5, and 2.0 M benzene in ethanol. The linearity is adequate for the purpose of determining the initial optical densities D_0 which can be recovered from the intercepts, $\ln (k_1\epsilon[S]D_0^{-1} + k_2)$ using eq 3 and the preceding values of $k_1\epsilon$ and k_2. These are 0.104, 0.083, 0.077, and 0.070 in 0.5, 1.0, 1.5, and 2.0 M benzene. In alcohol alone at 700 nm the initial optical density was 0.132. The slopes in Figure
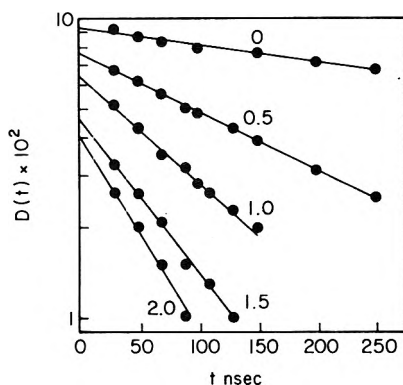
Figure 3. The decay of e_{sol}^- in 0, 0.5, 1.0, 1.5, and 2.0 M C_6H_6 in ethanol containing 10^{-2} M NaOH in terms of eq 4.
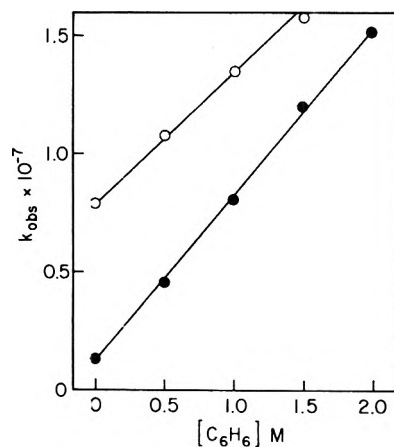
Figure 4. The dependence of k_{obsd} vs. $[C_6H_6]$ from the data of Figure 3 and eq 4 for ethanol (●) and 1-propanol (O).

2 give 0.4, 0.6, 1.0, and 1.1 × 10^7 M^{-1} sec^{-1} for k_1 in the same order of concentrations. These values are in adequate agreement with the value $k_1 = 5.8 × 10^6$ M^{-1} sec^{-1} which has been reported by Holeman, et al.,[15] since the present results drift systematically with the concentration of benzene. The principal point here is that the extrapolation procedure is based upon a kinetic model which is adequate, although cumbersome.

It was observed subsequently that e_{sol}^- in ethanol alone decayed more slowly and exponentially with addition of 10^{-2} M NaOH. In these solutions, therefore, eq 4 applies.

$$-d[e_{sol}^-]/dt = k_1[e_{sol}^-][S] + k_2'[e_{sol}^-] = k_{obsd}[e_{sol}^-] \quad (4)$$

These conditions were more attractive and another series of experiments was performed. Again, the kinetic details are not under investigation but it is required that $k_{obsd} = k_1[S]$ + constant and the value of k_1 must be plausible for the solutions used. The spectra of e_{sol}^- at $t = 0$ are included in Figure 1 for 0 and 1.5 M benzene. The average D_0 for the benzene solutions decreased by 1/2.10 and 2.10D_0 for 1.5 M benzene is plotted to facilitate comparison. No adjustment has been made for the different doses in the two series of experiments. The rates of decay of e_{sol}^- in 0, 0.5, 1.0, 1.5, and 2.0 M benzene with 10^{-2} M NaOH appear in Figure 3. From these slopes and eq 4, $k_{obsd} = k_1[S] + k_2'$ and the data for k_{obsd} vs. $[C_6H_6]$ in Figure 4 yield $k_1 = 6.8 × 10^6$ M^{-1} sec^{-1} which is close to the average value of the preceding series, 8.0 × 10^6 M^{-1} sec^{-1}. The value of k_2' is of no concern. The dependence of the initial optical densities at 700 nm upon the concen-
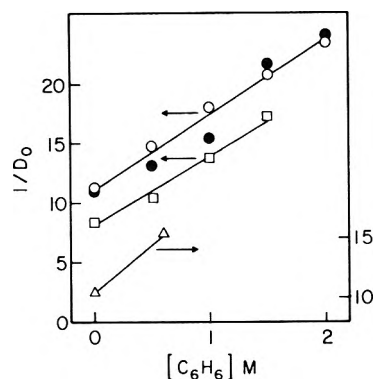
Figure 5. The dependence of the initial optical density D_0 upon the concentration of C_6H_6 in neutral (●) and alkaline ethanol solutions (O), in alkaline 1-propanol (□), and in alkaline glycol (△).
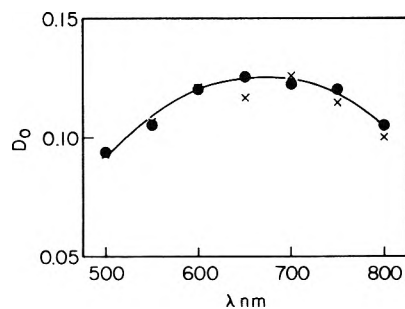
Figure 6. The spectra at $t = 0$ of e_{sol}^- in 10^{-2} M NaOH in 1-propano (O) and with addition of 10^{-2} M NaOH and 1.5 M C_6H_6 (X). The scaling factor is 2.1 (X) for 1.5 M C_6H_6.
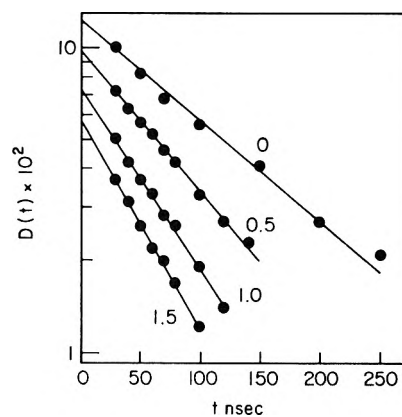
Figure 7. The decay of e_{sol}^- in 0, 0.5, 1.0, and 1.5 M C_6H_6 in 1-propanol containing 10^{-2} M NaOH in terms of eq 4.

tration of benzene for both series of measurements appears in Figure 5.

1-Propanol. Experiments in 1-propanol with 10^{-2} M NaOH were similar to those of the second series in ethanol. The spectra at $t = 0$ of e_{sol}^- appear in Figure 6 and the decay of e_{sol}^- appears in Figure 7. The dependence of k_{obsd} on $[C_6H_6]$ is included in Figure 4, from which one obtains $k_1 = 5.6 × 10^6$ M^{-1} sec^{-1}. The dependence of D_0 on $[C_6H_6]$ is included in Figure 5.

1,2-Ethanediol. The e_{sol}^- in ethylene glycol containing 10^{-2} M NaOH did not decay exponentially but was formally second order. The decay was exponential with addition of 0.1 M NaOH. Only 0.5 M benzene solutions were examined because of solubility limitations. Again the decay was linear in 1/OD at 10^{-2} M NaOH and linear in log OD at 0.1 M NaOH. The appropriate linear extrapola-
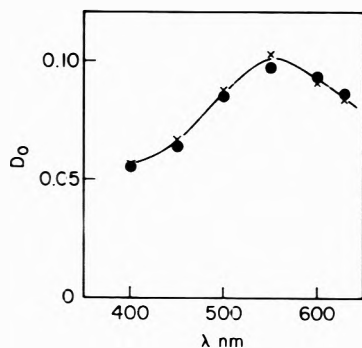
Figure 8. The spectra at $t = 0$ of e^-, in ethylene glycol and 10^{-2} M NaOH (●) and with 0.5 M C_6H_6 (×). The scaling factor is 1.58 for 0.5 M C_6H_6 (×).

tions were used to measure the spectra at $t = 0$. They appear in Figure 8.

To measure k_1 for e_{sol}^- and C_6H_6 eq 3 was used for ethylene glycol, as for ethanol, to give $k_1 \cong 5.2 \times 10^6$ M^{-1} sec^{-1} in 0.1 M NaOH. The initial optical densities at 0 and 0.5 M benzene were 0.110 and 0.077 in 10^{-2} M NaOH (30% decrease); they were 0.097 and 0.065 in 0.1 M NaOH (33% decrease).

Discussion

The results presented here provide evidence for two regimes of electron scavenging. The slow reaction which is described by $k_1[S][e_{sol}^-]$ is of interest here only to the extent that it can establish the size of the residual population of $[e_{sol}^-] = D_0/\epsilon l$. Since D_0 diminished steadily as the concentration of benzene increased there must be an earlier regime of electron scavenging which cannot be accounted for in terms of $k_1[S][e_{so}^-]$ when $1/k_1[S] \cong 10^{-7}$ sec. As an adequate approximation the small contribution from scavenging in spurs will be neglected. Prompt scavenging of electrons by benzene cannot involve e_{sol}^- to any significant extent. It will be assumed that all electrons are initially dry and equally accessible to reaction with benzene. Since it is difficult to scavenge even half of the initial population there must be a very fast and competitive solvation which terminates the early regime. This termination process is not to be identified with the relaxed e_{sol}^- but with the initial act of localizing the electron in a shallow potential well.

It is commonly assumed that electron scavenging and solvation involve thermalized electrons. In the gas phase, however, a transient molecular ion RX^- must be a precursor of X^- formed by dissociative attachment and often has a positive energy threshold. Also, there are negative ion states which have insufficient energy to dissociate and in polar liquids a hot electron could first produce a temporary negative molecular ion M^-, then solvate by $M^- \rightarrow e_{sol}^-$. This mechanism is not necessarily less important than trapping by preexisting cavities.

Since it is quite impossible to demonstrate to what extent hot processes contribute to the early regime a completely generalized description will be adopted. To avoid details of electron scattering the liquid is replaced by a set of random lattice sites which the electron encounters at an effective frequency ν_1. Some fraction X of these sites are occupied by chemically reactive traps with the probability of trapping at an encounter taken as unity. The reciprocal of the mean solvation time is ν_s, the frequency of reactive encounters at solvation sites. In terms of the optical densities of e_{sol}^- at zero time in solvent, D_0^0, and in

solution, D_0, the dry-electron scavenging efficiency can be described by eq 5. An estimated lower limit to ν_{sol} is pro-

$$\frac{D_0^0 - D_0}{D_0^0} = \frac{\nu_1 x}{\nu_1 x + \nu_s} \quad (5)$$

vided by identifying the solvation time ν_{sol}^{-1} with the dielectric relaxation time τ' at constant electric displacement. In terms of the high- and low-frequency dielectric constants, ϵ_∞ and ϵ_s, Mozumder[4] has shown that eq 6 applies

$$\tau' = (\epsilon_\infty/\epsilon_s)\tau \quad (6)$$

where τ is the ordinary dielectric relaxation time. For ethanol, 1-propanol, glycol, and glycerol the values of τ' are 44, 20, 60, and 170 psec.[4] The decrease in D_0 of e_{sol}^- with 0.5 M benzene was 14% in ethanol, 22% in propanol, and 32% in glycol. For 0.5 M acetone in glycerol the decrease was $\sim$40%.[16] The latter was almost constant over a wide range of temperature and viscosity. The correlations are both qualitatively and quantitatively inadequate. Also, Beck and Thomas[17] observed solvation times approximating 3 and 50 psec for ethanol and 1-propanol, respectively, but these are not directly related to ν_s^{-1}.

From Figure 5. $\nu_1/\nu_s = 9$ after converting from molarity to mole fraction. This indicates a much higher density of solvation sites than is commonly assumed.

Electron scavenging in liquid alkanes conforms to simple rate laws and for one solute (biphenyl) in several nonpolar solvents k is empirically proportional to the square root of the mobility.[14] For neohexane $k(e^- + C_{12}H_{10}) = 1.3 \times 10^{13}$ M^{-1} sec^{-1} and $\mu = 10$ cm^2 V^{-1} sec^{-1}. If $\mu \cong 10^2$ cm^2 V^{-1} sec^{-1} for the quasi-free electron, then $k \cong 4 \times 10^{13}$ M^{-1} sec^{-1} while it remains in this state. If this value can be transferred to the dry electron in ethanol, then $\nu_1 \cong 6 \times 10^{14}$ sec^{-1} and $\nu_s^{-1} \cong 10^{-14}$ sec. This leads to contradictions because the short lifetime of the electron broadens the zero-point energy to $\Delta E \cong h/\Delta t \cong 0.4$ eV. This arises from an inherent limitation of the simple kinetic model which behaves properly only for small $k[S]$ when $\Delta t > 10^{-12}$ sec. Neither ΔE nor Δt can be separately established within the framework of chemical kinetics for the experimental conditions under consideration and the uncertainty principle itself should be considered.

In terms of the energy of the electron, $\Delta E = \frac{1}{2}m_e v^2 = \frac{1}{2}m_e \nu_1^2 a^2$ where $a \cong 4.6 \times 10^{-8}$ cm is the mean point-to-point lattice constant and $\Delta t = \nu_s^{-1}$. We have eq 7 from the uncertainty principle

$$\frac{1}{2}m_e \nu_1^2 a^2/\nu_s \cong h \quad (7)$$

and eq 8 from the present experiments

$$\nu_1/\nu_s = 9 \quad (8)$$

Consequently $\nu_1 \cong 7 \times 10^{14}$ sec^{-1} and $\nu_s \cong 8 \times 10^{13}$ sec^{-1}. From $v = \nu_1 a$ we find $\Delta E \cong 0.3$ eV, with $E > \Delta E$.

Possibly the situation can be described as follows. For $k[S] \lesssim 10^{12}$ sec^{-1} the zero point energy of e^- is well defined provided e^- has become thermalized As [S] increases e^- may be scavenged before thermalization and E increases because of the conjugate decrease in Δt. The early regime of prompt or dry-electron scavenging is nonclassical.

At the onset of the slow regime one is dealing with the classical entity e_{sol}^-. If the initial act of localization (solvation) coincides with partial thermalization, $\Delta E \cong 2(\frac{3}{2}kT)$ and $\Delta t \cong 8 \times 10^{-14}$ sec. valid for small [S].[18]

An alternative possibility is that 0.3 eV is the minimum or zero-point energy of the dry electron in the solvent. If the average scattering mean free path is small as a result of randomness, the spread in momentum is large and the electron cannot thermalize. If $\nu_s^{-1} \cong 10^{-14}$ sec is the time required for the energy of the electron to minimize, it is much less than the value which is generally accepted.

There is an electron resonance in ethanol at a few tenths of 1 eV which may be attributed to a temporary negative molecular ion state[19] or to inelastic scattering by a fluctuation potential.[20] Both models indicate that trapping and solvation are associated with the resonance. The 0.3-eV state of e^- in ethanol is again expected to be short lived and to lead to formation of e_{sol}^-.

Acknowledgment. The authors are indebted to Professor John L. Magee and Dr. K. Paul Funabashi for helpful discussion.

References and Notes

(1) On leave of absence from Tokyo Metropolitan University.
(2) The Radiation Laboratory of the University of Notre Dame is operated under contract with the U. S. Atomic Energy Commission. This is AEC Document No. COO-38-920.
(3) A. Samuel and J. L. Magee, *J. Chem. Phys.*, **21**, 1080 (1953).
(4) A. Mozumder, *J. Chem. Phys.*, **50**, 3153 (1969).
(5) M. J Bronskill, R. K. Wolf, and J. W. Hunt, *J. Chem. Phys.*, **53**, 4201 (1970).
(6) H. A. Schwarz, *J. Chem. Phys.*, **55**, 3647 (1971).
(7) G. Czapski and E. Peled, *J. Phys. Chem.*, **77**, 893 (1973).
(8) A. M. Koulkès-Pujo, B. D. Michael, and E. J. Hart, *Int. J. Radiat. Phys. Chem.*, **3**, 333 (1971).
(9) W. H. Hamill in "Radical Ions," E. T. Kaiser and L. Kevan, Ed., Interscience, New York, N. Y., 1968, p 321.
(10) S. Khorana and W. H. Hamill, *J. Phys. Chem.*, **74**, 2885 (1970).
(11) T. Sawai and W. H. Hamill, *J. Phys. Chem.*, **73**, 2750 (1969).
(12) E. J. Hart, S. Gordon, and J. K. Thomas, *J. Phys. Chem.*, **68**, 1271 (1964).
(13) A. Mozumder, *J. Chem. Phys.*, **55**, 3026 (1971).
(14) G. Eeck and J. K. Thomas, *J. Chem. Phys.*, **57**, 3649 (1972).
(15) J. Holeman, S. Karolczak, J. Kroh, J. Mayer, and M. Mieńska, *Int. J. Radiat. Phys. Chem.*, **1**, 457 (1969).
(16) T. Kajiwara and J. K. Thomas, *J. Phys. Chem.*, **76**, 1700 (1972).
(17) G. Eeck and J. K. Thomas, *J. Phys. Chem.*, **76**, 3856 (1972).
(18) In a recent report on positive hole migration in H_2O and D_2O (H. Ogura and W. H. Hamill, *J. Phys. Chem.*, **77**, 2952 (1973)) it was assumed that H_3O^+ was formed by H-atom transfer between H_2O and H_2O^+ at $\Delta t = \frac{1}{2}$ (vibrational period), on the average. This required (1) no energy barrier or (2) vibrational y hot reactants. The uncertainty principle was overlooked. By hypothesis $\Delta t = 5 \times 10^{-15}$ sec. The conjugate uncertainty in energy is $\Delta E \cong h/\Delta t \cong$ 0.8 eV, which is not inconsistent with vibrationally unrelaxed reagents at ~ 5 fsec after the primary act. Since Δp is now $\sim 4.4 \times 10^{-20}$ g cm/sec, $\Delta X \cong 1.4 \times 10^{-7}$ cm. Consequently, the electron vacancy may reside on any of $\sim 50H_2O$. The experimental results indicated $\sim 25H_2O$ (or D_2O).
(19) K. Hiraoka and W. H. Hamill, *J. Chem. Phys.*, **57**, 3870 (1972).
(20) K. Funabashi and T. Kajiwara, *J. Phys. Chem.*, **76**, 2726 (1972).

Pulse Radiolysis of Liquid *n*-Pentane and *n*-Pentane–Oxygen Solutions. Rate Constants and Activation Energies for Second-Order Decay of Pentyl and Pentylperoxy Radicals

L. W. Burggraf and R. F. Firestone*

Department of Chemistry, The Ohio State University, Columbus, Ohio 43210 (Received September 14, 1973)

Absorption spectra for pentyl radicals in liquid *n*-pentane and in water at 24° have been measured, using apparatus which minimizes signals induced by scattered light. Rate constants for pentyl + pentyl and peroxypentyl + peroxypentyl reactions at room temperature and lower temperatures have been determined. At 24°, $k_{P+P} = 4.7(\pm 0.5) \times 10^9 \, M^{-1} \, sec^{-1}$ in *n*-pentane, $1.2(\pm 0.2) \times 10^9 \, M^{-1} \, sec^{-1}$ in water, and $k_{2PO_2} = 2.0(\pm 0.3) \times 10^6 \, M^{-1} \, sec^{-1}$ in *n*-pentane. Apparent activation energies are 0.7 ± 0.3 and 2.6 ± 0.4 kcal/mol, respectively, in *n*-pentane. Effects of diffusion on reactions of these and other alkyl radicals are discussed in the context of a simple model proposed by Noyes. Discrepancies between estimated diffusion rate constants and observed overall rate constants are shown to be attributable to steric factors of the order 10^{-2} for homogeneous second-order decay of alkyl radicals in solution.

Introduction

The steady-state radiolysis of saturated liquid hydrocarbons and especially cyclohexane, *n*-hexane, and *n*-pentane has been extensively investigated.[1,2] The following general mechanism accounts for the major products at moderate dose rates

$$RH \longrightarrow H, R, R', \text{"molecular" products} \quad (1)$$

$$H + RH \longrightarrow H_2 + R \quad (2)$$

$$R + R \longrightarrow \text{addition and} \quad (3)$$

$$R + R' \longrightarrow \text{disproportionation} \quad (4)$$

$$R' + R' \longrightarrow \text{products} \quad (5)$$
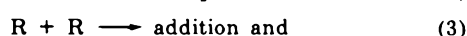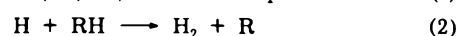
where RH represents an alkane molecule, R represents radical(s) formed by C–H bond rupture, R' represents smaller radicals formed by C–C bond rupture, and H represents the hydrogen atom.

Recently the pulse radiolysis technique has been applied to the study of the radiation chemistry of several alkanes.[3-5] Ebert, *et al.*,[3] reported observation of a transient absorption spectrum in pure liquid cyclohexane between 230 and 300 nm which was assigned to the cyclohexyl radical. Sauer and Mani[4] reported transient spectra in cyclo-

hexane and n-hexane in the same region which were convincingly assigned to cyclohexyl and hexyl radicals, respectively, by producing similar transient spectra in aqueous solutions of these hydrocarbons under conditions such that only abstraction of a hydrogen atom from the hydrocarbon molecules was important.

Rate constants reported[3,4] for second-order decay of cyclohexyl radicals in cyclohexane agree within a factor of 2, but the extinction coefficients reported by Sauer and Mani[4] were up to five times those given by Ebert, et al.,[3] and the maximum in the spectrum reported by Sauer and Mani was observed at a shorter wavelength. Both reports mention difficulties in reliably measuring absorbance values in the near ultraviolet, because of severe light scattering. Spectral shape is, as is well known, strongly dependent on the success of measures taken to minimize signals induced by scattered light, and discrepancies between reported extinction coefficients and the wavelength of maximum absorption are to be expected when unequally effective measures are taken. An additional cause of such discrepancies can be the rapid formation of stable radiolysis products which absorb in the same spectral region. Reitberger[5] has observed a residual absorption spectrum in methylcyclohexane following decay of the methylcyclohexyl radical which he attributed to 1-methylcyclohexene and found it important to take residual absorbance data into account in order to rationalize the kinetics of decay of the radicals. In this work we have, accordingly, used an optical system which greatly reduces scattered light signals and have taken care to record absorption spectra present after decay of the radicals.

Attempts have been made to understand radical decay kinetics in terms of radical–radical reactions whose rates are diffusion controlled.[4,5] Observed rates are in order of magnitude agreement with calculated diffusion-controlled rates, but the experimental rate constants are consistently less than calculated values by amounts considerably exceeding experimental errors.

Several investigators[6-8] have used oxygen as a scavenger for cyclohexyl radicals in pulse radiolysis studies in cyclohexane. The cyclohexylperoxy radical spectrum exhibits an absorption maximum at 255 nm in cyclohexane.[8] The mechanism invoked to rationalize the decay kinetics is[7-10]

$$RH \longrightarrow R + H \tag{6}$$

$$H + RH \longrightarrow H_2 + H \tag{7}$$

$$R + O_2 \longrightarrow RO_2 \tag{8}$$

$$2RO_2 \longrightarrow ROH + R(-H){=}O + O_2 \tag{9}$$

$$R' + O_2 \longrightarrow RO_2' \tag{10}$$

$$RO_2' + RO_2 \longrightarrow ROOR' + O_2 \tag{11}$$
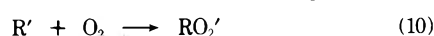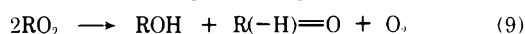
where R' represents smaller radicals formed in n-pentane by C–C rupture as well as by H atoms. McCarthy and MacLachlan[7] and Simic and Hayon[8] reported values for k_9 roughly 10^{-4} times the calculated diffusion limited value. McCarthy and MacLachlan[7] reported an activation energy of zero between 25 and 71° and, thus, attributed the discrepancy to a large steric hindrance.

This article reports absorption spectra of transient species formed by pulse radiolysis of n-pentane, aqueous solutions of n-pentane and n-pentane in the presence of oxygen and effects of temperature on the rate constants for decay of these species. Measured values of the rate constants for these and other alkyl radicals[4] are interpreted with the aid of Noyes' model describing effects of diffusion upon reactions in solution.[11]

Experimental Section

The general technique of pulse radiolysis employing a spectrophotometric detection system has been described elsewhere.[12-14] The high-energy electron pulse was provided by a Varian V-7715A linear accelerator, using 4-MeV electrons. Rectangular pulses variable from 0 1 to 1.3 μsec at a beam current of 320 mA were generally used in this work. The dose delivered was proportional to pulse length. Shorter pulses variable from 20 to 85 nsec at a current of 645 mA were also employed using the stored energy mode. The decay time of all pulses was approximately 6 nsec, i.e., very much less than the initial decay times of the transient species. The focused electron beam was roughly circular with approximately 2 cm diameter at the plane of entry into the reaction cell and provided essentially uniform particle density throughout the cell contents. Rectangular quartz cells with high-purity silica windows (8 × 12 mm inside dimensions) and 12 × 20 mm sides normal to the electron beam were employed.

The optical system normally used[14] was shown to transmit unacceptably high scattered light intensities in the 200–300-nm region. A modification shown in Figure 1 was used successfully. The 500-W Osram xenon discharge lamp was used in a steady-state mode for study of the decay of pentylperoxy radicals and in a pulsed high-intensity mode in order to obtain sufficient incident intensity for reliable pentyl radical absorbance measurements in the ultraviolet. The intensity vs. time profile of the lamp was virtually constant for 20 μsec following attainment of its maximum. The incident light beam was passed through the irradiation cell and reflected back on itself by a first surface aluminum coated concave mirror of 1.00 m diameter (M_1). After reflection from a flat first surface mirror (M_2) the beam was brought to focus on a 1.5-mm vertical slit and distributed across the face of a 3-in., 60° fused silica prism oriented at angle Φ with respect to the beam and set to the angle of minimum deviation[15] for each desired wavelength setting. The dispersed beam fell upon the entrance slit of a Bausch and Lomb high-intensity, 33-86-25, grating monochromator, equipped with a Bausch and Lomb 33-86-01 grating (2700 grooves/mm) blazed at 250 nm. The monochromator and photomultiplier (RCA 7200, S19) were secured on a movable arm whose pivot point lay directly below the center of the prism, and the dispersed spectrum was scanned by simultaneously varying angle θ and the grating angle. The signal from the photomultiplier was passed to a Philbrick Nexus amplifier and thence to a Tektronix 555 dual trace oscilloscope. All traces were recorded on Polaroid Type 107 film.

Samples irradiated at temperatures below room temperature were maintained at constant temperature in a device essentially similar to that used by Arai, et al.[16]

Phillips Research Grade n-pentane (99.98% minimum purity) was further purified by washing three or more times with 1/3 of its volume of concentrated sulfuric acid and rinsing five or more times with 1/4 of its volume of triply distilled water. The n-pentane was then dried by passage through phosphoric anhydride. Major impurities were various unsaturates, principally pentenes. This procedure reduced pentene concentrations below the limits of detectability of an F & M Model 609 flame ionization gas chromatograph (ca. 10^{-6} mol %).

Pure n-pentane samples were outgassed by repeated freeze–pump–thaw cycles followed by distillation from phosphoric anhydride into irradiation cells on a greaseless Pyrex vacuum line. Oxygen concentrations in n-pentane
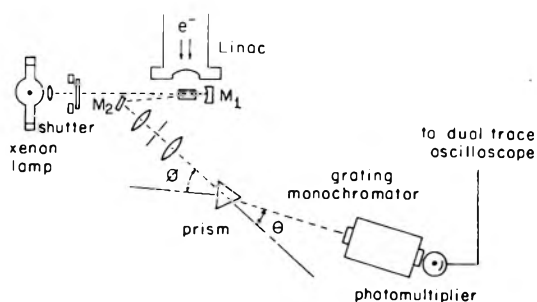
Figure 1. Schematic diagram of the fast spectrophotometric detection system.

Figure 2. Apparent absorbance, A', as a function of the true absorbance, A, at various values of the ratio of the detector's response to scattered vis-a-vis transmitted light.

samples irradiated in the presence of oxygen were calculated from the relation, $v = 0.576p$ at $0°$,[17] where p is the equilibrium oxygen pressure above solution (atmospheres) and v is the volume ($25°$, 1.00 atm) of oxygen dissolved per unit volume of n-pentane; all such sample solutions were prepared at $0°$. Aqueous solutions saturated with n-pentane and nitrous oxide were prepared from triply distilled water and Liquid Carbonic Corp. USP nitrous oxide.

The dosimetry method described by Sauer and Mani[4] was used. Observations of the I_2^- transient were made at 385 nm, assuming a 100-eV yield equal to 2.4 and an extinction coefficient equal to $1.4 \times 10^4 \ M^{-1} \ cm^{-1}$ as determined by Thomas.[18] The dose delivered to n-pentane was assumed equal to the product of the appropriate ratio of electron densities and the dose delivered to the aqueous dosimeter solution. The dose delivered to a given sample of n-pentane was calculated from the average of doses delivered to dosimeter samples in pulses immediately before and after that delivered to the n-pentane sample. The observed dose per pulse varied within $\pm 5\%$ from pulse to pulse in a given sequence.

Results

The measured apparent absorbance can be related to the true absorbance by the expression, $A' = \log (1 + \mu)/(10^{-A} + \mu)$, where μ is the ratio of the detector's response to scattered light to the detector's response to light transmitted by the nominal bandpass of the monochromator system in the absence of absorbing species.[19] Figure 2 shows that at absorbance values recorded in this work A' is essentially linear with respect to A at μ values as great as 2.0. Figure 3 demonstrates consistently that observed linear variation of the measured absorbance with respect to dose is no indication that scattered light is not contributing very significantly to the detector signals; both plots are linear within experimental limits of precision, even though at least 61% of the signal measured using only the grating monochromator is induced by scattered light at 220 nm ($\mu = 1.59$). We found use of the quartz prism plus Bausch and Lomb monochromator (Figure 1) most effective in rejecting scattered light and the Bausch and Lomb monochromator alone to be least effective of four systems tested. Use of two Bausch & Lomb monochromators in series was more effective than use of interference filters and one Bausch and Lomb monochromator, but less effective than the prism-grating–monochromator system.

Figure 4 presents absorption spectra of the transient species in pure air-free n-pentane and in air-free aqueous n-pentane solution saturated with nitrous oxide at 1-atm pressure. Nitrous oxide may be assumed to convert hydrated electrons into OH radicals quantitatively under
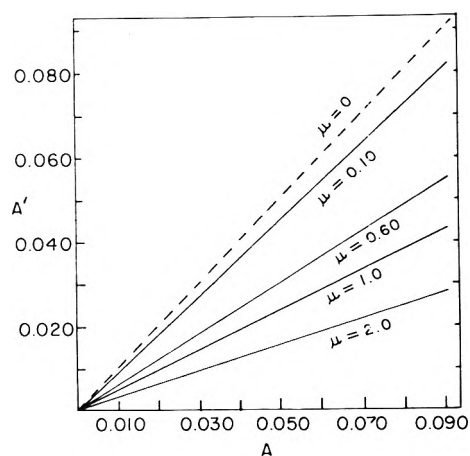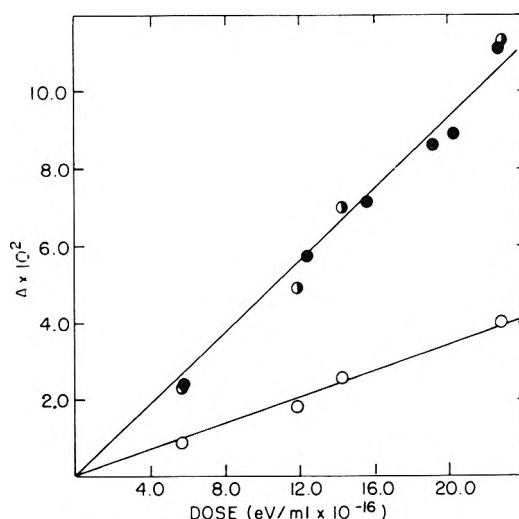
Figure 3. Absorbance of pentylperoxy radicals at 220 nm: ●, measured with the apparatus of Figure 1; O, measured with the grating monochromator alone; ◑, latter values corrected for μ = 1.59.

these conditions.[20a] Hydrogen atoms and hydroxyl radicals react as follows[20a]

$$OH + RH \longrightarrow H_2O + R \tag{12}$$

$$OH + OH \longrightarrow H_2O_2 \tag{13}$$

$$H + OH, R \longrightarrow H_2O, RH \tag{14}$$

$$H + RH \longrightarrow H_2 + R \tag{15}$$

$$H + H \longrightarrow H_2 \tag{16}$$

$$R + R \longrightarrow products \tag{17}$$
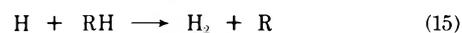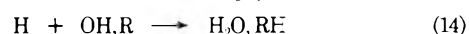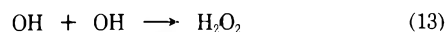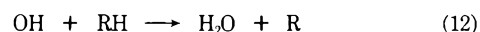
where[2,20] $k_{12} = 10^9$, $2k_{13} = 1.2 \times 10^{10}$, $k_{14} = 10^{10}$, $k_{15} = 4 \times 10^6$, and $2k_{16} = 2 \times 10^{10}$ (all in $M^{-1} \ sec^{-1}$). At half millimolar n-pentane concentration[21] and a dose equal to 6×10^{16} eV/ml, the latter corresponding to an initial OH concentration of about $6 \times 10^{-6} \ M$, it is estimated from rate constant data that more than 88% of OH radicals were consumed by reaction 12. Figure 5 demonstrates that the absorbance of the transient species in this solution varies linearly with dose, i.e., with respect to the initial OH concentration, and indicates that, in any event, reaction 12 converts OH radicals to pentyl radicals without detectable competition from reaction 13. In the same dose range hydrogen atoms, then, most likely react with pentyl
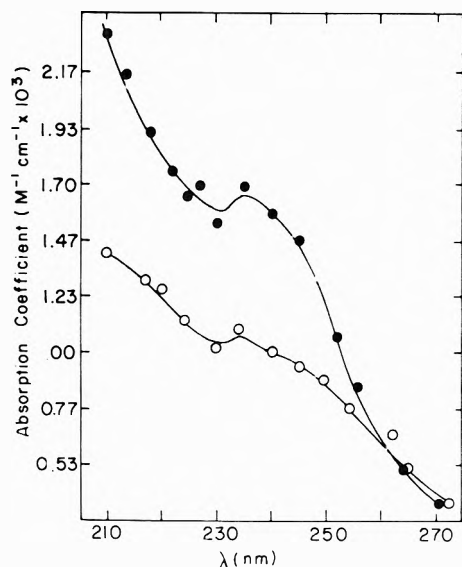
Figure 4. Molar absorption coefficients of pentyl radicals in n-pentane, ●, and in aqueous solution, O.
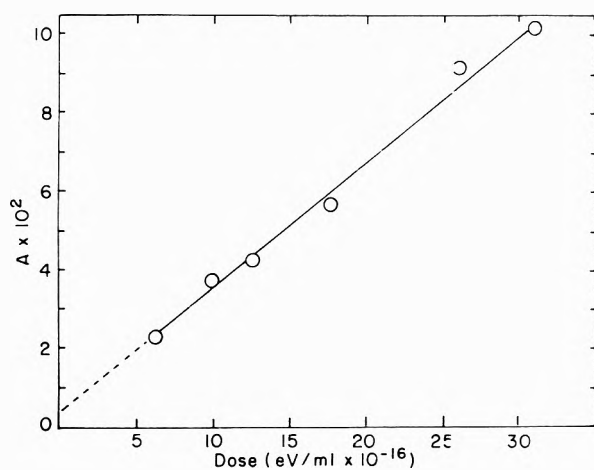
Figure 5. Absorbance of transient species in N_2O-saturated aqueous solution of n-pentane as a function of absorbed dose at 234 nm.

Figure 6. Absorbance of peroxy radicals in air-saturated n-pentane following a 3.7×10^{17} eV cc⁻¹ electron pulse.

radicals. The best estimate of the yield of pentyl radicals under these conditions is, accordingly, $G(\text{pentyl}) = G(\text{OH}) - G_H = G(e_{aq}) + G_{OH} - G_H = 4.9 \pm 0.2$ radicals/100 eV. The similarity of the spectra of the transient species formed in n-pentane and in aqueous solution of n-pentane and N_2O indicates that both spectra are pentyl radical absorption spectra.

Values for the molar absorption coefficient of pentyl radicals in n-pentane are based on an average dose of 1.9 × 10^{17} eV/ml delivered by a 0.6-μsec pulse and a 100-eV yield of pentyl radicals equal to 3.9 radicals/100 eV.[22,23] Previous work[22,23] indicates that about 7% are 1-pentyl radicals, 63% are 2-pentyl radicals, and 30% are 3-pentyl radicals at 25°. The less intense absorption spectrum of pentyl radicals in aqueous solution is probably caused by spectral broadening in the polar solvent and a different mixture of 1-, 2-, and 3-pentyl radicals. Hexyl radical spectra in n-hexane and in aqueous solution[4] bear a similar relationship to one another.

Figure 6 presents the transient absorption spectrum observed immediately after delivery of a 3.7 × 10^{17} eV/ml pulse to air-saturated n-pentane at 1 atm pressure and 24°. This spectrum is attributed to peroxy radicals formed

by all radical species produced in irradiated n-pentane.[22,23] The HO_2 radical is known to absorb in this region and exhibits a maximum absorbance at 230 nm in aqueous solution.[13] Observation that the maximum in Figure 6 occurs at a longer wavelength suggests that the pentylperoxy radical absorption maximum occurs at a longer wavelength than that of HO_2 and, presumably, those of the smaller organic peroxy radicals. This suggestion is supported by the observation[8] that the peroxycyclohexyl radical absorption maximum lies at about 255 nm. Previous work[22] has shown that about 26% of the scavengable pentyl radicals are formed by hydrogen atom abstraction from pentane by smaller radicals at room temperature. In the presence of oxygen, reactions 18 and 19, therefore, compete for the smaller radicals

$$R' + RH \longrightarrow R'H + R \qquad (18)$$

$$R' + O_2 \longrightarrow R'O_2 \qquad (19)$$

where R' represents H, CH_3, C_2H_5, and C_3H_7 radicals.[22] Thus, in order to identify a wavelength at which only peroxypentyl radicals absorb significantly, we have measured the absorbance as a function of O_2 concentration at wavelengths on the longer wavelength tail of the spectrum of Figure 6. Figure 7 is a plot of absorbance at 290 nm as a function of O_2 concentration. The solid line has been calculated by assuming that reaction 19 is diffusion limited and that $k_{18} \simeq 4 \times 10^6 \ M^{-1} \sec^{-1}$ at 24°, i.e., $k_{19}/k_{18} \simeq 3 \times 10^3$; the value at zero O_2 concentration is set equal to that at 4.14 mM divided by $(1 - 0.26)$ by assuming that essentially all H atoms and smaller radicals are removed by O_2 at the latter concentration. This figure demonstrates within experimental error that the dependence of the pentylperoxy yield on the O_2 concentration is consistent with reasonable estimates of k_{19}/k_{18} and measured values of the relative yields of pentyl radicals and smaller radicals capable of abstracting hydrogen from pentane and indicates that only pentylperoxy radicals absorb appreciably at 290 nm. All rate data concerning pentylperoxy radical decay were taken at this wavelength in 4 mM oxygen solutions using the xenon discharge lamp in a steady-state mode.

Figure 8 is a homogeneous second-order plot of the decay of pentyl radicals in air-free liquid n-pentane at 24°. A_{00} is the residual absorbance of olefinic products at 240 nm; A_{00}/A_0 equals 0.093 for data represented in Figure 8. Since pentyl radicals are removed in part by reactions
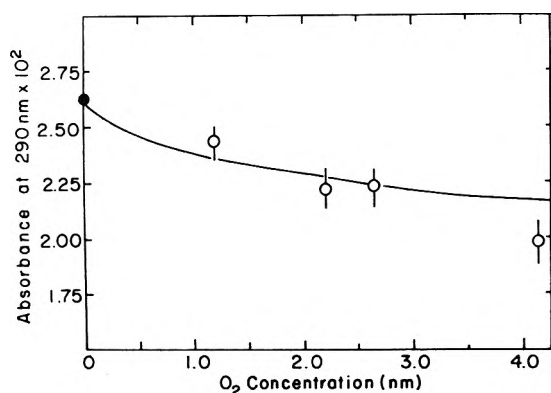
Figure 7. Absorbance of peroxy radicals in oxygen-saturated n-pentane at 290 nm: O, measued values; ●, value at zero (O_2) calculated from measured fraction of peroxy radical yield attributable to pentyl radicals. The solid line is calculated from the mechanism for competition between O_2 and n-pentane for H atoms and the smaller radicals.

Figure 10. Homogeneous second-order plot of the decay of pentylperoxy radicals in n-pentane containing 4 mM oxygen at 24° and 290 nm.

Figure 8. Homogeneous second-order plot of the decay of pentyl radicals in n-pentane at 24° and 240 nm.

Figure 11. Arrhenius plot of the radical–radical decay constant for pentylperoxy radicals in n-pentane.

vides an apparent activation energy of 0.7 (±0.3) kcal/mol between −84 and 0°.

Figure 10 is a homogeneous second-order plot of the decay of pentylperoxy radicals monitored at 290 nm in the presence of 4 mM oxygen. Assigning a yield of scavengable pentyl radicals equal to 2.7 radicals/100 eV in n-pentane at room temperature,[22] we calculate a molar absorption coefficient equal to 910 ± 50 M^{-1} cm^{-1} at 290 nm for the pentylperoxy radicals. The initial rapid decay which occurs during the first 10 msec in Figure 10 is attributed to faster reactions of smaller peroxy radicals with pentylperoxy radicals. The slope exhibited at longer times is attributed to the disproportionation of pentylperoxy radicals. The rate constant for this reaction at 24° is k_9 = 2.0(±0.2) × 10^6 M^{-1} sec^{-1}. Figure 11 illustrates the temperature dependence of k_9 and indicates that the apparent activation energy for the disproportionation reaction is 2.6(±0.4) kcal/mol between −40 and 30°.

Figure 9. Arrhenius plot of the radical–radical decay constant for pentyl radicals in n-pentane.

with smaller radicals and rate constants for reactions 3–5 are not known for the several radical species, we assume statistical relative values, i.e., $2k_3 = k_4 = 2k_5$ for all radical species. Thus, k_3 = (slope)(1ϵ)/2[1 + (R')$_0$/(R)$_0$], where (R')$_0$/(R)$_0$ is a constant equal to 0.32 at room temperature.[22] The average value for k_3 determined from absorbance data measured at 235, 240, 245, and 272 nm is 4.7(±0.5) × 10^9 M^{-1} sec^{-1} at 24°. The corresponding rate constant for decay of pentyl radicals in water solution is 1.2(±0.2) × 10^9 M^{-1} sec^{-1} at 24°. The dependence of k_3 on reaction temperature is shown in Figure 9, which pro-

Discussion

The measured rate constants for decay of hexyl, cyclohexyl, and methylcyclohexyl radicals in hexane, cyclohexane, and methylcyclohexane respectively[4,5] are consistently smaller than $2\pi\rho D'$, the value predicted by the Smoluchowski equation for diffusion limited reactions of like radicals. This is also true regarding reactions of pentyl radicals in n-pentane. Noyes[11] has presented a simple model which provides a reasonable basis for calculating the rate constant for reaction in solvent cages when the

TABLE I: Summary of Observed and Calculated Data Concerning Reactions of Pentyl, Hexyl, and Cyclohexyl Radicals in Liquid Solutions at 25°

Radical	Solvent	Rate constants, M^{-1} sec^{-1} $\times$ 10^{-9}			
		k_{obsd}	k_D	k	p^d
Pentyl	n-Pentane	4.7 ± 0.5	13	8.3	0.048
Pentyl	Water	1.2 ± 0.2	3.6^a	1.9	0.013
Hexyl	n-Hexane	3.1 ± 0.9^b	11	4.4	0.026
Hexyl	Water	1.2 ± 0.2^b	3.2^a	1.9	0.011
Cyclohexyl	Cyclohexane	2.0 ± 0.6^b	14	2.3	0.014
Cyclohexyl	Water	1.4 ± 0.2^b	4.3^c	2.1	0.012

^{a} D' taken as twice D for diffusion of n-pentane or n-hexane in water, using rule, $D_n = 1.235 D_{n+1}$, where n = no. of carbon atoms in n-alkane, and measured value of D for n-butane at 25°; P. A. Witherspoon and D. N. Saraf, J. Phys. Chem., 69, 3752 (1965). ^{b} Data from ref 4. ^{c} D' taken as twice D for diffusion of cyclohexane in water at 25°; L. Bonoli and P. A. Witherspoon, J. Phys. Chem., 72, 2532 (1968). ^{d} All p values are uncertain within ca. ±80% because of uncertainties in E_{obsd} and k_{obsd}/k values.

overall experimental value is known. The overall process is visualized as occurring in two consecutive steps, viz., net diffusion to within an assumed encounter radius ρ followed by reaction in the solvent cage. Let k be the rate constant for reaction in the solvent cages, k_{obsd} the measured overall rate constant, D' the relative diffusion coefficient of like radicals in solution, C_{00} the concentration of radicals separated by distances much greater than ρ, C_ρ the concentration of radicals at center to center distance ρ, and Φ the net average flux of radicals toward one another. Then, following Noyes,[11] $k = k_{obsd}(2\pi D')/(2\pi\rho D' - k_{obsd}) = k_{obsd} k_D/(k_D - k_{obsd})$, where k_D is the diffusion limited specific rate. Taking D' equal to the coefficient for self-diffusion in n-pentane,[24] and ρ equal to the collision diameter in gaseous pentane,[25] we obtain $k_D = 1.26 \times 10^{10}$ M^{-1} sec^{-1} and $k = 7.8 \times 10^9$ M^{-1} sec^{-1} at 25°.

Since $k_{obsd}/k = 1 - k_{obsd}/k_D$, the activation energy for reaction in the solvent cages is given by $E_a = [(k_{obsd}/k_D)R/(k_{obsd}/k_D - 1)][T + (\Delta E_{vis} - E_{obsd})/R] + E_{obsd}$, assuming Arrhenius form dependence of k, k_{obsd}, and viscosity on temperature and Stokes law for the form of the dependence of D' on viscosity. Since ΔE_{vis} for n-pentane equals 1.36 kcal/mol,[26] it is found that E_a equals -0.04 kcal/mol, i.e., that reaction of pentyl radicals requires zero thermal activation energy in the solvent cages at room temperature, within experimental error. Thus, the slowness of the observed reaction relative to that of diffusion is attributable to a radical orientation, or steric, factor. Assuming a specific collision frequency, $Z' = \bar{Z}/c^2$, equal to the hard-sphere gaseous phase value, one may write the steric factor as $p = (k/Z') \exp(E_a/RT)$, where $Z' = \pi\rho^2(4kT/\pi m)^{1/2}$. We find, accordingly, that p equals 0.048 for pentyl + pentyl reaction in n-pentane. Table I summarizes k_{obsd}, k_D, k, and p values for pentyl, hexyl, and cyclohexyl radicals; p values are based on the assumption that E_a is zero for the cage reactions. In each instance the observed overall reaction rate is diffusion influenced, but not diffusion limited, and reasonable steric factors are sufficient to account for the relatively slow rates of reactions in the solvent cages. It is also interesting that the measured rate of decay of cyclohexyl radicals in water is smaller than in cyclohexane, simply because k_D in water is smaller, but that the specific reaction rates of pentyl and hexyl radicals are only one-fourth and one-third as great in water cages as in hydrocarbon cages. Speculation concerning the meaning of this difference in the effect of changing solvent is not justified in the context of the simple model which we have used to estimate the cage reaction rates.

It is apparent that k_{obsd}/k_D for the decay of pentylper-

oxy radicals in n-pentane is of the order 10^{-4}. Thus, this reaction is neither diffusion limited nor diffusion influenced and $k = k_{obsd} = 2.0(\pm0.3) \times 10^6$ M^{-1} sec^{-1} at 25°. Similarly, $E_a = E_{obsd} = 2.6(\pm0.4)$ kcal/mol. Simic and Hayon[8] have proposed a consecutive three step mechanism for removal of cyclohexylperoxy radicals in cyclohexane, viz., $2RO_2 \rightarrow X \rightarrow Y \rightarrow$ products, and have reported $k_{RO_2} = 1.2 \times 10^6$ M^{-1} sec^{-1}, $k_X = 5$ sec^{-1}, and $k_Y = 0.15$ sec^{-1} at room temperature. We have been unable to detect any evidence for light absorbing species analogous to X and Y in the present work. It has been suggested[27,28] that the second-order radical–radical step forms a tetroxide intermediate. The Russell mechanism[28] postulates formation of a tetroxide "activated complex" in a highly strained cyclic configuration, e.g.

$$2 C_4H_9 - \overset{\displaystyle H}{\underset{\displaystyle H}{C}} - O - O \longrightarrow C_4H_9 - \overset{\displaystyle H}{\underset{\displaystyle H}{C}} \cdots \longrightarrow \text{products}$$
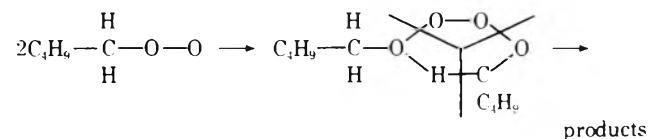
Assuming a 7-Å collision diameter and, again, that the hard-sphere gaseous phase specific collision frequency is applicable, we find a steric factor equal to 0.001. This value and that of the energy of activation are consistent with formation of such an intermediate, but, of course, do not exclude other possibilities.

References and Notes

(1) R. A. Holroyd, in "Organic Liquids," P. Ausloos, Ed., Interscience, New York, N. Y., 1968.
(2) T. Gaumann and J. Hoigne, "Aspects of Hydrocarbon Radiolysis," Academic Press, New York, N. Y., 1968.
(3) M. Ebert, J. P. Keene, E. J. Land, and A. J. Swallow, Proc. Roy. Soc., Ser. A, 287, 1 (1965).
(4) M. C. Sauer and I. Mani, J. Phys. Chem., 72, 3856 (1968).
(5) T. Reitberger, Radiochem. Radioanal. Lett., 6, 349 (1970).
(6) R. L. McCarthy and A. MacLachlan, Trans. Faraday Soc., 57, 1107 (1961).
(7) R. L. McCarthy and A. MacLachlan, J. Chem. Phys., 35, 1625 (1961).
(8) M. Simic and E. Hayon, J. Phys. Chem., 75, 1677 (1971).
(9) G. Dobson and G. Hughes, J. Phys. Chem., 69, 1814 (1965).
(10) R. Blackburn and A. Charlesby, Trans. Faraday Soc., 62, 1159 (1966).
(11) R. M. Noyes, Progr. React. Kinet., 1, 126 (1961).
(12) L. M. Dorfman, I. A. Taub, and R. E. Buhler, J. Chem. Phys., 36, 3051 (1962).
(13) G. Czapski and L. M. Dorfman, J. Phys. Chem., 68, 1169 (1964).
(14) W. D. Felix, B. L. Gall, and L. M. Dorfman, J. Phys. Chem., 71, 384 (1967).
(15) R. A. Sawyer, "Experimental Spectroscopy," Dover Publications, New York, N. Y., 1963.
(16) S. Arai, E. L. Tremba, J. R. Brandon, and L. M. Dorfman, Can. J. Chem., 45, 1119 (1967).

(17) H. Stephen and T. Stephen, "Solubilities of Inorganic and Organic Compounds," Vol. 1, Part 1, Macmillan Co., New York, N. Y., 1963, p 575.

(18) J. K. Thomas, Trans. Faraday Soc., 61, 702 (1965).

(19) Let $S(\lambda)$ be the detector's sensitivity function, dI_0 the intensity distribution function of light excepting scattered light incident on the detector in the absence of absorbing species, dI the intensity distribution function of light excepting scattered light incident on the detector in the presence of absorbing species, dI_s the intensity distribution of scattered light incident on the detector, $\lambda_2 - \lambda_1$ the bandpass of the monochromator system, A' the apparent absorbance, and A the true absorbance (all with the center of the bandpass set at $(\lambda_2 - \lambda_1)/2$). The apparent absorbance is given by

$$A' = \log\left\{\left[\int_{\lambda_1}^{\lambda_2} S(\lambda)\, dI_0 + \int_0^\infty S(\lambda)\, dI_s\right] \Big/ \left[\int_{\lambda_1}^{\lambda_2} S(\lambda)\, dI + \int_0^\infty S(\lambda)\, dI_s\right]\right\}$$

Let $\mu = \int_0^\infty S(\lambda)\, dI_s / \int_{\lambda_1}^{\lambda_2} S(\lambda)\, dI_0$. Then, since $\int_{\lambda_1}^{\lambda_2} S(\lambda)\, dI_0 / \int_{\lambda_1}^{\lambda_2} S(\lambda)\, dI = 10^A$, $A' = \log(1 + \mu)/(10^{-A} + \mu)$. It is assumed that dI_s is unaffected by absorption (a good approximation at lower A values).

(20) (a) M. S. Matheson and L. M. Dorfman, "Pulse Radiolysis," The M. .T. Press, Cambridge, 1969; (b) N. R. Greiner, J. Chem. Phys., 53, 1070 (1970).

(21) C. McAuliffe, Nature (London), 200, 1092 (1963).

(22) W. P. Bishop and R. F. Firestone, J. Phys. Chem., 74, 2274 (1970).

(23) H. A. Holroyd and G. W. Klein, J. Amer. Chem. Soc., 84, 4000 (1962).

(24) R. D. Burkhart and J. C. Merrill, J. Chem. Phys., 46, 4985 (1967).

(25) N. Dyson and A. B. Littlewood, Trans. Faraday Soc., 63, 1895 (1967).

(26) F. D. Rossini, et al., "Selected Values of Physical and Thermodynamic Properties of Hydrocarbons and Related Compounds," A.P.I. Research Project 44, Carnegie Press, Pittsburgh, 1953.

(27) K. U. Ingold, Accounts Chem. Res., 2, 1 (1969).

(28) G. A. Russell, J. Amer. Chem. Soc., 79, 3871 (1957).

The Influence of Molecular Structure on Optical Absorption Spectra of Solvated Electrons in Alcohols

Robert R. Hentz* and Geraldine A. Kenney-Wallace[1]

Department of Chemistry and the Radiation Laboratory,[2] University of Notre Dame, Notre Dame, Indiana 46555 (Received November 14, 1973)

Absorption spectra were determined for solvated electrons, e_s^-, in 25 neat alcohols and three alkane solutions of 1-hexadecanol by pulse radiolysis at 30°. Each spectrum is a structureless band that is asymmetric with respect to energy (similar to a photodetachment spectrum); the spectrum was present within a 5-nsec pulse and showed no change in shape or position with time. The product of 100-eV yield, $G(e_s^-)$, at 5 nsec and extinction coefficient at the absorption maximum also was measured relative to the same product for water. Such results for six of the alcohols are compared with published values for 30 psec, 5 nsec, and $\sim$1 μsec, and values of $G(e_s^-)$ are calculated from $G(e_{aq}^-)$ for each time. The 30-psec yields suggest that a longer solvation time allows a larger fraction of high-mobility dry electrons to undergo geminate recombination prior to solvation. Transition energy at the spectral absorption maximum, E_{max}, is within ±0.06 eV of 1.87 eV for methanol and each normal alcohol from C_4 through C_{11} (for which static dielectric constant, D_s, varies from 33 to 6). For alcohols with a branched alkyl group, E_{max} is smaller and sensitive to the number and size of branches and distance of the branch point from OH. Band width at half-maximum is within ±0.1 eV of 1.5 eV for 19 of the alcohols and narrows to less than 1.0 eV for the four alcohols with $E_{max} < 1.0$ eV. The results require a model for e_s^- in which (1) a long-range interaction dependent on D_s does not significantly affect the absorption spectrum, (2) binding and transition energies are determined by interaction of the electron with an optimum configuration of OH dipoles in a small solvation domain, perhaps a single shell, and (3) the optimum configuration is affected by molecular structure of the alcohol.

Introduction

Optical absorption spectra have been reported for electrons in a large number of solvents (ranging in polarity from that of an alkane[3] to that of water[4]), and a variety of theoretical models have been presented for interpretation of the spectra and other properties of such solvated electrons (denoted by e_s^-).[5] Certain of the results show unambiguously that electron solvation is not governed by such macroscopic properties as the optical and static dielectric constants (denoted by D_0 and D_s, respectively) and dielectric relaxation times. Consequently, electron

solvation is not determined solely by a long-range interaction with a virtually continuous dielectric medium (the only attractive interaction postulated in some earlier models[6]). For example, the wavelength at the absorption maximum (λ_{max}) of the solvated-electron spectrum at room temperature is 650 nm[7] for 1-decanol ($D_s = 7.8$), 680 nm[7] for 1-butanol ($D_s = 17$), 1900 nm[8] for ammonia ($D_s = 17$), 640 nm[7] for methanol ($D_s = 33$), and $\geq$1500 nm[9] for dimethyl sulfoxide ($D_s = 47$). Also, in a number of solvents, the fully developed solvated-electron spectrum has been observed at a time short compared to dielectric re-
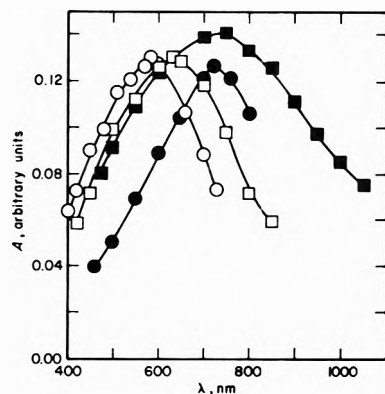
Figure 1. Absorption spectra of e_s^- at 30°: O, 1,2-ethanediol; □, methanol; ●, ethanol; ■, 2-methoxyethanol (displaced up 0.01 units).

laxation times.[10-14] Of particular significance with regard to the nature of solvated electrons is the observation of an electron absorption spectrum in water vapor[15] at densities down to 0.02 g ml^{-1}. Such results indicate that electron solvation involves short-range interactions, among the electron and proximate molecules, that are determined by the composition and structure of the solvent molecule. Accordingly, some recent theoretical models include both a long-range polarization interaction and a short-range interaction between the electron and molecules in a first solvation shell.[16-19]

The liquid alcohols, because of the extensive diversity of their bulk properties and molecular structures, are an excellent class of solvents for identification and assessment of the factors that influence electron solvation. A preliminary report on optical absorption of e_s^- in 22 alcohols (for 15 of which the e_s^- spectrum has not been reported) has been published.[7] In that communication, the wavelength and transition energy (E_{max}) at the absorption maximum were given for e_s^- in each of the alcohols, and implications of the results were discussed. In this paper, a full account of the alcohol study (with results for some additional alcohols) and the spectra are presented. The results present a challenge for theoretical models of the solvated electron.

Experimental Section

The alcohols used were the best grades obtainable from Fisher Scientific or Eastman Kodak. The 1-hexadecanol was recrystallized from cyclohexane, and the other alcohols were purified by distillation with a Nester-Faust spinning-band column. The purified alcohols were checked for impurities by gas chromatography. Water content never exceeded 0.1% and generally was less than 0.05%. Hexane, 2-methoxyethanol, 2-ethoxyethanol, cyclohexane, hexadecane, and 2,2,4-trimethylpentane were obtained from Burdick Laboratories (Distilled-in-Glass) and were used without further purification. All solvents were examined for impurity optical absorptions. Lifetime and initial absorbancy of e_s^- provided additional criteria of solvent purity and were frequently checked for samples subjected to many pulses.

Samples were irradiated in quartz cells (1 × 1 × 3 cm); each cell was fitted with a Teflon stopcock through which could be inserted a capillary tube for deaeration or a syringe for introduction of a solute. Glassware was thoroughly cleaned and then baked in an annealing oven prior to use. Samples were deaerated in the cells with either dry

nitrogen or argon which remained in the closed cell at a pressure slightly above atmospheric. Unless stated otherwise, the experimental temperature was 30 ± 2°.

Samples were irradiated with 5- or 10-nsec pulses of ~8-MeV electrons from the Notre Dame Arco Model LP-7 linear accelerator. Light sources used for optical absorption measurements were a 450-W xenon lamp (Ushio UXL 451-0) pulsed to 600 A, a 4-mW He–Ne laser (Spectra Physics Model 135 CW), and a 21-W pulsed GaAs injection laser diode.[20] Light transmitted by the sample was focussed onto the slits of a Bausch and Lomb 33-86-25 monochromator containing either a 33-86-03 infrared or 33-86-02 visible grating. Light from the monochromator exit slit (widths in the range 0.5-1 mm) was focussed to fill the active area of a photodiode. Corning filters were placed between light source and cell to remove wavelengths less than 300 nm and before the monochromator entrance slit to eliminate second-order contributions.

Light intensity was measured with a 50-ohm impedance-matched system in which a photodiode was coupled to a Lecroy (Model 133) nanosecond linear amplifier with a 100-fold gain. The photodiode was either a Hewlett-Packard HP4207 PIN photodiode (400-1050 nm), a United Detector Technology PIN 10 silicon photodiode (400-1100 nm), or a special Philco Ford L4521 photodiode (800-1550 nm). The output signal displayed on a Tektronix 7904 (500 MHz) oscilloscope was photographed on Polaroid 410 high-speed film. Initial light intensity was recorded on a Tektronix 564 storage oscilloscope. Measurement of the 10-90% response time of the detection system, using a pulse from a light emitting diode, gave ≤1 nsec with the HP4207, ~15 nsec with the L4521, and ~30 nsec with the more sensitive UDT photodiode (with an active area of 1 cm^2). Linearity of the photodetectors for small absorptions was checked with neutral density filters. The smallest absorption detectable was ~0.1%.

Triply distilled, deaerated water was used for dosimetry. Sample absorbancies were normalized to the same dose by comparison of the sample absorbancy with that of e_{aq}^- produced in the dosimeter in an identical irradiation cell in the same position with fixed pulse conditions. From absorbancy at the maximum of the oscilloscope trace with $G(e_{aq}^-) = 3.5$[21] and published extinction coefficients,[22] 5×10^{17} eV ml^{-1} is estimated as a typical dose for a 10-nsec pulse to water.

Results

Absorption spectra (absorbancy, A, in arbitrary units vs. λ) of e_s^- are presented in Figures 1-5 for almost all the alcohols studied in this work. Each value of A in the figures is the average of many measurements over the course of the work. The spectra for 3-ethyl-3-pentanol and 2-ethoxyethanol are indistinguishable from those shown for 3-methyl-3-pentanol and 2-methoxyethanol, respectively. Assignment of each spectrum to e_s^- was confirmed by diagnostic tests with known electron scavengers.

The e_s^- spectrum for each alcohol was present immediately within a 5-nsec pulse. Decay of e_s^- was studied at wavelengths close to and on either side of λ_{max}. Representative traces are shown in Figure 6. In most of the alcohols, an initial fast decay for 100-200 nsec (ascribed to nonhomogeneous combination of "spur" or geminate solvated electrons and cations[23]) was followed by a slower decay with a first half-time of the order of 1 μsec. Such a half-time is consistent with that expected for second-order
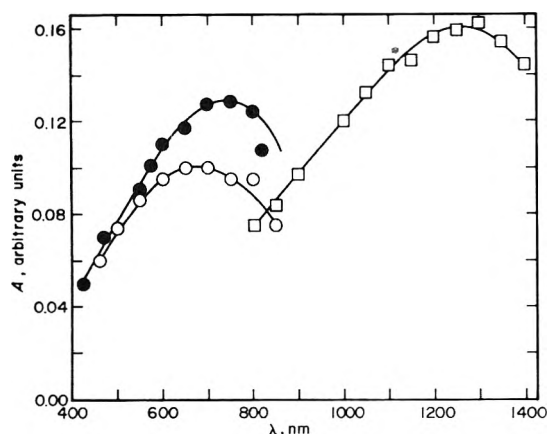
Figure 2. Absorption spectra of e_s^- at 30°: O, 1-butanol; ●, 2-butanol; □, 2-methyl-2-propanol.
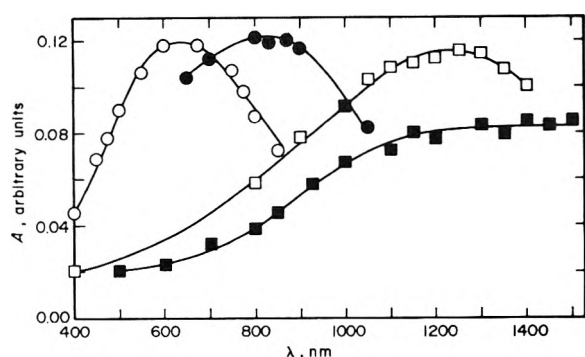
Figure 3. Absorption spectra of e_s^- at 30°: O, 1-pentanol; ●, cyclopentanol; □, 2-methyl-2-butanol; ■, 3-methyl-3-pentanol (displaced up 0.01 units).
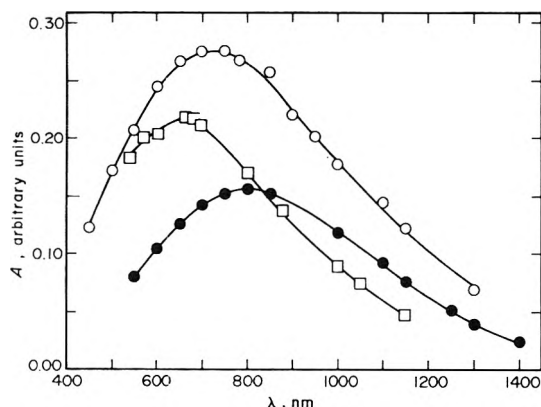
Figure 4. Absorption spectra of e_s^- at 30°: □, 1-hexanol (displaced down 0.04 units); O, cyclohexanol; ●, 4-methylcyclohexanol (displaced down 0.08 units).

homogeneous decay of e_s^- at the doses used. An appreciably larger decay rate was observed in some of the branched alcohols, e.g., in 2-methyl-2-propanol (cf. Figure 6) and especially in 2-methyl-2-butanol. In each alcohol at 30°, the decay rate was the same over the entire spectrum; in particular, no time-dependent spectral change was detectable at wavelengths greater than 1050 nm (within the 15-nsec resolution of the photodetector for such wavelengths). However, with 2-methyl-2-propanol and 2-methyl-2-butanol at temperatures near their respective freezing points of 25 and −9°, λ_{max} exhibited a reproducible hypsochromic shift of 50–100 nm over the first 30–50 nsec and subsequently remained constant.
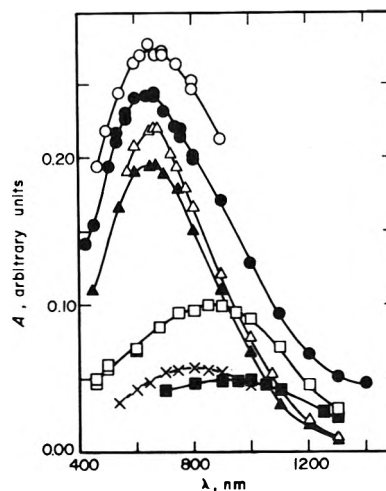
Figure 5. Absorption spectra of e_s^- at 30°: O, 1-nonanol (displaced up 0.08 units); ●, 1-decanol (displaced up 0.04 units); △, 1-undecanol; ▲, 1-octanol; □, 2-octanol; ■, 4-heptanol; X, 5 mol % 1-hexadecanol in cyclohexane.
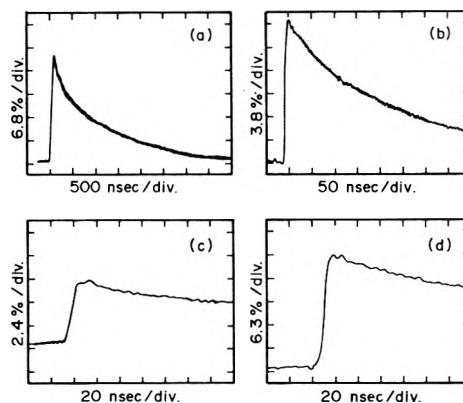
Figure 6. Time dependence of the optical absorption of e_s^- in the pulse radiolysis of alcohols: (a) 4-methylcyclohexanol at 750 nm; (b) 2-methyl-2-propanol at 1000 nm; (c) cyclopentanol at 740 nm; (d) 1-nonanol at 800 nm.

For each of the solvents studied, E_{max} and $W_{1/2}$ (band width at half-maximum) of the e_s^- spectrum are given in Table I along with D_s. Also given in Table I is $(G\epsilon_{max})_s/(G\epsilon_{max})_{aq}$[26] which is the product of (1) the electron density of water divided by that of the solvent and (2) the λ_{max} absorbancy of e_s^- divided by that of e_{aq}^- for the time at which maximum absorption occurs (cf. Figure 6) immediately after a 10-nsec pulse, corresponding in effect to a time of ∼5 nsec after a pulse of infinitesimal duration. Except for $W_{1/2}$ for e_s^- in ethanol, which appears to be too small, the values of E_{max} and $W_{1/2}$ in Table I agree well with published values[27,28] for e_s^- in methanol, ethanol, 1,2-ethanediol, 1-propanol, 2-propanol, and 1-butanol. Spectra have not been reported for e_s^- in the other alcohols.

In Table II, values of $(G\epsilon_{max})_s/(G\epsilon_{max})_{aq}$ from this work are compared with values taken or calculated from published work. Agreement with the values calculated from data of Baxendale and Wardman,[23] for essentially the same conditions, is reasonably good except for ethanol. Values of $G(e_s^-)$ also are given in Table II. $G(e_s^-)$ at 30 psec or 5 nsec is the product of (1) $G(e_{aq}^-)$ at the corresponding time, (2) $(G\epsilon_{max})_s/(G\epsilon_{max})_{aq}$ at the corresponding time divided by the μsec value, and (3) $G(e_s^-)$ at a μsec divided by $G(e_{aq}^-)$ at a μsec. For 30 psec and 5 nsec

TABLE I: Spectral Data and Relative Yields for Solvated Electrons

Solvent	D_s^a	E_{max}, eV	$W_{1/2}$, eV	$(G\epsilon_{max})_s/(G\epsilon_{max})_{aq}^b$
Methanol	32.6	1.93	1.4	0.38
Ethanol	24.3	1.70	~1.3^d	0.42
1.2-Ethanediol	37.7	2.13	1.4	0.38
2-Methoxyethanol		1.67	1.5	0.33
2-Ethoxyethanol		1.67	1.5	0.33
1-Propanol	20.1	1.67		
2-Propanol	18.3	1.49		0.39
1-Butanol	17.1	1.82	1.5	0.38
2-Butanol	17.9	1.67	1.4	0.42
2-Methyl-2-propanol	10.9	0.97	~0.8^d	0.46
1-Pentanol	13.9	1.90	1.4	0.37
3-Methyl-1-butanol	14.7	1.79		
2-Methyl-2-butanol	5.8	0.99	~0.8^d	0.34
Cyclopentanol	15^c	1.50	~1.4^d	0.48
3-Methyl-3-pentanol	5^c	≤0.82	>0.9^d	≥0.24
3-Ethyl-3-pentanol	5^c	≤0.82	>0.9^d	≥0.24
1-Hexanol	13.3	1.84	~1.5^d	0.37
Cyclohexanol	15.0	1.65	1.5	0.36
4-Methylcyclohexanol		1.54	~1.6^d	0.38
4-Heptanol	5.9	1.34	~1.5^d	>0.13
1-Octanol	10.3	1.90	1.5	0.34
2-Octanol	7.8	1.44	1.6	0.28
1-Nonanol	9.1	1.85	~1.5^d	0.33
1-Decanol	7.8	1.90	1.5	0.33
1-Undecanol	5.9	1.84	~1.5^d	0.35
Cyclohexane–5 mol % 1-hexadecanol	2^c	1.54	~1.4^d	
2,2,4-Trimethylpentane–5 mol % 1-hexadecanol	2^c	1.24		
Hexadecane–10 mol % 1-hexadecanol	3^c	1.65		

^{a} Values are for 25° and are from ref 24 except for those with a superscript. ^{b} Ratio of λ_{max} absorbancy of e_s^- to that cf e_{aq}^- (appropriately corrected by the ratio of electron densities) for a time immediately after a 10-nsec pulse (corresponding to the maximum in the oscilloscope trace; cf. Figure 6). ^{c} Upper limit estimated from data in ref 25. ^{d} Values based on a large extrapolation or assumption of symmetry of the plot of A vs. λ.

in Table II, the first and second values of $G(e_s^-)$ for each alcohol are calculated from (1) first and second values. respectively, for $(G\epsilon_{max})_s/(G\epsilon_{max})_{aq}$ at the corresponding time and (2) the first μsec value of $(G\epsilon_{max})_s/(G_{max})_{aq}$ for each alcohol except 1-butanol, for which the second μsec value necessarily was used.

Discussion

Each of the spectra obtained for e_s^- in this study (cf. Figures 1–5), like all e_s^- spectra that have been reported, is a structureless band that is asymmetric with respect to energy (similar in appearance to a photodetachment spectrum). For 19 of the alcohols, values of $W_{1/2}$ (given in Table I except that for ethanol which is taken to be 1.55 eV[27,28]) deviate from 1.5 eV by no more than the error limits (±0.1 eV). However, values of $W_{1/2}$ are particularly small for the four alcohols with E_{max} less than 1.0 eV. Though the four smallest values of $W_{1/2}$ were estimated by assumption of symmetry of the plot of A vs. λ, such an estimate differs from the correct value by less than 10% for each e_s^- spectrum sufficiently complete for measurement of $W_{1/2}$. Thus, there appears to be a definite narrowing of the e_s^- spectrum to $W_{1/2}$ less than 1.0 eV for the four alcohols for which E_{max} of the spectrum is less than 1.0 eV. However, absence of a general correlation between E_{max} and $W_{1/2}$ is illustrated by comparison of the results in Table I with[4] E_{max} = 1.73 eV and $W_{1/2}$ = 0.93 eV for e_{aq}^-.

Previous work[10-14] has shown that electron solvation time in a number of polar solvents is short compared to the relevant measured relaxation time $(\tau_1)^{[33]}$ which is for the process that largely determines D_s, namely, a rotation of solvent molecules that involves the rupture of hydrogen bonds. From results obtained in pulse radiolysis of ice,[10] ethanol glass at 77°K,[11] and some liquid alcohols at temperatures near their freezing points,[13] it is especially evident that electron solvation is not governed by a macroscopic relaxation rate (even that obtained by modification of the measured relaxation rate for constancy of charge as suggested by Mozumder[34]). Rather, such results suggest that electron solvation involves a more rapid local relaxation of solvent molecules in the intense coulombic field of a contiguous electron. Relaxation times reported for alcohols (including all normal alcohols through 1-undecanol)[33] indicate that τ_1 is unlikely to exceed 2.5 nsec at 30° in any solvent studied in this work. Thus, presence of the e_s^- spectrum within a 5-nsec pulse and absence of any detectable time dependence of the spectral shape or position (except for 2-methyl-2-propanol and 2-methyl-2-butanol near their freezing points) is consistent with results and implications of previous work.

Values of $(G\epsilon_{max})_s/(G\epsilon_{max})_{aq}$ in Table I relate to the yield of solvated electrons that survive ~5 nsec after a pulse of infinitesimal duration. That yield includes some solvated electrons that subsequently will undergo geminate recombination, i.e., $G(e_s^-)_g$ at 5 nsec, and others that will escape geminate recombination and constitute the free yield, $G(e_s^-)_f$, which is given as the microsecond yield in Table II. Owing to probable differences in values of ϵ_{max} for e_s^- in the different alcohols and complexity of the factors[35,36] that determine $G(e_s^-)_g$ at 5 nsec and $G(e_s^-)_f$, comparison of the values for $(G\epsilon_{max})_s/(G\epsilon_{max})_{aq}$ is not meaningful. For some of the alcohols, as shown in Table II, availability of additional information permits calculation of $G(e_s^-)$ at 30 psec and 5 nsec for comparison with the microsecond yield, i.e., $G(e_s^-)_f$. With exclusion of the first 5-nsec result for ethanol and the second 30-psec result for 2-propanol, there is a reasonable trend in $G(e_s^-)$ with time for each alcohol in Table II. Of particular interest is an indication that $G(e_s^-)$ at 30 psec decreases as τ_1 increases in the following sequence: water, methanol, ethanol, propanols, butanol. Though the macroscopic τ_1 does not correspond to the electron solvation time (τ_s), both τ_1 and τ_s probably are governed in a similar manner by the same physical factors and, as indicated by some recent results,[12,13] an increase in τ_1 probably signifies an increase in τ_s. Thus, the apparent trend in 30-psec values of $G(e_s^-)$ suggests that a larger τ_s allows a larger fraction of the high-mobility dry electrons[35-38] to undergo geminate recombination prior to solvation.

In the preliminary report[7] on the present work, absence of any kind of correlation between E_{max} and either D_s or $(1/D_0 - 1/D_s)$ was noted. Consequently, it was concluded that a long-range interaction determined by D_s (such as that postulated in polaron or dielectric continuum models[6]) has a negligible effect on E_{max} and, therefore, that a short-range interaction largely determines the binding and transition energies of e_s^- in the alcohols. Indeed, it does not seem possible to reconcile the results in Table I and the figures with any model in which long-range interactions significantly affect the e_s^- spectrum. Such results indicate that the dipole moment of the OH bond is the crucial determinant of the strength of a short-range inter-

TABLE II: Time Dependence of Solvated-Electron Yields

Solvent	$(G\epsilon_{max})_s/(G\epsilon_{max})_{aq}$			$G(e_s^-)$		
	30 psec[a]	5 nsec[b]	μsec[c]	30 psec[d]	5 nsec[d]	μsec
H₂O	1.0	1.0	1.0	4.0[e]	3.5[e]	2.7[f]
CH₃OH	0.39	0.38	0.37	3.1	2.7	2.0[g]
	0.37	0.34	0.36	3.0	2.4	
C₂H₅OH		0.42	0.30		3.1	1.7[g]
	0.33	0.36	0.30	2.8	2.6	
(CH₂OH)₂	0.39	0.38	0.34			
	0.36					
1-C₃H₇OH	0.42		0.26	2.9		1.2[h]
	0.33			2.3		
2-C₃H₇OH	0.44	0.39	0.28	2.8	2.2	1.2[i]
	0.29	0.41	0.32	1.8	2.3	
1-C₄H₉OH	0.36	0.38		2.3	2.1	1.1[j]
		0.35	0.26		1.9	

[a] The first result for each alcohol is from ref 29; the second result is calculated from data in ref 21 except that for (CH₂OH)₂ which is from ref 12. [b] The first result for each alcohol is from this work; the second result is calculated from data in ref 2? using $G(e_{aq}^-) = 3.5^{21}$ and $\epsilon_{max} = 1.85 \times 10^4 M^{-1} cm^{-1}$ for e_{aq}^-. [c] Using $G(e_{aq}^-) = 2.7$ and $\epsilon_{max} = 1.85 \times 10^3 M^{-1} cm^{-1}$ for e_{aq}^-, the first result for each alcohol is calculated from data in ref 27 and the second from data in ref 23. [d] As described in the text, first and second results for each alcohol are calculated from (1) first and second results, respectively, in the corresponding column of $(G\epsilon_{max})_s/(G\epsilon_{max})_{aq}$ and (2) the first μsec result for each alcohol except 1-C₃H₉OH. [e] Reference 21. [f] Reference 4. [g] Reference 30. [h] Reference 31. [i] Reference 32. [j] Estimate.

action that is modulated by the alkyl group. Thus, as suggested in the preliminary report, the results are qualitatively compatible with a model in which (1) the binding and transition energies of e_s^- in the alcohols are determined by interaction of the electron with an optimum configuration of OH dipoles in a small solvation domain, perhaps a single shell, and (2) the optimum configuration for e_s^- is affected by molecular structure of the alcohol.

In accord with the proposed model, there is little variation in E_{max} (cf. Table I) for the *normal* alcohols from C_1 to C_{11} except for the somewhat lower values for ethanol and 1-propanol. Such approximate invariance of E_{max} may extend to neat 1-hexadecanol, the values in Table I for alkane solutions probably being 0.2–0.3 eV lower than E_{max} for the neat alcohol (as observed with other alcohols[7,39,40]). Also noteworthy is the small effect on E_{max} of substitution of methoxy or ethoxy for a primary hydrogen atom of ethanol. In such alcohols the OH dipoles evidently attain an optimum configuration in solvation of an electron without appreciable hindrance by the attached chains which extend radially into the solvent. However, for alcohols with branched alkyl groups, the smaller values of E_{max} indicate a less favorable interaction between the electron and OH dipoles. Indeed, from comparison of E_{max} for alcohols which differ in number and size of branch groups and distance of the branch point from OH, it is evident that the optimum configuration of e_s^- is very sensitive to the effect of steric hindrance. Such effects are especially well illustrated by the e_s^- spectra in Figures 2–5. Again, the irrelevance of D_s should be noted; compare in Table I, for example, 2-methyl-2-propanol with 1-octanol or 2-methyl-2-butanol with 1-undecanol. Additional support for the foregoing arguments is provided by published spectra for e_s^- in dimethyl sulfoxide ($D_s = 47$) with $E_{max} \leq 0.83$ eV[9] and in hexamethylphosphoric triamide ($D_s = 30$) with $E_{max} = 0.55$ eV.[41,42] Such results suggest that in both solvents the electron is situated in the alkane-like environment of the positive ends of the molecular dipoles (as noted by Nauta and van Huis[41]) and the binding energy is diminished by steric hindrance between the bulky molecules in the solvation shell. Finally, the comparatively large values of $E_{max} = 2.13$ eV for ethylene glycol and $E_{max} = 2.35$ eV for glycerol[28] suggest a chelate structure with enhanced binding energy.

There is at present no satisfactory theoretical model for quantitative, or even semiquantitative, interpretation of the e_s^- spectra now available. The most thorough and sophisticated theoretical treatment reported is for e_s^- in liquid ammonia;[18] however, the spectrum calculated for e_s^- in that treatment bears no resemblance to the observed spectrum.[43] From results of the present work it is clear that a satisfactory theoretical treatment of the solvated electron requires a model in which (1) a long-range interaction dependent on D_s does not significantly affect the absorption spectrum and (2) adequate consideration is given to the effect of composition and structure of the solvent molecule on topography of the solvation domain and, thereby, on the strength of the interaction between the electron and the relevant bond or group dipole of each molecule in the solvation domain.[44]

References and Notes

(1) Sterling Chemistry Laboratory, Yale University, New Haven, Conn. 06520

(2) The Radiation Laboratory of the University of Notre Dame is operated under contract with the U. S. Atomic Energy Commission. This is AEC Document No. C00-38-925.

(3) H. A. Gillis, N. V. Klassen, G. G. Teather, and K. H. Lokan, Chem. Phys. Lett., 10, 481 (1971).

(4) E. J. Hart and M. Anbar, "The Hydrated Electron," Wiley-Interscience, New York, N. Y., 1970, pp 40 and 41.

(5) Reference to all papers on solvated electrons would require an extensive bibliography; instead, reference is made throughout this paper to papers that are considered particularly relevant or illustrative.

(6) J. Jortner, J. Chem. Phys., 30, 839 (1959); Radiat. Res. Suppl., 4, 24 (1964).

(7) R. R. Hentz and G. Kenney-Wallace, J. Phys. Chem., 76, 2931 (1972).

(8) J. Corset and G. Lepoutre in "Solutions Métal-Ammoniac," G. Lepoutre and M. J. Sienko, Ed., W. A. Benjamin, New York, N. Y., 1964, p 187.

(9) D. C. Walker, N. V. Klassen, and H. A. Gillis, Chem. Phys. Lett., 10, 636 (1971); R. Bensasson and E. J. Land, ibid., 15, 195 (1972).

(10) I. A. Taub and K. Eiben, J. Chem. Phys., 49, 2499 (1968).

(11) J. T. Richards and J. K. Thomas, J. Chem. Phys., 53, 218 (1970).

(12) M. J. Bronskill, R. K. Wolff, and J. W. Hurt, J. Chem. Phys., 53, 4201 (1970); L. Gilles, J. E. Aldrich, and J. W. Hunt, Nature (London), Phys. Sci., 243, 70 (1973).

(13) J. H. Baxendale and P. Wardman, J. Chem. Soc., Faraday Trans. 1, 69, 584 (1973).

(14) P. M. Rentzepis, R. P. Jones, and J. Jortner, J. Chem. Phys., 59, 766 (1973).

(15) A. Gaathon, G. Czapski, and J. Jortner, J. Chem. Phys., 58, 2648 (1973).

(16) K. Fueki, D.-F. Feng, and L. Kevan, J. Amer. Chem. Soc., 95, 1398 (1973).

(17) D. A. Copeland, N. R. Kestner, and J. Jortner, J. Chem. Phys., 53,

1189 (1970).
(18) N. R. Kestner and J. Jortner, *J. Phys. Chem.*, **77**, 1040 (1973).
(19) M. D. Newton, *J. Chem. Phys.*, **58**, 5833 (1973).
(20) G. A. Kenney-Wallace and D. W. Schult, to be submitted for publication.
(21) R. K. Wolff, M. J. Bronskill, J. E. Alcrich, and J. W. Hunt, *J. Phys. Chem.*, **77**, 1350 (1973).
(22) B. D. Michael, E. J. Hart, and K. H. Schmidt, *J. Phys. Chem.*, **75**, 2798 (1971).
(23) J. H. Baxendale and P. Wardman, *Chem. Commun.*, 429 (1971).
(24) R. C. Weast, Ed., "Handbook of Chemistry and Physics," 50th ed., Chemical Rubber Publishing Co., Cleveland, Ohio, 1969–1970.
(25) F. Buckley and A. A. Maryott, *Nat. Bur. Stand. (U.S.), Circ.*, **589** (1958).
(26) G is the number of solvated electrons present at a given time per 100 eV of energy deposited in the solvent, and ϵ_{max} is the extinction coefficient at λ_{max}.
(27) M. C. Sauer, Jr., S. Arai, and L. M. Dorfman, *J. Chem. Phys.*, **42**, 708 (1965).
(28) S. Arai and M. C. Sauer, Jr., *J. Chem. Phys.*, **44**, 2297 (1966).
(29) S. C. Wallace and D. C. Walker, *J. Phys. Chem.*, **76**, 3780 (1972).
(30) K. N. Jha, G. L. Bolton, and G. R. Freeman, *J. Phys. Chem.*, **76**, 3876 (1972).
(31) G. R. Freeman, *Actions Chim. Biol. Radiat.*, **14**, 73 (1970).
(32) K.-D. Asmus, S. A. Chaudhri, N. B. Nazhat, and W. F. Schmidt, *Trans. Faraday Soc.*, **67**, 2607 (1971).
(33) S. K. Garg and C. P. Smyth, *J. Phys. Chem.*, **69**, 1294 (1965); W.

P. Conner and C. P. Smyth, *J. Amer. Chem. Soc.*, **65**, 382 (1943); G. P. Johari and C. P. Smyth, *ibid.*, **91**, 6215 (1969).
(34) A. Mozumder, *J. Chem. Phys.*, **50**, 3153 (1969).
(35) R. H. Schuler and P. P. Infelta, *J. Phys. Chem.*, **76**, 3812 (1972).
(36) G. R. Freeman, *Advan. Chem. Ser.*, **No. 82**, 339 (1968); M. G. Robinson and G. R. Freeman, *Can. J. Chem.*, **51**, 1010 (1973).
(37) W. F. Schmidt and A. O. Allen, *J. Chem. Phys.*, **52**, 4788 (1970); R. M. Minday, L. D. Schmidt, and H. T. Davis, *J. Chem. Phys.*, **54**, 3112 (1971); F. M. Minday, L. D. Schmidt, and H. T. Davis, *J. Phys. Chem.*, **76**, 442 (1972); J.-P. Dodelet and G. R. Freeman, *Can. J. Chem.*, **50**, 2667 (1972).
(38) W. H. Hamill, *J. Chem. Phys.*, **49**, 2446 (1968).
(39) T. J. Kemp, G. A. Salmon, and P. Wardman in "Pulse Radiolysis," M. Ebert, J. P. Keene, A. J. Swallow, and J. H. Baxendale, Ed., Academic Press, London, 1965, pp 247–257.
(40) L. B. Magnusson, J. T. Richards, and J. K. Thomas, *Int. J. Radiat. Phys. Chem.*, **3**, 295 (1971).
(41) H. Nauta and C. van Huis, *J. Chem. Soc., Faraday Trans. 1*, **68**, 647 (1972).
(42) J. M. Brooks and R. R. Dewald, *J. Phys. Chem.*, **72**, 2655 (1968).
(43) See Figure 12 of ref 18 for a comparison that includes a calculated line shape for a 1s → 2p transition and estimated energies for transitions to higher bound states and to the continuum.
(44) Results and conclusions similar to certain of those in this and the preliminary (ref 7) report have been presented in a paper on electrons trapped in aliphatic amine glasses by T. Ito, K. Fueki, A. Namiki, and H. Hase, *J. Phys. Chem.*, **77**, 1803 (1973).

Low-Temperature Pulse Radiolysis. I. Negative Ions of Halogenated Compounds

Shigeyoshi Arai,* Seiichi Tagawa, and Masashi Imamura

The Institute of Physical and Chemical Research, Wako-shi, Saitama 351, Japan   (Received July 9, 1973)

Publication costs assisted by the Institute of Physical and Chemical Research

The absorption spectra and kinetic behavior of the species produced in irradiated ethanol solutions of 1- and 2-chloronaphthalenes, 4-chlorobiphenyl, 1- and 2-bromonaphthalenes, and 2- and 4-bromobiphenyls have been studied using pulse radiolysis at 100°K. The spectra observed are ascribed to the parent negative ions of these halogenated compounds. The negative ions of the chlorinated compounds have long lifetimes and an appreciable part remains even at a few seconds after the pulse. On the other hand, the negative ions of the brominated compounds disappear in a complicated manner within 100 msec. Ethanol solutions of 1,2,3-trichlorobenzene and tetrachloroethylene give intense absorptions in the ultraviolet region which may also be ascribed to the negative ions of these solutes. Pulse radiolysis of ethanol solutions of benzyl chloride gives only absorption due to benzyl radicals. The negative ion of benzyl chloride dissociates into a benzyl radical and a chloride ion at 100°K.

Introduction

Halogenated compounds are frequently used as an effective electron scavenger in the radiolysis of various chemical substances. This is based on the fact that halogenated compounds are highly reactive toward electrons, and when an electron attaches to the molecule it dissociates into a neutral radical and a halide ion. The yield of the electron can be determined[1,2] from the quantitative analysis of the products originating from so-called dissociative attachment. Recent papers[3-5] on electron attachment in the gas phase demonstrated that some halogenated compounds form parent negative ions which are metastable.

We made a low-temperature pulse radiolysis study of halogenated compounds in order to obtain information relating to the negative ions. The present paper mainly describes their absorption spectra and kinetic behavior in ethanol glasses at 100°K.

Experimental Section

Ethanol (99.5 vol %) obtained from Wako Pure Chemical Industries was used without further purification. 2-Chloronaphthalene and 2-bromonaphthalene from Tokyo Kasei, 4-bromobiphenyl from K & K, and 1,2,3-trichlorobenzene from Merck were all recrystallized from ethanol solutions. Benzyl chloride and tetrachloroethylene from Wako Pure Chemical Industries, 1-chloronaphthalene and 2-bromobiphenyl from Tokyo Kasei, 1-bromonaphthalene from NPC Laboratory, and 4-chlorobiphenyl from Gas-Chro Industries were all used without further purification.

The source of electron pulses was a Mitsubishi Van de Graaff accelerator. The energy was 2.7–2.8 MeV and the
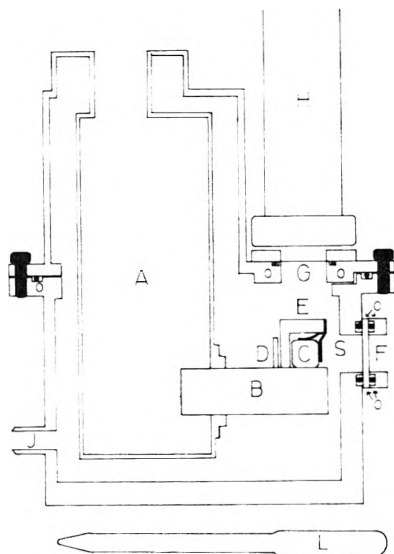
Figure 1. Low-temperature apparatus and reaction cell: A, liquid nitrogen container; B, copper block; C, reaction cell; D, mirror; E, cell holder; F, quartz window; G, aluminum window; H, Van de Graaff; J, air outlet; S, spring; O, rubber O-ring; L, type A reaction cell.

pulse duration was 1.0 or 2.0 μsec. The current was adjusted in the range of 50–200 mA so that an absorbing species was produced at a concentration appropriate for optical observation. The electron beam had a diameter of approximately 12 mm at the aluminum window of the low-temperature apparatus. Although precise dosimetry was not needed for the present experiments, it was known from earlier measurements using a ferrocyanide dosimeter that the 1.0-μsec pulse at a current of 100 mA gives a dose of 9000 rads.

The spectrophotometric observation technique is essentially identical with those commonly employed in pulse radiolysis studies.[6] An Ushio 150-W xenon lamp was used as an analyzing light source. The monochromator was a Bausch & Lomb Type 33-86-25 instrument. Three different gratings were used with the following wavelength ranges and reciprocal dispersions: 200–400 nm, 3.2 nm/mm; 350–800 nm, 6.4 nm/mm; 700–1600 nm, 12.8 nm/mm. The exit slit was generally set at a width of 0.5 mm. The optical absorption was determined using either a Hamamatsu R374 photomultiplier (wavelengths below 750 nm) or a Hamamatsu R316 photomultiplier (wavelengths above 700 nm). Pulse intensity was monitored with a core sensor each time. Although variations in pulse intensity were less than 10%, the observed optical density was corrected assuming that the optical density is directly proportional to the pulse intensity. Corrected values were reproduced within 5% or less.

Figure 1 shows a brief sketch of the low-temperature apparatus and an irradiation cell made of Suprasil quartz. A deaerated ethanol solution was sealed in a type A cell (optical part: 1 × 1 cm square tube, length 5 cm) and frozen rapidly by dipping into liquid nitrogen. Then the cell was mounted inside the low-temperature apparatus in such a way that it was pressed tightly to a copper block cooled to 77°K. A part of this copper block juts into a large liquid nitrogen container. The air inside the apparatus was pumped out to a pressure of 10^{-3} mm. The electron beam entered into the apparatus through a thin aluminum window and the analyzing light beam through a quartz window. The analyzing light beam was reflected in

the reverse direction after passing a cell. Therefore the light path length (2.0 cm) was twice the width of the cell.

The temperature of the sample was measured separately under the same conditions. A thermocouple was inserted into the sample so that the junction was placed in the middle of the light path. When frozen ethanol was mounted inside the low-temperature apparatus, the temperature rose rapidly and then reached a constant value within 5 min. The temperatures were 97, 100, 100, and 102°K for the different measurements in which the position of the junction was slightly varied.

Results and Discussion

The results obtained on the pulse radiolysis of pure ethanol were essentially the same as those reported by Richards and Thomas.[7] The intense absorption due to trapped electrons appeared in the wavelength region of 300–1000 nm. The absorption at around 1000 nm decreases rapidly within 50 μsec or so, while the absorption at around 600 nm increases slightly. The peak is located at 650 nm at 170 μsec after pulse.

1- and 2-Chloronaphthalenes. Figure 2 shows the absorption spectrum obtained on the pulse radiolysis of the ethanol solution of 0.16 M 1-chloronaphthalene. Unless otherwise stated in figure legends, the spectra presented in this paper were determined at 100°K at about 2 μsec after pulse. Addition of 1-chloronaphthalene to ethanol removes the absorption due to trapped electrons and gives a different spectrum with peaks at 370, 690, and 760 nm. This fact indicates that electrons react with 1-chloronaphthalene in the ethanol glass. Under the present experimental conditions a concentration higher than 0.1 M was necessary to scavenge all of the electrons. A sharp peak at 420 nm superimposed upon the broad absorption band in the ultraviolet region is in good agreement with that of the triplet state of 1-chloronaphthalene,[8] which may be, at least in part, produced by the direct action of ionizing radiation on the solute. The spectrum observed resembles that of the negative ion of naphthalene in overall appearance as seen in Figure 2. This fact suggests that it is ascribed to a negative ion of 1-chloronaphthalene, which is formed by attachment of the electron as already reported for various aromatic hydrocarbons.[9] The spectroscopic study on benzene derivatives by Kimura and Nagakura[10] has shown that the spectra of chlorobenzene and bromobenzene can be interpreted as the shift or split of the corresponding benzene bands. Porter and Ward[11] have reported that the spectrum of a benzyl radical resembles those of *o*-, *m*-, and *p*-chloro-substituted radicals very closely. These studies indicate that chlorine and bromine are only in weak interaction with π-orbitals of aromatic compounds. A similar situation may hold also for the negative ion of 1-chloronaphthalene. It should be noted that the pulse radiolysis of the same solution at room temperature gives no absorption in the visible region and weak absorption in the ultraviolet region. The spectrum shown in Figure 3 was obtained on the pulse radiolysis of the ethanol solution of 0.17 M 2-chloronaphthalene. It may be ascribed to the negative ion of 2-chloronaphthalene. The sharp peaks at 420 and 400 nm are obviously due to the triplet state of the solute.[8]

The negative ions of both 1- and 2-chloronaphthalenes decay very slowly in glassy ethanol at 77°K. Only several per cent of the total concentration disappears within the initial period of 1 msec and an appreciable amount remains even at a few seconds after the pulse. The colors of
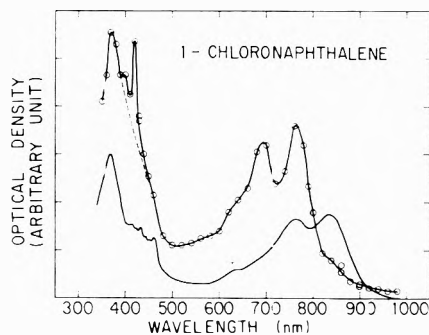
Figure 2. The absorption spectrum observed for an ethanol solution of 0.16 *M* 1-chloronaphthalene (circles). The absorption spectrum of the negative ion of naphthalene (solid line).
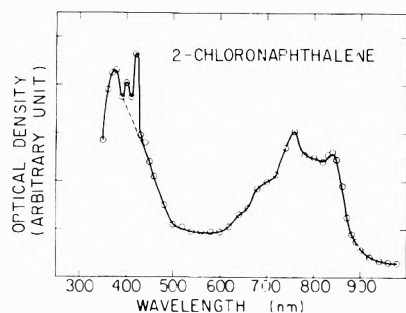
Figure 3. The absorption spectrum observed for an ethanol solution of 0.17 *M* 2-chloronaphthalene.
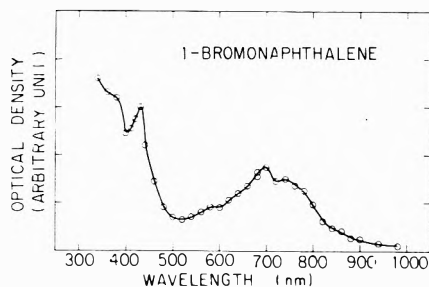
Figure 4. The absorption spectrum observed for an ethanol solution of 0.15 *M* 1-bromonaphthalene.

Figure 5. The absorption spectrum observed for an ethanol solution of 0.15 *M* 2-bromonaphthalene.
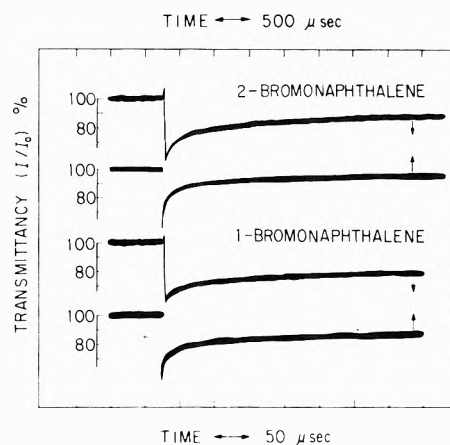
Figure 6. The decay curves observed for 1- and 2-bromonaphthalenes in ethanol at 77°K. The time scale (50 or 500 μsec per division) used for each curve is shown by a small arrow. Top two, 0.15 *M* 2-bromonaphthalene, at a wavelength of 760 nm. Bottom two, 0.15 *M* 1-bromonaphthalene, at a wavelength of 700 nm.

the irradiated solutions are removed readily by illumination with visible light. This fact also supports the previous assignments of the spectra.

1- and 2-Bromonaphthalenes. Figures 4 and 5 show the absorption spectra obtained on the pulse radiolysis of the ethanol solutions of 1- and 2-bromonaphthalenes, respectively. These spectra may be ascribed to the negative ions of both solutes. The absorption band of the triplet state was reported[8] to be located at 424 nm for 1-bromonaphthalene and at 423 nm for 2-bromonaphthalene.

Figure 6 shows the decay curves observed for the negative ions of both 1- and 2-bromonaphthalenes in ethanol glass at 100°K. The absorptions due to these ions decay in a similar manner throughout the entire wavelength region examined. No change in the spectral shape occurs during the decay process, different from the previous observation on the trapped electron[7] or the negative ion of benzophenone.[12] Therefore, the decay curves are considered to exhibit decreases in the concentrations of both ions. If the negative ion decomposes under a thermal equilibrium condition, its decay kinetics fits the first-order rate law. The results obtained are obviously different from this case. The recombination between the negative ions of bro-

monaphthalenes and positive ions produced by radiation may be ruled out because the negative ions probably cannot move about in rigid ethanol glass. It should be pointed out that such recombination does not occur, at least at an appreciable rate, even in the cases of chloronaphthalenes the molecular weight of which is lower than that of bromonaphthalenes. We think that the negative ions of bromonaphthalenes trapped in the site favorable to the formation of bromide ions decompose much more easily into naphthyl radicals and bromide ions. In such a site the hydroxyl hydrogen of ethanol probably occupies the position closer to bromine of the negative ion of bromonaphthalenes. In other sites the negative ions may decompose either at a fast rate after the solvent molecules around the solute ion re-orient or at a slow rate without orientation. As a result, the negative ions are expected to decay in a complicated manner as seen in Figure 6.

4-Chloro-, 4-Bromo-, and 2-Bromobiphenyls. Figures 7, 8, and 9 show the absorption spectra assigned to the negative ions of 4-chloro-, 4-bromo-, and 2-bromobiphenyls, respectively. The spectral shapes of these ions, particularly of 4-chlorobiphenyl, resemble that of the negative ion of biphenyl again. Although the absorption bands due to the triplet state are not known for these compounds, they may be located in the vicinity of 350 nm judging from T–T absorption of biphenyl.[13] The negative ion of 4-chlorobiphenyl scarcely decays, at least during the initial period of 1 msec, while the negative ions of 4- and 2-bromonaph-
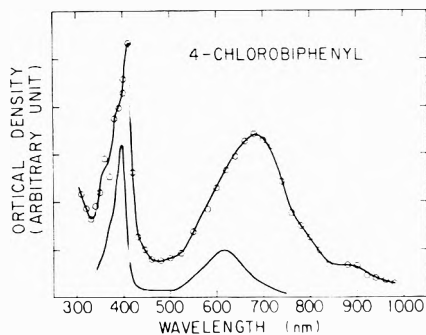
Figure 7. The absorption spectrum observed for an ethanol solution of 0.089 M 4-chlorobiphenyl (circles). The absorption spectrum of the negative ion of biphenyl (solid line).
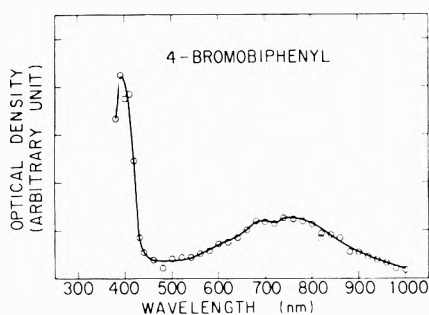
Figure 8. The absorption spectrum observed for 0.15 M 4-bromobiphenyl in a mixture of ethanol and ethyl ether at a volume ratio of 1 to 1.
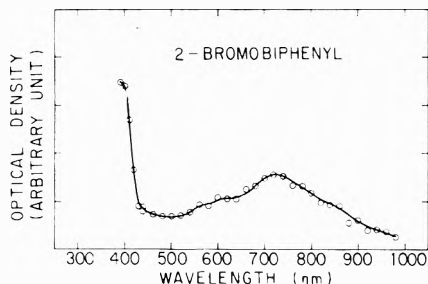
Figure 9. The absorption spectrum observed for an ethanol solution of 0.15 M 2-bromobiphenyl.

thalenes decay in a manner similar to those observed for the negative ions of bromonaphthalenes.

1,2,3-Trichlorobenzene and Tetrachloroethylene. Figure 10 shows the absorption spectra obtained on the pulse radiolysis of the ethanol solutions of 1,2,3-trichlorobenzene and tetrachloroethylene. The intense bands in the uv region cannot be observed when these solutions are irradiated at room temperature. These spectra may be ascribed to the negative ions of the solute molecules. In the case of tetrachloroethylene, however, one cannot exclude the possibility that the absorption band at 340 nm is due to Cl_2^- produced by reaction 1.

$$C_2Cl_4 + e^- \rightarrow C_2Cl_3 + Cl_2^-$$ (1)
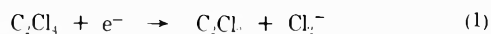
Benzyl Chloride. Figure 11 shows the absorption spectrum observed for the irradiated ethanol solution of 0.20 M benzyl chloride immediately after the pulse. It agrees with the well-known spectrum of a benzyl radical.[14] The absorption accumulates for each pulse. Contrary to the negative ions of other halogenated compounds, this absorption does not fade out on illumination with uv light. Higashimura, *et al.*,[15] recently observed the absorption
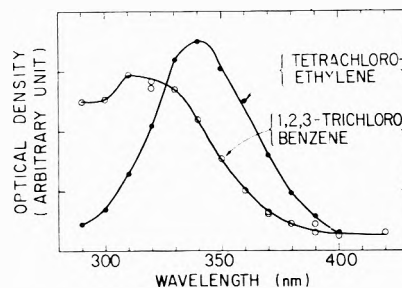
Figure 10. The absorption spectra observed for ethanol solutions of 0.22 M 1,2,3-trichlorobenzene (circles) and 0.49 M tetrachloroethylene (solid circles).
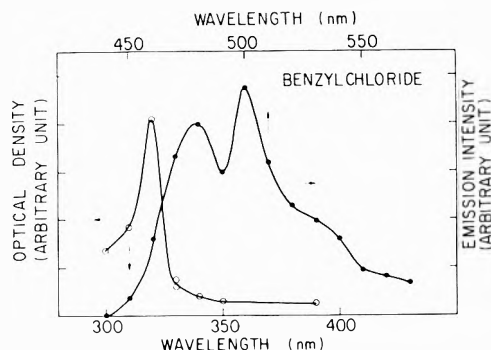
Figure 11. The absorption (circles) and emission (solid circles) spectra observed for an ethanol solution of 0.20 M benzyl chloride immediately after pulse. The emission spectrum was corrected for the wavelength response of the photomultiplier by use of the manufacturer's standard curve.

band at 340 nm on the γ radiolysis of the ethanol solution of benzyl chloride at 4°K. When the temperature of the solution was raised to 77°K, this band was found to disappear and the intensity of the absorption due to a benzyl radical to increase remarkably. It is quite probable that the absorption band at 340 nm is ascribed to the negative ion of benzyl chloride. We could not observe a corresponding band on the pulse radiolysis of the same system. All benzyl radicals were produced simultaneously with pulse irradiation. Therefore, the negative ion may immediately decompose into a benzyl radical and a chloride ion at 100°K although stable at 4°K.

Figure 11 also shows the emission spectrum observed for the ethanol solution of benzyl chloride. The half-life is 0.9 μsec. The emission occurs in the same region as that previously attributed to benzyl does.[11,16] The detailed analysis of the emission spectrum of a benzyl radical has been made by Leach and his coworkers,[16,17] who determined the 0-0 band in the gas phase as 22001.5 cm^{-1}. Since the bond dissociation energy of C-Cl of benzyl chloride is reported to be 66 kcal/mol, the energy of 129 kcal/mol is necessary to produce excited benzyl from benzyl chloride. It is much higher than the electron affinity of Cl (83.2 kcal/mol) in the gas phase. Excited benzyl may be produced either by the direct effect of ionizing radiation on the solute or by energy transfer from highly excited ethanol to the solute. Identical emission appeared on the pulse radiolysis of the ethanol solution of benzyl bromide.

The absorption spectra observed for the negative ions of halogenated aromatic hydrocarbons indicate that the excess electron occupies the π-orbital of the aromatic ring. The dissociation occurs when the excess electron is localized in the Ar–X bond of negative ion, where Ar represents the radical of an aromatic hydrocarbon. The kinetic

behavior of the negative ion in various solvents is under study.

References and Notes

(1) J. M. Warman, K.-D. Asmus, and R. H. Schuler, *J. Phys. Chem.*, **73**, 931 (1969).
(2) T. Kimura, K. Fueki, and Z. Kuri, *Bull. Chem. Soc. Jap.*, **43**, 3090 (1970).
(3) W. E. Wentworth, R. S. Bechker, and R. Tung, *J. Phys. Chem.*, **71**, 1652 (1967).
(4) W. E. Wentworth, R. George, and H. Keith, *J. Chem. Phys.*, **51**, 1791 (1969).
(5) J. C. Steelhammer and W. E. Wentworth, *J. Chem. Phys.*, **51**, 1802 (1969).
(6) A. Kira, S. Arai, and M. Imamura, *Rep. Inst. Phys. Chem. Res.*, **47**, 139 (1971).
(7) J. T. Richards and J. K. Thomas, *J. Chem. Phys.*, **54**, 293 (1970).
(8) M. Z. Hoffman and G. Porter, *Proc. Roy. Soc., Ser. A*, **268**, 46 (1962).
(9) S. Arai and L. M. Dorfman, *J. Chem. Phys.*, **41**, 2190 (1964); W. H. Hamill in "Radical Ions," E. T. Kaiser and L. Kevan, Ed., Interscience, New York, N. Y., 1968, p 321.
(10) K. Kimura and S. Nagakura, *Mol. Phys.*, **9**, 117 (1965).
(11) G. Porter and B. Ward, *J. Chim. Phys.*, **61**, 1517 (1964).
(12) M. Hoshino, S. Arai, and M. Imamura, submitted for publication.
(13) G. Porter and M. W. Windsor, *Proc. Roy Soc., Ser. A*, **245**, 238 (1958).
(14) J. B. Gallivan and W. H. Hamill, *Trans. Faraday Soc.*, **61**, 1960 (1965).
(15) T. Higashimura, A. Namiki, M. Noda, and H. Hase, *J. Phys. Chem.*, **76**, 3744 (1972).
(16) L. Grajcar and S. Leach, *J. Chim. Phys.*, **61**, 1523 (1964).
(17) C. Cossart-Magos and S. Leach, *J. Chem. Phys.*, **56**, 1534 (1972).

Hydroxyl Radical Reactions with Phenols and Anilines as Studied by Electron Spin Resonance[1]

P. Neta and Richard W. Fessenden*

Radiation Research Laboratories, Center for Special Studies and Department of Chemistry, Mellon Institute of Science, Carnegie-Mellon University, Pittsburgh, Pennsylvania 15213 (Received May 7, 1973; Revised Manuscript Received October 11, 1973)

The radicals produced by reaction of OH with a number of carboxy-substituted phenols, aminophenols, and anilines have been studied by the *in situ* radiolysis esr technique. The radicals produced from the phenols are identified as of the phenoxyl type and are formed by addition of OH to the ring followed by elimination of water. In the case of 5-hydroxyisophthalic acid the intermediate hydroxycyclohexadienyl radical was of long enough lifetime to be observed. Also present in the esr spectra of the phenols were signals from corresponding ortho and para semiquinone radical anions. These latter radicals are believed to be produced in secondary reactions from dihydroxy compounds formed upon bimolecular reaction of the phenoxyl radicals. The aminophenols produced spectra with g factors of ~2.0037 in contrast to the values of ~2.0047 found for phenoxyl radicals. These spectra are assigned to aminophenoxyl radicals. A small amount of deamination to form the corresponding semiquinone radical was also found. The three anilines studied all gave spectra which could be ascribed to anilino radicals (RNH). Parameters of the unsubstituted radical C_6H_5NH are $g = 2.00331$ and $a^N = 7.95$, $a_{NH}^H = 12.94$, $a_o^H = 6.18$, $a_m^H = 2.01$, and $a_p^H = 8.22$ G.

Introduction

Hydroxyl radicals are known to add to aromatic rings to form hydroxycyclohexadienyl radicals and in a number of cases these radicals have been observed by esr (see *e.g.*, ref 2-4). Pulse radiolysis experiments have shown that when the reacting compound contains an OH group water elimination follows the initial addition.[5,6]
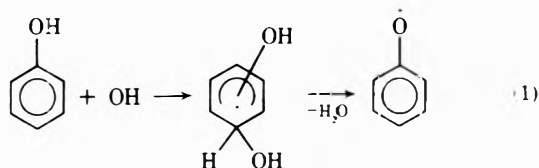
This elimination is a first-order process, catalyzed by H^+

or by OH^-, and its uncatalyzed rate constant is $\leq 10^3$ sec^{-1} for phenol[5] and 4.6×10^4 sec^{-1} for hydroquinone.[6] In accord with this mechanism, the esr spectra observed[4] with several phenols in the Ti^{III}-H_2O_2 system showed the presence of the OH adducts in slightly acid solution and the phenoxyl radicals at higher acidities. However, in alkaline solution only radicals of the benzosemiquinone type were observed.[4] The latter finding together with similar observations in the radiolysis of hydroxybenzoic acids[7] and in the photolysis of phenol[8] suggest the importance of secondary reactions in these steady-state experiments. The *in situ* radiolysis esr experiments reported here were undertaken in order to further investigate the reactions for various substituted phenols and were extended to hydroxyphenols, aminophenols, and anilines in an attempt to investigate the chemistry of those systems as well.

Experimental Section

The aromatic compounds were of the purest grade commonly available and were used without further purification. Most of them were obtained from Eastman Organic Chemicals and from Aldrich Chemical Co. and were 98–99% pure. The two aminohydroxybenzoic acids and the aminohydroxybenzenesulfonic acid were obtained from Pfaltz and Bauer. Aqueous solutions containing from 10^{-4} to 10^{-2} M of the organic compound were saturated with N_2O in order to convert e_{aq}^- into OH. The details of the *in situ* radiolysis steady-state esr experiments are similar to those previously described.[2]

Esr Observations and Reaction Mechanisms

Addition of OH to an aromatic ring can lead to a number of different intermediate hydroxycyclohexadienyl radicals depending upon the site of reaction. However, because the subsequent elimination reaction usually involves the OH group added in the initial step the final radical (*e.g.*, phenoxyl) will be the same for any position of reaction. Elimination of water following addition at the position of a substitutent other than an OH group can also produce the phenoxyl radical but elimination of the substituent may also take place, in effect, replacing that substituent by an OH group.

The compounds studied can be divided into four types which can react with OH in somewhat different ways. Phenol and its carboxy derivatives can react as in reaction 1 to give phenoxyl radicals. The ortho and para dihydroxy compounds can react in a similar way to give semiquinone radicals. With the aminophenols the most probable type of radical is aminophenoxyl but addition at the NH_2 position followed by loss of NH_3 could produce a semiquinone radical. Finally, with anilines addition at any position but that of the NH_2 group should give anilino radicals by water elimination while addition at the site of the NH_2 group could be followed by elimination of either H_2O or NH_3 to give, respectively, the anilino or phenoxyl radicals.

In discussing the specific reaction mechanisms below the identity of the radicals as given in the tables will be assumed to be correct. In most cases a comparison of the hyperfine parameters for a given type of radical with substituents in various positions leaves little question as to their identities. Further discussion of the hyperfine constants will be given in a later section.

Phenol. The esr spectra observed with irradiated aqueous solutions of phenol (10^{-3} M and saturated with N_2O) at pH 9.3 and 12.2 were similar and consisted of the lines of three different radicals. The least intense set of lines (with hyperfine constants and g factor as shown in Table I) corresponds to the known spectrum of phenoxyl radical.[9–11] The most intense lines correspond to the o-benzosemiquinone radical anion (VIII, Table II) and the third set of lines to the p-benzosemiquinone radical anion (XV, Table II). The peak heights of the unit intensity lines of the ortho and para benzosemiquinone ions were 6 and 1.5 times those of the phenoxyl radicals. However, the semiquinone radicals are relatively long lived and under conditions of quantitative production (*i.e.*, from hydroquinone) give signals about two orders of magnitude higher. From this fact it must be concluded that in the phenol system the yield of semiquinones is relatively small and can be attributed to secondary reactions. In support of

this interpretation, it was found that the intensities of their spectra decreased at higher flow rates.

The secondary reactions leading to the formation of the semiquinones are most probably the disproportionation of the phenoxyl radicals to produce hydroquinone, catechol, and phenol followed by reaction of OH with these dihydroxy compounds. To explain the production of the dihydroxy compounds it is suggested that disproportionation takes place by electron transfer (reaction 2) to form a neg-

(2)
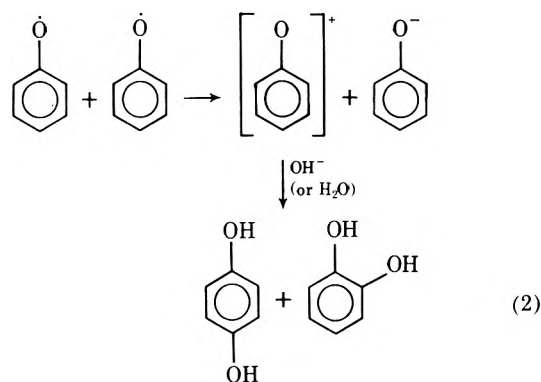
ative ion (phenoxide) and a positive ion which can then be neutralized by reaction with H^+ and OH^-, respectively, or by reaction with H_2O. The positive ion can thus yield dihydroxybenzenes, most likely hydroquinone and catechol as main products. Disproportionation of radicals by electron transfer has also been suggested to explain recent results with several uracil derivatives.[12,13]

Similar observations have been made on phenol in a photolytic experiment[8] where multiply oxygenated radicals were also found. These radicals were ascribed to secondary reactions similar to the above, but a somewhat different reaction was proposed to account for formation of the hydroquinone. In the Ti^{III}–H_2O_2–phenol system at neutral or basic pH the conversion of the initial OH adducts to semiquinone radicals is even more efficient with only the latter spectra observed.[4] Although a direct conversion by H_2O_2 of the hydroxycyclohexadienyl radicals to semiquinone has been proposed[4] it is more likely that an indirect path is involved *via* the dihydroxy compounds as suggested here. Both the metal ions and the H_2O_2 could facilitate oxidation of the primary radicals and increase the importance of the secondary products. The radiolytic and photolytic[8] experiments show that such oxidants are not necessary for the observation of these secondary products.

Salicylic Acid. The o-carboxyphenoxyl radical has been observed with irradiated solutions of salicylic acid at all pH values. The hyperfine constants and g factor changed slightly around pH 3 (radicals II and III, Table I). This region must be the pK for the carboxyl group although the carboxyl proton splitting was not observed at the low pH region.

Secondary radicals of the semiquinone type have also been observed. As in the case of phenol these radicals are produced by oxidation of the dihydroxy compounds formed by hydroxylation of the initial compound at positions ortho and para to the hydroxyl group. This pattern of secondary reaction is maintained for the other phenols to follow. The 3-carboxy-1,2-semiquinone radical was present as a monoanion at pH 3–4 (X, Table II), its esr lines were weak at pH 7, and at pH 9–12 it was in the dianion form (IX, Table II). The 2-carboxy-1,4-semiquinone

TABLE I: Esr Parameters of Phenoxyl Radicals[a]

Radical	a_o^H	a_m^H	a_p^H	g factor
I (phenoxyl radical)	6.61 (2)	1.85 (2)	10.22	2.00461
II (o-carboxylate phenoxyl); pK ~ 3	6.39	1.84; 1.78	9.98	2.00476
III (o-carboxyl phenoxyl)	7.11	2.09; 1.23	10.20	2.00459
IV (m-carboxylate phenoxyl)	6.82; 6.56	1.83	9.99	2.00472
V (p-carboxylate phenoxyl)	6.53 (2)	1.93 (2)		2.00477
VI (3,5-dicarboxylate phenoxyl); pK	6.75 (2)		9.80	2.00481
VII (3,5-dicarboxyl phenoxyl)	6.87 (2)		9.72	2.00494
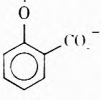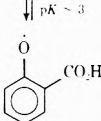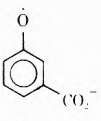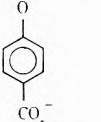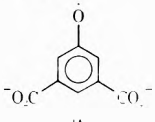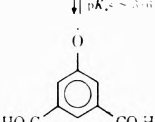
[a] Hyperfine constants are given in gauss and are accurate to ±0.03 G. The number of nuclei displaying the splitting is given in parentheses if different than one. The g factors are determined relative to the peak from the silica cell and are accurate to ±0.00005.

radical has been observed only in its dianion form at pH 9-12 (XVI, Table II). At pH 12 a fourth radical was also found and identified to be the noncarboxylated o-semiquinone, resulting apparently from the small contribution of the decarboxylation reaction by OH radicals.[14] As in the case of phenol the line intensities of the semiquinones decreased with increase in flow rate.

m-Hydroxybenzoic Acid. The 3-carboxyphenoxyl radical was observed at pH 6 and 12 (Table I). At pH 6 one additional radical was present with similar esr line intensities and was identified as the 4-carboxy-1,2-benzosemiquinone (XI, Table II). Its line intensities increased about tenfold at pH 12 and a third radical with weaker lines was found which was identified as the 3-carboxy-1,2-semiquinone (IX). These two semiquinones are produced following the hydroxylation of *m*-hydroxybenzoate at the two positions ortho to the OH group. Hydroxylation at the para position should result in radical XVI but this radical was not observed.

p-Hydroxybenzoic Acid. The phenoxyl radical V (Table I) was observed at pH 4.5-12. Only one semiquinone (XI) is expected to be formed from this compound and it was observed at pH 6-12.

5-Hydroxyisophthalic Acid. The irradiation of aqueous solution of this compound at pH 12 gave rise to an esr spectrum composed of lines of three different radicals with relative unit line intensities of 1:2.5:30. The least intense spectrum was that of the phenoxyl radical VI (Table

I). The most intense was the dicarboxy-o-semiquinone XII (Table II) and the third radical was the dicarboxy-p-semiquinone XVIII (Table II). At pH 6.6 the phenoxyl radical spectrum did not change. However, the o-semiquinone appeared in the protonated form XIII with line intensities ~50 times lower, and the p-semiquinone was not clearly observed. At this pH many additional lines were observed which can be assigned to the hydroxycyclohexadienyl radical
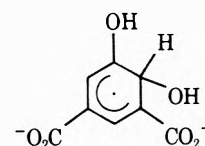
with a 23.03-G proton splitting characteristic of the H on the carbon where OH added. Four other proton splittings were observed, 2.10 and 1.64 G due to the ring protons meta to the addition site, and 0.68 and 0.46 G due to the OH protons. The g factor is 2.00313. This radical represents the only case in the present study where the initial adduct was observed. Apparently the two carboxyl groups stabilize the radical against elimination of water. This adduct was not seen either at the higher or at the lower pH values because of the acid- and base-catalyzed water elimination.

At pH 3 the phenoxyl radical showed slightly different parameters and was most probably protonated (VII, Table

TABLE II: Esr Parameters of Benzosemiquinone Radicals[a]

Radical	a_3^H	a_4^H	a_5^H	a_6^H	a_{OH}^H	g factor
			Ortho			
VIII	0.76	3.66	3.66	0.76		2.00455
IX		3.92	3.45	0.67		2.00457
X		6.59	1.55	2.89	0.57	2.00438
XI	1.25		3.26	0.73		2.00471
XII		3.00		1.22		2.00471
XIII		5.94		3.26	0.37	2.00456
XIV		5.47		3.77	0.25	2.00463
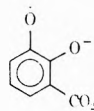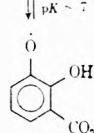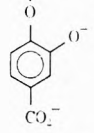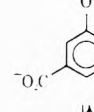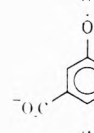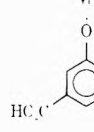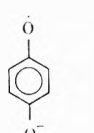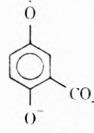
Radical	a^H (ortho a.id meta)	a_{OH}^H	g factor
	Para		
XV	2.38 (4)		2.00455
XVI	2.57; 2.20; 2.01		2.00464
XVII	4.90; 2.51; 1.35[b]	0.81	2.00455
XVIII	1.86 (2)		2.00474
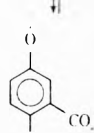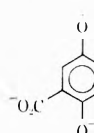
[a] See footnote to Table I. [b] It is not clear whether the radical is 3-carboxy-4-hydroxyp 1enoxyl as indicated, with 4.90- and 2.51-G splittings by the ortho protons and 1.35 G by the meta proton, or 2-carboxy-4-hydroxyphenoxyl with 4.90-G splitting by an ortho proton and 2.51 and 1.35 G by the meta protons.

TABLE III: Esr Parameters of Aminophenoxyl Radicals[a]

Radical		a_2^H	a_3^H	a_4^H	a_5^H	a_6^H	$a_{NH_2}^H$	a^N	g factor
XIX			<0.1	4.31	1.01	2.94	5.30 (2)	4.76	2.00372
XX				5.14	1.68	2.55	5.14 (2)	4.45	2.00369
XXI			<0.1	4.02		1.49	5.09 (2)	4.51	2.00389
XXII				0.49	1.27	2.30	5.80 (2)	5.08	2.00369
XXIII		2.76	1.77		1.77	2.76	5.53 (2)	5.21	2.00377
XXIV			1.62		1.44	2.94	5.22 (2)	5.07	2.00388
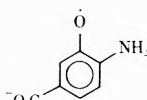
[a] See footnote to Table I.

TABLE IV: Esr Parameters of Anilino Radicals[a]

Radical		a_o^H	a_m^H	a_p^H	a_{NH}^H	a^N	g factor
XXV		6.18 (2)	2.01 (2)	8.22	12.94	7.95	2.00331
XXVI		6.27	2.10; 1.82	8.11	12.61	7.67	2.00341
XXVII		6.11 (2)	2.09 (2)		12.59	7.65	2.00344
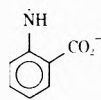
[a] See footnote to Table I.

I). The o-semiquinone radical was also completely protonated at this pH (XIV, Table II).

2,3-Dihydroxybenzoic Acid. This compound yields the semiquinones IX or X (Table II) directly by reaction with OH and elimination of water. The radicals should, therefore, be produced in full yields and their line intensities were, in fact, much higher than in the previous cases. At pH 12 the spectrum of radical IX was ~60 times more intense than that observed in the cases of salicylic and m-hydroxybenzoic acids at the same pH where radical IX is a secondary product. The monoanion X observed at pH 3.5 had a spectrum about two orders of magnitude less intense than that of the dianion (IX) at pH 12.

2,5-Dihydroxybenzoic Acid. In this case radicals XVI and XVII were observed at pH 12 and 3, respectively, and

the line intensities were comparable to those of IX and X observed with the previous compound.

o-Aminophenol. The radical observed with neutral solutions of this compound was identified as the o-aminophenoxyl XIX (Table III). Evidently it is produced following OH addition by elimination of water involving the OH and not the NH_2 group. The spectrum of XIX did not change between pH 7 and 9 but was absent at pH 11-14. It is possible that at the high pH the NH_2 protons exchange with water and cause line broadening which results in the disappearance of the spectrum.

The m-aminophenol was also examined but for reasons which are not clear at this time the spectrum had a very low signal-to-noise ratio.

2-Amino-3-hydroxybenzoic Acid. This compound be-

haves similarly to o-aminophenol and radical XX (Table III) was observed. The spectrum of this radical also disappeared at pH >12 and a different radical was found at pH 14. This radical was identified as IX and its line intensities were ~200 times smaller than those observed using 2,3-dihydroxybenzoic acid. It appears that the NH_2 group in the original compound is replaced by an OH group with a very low yield and the resulting radical only becomes observable when the spectrum of the main radical XX disappears. The replacement of NH_2 by OH to form radical IX can only take place via OH addition to the 2 position.

(3)

OH adducts at other positions

XX   IX
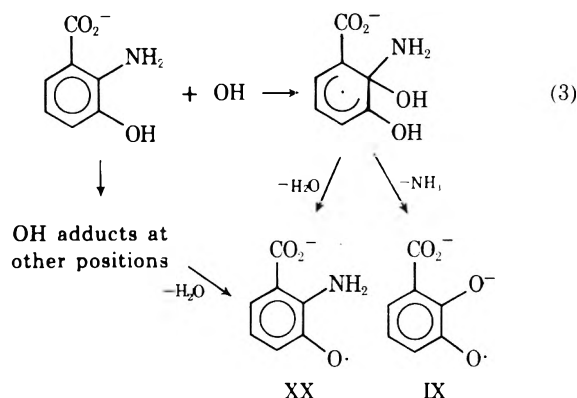
3-Amino-4-hydroxybenzenesulfonic Acid. With this compound only the phenoxyl radical (XXII, Table III) was observed. The spectrum became weaker at pH >11 and no lines were observed at pH 14.

p-Aminophenol. The p-aminophenoxyl radical (XXIII, Table III) was observed at pH 3.5-11. The intensity of the spectrum decreased at pH <6 and at pH >10. The disappearance of the spectrum at pH ~3 could be a result of protonation of NH_2 to NH_3^+ causing line broadening, and its disappearance at pH >11 is a result of exchange of the NH_2 protons as suggested above. At pH 11-14 very weak lines were observed which can be assigned to the p-benzo-semiquinone radical and, therefore, suggest a low yield of deamination similar to that outlined in reaction 3.

5-Amino-2-hydroxybenzoic Acid. The results here were similar to those with the previous amino compounds. The phenoxyl radical XXIV (Table III) was observed in neutral solutions, its spectrum disappeared in alkaline solutions, and at pH 12 only a weak spectrum of the semiquinone XVI was observed.

Aniline. The hydroxycyclohexadienyl radical produced from aniline can eliminate water only through loss of one of the NH_2 hydrogens to produce an anilino radical XXV. This mechanism has also been suggested on the basis of recent pulse radiolysis results.[15]

(4)
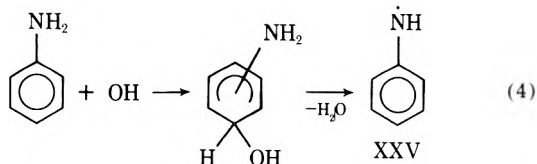
The esr spectrum observed at pH 6-12 is assigned to this radical (Table IV). Neither the initial adduct nor secondary radicals have been observed in this case. The intensity of the spectrum was weaker in neutral than in alkaline solutions probably because of the slowness of water elimination in the neutral region.

Anthranilic Acid. The o-carboxyanilino radical XXVI

(Table IV) was observed at pH 7-13.3 and again the line intensity increased in going from pH 7 to 9 to 11. No other radical was detected.

p-Aminobenzoic Acid. The p-carboxyanilino radical XXVII (Table IV) was present in the irradiated solution between pH 6 and 13. With this compound a secondary radical, with a somewhat similar line intensity, XXI (Table III) was also detected. The formation of this aminophenoxyl radical suggests that the anilino radicals, similarly to phenoxyl radicals, react with each other by electron transfer resulting in hydroxylation.

(5)
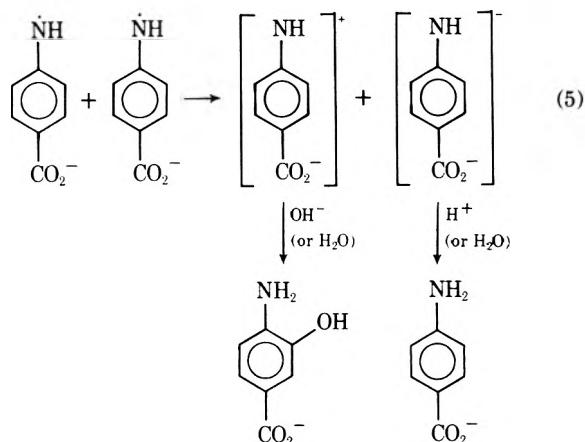
Esr Parameters

The esr parameters of the phenoxyl radical agree with those previously reported.[10] The other radicals in Table I have not been reported previously. In each case, however, the parameters for the particular positions differ little from those of the unsubstituted radical, confirming the assignments. The carboxyl group is seen to have very little effect on the spin distribution.

The hyperfine constants for the ortho and para benzo-semiquinone radical anions also agree with those reported for aqueous solution[8,16,17] and those of the derivatives follow with little change in value. The hyperfine values for the neutral semiquinone radicals X, XIII, XIV, XVII present more of a problem in that protonation can occur on either of the oxygens which, in these substituted radicals, are not equivalent. The positions of protonation as given in Table II were chosen to give better agreement with the values for the unsubstituted radicals. The structure assigned to radical XIII correlates the splittings of 3.26 and 5.94 G with those of 4.30 and 8.72 G for the ortho and para protons[16] in the unsubstituted radical. The alternative assignment is much less satisfactory in that the observed values would then have to be correlated with the values for the meta protons of 1.92 G.[16] The structures of radicals X and XIV are assigned by comparison with radical XIII.

The radicals obtained from the aminophenols clearly display hyperfine constants of an NH_2 group with equivalent protons and thus an aminophenoxyl radical is indicated. The only other possibility is a radical of the type $C_6H_5NH_2^+$ but the existence of the anilino radicals of Table IV in the form C_6H_5NH at similar pH values rules out this possibility. The most striking effect of the amino group in the aminophenoxyl radicals of Table III is to decrease the g factor from ~2.0047 to ~2.0037. This effect indicates a rather large transfer of spin density from the oxygen to the NH_2 group where the perturbation of the g factor should be less. The ring proton splittings are also

more comparable with the values for the neutral semiqui-none radicals than with those for phenoxyl. The assignment of hyperfine constants to particular protons is made by internal comparisons among the various radicals and by comparison with the neutral semiquinones. In particular the similar splittings for XIX and XX and the small value of 0.49 G for XXII clearly establish that assignment of one splitting of <0.1 G for a_3^H cf XIX is not at all unreasonable.

The anilino radicals listed in Table IV have similar hyperfine parameters to those given for the tri-*tert*-butylanilino radical observed by Atherton. *et al.*[18] The small g factor (2.0033) and relatively large nitrogen hyperfine constant seem appropriate for this type of radical. The agreement between the hyperfine constants for the three radicals in Table IV confirms the assignment to specific positions on the ring.

Exchange of the NH_2 protons of the aminophenoxyl radicals as a result of the equilibrium $\bar{R}NH_2 + OH^- \rightleftharpoons \bar{R}NH^- + HOH$ is expected to broaden the lines somewhere above pH 10.[19] The disappearance of the spectra at pH ~11 are in accord with this expectation. However, at some higher pH the lines should again narrow to give a spectrum of the radical which shows no splitting by the NH_2 protons. Although the spectrum is expected to reappear at about pH 14 no spectrum was found in the several cases where experiments were carried out near this pH. It is not clear whether the lines have not fully narrowed by pH 14 or whether the reaction, which must now involve O^- rather than OH (pK of OH = 11.9),[20] leads to a different product.

Summary

The major product of the reaction of OH with phenols is shown by the results above to be a phenoxyl radical. This product is formed *via* water elimination from an OH ad-duct of the hydroxycyclohexadienyl type but in only one case could this intermediate be detected on the time scale of the esr experiments. Observed in addition to the phenoxyl radicals were moderately intense signals of semiquinone radicals produced in secondary processes from dihydroxy compounds formed upon bimolecular reaction of the phenoxyl radicals. In the case of the aminophenols OH addition resulted mainly in the formation of aminophenoxyl radicals but a minor reaction at the site of the amino group was found to result in deamination and production of the semiquinone radical. Reaction of OH with several anilines yielded the corresponding anilino radicals.

References and Notes

(1) Supported in part by the U. S. Atomic Energy Commission.
(2) K. Eiben and R. W. Fessenden, *J. Phys. Chem.*, **75**, 1136 (1971).
(3) T. Shiga, T. Kishimoto, and E. Tomita, *J. Phys. Chem.*, **77**, 330 (1973).
(4) C. R. E. Jefcoate and R. O. C. Norman, *J. Chem. Soc. B*, 48 (1968).
(5) E. J. Land and M. Ebert, *Trans. Faraday Soc.*, **63**, 1181 (1967).
(6) G. E. Adams and B. D. Michael, *Trans. Faraday Soc.*, **63**, 1171 (1967).
(7) E. Eiben, unpublished results.
(8) M. Cocivera, M. Tomkiewicz, and A. Groen, *J. Amer. Chem. Soc.*, **94**, 6598 (1972).
(9) W. T. Dixon and R. O. C. Norman, *Proc. Chem. Soc., London*, 97 (1963); *J. Chem. Soc.*, 4857 (1964).
(10) T. J. Stone and W. A. Waters, *Proc. Chem. Soc. (London)*, 253 (1962).
(11) T. J. Stone and W. A. Waters, *J. Chem. Soc.*, 213 (1964).
(12) H. R. Haysom, J. M. Phillips, and G. Scholes, *J. Chem. Soc., Chem. Commun.*, 1082 (1972).
(13) H. Zemel and P. Neta, *Radiat. Res.*, **55**, 393 (1973).
(14) R. W. Matthews and D. F. Sangster, *J. Phys. Chem.*, **69**, 1938 (1965).
(15) H. Christensen, *Int. J. Radiat. Phys. Chem.*, **4**, 311 (1972).
(16) I. C. P. Smith and A. Carrington, *Mol. Phys.*, **12**, 439 (1967).
(17) See also other references quoted in ref 8 and 16.
(18) N. M. Atherton, E. J. Land, and G. Porter, *Trans. Faraday Soc.*, **59**, 818 (1963).
(19) G. P. Laroff and R. W. Fessenden, *J. Phys. Chem.*, **77**, 1283 (1973).
(20) J. Rabani and M. S. Matheson, *J. Phys. Chem.*, **70**, 761 (1966).

Comparative Ultrasonic Absorption Studies of Association in Solutions of Ethanol and of 2,2,2-Trifluoroethanol

R. Zana

C.N.R.S., Centre de Recherches sur les Macromolecules, Strasbourg, Cedex 67083, France (*Received October 15, 1973*)

Ultrasonic absorption measurements have been carried out on solutions of ethanol and 2,2,2-trifluoroethanol in cyclohexane, ethyl iodide, toluene, and 1,2-dichloroethane. The results indicate that the self-association of the two alcohols increases in the order 1,2-dichloroethane < toluene < ethyl iodide < cyclohexane and that association is more extensive in ethanol than in trifluoroethanol solutions.

Infrared[1] and nmr[2] studies seem to indicate that in dilute solutions ethanol is more associated than 2,2,2-trifluoroethanol. On the other hand, from the ir spectrum of trifluoroethanol it was inferred that an appreciable amount of alcohol molecules are either nonassociated or internally hydrogen bonded to fluorine.[1,3-5] More recent-ly, it was found[6] that "association constants of alkali metal and tetraalkylammonium halides in trifluoroethanol differ from those in the nearly isodielectric solvent ethanol in magnitude and in cation and anion dependence." These differences were also attributed to differences in the self-association of the two alcohols. The purpose of this note is
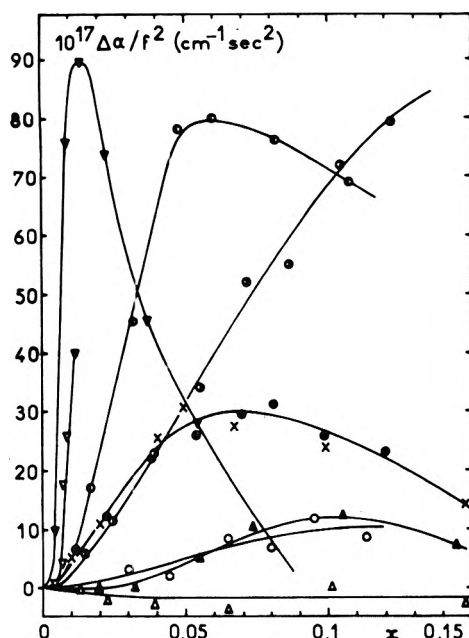
Figure 1. Variation of $\Delta\alpha/f^2$ vs. alcohol mole fraction x at 6.49 MHz for ethanol (▼) and trifluoroethanol (▽) in cyclohexane and at 9.08 MHz for ethanol in toluene (●), 1,2-dichloroethane (▲), and ethyl iodide (◐), and for trifluoroethanol in toluene (○), 1,2-dichloroethane (△), and ethyl iodide (◓). The crosses (×) are the results from ref 7 for ethanol in toluene at 2.27 MHz.

to present additional evidence based on ultrasonic absorption measurements that association is stronger in solutions of ethanol than of trifluoroethanol.

It must be first remembered that the ultrasonic absorption of solutions of normal alcohols in inert or weakly H-bonded solvents goes through a maximum when the alcohol mole fraction x is increased.[7] The maximum occurs at a mole fraction x_P generally below 0.1. In a previous work[7] we have shown this maximum to be associated with the formation of aggregates of alcohol molecules larger than dimers. For a given solvent, whichever the kinetic scheme adopted for the self-association of alcohol molecules, the lower the value of x_P the larger the association constant. Also, the stronger the interaction between alcohol and solvent molecules (through H bonds), the smaller the amplitude of the absorption maximum. These results led us to use ultrasonic absorption to compare the self-association of ethanol and trifluoroethanol in various solvents.

The measurements were performed by means of the standard pulse technique.[8] The sample of 2,2,2-trifluoroethanol was purchased from Fluka, West Germany (purity >99.5% from gas chromatography). The two alcohols were studied in solutions of cyclohexane at 6.49 MHz and of 1,2-dichloroethane, toluene, and ethyl iodide at 9.08 MHz. The results obtained at 25° are shown in Figure 1 where the quantity $\Delta\alpha/f^2$ ($\Delta\alpha = \alpha - \alpha_0$, difference between the absorption coefficients of solution and solvent, f = frequency) is plotted as a function of the alcohol mole fraction x. For the above four solvents the quantity α_0/f^2 was found to be 195, 144, 86, and 57 × 10^{-17} cm^{-1} sec^2, respectively, in good agreement with the literature values.[9] The quantity α/f^2 was also measured for trifluoroethanol and found to be (135 ± 3) × 10^{-17} cm^{-1} sec^2, in the range 6.5–21.8 MHz. The limited solubility of trifluoroethanol in cyclohexane prevented us from investigating a larger range of mole fraction.

Figure 1 shows that the curves for trifluoroethanol are always below those for ethanol. On the other hand, while all of the curves for ethanol go through a distinct maximum, those for trifluoroethanol have a sigmoidal shape in the range of mole fraction investigated. This result has important implications with regards to the extent of association of the two alcohols. Indeed, we have previously[7] pointed out that the curve $\Delta\alpha/f^2$ vs. x at low frequency ($f \ll$ relaxation frequency) is sigmoidal when association is restricted to dimerization and that it goes through a maximum when association proceeds further. From the results of other workers[9a,10-12] the frequencies used in this work (6.49 and 9.08 MHz) appear to be well below the relaxation frequencies usually found for solutions of alcohols. Also the results for ethanol in toluene at 2.27 MHz[7] and at 9.08 MHz (this work) fall on the same curve of Figure 1, within the experimental error (±3 × 10^{-17} cm^{-1} sec^2). It may thus be considered that the results shown in Figure 1 correspond to low-frequency results. The shape of the curves $\Delta\alpha/f^2$ vs. x therefore appears to indicate that in trifluoroethanol solutions associated species are mostly dimers while in ethanol solutions larger aggregates are also present.

The values of x_P (see Figure 1) indicate that the association constant of ethanol in the above four solvents increases in the order 1,2-dichloroethane < toluene < ethyl iodide < cyclohexane. The amplitude of the absorption maxima for ethanol and of the excess absorptions for trifluoroethanol also increase in the same order. These quantities are related to the enthalpy change ΔH_0 for the association process and to a first approximation the above sequence gives the ΔH_0's in the above solvents in the order of increasing absolute value.

Finally, Figure 1 shows that the measured $\Delta\alpha/f^2$ values are very small for the two alcohols in 1,2-dichloroethane, thereby indicating a smaller self-association of alcohols in this solvent. Such a result is in line with that of Guerin and Gomel[13] who reported that association constants are much smaller in 1,2-dichloroethane than in cyclohexane. This fact is likely to be due to H bonding between chloride atoms of the solvent and OH groups of alcohol molecules, which competes with the self-association of alcohol molecules.

In conclusion, the results of Figure 1 clearly show that trifluoroethanol is less associated than ethanol in the four solvents investigated in this work. This conclusion is likely to remain valid for the pure alcohols and supports the results of other workers.[1-6]

References and Notes

(1) A. Kivinen and J. Murto, Suomen Kemi. B, **40**, 6 (1967).
(2) B. Rao, P. Venkateswarlu, A. Murthy, and C. Rao, Can. J. Chem., **40**. 387 (1962).
(3) R. N. Hazeldine, J. Chem. Soc., 1757 (1953).
(4) C. Cannon and B. Stage, Spectrochim. Acta. **13**, 253 (1958).
(5) P. Krueger and H. Mettee, Can. J. Chem., **42**, 340 (1964).
(6) F. D. Evans, J. A. Nadas, and M. A. Matesich, J. Phys. Chem., **75**, 1708 (1970).
(7) J. Lang and R. Zana, Trans. Faraday Soc., **66**, 597 (1970), and references therein.
(8) J. Andreae, R. Bass, E. Heasell, and J. Lamb, Acustica. **8**, 131 (1958).
(9) (a) V. Solovyev, C. Montrose, M. Watkins, and T. Litovitz, J. Chem. Phys., **48**, 2155 (1968); (b) L. Bergmann, "Der Ultraschall," S. Hirzel Verlag, Zurich, 1954, pp 464–466; (c) E. Heasell and J. Lamb, Proc. Roy. Soc., Ser. B. **69**, 869 (1956).
(10) J. Rassing and B. N. Jensen, Acta Chim. Scand., **24**, 855 (1970).
(11) F. Garland, J. Rassing, and G. Atkinson, J. Phys. Chem., **75**, 3182 (1971).
(12) R. S. Musa and M. Eisner, J. Chem. Phys., **30**, 227 (1959).
(13) M. Guerin and M. Gomel, J. Chim. Phys. Physicochim. Biol., **70**, 953 (1973).

Temperature Dependence of Hyperfine Coupling for Copper Complexes in NaY Zeolite[1a]

J. C. Vedrine,[1b]* E. G. Derouane, and Y. Ben Taarit

Institut de Recherches sur la Catalyse, F-69100 Villeurbanne, France and Institut de Chimie del'Université, B-4000 Liège 1, Belgium (Received July 30, 1973)

Publication costs assisted by Institut de Catalyse, CNRS

The epr spectra of Cu(II) complexes with ammonia and pyridine formed in the cages of NaY zeolite have been investigated as a function of temperature. The parallel component of the Cu^{2+} hyperfine splitting decreases with temperature increasing from 4.2 to 400°K. This temperature dependence results from a vibration with sharp frequency coupling to the hyperfine splitting and it is shown to obey a law of the type $C_{\parallel}(T) = C_{\parallel}(0) - L_{\parallel}[\coth(\hbar\omega/2kT) - 1]$, where ω is the molecular Cu–N stretching vibration frequency. Far-ir data are found to be in excellent agreement with the epr determined values and support the present interpretation of the temperature effect. The Cu–N molecular vibration frequency is found to depend greatly on the interaction of the complex with its surroundings, hence giving a way of determining its location in the zeolitic structure.

Introduction

In the recent years, several epr studies have dealt with the investigation of copper-exchanged zeolites and the subsequent formation therein of complexes with ligands such as ammonia and pyridine.[2-5] In the particular case of highly exchanged $Cu^{2+}Y$ zeolites, Gallezot, *et al.*,[6] have determined the location of these complexes in the zeolitic structure by X-ray diffraction.

It is generally assumed, in the interpretation of the epr spectra of paramagnetic centers in solids, that the paramagnetic species (a transition metal ion, for example) and its surroundings (*i.e.*, the ligands) are static. However, vibrations of both the paramagnetic ion and of the lattice are present and influenced by temperature. Hence, the mean distance between the central ion and its ligands varies with temperature, producing in addition a variation in the unpaired electron wave function. With that respect, the temperature dependence of the hyperfine coupling constants and of the g tensor values of various systems has recently been studied in order to gain information on the host lattice or molecular entity dynamics. Such temperature effects have been ascribed to the mixing of excited s-like configurations into $3d^n$ configurations ground states by orbit–lattice interactions,[7-11] to lattice vibrations in surface centers,[12] and to both lattice and molecular vibrations in diatomic halogen centers.[14,15] Depending on the type of system and the nature of the effect which is considered, the hyperfine coupling may decrease[7-11,14,15] or increase[12,13] with increasing temperature.

The purpose of the present paper is to investigate the temperature dependence of the hyperfine coupling (hfs) of the Cu^{2+} ($I = 3/2$) ion in its complexes with ammonia or pyridine ligands in the particular case of weakly exchanged CuY zeolites. Our results will be discussed in terms of molecular vibration dynamics and compared to far-ir data.

This work shows in addition and in the line of very recent work, *i.e.*, laser Raman spectroscopy applied to the investigation of zeolites and adsorbed molecules,[16] that epr can provide in some cases a useful means of expanding the range of observable vibration frequencies from the rather limited and tedious region of the ir spectra (below 1200 cm^{-1}) down to about 100 cm^{-1}, a spectral region where most solids have a strong and continuous absorption background.

Experimental Section

1. Materials. Sodium ions of Linde NaY starting material were exchanged by cupric ions using suitable amounts of a dilute $CuSO_4$ solution in order to reach the desired unit cell (uc) composition. The epr measurements were performed on samples of which the uc composition, shown by chemical analysis, was $Cu_2Na_{52}(AlO_2)_{56}(SiO_2)_{136}$. Ir experiments were performed on samples with higher Cu^{2+} content ($Cu_{16}Na_{24}Y$) in order to increase the intensity of ir Cu–N band.

Prior to any absorption the epr samples were treated at 500° in oxygen, then evacuated for 10 hr to a final pressure of 10^{-5} Torr. They were further subjected to one of the following treatments: (A) the CuY catalyst was equilibrated with NH_3 at 100°, then cooled to room temperature and evacuated for 3 hr; (B) the previous sample was only briefly evacuated for several minutes instead of 3 hr; (C) the CuY zeolite was equilibrated with pyridine vapor, excess base being removed at 150° for 3 hr; (D) the initial NaY zeolite was equilibrated with a solution of $Cu(NH_3)_4(NO_3)_2$ prepared by dissolution of $Cu(NO_3)_2$ crystals in absolute ethanol and saturation with liquid ammonia. The excess solvent was removed by evacuation at room temperature.

Some epr samples were also prepared by equilibrating the untreated CuY zeolite with NH_4OH or pyridine. The data obtained were very close to those reported for samples A and C,[2a] which allowed comparison of epr and ir results.

2. Techniques. The epr spectra were recorded on a Varian E-12 epr spectrometer equipped with the E-235 large sample access cavity. Variable temperature between 77 and 400°K was achieved with the commercial E-257 accessory, the temperature being measured within 0.2°K by a Pt calibrated resistor connected to a digital thermometer (Brion-Leroux, Pyrodigit). Liquid helium temperature measurements were made with a home-made cryostat of the cold finger type.[17] Enlarged scans were performed in order to achieve maximum accuracy in the determination of the epr parameters.

For far-ir measurement the $Cu_{16}Y$ powder in its hydrated form was pressed between two CsI infrared windows and equilibrated with either NH_4OH or pyridine. The spectra were immediately recorded at room temperature on

a Perkin-Elmer Model 225 spectrophotometer between 800 and 200 cm^{-1}.

Results

The well-known polycrystalline powder spectra of Cu^{2+} ions ($I_{Cu} = 3/2$) in axially symmetrical environment exhibit four lines of low intensity associated with the $g_{\shortparallel}$ resonance and four more or less resolved lines of higher intensity associated with the $g_{\perp}$ feature.[18,19] The epr spectra of nitrogen-bonded copper complexes such as, for example, $Cu(NH_3)_4{}^{2+}$ and $Cu(C_5H_5N)_4{}^{2+}$ show in addition, on the $g_{\perp}$ resonance, superhyperfine lines due to the interaction of the unpaired electron of the Cu^{2+} ion with the neighboring nitrogen nuclei ($I = 1$). Such superhyperfine splittings may in principle occur on each parallel and perpendicular line. However, in the particular case of such complexes stabilized in zeolites the nitrogen hyperfine splittings are not resolved on the parallel features while the perpendicular lines are split into numerous superhyperfine lines of which the resolution depends on the nature of the ligands, the evacuation temperature of the initial material, and the presence or not of an excess gas or vapor phase. Consequently, the analysis of the perpendicular features is rather difficult and the temperature dependence of the perpendicular lines has not been investigated in detail, since no significant change in line shape was observed as a function of temperature.

Table I reports the temperature dependence of the magnetic parameters of various Cu(II) complexes in Y zeolite. The four parallel Cu hyperfine lines are separated by a spacing $C_{\shortparallel}$ and the $g_{\shortparallel}$ value has been measured at the middle point between the second and third ($m_I = -1/2$ and $m_I = +1/2$) components. Second-order shifts have not been taken into account in the present study as they are small for the parallel components and have no influence on the shift of the parallel components with increasing temperature. Consequently the $C_{\shortparallel}$ spacings (i.e., the Cu hyperfine splitting) have been evaluated between the first and second parallel components ($m_I = -3/2$ and $m_I = -1/2$, respectively). It is readily seen from the data reported that the $C_{\shortparallel}$ value decreases in all cases with increasing temperature, the $g_{\shortparallel}$ value being almost unaffected within experimental error.

By contrast, the g_{TP} value (which is actually the g value measured for the $g_{\perp}$ component at its turning point) shows an effect of both the temperature and the operating frequency. This observation will be discussed in more detail in a forthcoming paper; it is attributed to the presence of a high-field extra line such as those first reported by Neiman and Kivelson in the epr spectra of polycrystalline samples where both the C and g tensors were highly anisotropic.[19]

As seen from Figure 1 and Table II, the experimental variation of $C_{\shortparallel}$ with temperature can be described in all cases by the relation

$$C_{\shortparallel}(T) = C_{\shortparallel}(0) + L_{\shortparallel}[1 - \coth(\hbar\omega/2kt)] \qquad (1)$$

where $C_{\shortparallel}(T)$ and $C_{\shortparallel}(0)$ are the splittings observed respectively at the temperature T and at $0°K$, L and ω being constants for a given system, and the other symbols having their usual meanings. The full lines in Figure 1 are the theoretical variations predicted by using the values given in the captions or in Table II. The experimental points are plotted with their estimated errors. Table II also compares the vibration frequencies derived from the epr data (on samples of low Cu content) to those obtained

TABLE I: Magnetic Parameters of Cu(II) Complexes in Y Zeolite

Sample	T, °K	$C_{\shortparallel}(Cu)$, Oe (±1.0)	$g_{\shortparallel}$ (±0.003)
C:Cu(Pyr)$_4$			
	4.2	187	2.243
Pyridine	77	187	2.242
adsorbed from	91	187	2.243
the liquid on	131	187	2.241
CuY zeolite	173	183.5	2.244
	216	181	2.245
	297	176	2.244
A:Cu(NH$_3$)$_n{}^a$			
	4.2	180	2.236
Adsorption of	77	180	2.233
gaseous NH$_3$	91	179	2.238
(no excess)	131	176.5	2.240
on CuY zeolite	173	174	2.234
	203	172	2.241
	297	167	2.236
B:Cu(NH$_3$)$_n{}^a$			
	87	175	2.236
Adsorption of	124	175	2.236
gaseous NH$_3$	168	174	2.236
(in excess)	204	173	2.234
on Cu zeolite	243	172	2.233
	295	170	2.230
D:Cu(NH$_3$)$_4$			
	77	185	2.230
Impregnation of	87	184	2.233
Cu(NH$_3$)$_4{}^{2+}$	124	181	2.234
on NaY zeolite	168	178	2.235
	204	176	2.235
	243	173	2.236
	295	170	2.237

[a] Overlapping of superhyperfine lines of the $g_{\perp}$ and extraneous components does not allow to determine the number n of ammonia ligands which may be NH$_3$ pressure dependent.[20] The esr line shape for samples A and B are very similar with respect to the g values and the number and splitting of superhyperfine lines. One may then suppose that the value of n is equal for both samples.

TABLE II: Hyperfine-Coupling Data Fitted to

$\Delta C_{\shortparallel} = L_{\shortparallel}[1 - \coth(\hbar\omega/2kT)]$

Sample	$L_{\shortparallel}$, Oe	Epr, cm^{-1}	Ir, cm^{-1}
Cu(NH$_3$)$_n$ (A)	7.63	159 ± 10	
Cu(NH$_3$)$_n$ (B)	9.06	317 ± 10	311 ± 10
Cu–Py$_4$ (C)	17.0	291 ± 10	309 ± 10
Cu(NH$_3$)$_4$ (D)	3.58	70 ± 10	

from far-ir measurements (on samples of high Cu content) (Figure 2).

Similarly, as seen from Figure 3 and Table III, the experimental variation of $C_{\shortparallel}$ with temperature also obeys relatively well to the relationship

$$C(T) = C(0)(1 - BT^m) \qquad (2)$$

first proposed by Walsh, et al.,[7] at least at high temperature.

Interpretation and Discussion

1. Temperature Dependence of the Cu Hyperfine Coupling. As shown in ref 7-15, the temperature dependence of hyperfine couplings may be due to different causes.

The mixing of higher s configuration states into the ground state of Cu^{2+} ions[7-11] seems to be improbable since the 3d^9 to 3d^{8}4s^1 energy gap is known to be very large, i.e., nearly 70,000 cm^{-1}.[21] Anyway it could also be expressed in terms of coth ($\hbar\omega/2kT$).[10] Lattice vibrations may also account for such effects.[12,14] However, the NH$_3$
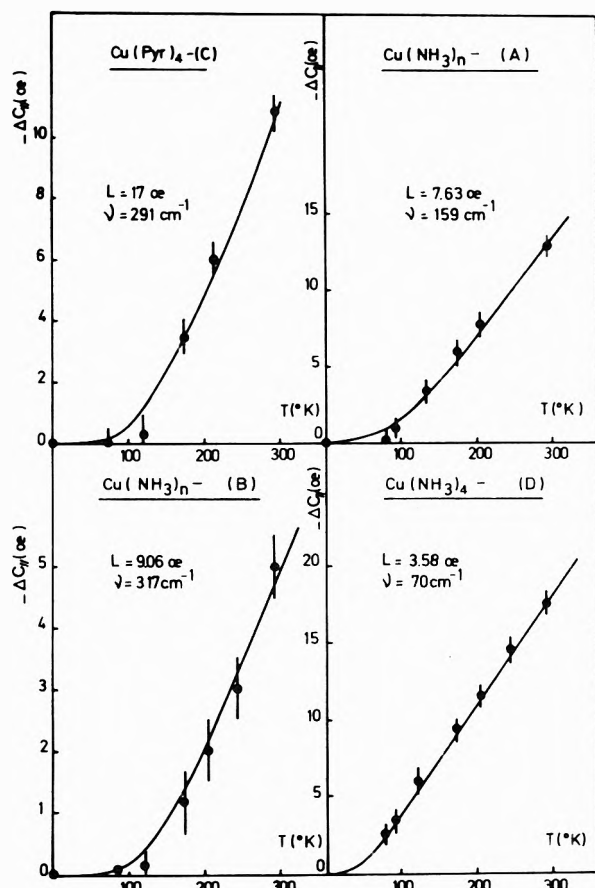
Figure 1. Temperature dependence of the esr $C_{||}$ hyperfine component of samples A, B, C, and D described in the text. The solid curves are considered to be the best fit of eq 19 to the experimental data. The straight line about each experimental point represents the experimental error.

TABLE III: Hyperfine Coupling Data Fitted to
$C(T) = C(0)(1 - BT^m)$

Sample	$C(0)$, Oe	B	m
$Cu(NH_3)_n$ (A)	180	1.59×10^{-5}	1.48
$Cu(NH_3)_n$ (B)	175	0.91×10^{-7}	2.22
$Cu-Py_4$ (C)	187	3.35×10^{-6}	1.71
$Cu(NH_3)_4$ (D)	187.5	8.27×10^{-5}	1.24

or C_5H_5N ligand molecules have been reported to stabilize the environment of the Cu^{2+} ions and to shield these ions from the perturbation produced by the environment.[3] Hence, it also seems reasonable to neglect the contribution of the zeolitic framework vibrations.

The explanation we propose considers the Cu–N molecular vibration in the complexes themselves. In the following, a few approximations will be made of which the most important are (i) the assumption that the electronic structure of the Cu complexes in the zeolite framework (either in the sodalite or supercage) can be approached by the theory of Kivelson and Neiman,[18] (ii) the anharmonicity of the Cu–N vibration potential well is neglected as our data are obtained at relatively low temperature; and (iii) it is supposed that the molecular vibration which is the most important is the in-phase breathing mode of the Cu–N₄ ring system.

Group theory allows the proper linear combination of ligand nitrogen orbitals with the copper d orbitals to form antibonding wave functions of which the form has been given by several authors.[18,22] In this scheme, and using
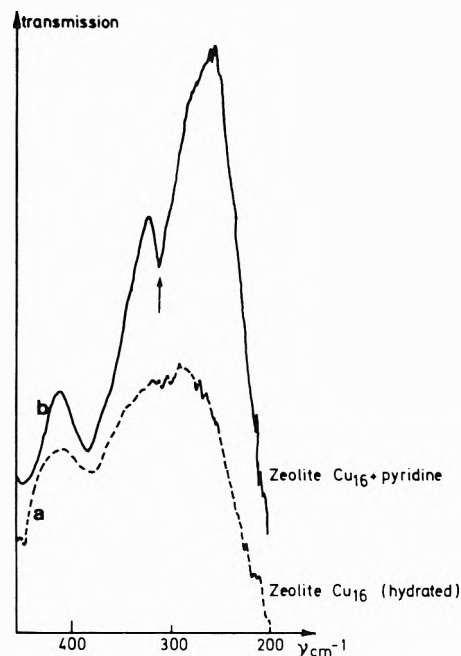
Figure 2. Far-infrared spectra (500–200 cm^{-1}) of a Cu_{16}-Y zeolite recorded at room temperature: (a) initial sample (in its hydrated form) and (b) sample contacted with pyridine.
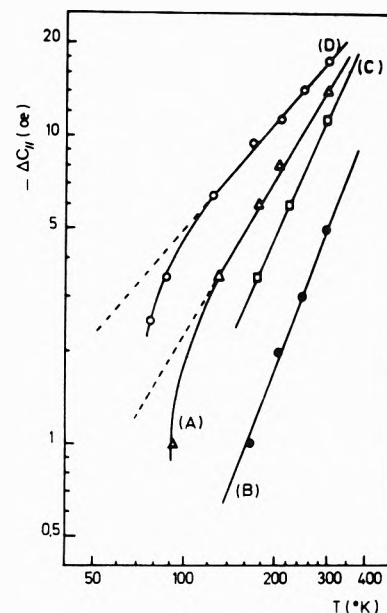
Figure 3. Temperature dependence of the $C_{||}$ hyperfine component as in Figure 1 but in log–log coordinates. The solid lines indicate the theoretical curves for B and m values of eq 20 given in Table III.

the notations of Gersmann, *et al.*, the spin Hamiltonian parameters for such an axial symmetry system are found to be[22]

$$g_{||} = 2.0023 - (8\lambda/\Delta E_{xy})[\alpha^2\beta^2 - f(\beta)] \quad (3)$$

$$g_\perp = 2.0023 - (2\lambda/\Delta E_{xz})[\alpha^2\delta^2 - g(\delta)] \quad (4)$$

$$C_{||} = P\left[-\alpha^2\left(\frac{4}{7} + K\right) - 2\lambda\alpha^2\left(\frac{4\beta^2}{\Delta E_{xy}} + \frac{3}{7}\frac{\delta^2}{\Delta E_{xz}}\right) \right] \quad (5)$$

$$C_\perp = P\left[\alpha^2\left(\frac{4}{7} - K\right) - \frac{22}{14}\frac{\lambda\alpha^2\delta^2}{\Delta E_{xz}} \right] \quad (6)$$

$$f(\beta) = \alpha\alpha'\beta^2 S + \alpha\alpha'\beta(1 - \beta^2)^{1/2}T(n)/2 \quad (7)$$

$$g(\delta) = \alpha\alpha'\delta^2 S + \alpha\alpha'\delta(1 - \delta^2)^{1/2}T(n)/2 \quad (8)$$

$$\alpha^2 + \alpha'^2 - 2\alpha\alpha'S = 1 \quad (9)$$

$$P = 2\gamma_{Cu}\beta_0\beta_n\langle d_{x^2-y^2}|R^{-3}|d_{x^2-y^2}\rangle = -0.036 \text{ cm}^{-1} \quad (10)$$

In these relations, α, β, and δ are the coefficients that characterize the ionic character of the molecular orbitals B_{1g}, B_{2g}, and E_g. The higher the value of these parameters, the higher will be the ionic bonding of the appropriate type. α^2 corresponds to the amount of mixing of the Cu $d_{x^2-y^2}$ orbital with the 4σ orbitals of the ligands. Complete ionicity corresponds to $\alpha^2 = 1$ while complete covalency leads to $\alpha^2 = 0.5$. Hence α^2 is the probability of finding the unpaired electron in the Cu $d_{x^2-y^2}$ orbital, while α'^2 is the probability of finding it in the ligands orbitals. α and α' are related by the normalization condition (9) where S is the overlap integral (0.093 for Cu–N).

β^2 and δ^2 give respectively a measure of the π in-plane (B_{2g}) and π out-of-plane (E_g) covalent bonding. For the free ion, the Fermi contact term, K, is 0.43 and the spin-orbit coupling constant is 828 cm^{-1}. $T(n)$ is an integral over the complex ligand functions (0.333).

As seen from eq 5, $C_{||}$ is proportional to the value of α^2, all the other parameters being constant if variations in β^2 and δ^2 are neglected as a first approximation. This seems reasonable as these coefficients relate to π bonding for which the overlap integral is negligible, and as the values of β and δ are nearly identical with unity.

From eq 9 and using the approximate value of α, solution of

$$\alpha \cong \alpha'S + (1 - \alpha'^2)^{1/2} \quad (11)$$

one gets

$$\alpha^2 \cong (1 - \alpha'^2)P^* + 2(1 - \alpha'^2)^{1/2}\alpha'S \quad (12)$$

Hence, the combination of eq 5 and 12 leads to

$$C_{||} = (1 - \alpha'^2)P^* + 2(1 - \alpha'^2)^{1/2}\alpha'P^*S \quad (13)$$

where

$$P^* = -P\left(\frac{4}{7} + K + \frac{8\lambda\beta^2}{\Delta E_{xy}} + \frac{6\lambda\delta^2}{7\Delta E_{xy}}\right) \quad (14)$$

Equation 13 shows clearly that the hyperfine splitting, $C_{||}$, will be a linear function of the variation of S, the overlap integral, with temperature. Indeed, one can assume that α' remains nearly constant as no change is observed in the ^{14}N superhyperfine splittings with temperature. On the other hand, it is obvious that the value of the overlap integral S will be temperature dependent. It is of the form

$$S = 2\langle d_{x^2-y^2}| - \sigma_x(R)\rangle \quad (15)$$

where R indicates that the value of S depends on the Cu–N bond length, which is in turn modulated by the Cu–N vibration. Expanding this relation into a Taylor series and calculating the expectation value of S with the wave function of the vibration leads, after averaging over all the vibrations, to matrix elements of type

$$\overline{\langle\nu|R - Ro|\nu\rangle} \text{ and } \overline{\langle\nu|(R - Ro)^2|\nu\rangle} \quad (16)$$

It has been shown by Makhanek[23] that the value of such matrix elements was proportional to

$$\coth (\hbar\omega/2kt) \quad (17)$$

ω being the frequency of the molecular vibration.

Hence it is concluded that the temperature dependence of the $C_{||}$ hyperfine coupling of Cu will fit a coth law.

Such a law can easily be derived on the basis of previous relations obtained by Assmus and Dreybrodt[15] (eq 2–5 of their paper) fitted to our case, i.e., coupling to the ^{63}Cu and ^{65}Cu nuclei and parallel orientation ($\theta = 0°$). The line shift to first order, for the m_I component, is given by

$$H(T) - H(0) = m_I^{Cu}L_{||}\left(1 - \coth \frac{\hbar\omega}{2kT}\right) \quad (18)$$

$L_{||}$ being the coefficient of the temperature dependent part of the parallel component of the C tensor.

Our hyperfine splitting being measured between the $m_I^{Cu} = -3/2$ and $m_I^{Cu} = -1/2$ components, knowing in addition that

$$C(T) = H_{-1/2}(T) - H_{-3/2}(T)$$

we get immediately the following relation

$$C(T) = C(0) + L_{||}(1 - \coth \frac{\hbar\omega}{2kT}) \quad (19)$$

which accounts for the experimental variations we observed. Hence, the value of ω measured from such a temperature dependence law can be assigned to the Cu–N molecular vibration modulation of the Cu hyperfine coupling tensor, and it is not surprising that it agrees closely with data obtained from far-ir measurements.

It is seen from eq 13 that the value of $L_{||}$ will depend on three main parameters, namely, α', ΔE_{xy}, and ΔE_{xz}. α' values are closely identical for the pyridine and ammonia complexes as seen from the ^{14}N superhyperfine splittings. Hence, as seen from eq 14, most of the effect will arise from the ΔE_{xy} term. This energy difference is known to be smaller in Cu(C$_5$H$_5$N)$_4^{2+}$ (about 16,500 cm^{-1}) than in Cu(NH$_3$)$_4^{2+}$ (near 19,000 cm^{-1}).[22] Hence, we would predict from eq 13 and 14 a higher $L_{||}$ value in the case of the pyridine complex. This is in agreement with the experimental data shown in Table II.

Small variations are also observed for the $L_{||}$ values measured for the various Cu(NH$_3$)$_n$-Y complexes. They are attributed to the environment effect which may change and shift the relative orbital energies by nonnegligible amounts.

Our trial to fit the data to expression

$$C(T) = C(0)(1 - BT^m) \quad (20)$$

first proposed by Walsh, et al.,[7] led us to find m values in the range 1.24–2.22 as shown from the log–log plot of Figure 2 and Table III. Such values are reasonable as the theory predicts $m = 2$ for $T < \theta_D/5$ decreasing to $m = 1$ for $T > 2\theta_D$. Hence, the higher the value of θ_D, the higher will be the value of m between 1 and 2. As the value of θ_D should be proportional to some frequency ω_D (by definition of the Debye temperature), it is not surprising at all that the higher m values are observed for the systems characterized by the higher Cu–N vibration frequencies. In fact a strict parallelism is observed as seen from the comparison of the data collected in Tables II (column 3) and III (column 4).

No detailed informations on the complexes dynamics can be obtained from such a plot although it seems to support qualitatively the general sequence of effect magnitude determined from the first treatment.

2. Localization of the Complexes. As shown before, it is the molecular vibration of the Cu–N bond which is the determining factor for the temperature dependence of the hyperfine coupling of the Cu^{2+} ion in such complexes.

Several interesting features can be pointed out by examining the data summarized in Table II.

Let us discuss first the case of the $Cu(NH_3)_n$ complexes. The sample obtained by contacting a sample of low copper content with ammonia is characterized by a smaller Cu-N vibration frequency than when an excess ammonia is present (samples A and B, respectively). It has been shown recently[6] that, in Y zeolites, the Cu^{2+} ion migrates from the S_I site (center of the hexagonal prism) towards the sodalite cage upon adsorption of ammonia. When a large excess of ammonia is introduced further migration of the cations can occur, for example, toward the supercage. If the ammonia-copper complex is located in the sodalite cage (sample A, no excess NH_3), taking a Cu-N bond length of the order of 1.9 Å and a N-H bond length of about 1 Å, the distance between the NH_3 protons and the oxygen ions of the sodalite cage is short enough, so that hydrogen bonding may occur. Such hydrogen bonds would weaken the Cu-N bond and consequently decrease the corresponding vibration frequency which is proportional to the square root of the Cu-N force constant. On the other hand, when such complexes are located in the supercage (sample B, excess NH_3), because of their relatively large free diameter (nearly 13 Å), hydrogen bonding will be negligible, i.e., the vibration frequency will be much higher and closer to that of the free complex (the Cu-N vibration frequency for the $Cu(NH_3)_4Cl_2$ free complex is 420 cm^{-1}). In order to ascertain these points, we tried to introduce in the NaY zeolitic material a $Cu(NH_3)_4(NO_3)_2$ complex in a convenient amount, since such a complex is obviously unable to enter the sodalite cage. The frequency evaluated from the epr data is much smaller than what one would expect for a tetraamine complex in the supercage for hexacoordination of copper by ligands, thereby weakening the Cu-N bond and decreasing the frequency. One may then suggest that this is due to steric hinderance effects in the supercages because of the too high copper complex concentration.

When such complexes are located in the supercages, and this is obviously the case in the presence of pyridine ligands, an excellent agreement is observed between the epr and ir data, and as observed previously the Cu-N frequency is close to that of the unperturbed complexes. No data are available on the Cu-N vibration frequency of $Cu(Py)_4^{2+}$ complexes in solution (i.e., free entities) although it is known that the Cu-N vibration frequency in both $CuCl_2Py_2$ and $CuBr_2Py_2$ is of 268 cm^{-1}. Note here that both the epr and ir determined Cu-N vibration frequencies for the pyridine and ammonia complexes in the supercages are very close to each other, which confirms our previous discussion. Hence, from such an interpretation of the temperature effect, one can also ascertain the location of these complexes and get some information on their interaction with the environment.

Conclusions

The accurate determination and the detailed analysis of the temperature dependence of the hyperfine coupling of the copper nucleus in Cu(II) paramagnetic complexes may give useful informations on the dynamics of such complexes, namely, on the Cu-N molecular vibration frequencies.

The purpose of such studies is mainly to expand the range of the observable spectrum from the rather limited region of the ir spectra as most of the substrates show very strong ir bands below 1200 cm^{-1}. The good agreement we found between the epr data and the far-ir results is very encouraging for the application of epr spectroscopy to such systems, when far-ir fails to give informations on surface species either because of the practically total absorption of the support or because of the low concentration in surface species.

The interaction between the adsorbed complex and the framework has been shown to affect strongly the central ion-ligand molecule vibration frequency. Consequently, the location of the complex in the zeolitic structure can be ascertained.

Note also that because of the temperature dependence they can show the hfs and g tensors parameters are not as reliable as they appear at first for the assignment of the location and electronic sturcture of such complexes.

References and Notes

(1) (a) This research was supported by grants from FRFC (Belgium) and from the "Accords Culturels Franco-Belges." (b) Institut de Recherches sur la Catalyse, Villeurbanne, France.
(2) (a) C. Naccache and Y. Ben Taarit, *Chem. Phys. Lett.*, **11**, 11 (1971); (b) J. Turkevich, Y. Ono, and J. Soria, *J. Catal.*, **25**, 44 (1972).
(3) E. F. Vansant and J. H. Lunsford, *J. Phys. Chem.*, **76**, 2860 (1972).
(4) I. R. Leith and H. F. Leach, *Proc. Roy. Soc., Ser. A*, **330**, 247 (1972).
(5) Y. Yamada, *Bull. Chem. Soc. Jap.*, **45**, 60 (1972).
(6) P. Gallezot, Y. Ben Taarit, and B. Imelik, *J. Catal.*, **26**, 295 (1972).
(7) W. M. Walsh, T. Jeener, and N. Bloembergen, *Phys. Rev. A*, **139**, 1338 (1965).
(8) E. Simanek and R. Orbach, *Phys. Rev.*, **145**, 191 (1966).
(9) F. Holuj, S. M. Quick, and M. Rosen, *Phys. Rev. B*, **6**, 3169 (1972).
(10) L. A. Bylinskaya, B. M. Kozyrev, and I. V. Ovchinnikov, *Proc. Colloq. AMPERE (At. Mol. Etud. Radio Elec.)*, **16**, 1000 (1971).
(11) L. A. Bylinskaya and I. V. Ovchinnikov, *Zh. Neorg. Khim.*, **17**, 3237 (1972).
(12) A. J. Tench, *Surface Sci.*, **25**, 625 (1971).
(13) L. A. Bylinskaya, B. M. Kosyrev, and I. V. Ovchinnikov, *Dokl. Akad. Nauk. SSSR*, **196**, 625 (1971).
(14) W. Dreybrodt, *Phys. Status Solidi*, **21**, 99 (1967).
(15) W. Assmus and W. Dreybrodt, *Phys. Status Solidi*, **34**, 183 (1969).
(16) C. L. Angell, *J. Phys. Chem.*, **77**, 222 (1973).
(17) The help of Dr. R. Blanpain in designing the liquid helium system is deeply acknowledged. Blueprints are available on request.
(18) D. Kivelson and R. Neiman, *J. Chem. Phys.*, **35**, 149 (1961).
(19) R. Neiman and D. Kivelson, *J. Chem. Phys.*, **35**, 156 (1961).
(20) K. I. Zamaraev and N. N. Thikomirova, *J. Struct. Chem. (USSR)*, **5**, 691 (1964).
(21) A. Abragam and M. H. L. Pryce, *Proc. Roy. Soc., Ser. A*, **230**, 206 (1951).
(22) H. R. Gersmann and J. D. Swalen, *J. Chem. Phys.*, **36**, 3221 (1962).
(23) A. G. Makhanek, *Sov. Phys., Opt. Spectrosc.*, **11**, 6 (1961).

Metachromasia of Basic Dyes Induced by Mercuric Chloride. II

M. K. Pal[*1] and Sudhir Kumar Ash

Department of Chemistry, Faculty of Science, University of Kalyani, Kalyani, West Bengal, India

(Received June 25, 1973; Revised Manuscript Received December 17, 1973)

Mercuric chloride induces strong metachromasia in dyes like thionine, methylene blue, and acridine orange, and weak metachromasia in crystal violet. Metachromasia induced by mercuric chloride is, in general, more hypsochromic and hypochromic than that induced by polyanions. Capri blue and rhodamine 6G are nonmetachromatic in the presence of mercuric chloride as they are in the presence of polyanions. This shows that the chromotropic ability of mercuric chloride is similar to that of a polyanion. Changes in the ultraviolet spectra of the dyes caused by the presence of mercuric chloride are similar to the change in the spectrum of aniline caused by mercuric chloride. This is interpreted in terms of the formation of mercuric chloride-dye complexes by donation of the lone pair of electrons of the terminal amino group of the dye to the mercury. A model has been proposed for the metachromatic dye-mercuric chloride compounds involving tetra- and hexacoordinated mercury.

Introduction

Some cationic dyes in the presence of suitable polyanions undergo spectral shift. This phenomenon is called metachromasia, and the substrates inducing such spectral changes in the dyes are called chromotropes. The polyanionic nature of the chromotropes capable of inducing metachromatic color changes in some cationic dyes and the aggregation theory of metachromasia are well established.[2-4] It has been shown[4,5] that a chromotrope need not be a macromolecule and compounds like ammonium molybdate, sodium inositol hexaphosphate, and inositol hexasulfate can act as chromotropes. Sylven[6] pointed out that some simple inorganic salts like potassium iodide, thiocyanate, tungstate, mercuric chloride, etc., give metachromatic red precipitates with dyes such as methylene blue, but the metachromasia induced by these salts could not be studied in detail because of the precipitation always associated with it. Recently, Pal and Ash[7] (part I of the series) have developed conditions where metachromasia is induced by mercuric chloride in dyes such as methylene blue and toluidine blue in solution without immediate precipitation and they could study such metachromasia spectrophotometrically. The authors observed that metachromasia of these dyes induced by mercuric chloride is more hypsochromic (blue shifted) as well as hypochromic (with reduced absorbance) than that induced by a strong chromotrope such as heparin.[8] The stoichiometry of the compounds formed between mercuric chloride and methylene blue varies between 2 dye:1 $HgCl_2$ and 1 dye:1 $HgCl_2$. The authors proposed a model of dye-mercuric chloride compound which explains the metachromatic spectral shift of the dye by aggregation theory.

The purpose of the present report is to describe the extension of this work to include several other metachromatic and nonmetachromatic dyes. Ultraviolet spectra of the dye-mercuric chloride systems were also studied to probe into the nature of the bond between dye and mercuric chloride. Also, ultraviolet spectra of aniline and mercuric chloride were studied and the results show that aniline forms a charge-transfer complex with mercuric chloride, probably by donating the lone pair electrons of its nitrogen since anilinium ion fails to form such complexes.

Experimental Section

Thionine (E. Merck), acridine orange (E.M.,), methylene blue (E.M., medicinal), crystal violet (E.M.,), capri blue (National Aniline Division, U.S.A.), mercuric chloride (E.M.,), potassium thiocyanate (E.M.,), and potassium iodide (E.M.,) have been used.

Absorbance was measured with a Beckmann DU-2 spectrophotometer with 1.0-cm silica cells. To estimate the amounts of dye, mercuric ion, or chloride left in the supernatant solution, methylene blue (10^{-2} to 10^{-3} M) and mercuric chloride (10^{-2} to 10^{-3} M) were mixed in different ratios and allowed to stand for 1 hr allowing the dye-mercuric chloride compound to precipitate. After removal of the precipitate by centrifugation, the chloride in the supernatant liquid was determined by conductometric titration with standard $AgNO_3$ solution.

It has been found that addition of a large excess of mercuric chloride to a dye solution of the order of 10^{-5} M does not give immediate precipitation at least for several hours, though under such conditions the dye still has its metachromatic color similar to that induced by a lesser amount of mercuric chloride. Thus the ultraviolet and visible spectra of the dye-mercuric chloride system could be recorded directly with the solution of the dyes in the presence of excess mercuric chloride.

Results

Figure 1A shows the absorption spectrum of 4.00×10^{-5} M thionine in water. Thionine is a metachromatic dye, and metachromasia of this dye is induced by the addition of chromotropes like chondroitin sulfate, heparin, etc.[9] Figure 1B gives the absorption spectrum of 4.00×10^{-5} M thionine in the presence of 6.2×10^{-4} N heparin. The absorption peak of the dye is shifted from 595 to 510 nm; as usual, the metachromatic spectral shift of the dye is hypsochromic as well as hypochromic. Figure 1C shows the absorption spectrum of 4.00×10^{-5} M thionine in the presence of 0.29 M mercuric chloride. It is obvious that metachromasia of thionine induced by mercuric chloride is more hypsochromic (blue shifted) and hypochromic (with reduced absorbance) than that induced by heparin.
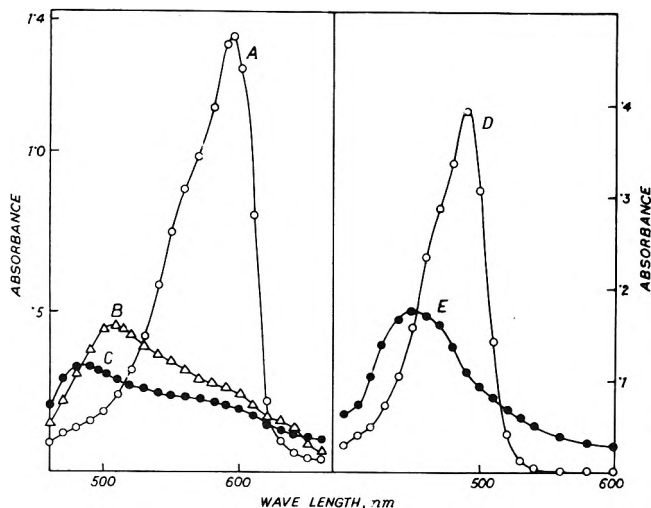
Figure 1. Absorption spectra of 4.00 × 10⁻⁵ M thionine in water (A), in presence of 6.2 × 10⁻⁴ N heparin (B), in presence of 0.29 M mercuric chloride (C), and absorption spectra of 1.34 × 10⁻⁵ M acridine orange in water (D) and in presence of 0.27 M mercuric chloride (E).

Figure 3. Absorption spectra of 1.34 × 10⁻⁵ M rhodamine 6G in water (A), in presence of 0.27 M mercuric chloride (B), and absorption spectra of 1.34 × 10⁻⁵ M capri blue in water (C) and in 0.27 M mercuric chloride (D).
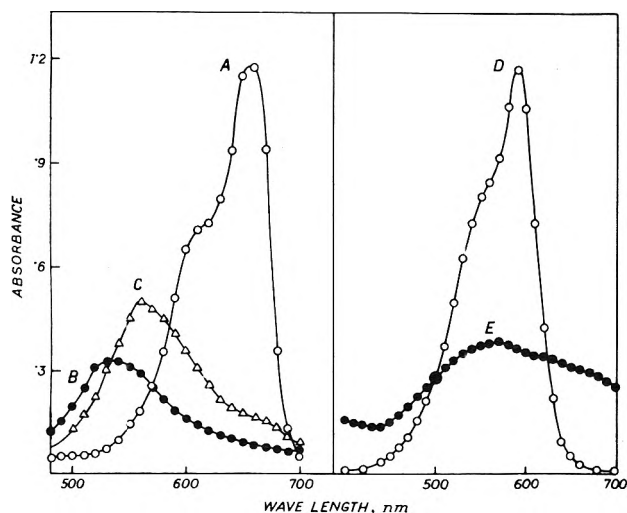
Figure 2. Absorption spectra of 1.99 × 10⁻⁵ M methylene blue in water (A), in presence of 0.25 M mercuric chloride (B), in 2.00 × 10⁻⁴ N heparin (C), and absorption spectra of 1.34 × 10⁻⁵ M crystal violet in water (D) and in presence of 0.27 M mercuric chloride (E).

This is the usual observation with all the other metachromatic dyes studied in this work except crystal violet. Figures 1D and 1E give the absorption spectra of 1.34 × 10⁻⁵ M acridine orange in water and in 0.27 M mercuric chloride, respectively. It is apparent that mercuric chloride also induces strong metachromasia in acridine orange.

Figures 2A, 2B, and 2C present the absorption spectra of 1.99 × 10⁻⁵ M methylene blue in water, in 0.25 M mercuric chloride, and in 2.00 × 10⁻⁴ N heparin, respectively. It is apparent that mercuric chloride induces more hypsochromic and hypochromic metachromasia in this dye also. This is also obvious visually because the metachromatic color of methylene blue induced by mercuric chloride is red in color unlike the purple color that is observed with chondroitin sulfate or heparin as the chromotrope. Curves 2D and 2E show the absorption spectra of 1.34 × 10⁻⁵ M crystal violet in water and in 0.27 M mercuric chloride, respectively. It is interesting to note that mercuric chloride fails to induce a sharp metachromatic band in this

dye; rather a flat absorption band is observed around 565 nm, which is the position of the so-called β band of this dye as observed, as a shoulder, in the absorption spectra of the dye itself (Figure 2D); in this respect mercuric chloride resembles iodine.[10] It should be pointed out that crystal violet gives a sharp metachromatic band at 510 nm in the presence of chromotropes such as chondroitin sulfate.[11]

Figure 3 shows the effects of the presence of mercuric chloride on the visible spectra of the two nonmetachromatic dyes rhodamine 6G and capri blue. Polyanionic chromotropes such as chondroitin sulfate and heparin cannot induce metachromasia in these two dyes though the fluorescence of rhodamine 6G is quenched in the presence of chromotropes. It is apparent from curves 3A and 3B that mercuric chloride does not induce metachromatic spectral shift in rhodamine 6G; rather the absorption peak of the dye is reduced to a great extent. In this respect the effect of mercuric chloride on the visible spectrum of rhodamine 6G is qualitatively similar to the effect of heparin.[12] Mercuric chloride does not have any effect on the visible spectrum of the dye capri blue as is apparent from the identical nature of the absorption spectra of the dye in the presence and absence of mercuric chloride (Figures 3C and 3D).

Sylven[6] reported formation of a red precipitate when potassium thiocyanate or potassium iodide were added to aqueous methylene blue solutions. We could not find any condition either where potassium iodide would give metachromasia with methylene blue in solution without precipitation; curve B in Figure 4 shows the reflectance spectrum of the precipitate that is obtained on mixing methylene blue and potassium iodide. It is apparent that the spectrum has a sharp metachromatic peak at 565 nm. Potassium thiocyanate in large excess, however, gives metachromasia with the dye in solution without immediate precipitation; curve C in Figure 4 gives the absorption spectrum of 1.09 × 10⁻⁵ M methylene blue in the presence of 0.09 M thiocyanate. Curve A is the spectrum of the dye alone.

Figure 5 shows the ultraviolet absorption spectrum of aniline and anilinium ion both in the presence and absence of mercuric chloride. Aniline in water gives a peak
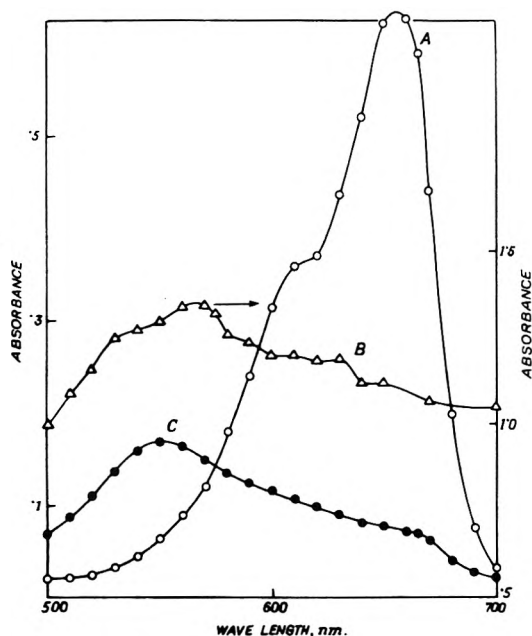
Figure 4. Absorption spectra of 1.09 × 10⁻⁵ M methylene blue in water (A), in presence of 0.09 M potassium thiocyanate (C), and reflectance spectrum of the precipitate that is obtained on mixing methylene blue and potassium iodide (B).
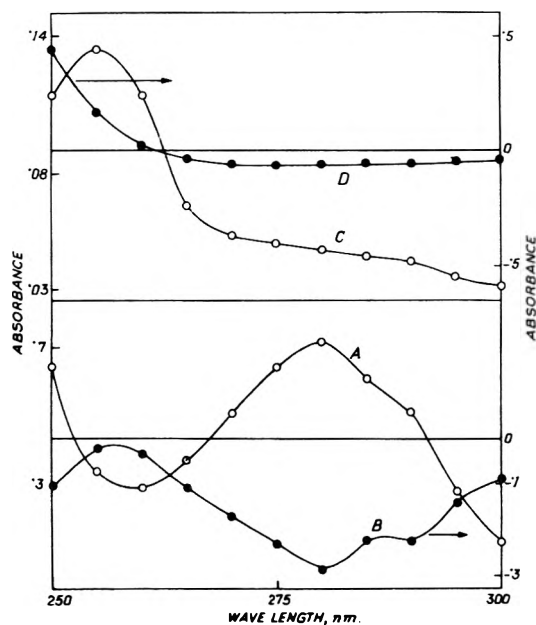
Figure 5. Ultraviolet absorption spectra of 5.45 × 10⁻⁴ M aniline in water (A) in 0.10 N HCl (C), and the difference between the experimental and the calculated spectra of a mixture of 5.45 × 10⁻⁴ M aniline and 3.98 × 10⁻³ M mercuric chloride in water (B) and in 0.10 N HCl (D). (For details see text.)

at 280 nm (curve A) corresponding to the $\pi \rightarrow \pi^*$ transition. In aniline the lone pair orbital of nitrogen is π in character and is in conjugation with the aromatic ring π system. This conjugation in turn causes the shift of the lowest $\pi \rightarrow \pi^*$ transition from 255 nm (as in benzene) to 280 nm. In the presence of HCl aniline forms the anilinium ion and thereby losses the lone pair electron of nitrogen; as a result the band at 280 nm is missing and the absorption is shifted to 255 nm (Figure 5C).

Figure 5B depicts the difference between the experimental spectrum of a mixture of 5.45 × 10⁻⁴ M aniline and
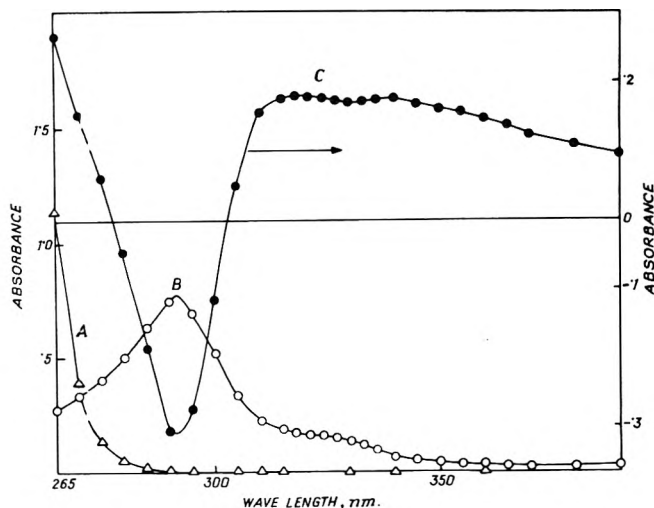
Figure 6. Ultraviolet absorption spectra of 0.26 M mercuric chloride in water (A), of 2.00 × 10⁻⁵ M methylene blue in water (B), and the difference of the spectra of a mixture of 2.00 × 10⁻⁵ M methylene blue and 0.26 M mercuric chloride in water and the sum of curves A and B (C).

3.98 × 10⁻³ M mercuric chloride in water and the added individual spectra of aniline and mercuric chloride at similar concentrations. It is apparent that the difference curve has a minimum at the absorption band of aniline and a peak at 255 nm, which is the position of the absorption band of anilinium ion. This indicates that in the complex formation between aniline and mercuric chloride the nitrogen lone pair electrons of aniline are involved. A similar difference spectrum with anilinium ion in place of aniline is rather flat around 280 nm.

Figure 6 shows the ultraviolet absorption spectra of 0.26 M mercuric chloride in water (A) and 2.00 × 10⁻⁵ M methylene blue in water (B). Curve C is the difference spectrum of a mixture of 2.00 × 10⁻⁵ M methylene blue and 0.26 M mercuric chloride in water and the sum of curves A and B. The difference curve C has a minimum at the position of the ultraviolet absorption maximum of methylene blue; in this respect the observation resembles the aniline–mercuric chloride system (Figure 5). Figure 7 depicts a similar set of curves obtained with the dyes acridine orange and rhodamine 6G. In both cases the respective difference curves have minima at the ultraviolet absorption peaks of the dyes and two maxima at shorter and longer wave lengths from these minima.

Figure 8 shows a similar set of curves from the dyes crystal violet and capri blue. It is interesting to note that the nature of these curves is quite similar for the metachromatic and nonmetachromatic dyes. This indicates that all these dyes studied interact with mercuric chloride in a similar way and the metachromatic spectral shifts that are observed with some dyes only are the aftereffects of this interaction.

The ultraviolet spectrum of the methylene blue–potassium thiocyanate system was also studied and the nature of the difference curve obtained is quite different from the methylene blue–mercuric chloride system, indicating that the nature of interactions of methylene blue–thiocyanate is different from that with mercuric chloride.

Figure 9 is the proposed model for the methylene blue–mercuric chloride system having 1:1 stoichiometry. The nature of the bond between methylene blue and mercuric chloride is of the donor–acceptor type, the lone pair elec-
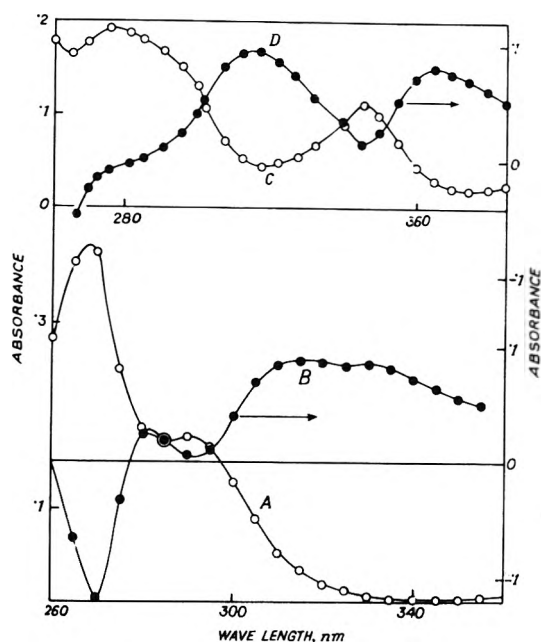
Figure 7. Ultraviolet absorption spectra of 1.34 × 10^{-5} M acridine orange in water (A), of 1.34 × 10^{-5} M rhodamine 6G in water (C), and the difference of the spectra of a mixture of 1.34 × 10^{-5} M acridine orange and 0.27 M mercuric chloride in water and the sum of curve A and the curve of 0.27 M mercuric chloride in water (B); the difference of the spectra of 1.34 × 10^{-5} M rhodamine 6G and 0.27 M mercuric chloride in water and the sum of curve C and the curve obtained with 0.27 M mercuric chloride in water (D).
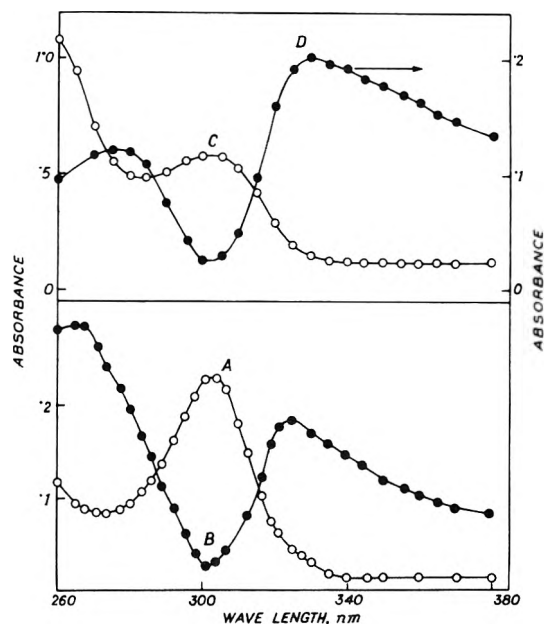
Figure 8. Ultraviolet absorption spectra of 1.34 × 10^{-5} M crystal violet in water (A), of 1.34 × 10^{-5} M capri blue in water (C), and the difference of the spectra of 1.34 × 10^{-5} M crystal violet and 0.14 M mercuric chloride in water and the sum of curve A and the curve obtained with 0.14 M mercuric chloride in water (B); the difference of the spectra of 1.34 × 10^{-5} M capri blue and 0.27 M mercuric chloride in water and the sum of curve C and the curve obtained with 0.27 M mercuric chloride in water (D).

tron of the terminal nitrogen of the dye being partly donated to mercury. In such a model the dye molecules will suffer effective aggregation which causes the metachromatic spectral shift.

Discussion

When polyanions in solution are mixed with cationic dyes, they form compounds primarily by electrostatic bonds, but only a few cationic dyes undergo a metachromatic spectral shift. Even when those dyes which are capable of metachromatic spectral shifts are mixed with a large excess of the polyanions, the dyes give their normal (orthochromatic) spectra. In the presence of a large excess of the polyanions the dye cations remain bound to the polyanions by means of electrostatic bonds, but only at remote sites so that no interactions between the bound dye cations are possible; this dye–dye interaction, thought to be hydrophobic in nature,[8,12-14] is accepted to be responsible for the metachromatic spectral shift. With this accepted part of the theory of metachromatic spectral shift it is to be pointed out that no satisfactory quantum mechanical interpretation for this spectral shift has been proposed yet which can explain why only some cationic dyes are metachromatic. Both acridine orange and rhodamine 6G undergo quenching of their fluorescence due to aggregation on their binding to the adjacent sites of polyanions,[12] but only acridine orange gives a metachromatic spectral shift under such a condition. Our aim in this paper is not to suggest any quantum mechanical interpretation of the metachromatic spectral shift in general but to interpret the metachromatic spectral shift caused by mercuric chloride in some of the dyes which are known to be metachromatic in the presence of polyanionic chromotropes.
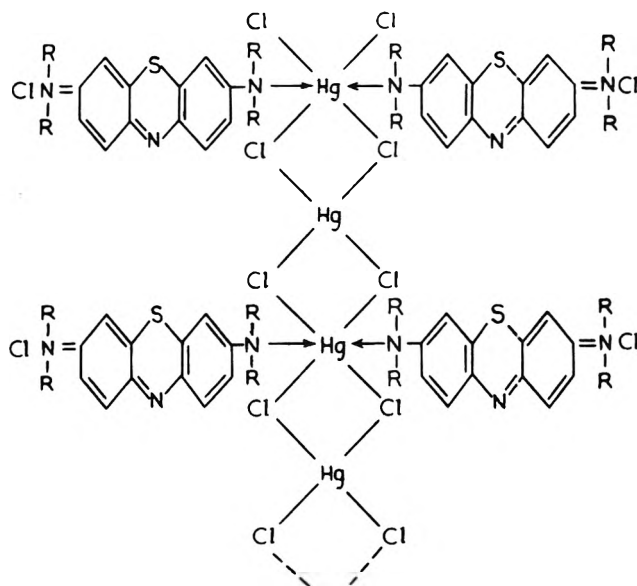
Figure 9. Proposed model for the methylene blue–mercuric chloride system having 1:1 stoichiometry of the dye and mercuric chloride.

It is apparent from Figures 1 and 2 that the well studied metachromatic dyes thionine, methylene blue, and acridine orange are strongly metachromatic in the presence of mercuric chloride; crystal violet fails to give a sharp metachromatic band in the presence of mercuric chloride though it has its α band depressed and enhanced absorbance in the shorter wavelength region of its visible absorption spectrum. The nonmetachromatic dyes capri blue and rhodamine 6G are also nonmetachromatic in the presence of mercuric chloride (Figure 3). This shows that the

chromotropic ability of mercuric chloride is similar to the chromotropic abilities of the polyanions. It seems that the chromotropes are responsible for creating suitable conditions for the dyes to be metachromatic, but it is absolutely the nature of the dyes which determines whether they will undergo metachromatic spectral shifts under such conditions.

Mercuric chloride is known to form tetra- and hexacoordinated complexes. Mercuric chloride also forms donor-acceptor complexes with the amines having 1 amine:1 $HgCl_2$ and 2 amines:1 $HgCl_2$ compositions.[15] It has been reported by us before[7] that methylene blue also forms such complexes with mercuric chloride. On analyzing the chloride content of the supernatant liquid after the mercuric chloride–methylene blue compounds had been centrifuged out, we have come to the conclusion that methylene blue chloride, and not the methylene blue cation, forms complexes with mercuric chloride. It is apparent from the structures of all the dyes studied in this report that all of them have terminal amino or substituted amino groups with lone pairs of electrons on the nitrogens. In this respect dye molecules are similar to aniline or N-substituted anilines. It is apparent from Figure 5A that aniline has an absorption band at 280 nm which is known to be due to $\pi \rightarrow \pi^*$ transition with the lone-pair nitrogen electrons conjugating with the aromatic ring π system. The difference curve B in the same figure has a minimum at 280 nm, indicating that in formation of the complex of aniline with mercuric chloride the lone-pair electrons of the amino nitrogen are involved. Anilinium chloride lacks the nitrogen lone-pair electrons and hence the peak at 280 nm; neither does it give any well defined difference curve in the presence of mercuric chloride (Figures 5C and D). It is apparent from Figures 6-8 that the shapes of the difference curves of the dyes methylene blue, acridine orange, crystal violet, capri blue, and rhodamine 6G in presence of mercuric chloride are similar to the difference curves obtained with aniline in place of the dyes, the difference curves have minima at the ultraviolet absorption peaks of the respective dyes and the higher values for the differences at the shorter and longer wavelengths of these minima. It is possible therefore that mercuric chloride and the dye molecules form complexes with the lone-pair electrons of the terminal amino groups being donated to mercury. The possibility of the involvement of ring nitrogen or sulfur atoms in methylene blue is excluded in view of the fact that dyes like crystal violet, which do not have such atoms, also form similar complexes with mercuric chloride. Even if formation of the mercury complex occurs through the partial donation of the lone pair electrons of the ring nitrogen or ring sulfur in some dyes, the overall picture of the aggregation mechanism will not be affected; only the orientation of the stacked dye molecules relative to the Hg–Hg chain would be changed.

Figure 9 shows the model for the metachromatic dye–mercuric chloride complex that we propose remembering the following facts: (i) mercuric chloride can exist as tetra- and hexacoordinated complex; (ii) methylene blue–mercuric chloride complexes have stoichiometry of one mole of methylene blue chloride per mole of mercuric chloride in presence of excess of mercuric chloride; and (iii) the dye molecules are bonded to mercuric chloride by partial donation of the lone pair electrons of the terminal nitrogen. In such a model interactions between the adja-

cent dye molecules bound at either site of the tetracoordinated mercuric chloride chain will possibly be similar to the interactions between dye cations bound to polyanion chromotropes.[2] These dye-dye interactions will cause the hypsochromic spectral shift in potentially metachromatic dyes. Formation of such a complex as represented in Figure 9 will be facilitated and stabilized by the fact that the metachromatic dye molecules prefer to occupy adjacent sites so that dye-dye interactions are possible. This is supported by the finding of Pal and Schubert[8,16] that when a moderate excess of chromotropes is added to a limited amount of potentially metachromatic dyes, the dye cations saturate as many chromotrope molecules as possible leaving the others almost free of dye. In the presence of excess dye the methylene blue–mercuric chloride complex has the composition 2 methylene blue chloride–1 mercuric chloride;[7] in such a complex all the Hg will be hexacoordinated instead of alternate Hg as shown in Figure 9. In such a case the dye molecules will suffer steric hindrance and will prefer to coordinate with alternate Hg when excess mercuric chloride is present. This happens also with polyanions of high charge density; in the presence of excess dye all the anionic sites of such a chromotrope are occupied by the dye cations but when excess chromotropes are available the dye cations occupy anionic sites with some gaps and exhibit metachromasia.[17] In the model in Figure 9, the aggregation of the dye molecules could be extended indefinitely as indicated by the dotted lines at one end, though the stacking of about ten dye molecules could be sufficient for the metachromatic spectral shift observed.[5] The position of the chlorine directly attached to the nitrogen of each dye is not precise and is meant to indicate that each dye cation will be associated with its chloride ion in the mercuric chloride–dye chloride complex, as is expected from the composition of the complex.

References and Notes

(1) Address correspondence to this author at Max-Planck-Institut für Biophysikalische Chemie, Post Box 968, D 3400 Göttingen-Nikolausberg, West Germany.
(2) D. F. Bradley and M. D. Wolf, *Proc. Nat. Acad. Sci. U. S.*, **45**, 944 (1959).
(3) (a) M. K. Pal and M. Schubert, *J. Phys. Chem.*, **67**, 1821 (1963); (b) K. K. Rohatgi and G. S. Singhal, *ibid.*, **70**, 1695 (1966).
(4) M. K. Pal and M. Biswas, *Histochemie*, **27**, 36 (1971).
(5) N. C. Mandal, B. B. Biswas, and M. K. Pal, *Histochemie*, **18**, 202 (1969).
(6) B. Sylven, *Quart. J. Microsc. Sci.*, **95**, 327 (1954).
(7) M. K. Pal and S. K. Ash, *Histochemie*, **34**, 135 (1973).
(8) M. K. Pal and M. Schubert, *J. Amer. Chem. Soc.*, **84**, 4384 (1962).
(9) L. Michaelis and S. Granick, *J. Amer. Chem. Soc.*, **67**, 1212 (1945).
(10) M. K. Pal, unpublished work.
(11) M. K. Pal and M. Schubert, *J. Histochem. Cytochem.*, **9**, 673 (1961).
(12) M. K. Pal, *Histochemie*, **5**, 24 (1965).
(13) P. Mukherjee and A. K. Ghosh, *J. Phys. Chem.*, **67**, 193 (1963).
(14) M. K. Pal and M. Chowdhury, *Makromol. Chem.*, **133**, 151 (1970).
(15) D. Grdenic, *Quart. Rev. Chem. Soc.*, **19**, 303 (1965).
(16) M. K. Pal and M. Schubert, *J. Phys. Chem.*, **65**, 872 (1961).
(17) M. K. Pal and M. Biswas, to be submitted for publication.

Intersystem Crossing Efficiency in the Hexacyanochromate(III) Ion

N. Sabbatini,[*1a] **M. A. Scandola,**[1a] **and V. Balzani**[1b]

Istituto Chimico dell 'Università, Centro di Studio sulla Fotochimica e Reattività degli Stati Eccitati dei Composti di Coordinazione del CNR, Ferrara, Italy, and Istituto Chimico "G. Ciamician" dell Universita. Bologna, Italy (Received September 24, 1973)

The direct and Ru(dipy)$_3^{2+}$-sensitized phosphorescence intensities of Cr(CN)$_6^{3-}$ in dimethylformamide solutions have been measured under the same experimental conditions. The results obtained show that the η_{isc}^{Cr}/γ ratio (η_{isc}^{Cr} = efficiency of the $^4T_{2g} \longrightarrow {}^2E_g$ intersystem crossing of Cr(CN)$_6^{3-}$; γ = fraction of Ru(dipy)$_3^{2+}$ triplets that are quenched by Cr(CN)$_6^{3-}$ via electronic energy transfer to give Cr(CN)$_6^{3-}$ (^2E_g)) is equal to 0.5. An upper limiting value of 0.5 has thus been established for η_{isc}^{Cr}. The comparison between these results and those previously obtained by other authors for the benzil–Cr(CN)$_6^{3-}$ system suggests that 0.5 is the actual value for η_{isc}^{Cr}.

Introduction

The photochemical[2-4] and photophysical[3-6] properties of Cr(III) complexes have been the object of extensive investigations in the past decade. The most recent information obtained from sensitization[7] and quenching[8-12] techniques have shown that the immediate precursor to photochemistry is the lowest quartet excited state ($^4T_{2g}$ in octahedral symmetry) and that the lowest doublet (^2E_g) is unreactive, at least in the case of Cr(CN)$_6^{3-}$.[7,11] For obtaining a complete rationalization concerning the fate of the exciting photons, the relative importance of the various steps which depopulate the excited states should be known. The efficiency[13] of the $^4T_{2g} \longrightarrow {}^2E_g$ intersystem crossing is one of the most important quantities in this regard. However, it is very difficult to measure.

In principle, the efficiency of intersystem crossing from the lowest spin-allowed excited state to the lowest spin-forbidden one can be evaluated in several ways, i.e.: (i) using the compound of interest as a donor in electronic energy transfer experiments and then measuring some quantities of the donor[14] or of the acceptor;[15-17] (ii) measuring the relative decrease in the fluorescence yield and the relative increase in the yield of the spin-forbidden state due to the introduction of a "heavy-atom" species to a solution of the compound of interest;[18] (iii) measuring the phosphorescence excitation spectrum over wavelength regions covering both the spin-allowed and the spin-forbidden absorption bands;[19,20] (iv) measuring the lifetime of the phosphorescing state and the quantum yield of phosphorescence, and evaluating the rate constant of the phosphorescence emission from the absorption spectrum;[21] (v) using the compound of interest as an acceptor and then comparing the direct and sensitized phosphorescence quantum yields. The first three methods, which have been extensively used for organic molecules,[22,23] are impracticable for most coordination compounds and especially for the Cr(III) complexes. The fourth method was used for some Cr(III) complexes in glassy solutions at low temperature,[21] but it is limited by the difficulty in evaluating the rate constant of the phosphorescence emission from the absorption spectrum. It should also be noted that Cr(III) complexes in liquid solutions usually do not emit strongly enough to allow a reliable measurement of the phosphorescence quantum yield. Thus, method v seems to be the more convenient one since, in practice, it only involves the measuring of phosphorescence intensities

and not quantum yields. However, it can only give, in principle, upper limiting values for the intersystem crossing efficiency (see Discussion). In the present paper, we will report the application of this last method to Cr(CN)$_6^{3-}$, using Ru(dipy)$_3^{2+}$ as a sensitizer. Since Cr(CN)$_6^{3-}$ does not emit in aqueous solution, the experiments were carried out in dimethylformamide.

Experimental Section

Materials. Tetra-n-butylammonium hexacyanochromate(III) was prepared from K$_3$[Cr(CN)$_6$] and tetra-n-butylammonium bromide, as indicated by Wasgestian.[11] Tris(2,2'-dipyridyl)ruthenium(II) chloride was synthetized and purified according to Burstall's indications.[24] Baker Instra-Analyzed dimethylformamide (DMF) was used.

Apparatus. Emission intensity measurements were performed with a Perkin-Elmer MPF-2A spectrofluorimeter, using an HTV R446F photomultiplier tube. Lifetimes were measured[25] with the apparatus described by Hutton, et al.[26]

Procedures. All of the experiments were carried out at 25°. The solutions were deaerated by bubbling pure nitrogen. Emission measurements were accomplished using the right angle illumination method. The emission intensities of both Ru(dipy)$_3^{2+}$ and Cr(CN)$_6^{3-}$ were measured on the same solutions. The Cr(CN)$_6^{3-}$ direct and sensitized emissions were measured using the same instrumental conditions, on solutions having the same absorbance (0.390) at the excitation wavelength (450 nm).

Results

When deaerated DMF solutions containing 7.8×10^{-2} M Cr(CN)$_6^{3-}$ were irradiated with 450-nm light, the well known[11] $^2E_g \longrightarrow {}^4A_{2g}$ phosphorescence was observed. Quantitative measurements of this emission were carried out at 796 nm (instead of at λ_{max} 805 nm[11]) because of the limitations in our equipment. In agreement with Wasgestian's observations,[11] we found that the Cr(CN)$_6^{3-}$ phosphorescence emission was strongly quenched by oxygen and water. We have also found that the addition of tetra-n-butylammonium bromide (up to 10^{-2} M) does not cause any quenching effect.

When deaerated DMF solutions containing 3.57×10^{-5} M Ru(dipy)$_3^{2+}$ were irradiated with 450-nm light, an emission was observed with maximum at 605 nm and lifetime ~0.8 μsec. These values are very similar to those
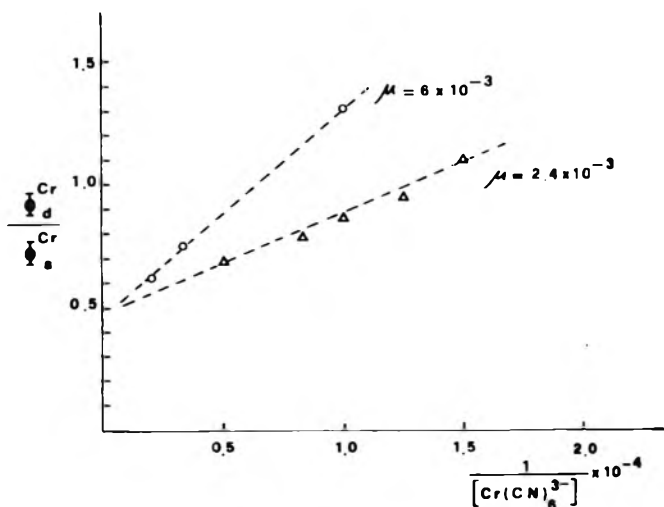
Figure 1. Plot of $\Phi_d{}^{Cr}/\Phi_s{}^{Cr}$ vs. $1/[Cr(CN)_6{}^{3-}]$ at two different ionic strengths. $\Phi_d{}^{Cr}$ and $\Phi_s{}^{Cr}$ are the quantum yields of the direct and Ru(dipy)$_3{}^{2+}$-sensitized phosphorescence emission of Cr(CN)$_6{}^{3-}$.
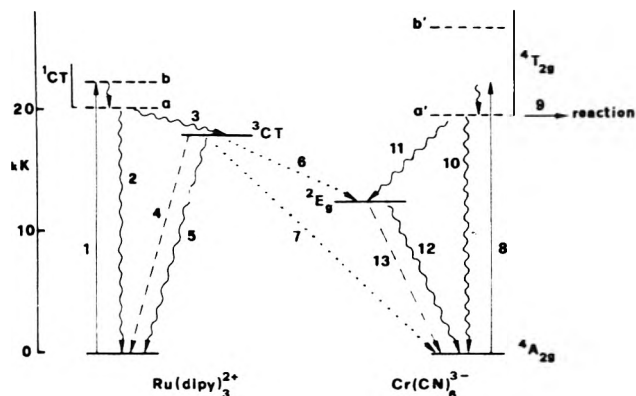
Figure 2. Energy level diagram for the Ru(dipy)$_3{}^{2+}$–Cr(CN)$_6{}^{3-}$ system. Solid arrows, absorptions or reaction; dashed arrows, radiative deactivations; dotted arrows, intermolecular quenchings; waved arrows, radiationless deactivations; b and b′ are the energies of the absorption maxima and, a and a′ are the presumable zero vibrational levels of the two excited states.

found for Ru(dipy)$_3{}^{2+}$ in aqueous solutions (λ_{max} 605 nm, $\tau \sim 0.7$ μsec),[27] so that the observed emission may be identified as the phosphorescence from the lowest charge-transfer (CT) triplet. The addition of tetra-n-butylammonium bromide (up to 10^{-2} M) did not cause any quenching of the Ru(dipy)$_3{}^{2+}$ phosphorescence.

Upon 450-nm excitation of deaerated DMF solutions containing 3.57×10^{-5} M Ru(dipy)$_3{}^{2+}$ and 6.7×10^{-5} to 1×10^{-3} M Cr(CN)$_6{}^{3-}$, both the 605 and 796-nm emissions were obtained. Since more than 99.8% of the incident light was absorbed by Ru(dipy)$_3{}^{2+}$, the observed emission at 796 nm had to be the Ru(dipy)$_3{}^{2+}$-sensitized phosphorescence of Cr(CN)$_6{}^{3-}$. Under the above conditions, the Stern-Volmer plot for the quenching of the Ru(dipy)$_3{}^{2+}$ phosphorescence by Cr(CN)$_6{}^{3-}$ showed a negative curvature as happens for aqueous solutions,[28] and which is to be attributed to the change in the ionic strength. For a solution containing 1×10^{-4} M Cr(CN)$_6{}^{3-}$, the lifetime of the Ru(dipy)$_3{}^{2+}$ phosphorescence was quenched in parallel with the phosphorescence intensity. This shows that there was no appreciable static

quenching under our conditions (see also ref 28). The Stern-Volmer quenching constant for the lowest quencher concentration used was higher than 4×10^{-4} M^{-1}. Since the lifetime of Ru(dipy)$_3{}^{2+}$ triplet was about 0.8 μsec under the experimental conditions used, the quenching constant k_q had to be $\geq 5 \times 10^{10}$ M^{-1} sec^{-1}, in fair agreement with the diffusion-controlled rate constant (7.6×10^{10} M^{-1} sec^{-1}) calculated from the Debye equation for ionic species.[29] When the Cr(CN)$_6{}^{3-}$ concentration was varied from 6.7×10^{-5} to 2×10^{-4} M and the ionic strength of the solutions was kept constant (2.4×10^{-3}) by adding tetra-n-butylammonium bromide, the Stern-Volmer plot was linear and its slope was lower than the initial slope of the Stern-Volmer plot obtained without adding tetra-n-butylammonium bromide. For a constant ionic strength of 6×10^{-3}, a linear Stern-Volmer plot, having an even lower slope, was obtained up to 5×10^{-4} M Cr(CN)$_6{}^{3-}$.

The intensity of the Ru(dipy)$_3{}^{2+}$-sensitized Cr(CN)$_6{}^{3-}$ emission was found to increase with increasing Cr(CN)$_6{}^{3-}$ concentration. For solutions at constant ionic strength (2.4×10^{-3} or 6×10^{-3}), linear plots were obtained for $1/I_s$ against $1/[Cr(CN)_6{}^{3-}]$ (see also Figure 1). Since the absorbance of the solutions as well as all of the other experimental conditions (see Experimental Section) were exactly the same for the experiments of direct and sensitized emission of Cr(CN)$_6{}^{3-}$, the ratio between the intensities of the direct and sensitized emission had to be equal to the ratio between the respective quantum yields. The $\Phi_d{}^{Cr}/\Phi_s{}^{Cr}$ vs. $1/[Cr]$ plots (where [Cr] is the concentration of Cr(CN)$_6{}^{3-}$) for the two different ionic strengths used are shown in Figure 1. Although the values are somewhat scattered because of the experimental errors, which are mostly due to the low sensitivity of our equipment at 796 nm, it seems safe to assume that both lines extrapolate to 0.5 for $\Phi_d{}^{Cr}/\Phi_s{}^{Cr}$, when $1/[Cr] = 0$.

Discussion

The energy level diagram for the Ru(dipy)$_3{}^{2+}$–Cr(CN)$_6{}^{3-}$ system is shown in Figure 2. For the sake of simplicity, the Cr(CN)$_6{}^{3-}$ $^2T_{2g}$ and $^2T_{1g}$ excited states, which lie between $^4T_{2g}$ and ^2E_g,[30] are not shown since they are assumed to deactivate rapidly to the lowest excited state of the same multiplicity, ^2E_g. The "back intersystem crossing" from ^2E_g to $^4T_{2g}$ is known[31] to be negligible for Cr(CN)$_6{}^{3-}$ and thus, it was not considered. According to the results of a recent investigation,[7] it is assumed that the energy transfer from Ru(dipy)$_3{}^{2+}$ (^{3}CT) to Cr(CN)$_6{}^{3-}$ cannot lead to Cr(CN)$_6{}^{3-}$ ($^4T_{2g}$). Since the Ru(dipy)$_3{}^{2+}$ phosphorescence intensity and lifetime are quenched in parallel (see Results), the donor state is definitely individualized as the lowest triplet, ^{3}CT. Back energy transfer from Cr(CN)$_6{}^{3-}$ (^2E_g) to Ru(dipy)$_3{}^{2+}$ (^{3}CT) cannot occur in view of the very high energy gap existing between the levels involved. Finally, note that step 6 (Figure 2) represents the electronic energy transfer from Ru(dipy)$_3{}^{2+}$ to Cr(CN)$_6{}^{3-}$ leading to the ^2E_g excited state, whereas step 7 represents a possible quenching of Ru(dipy)$_3{}^{2-}$ (^{3}CT) by Cr(CN)$_6{}^{3-}$ without concomitant formation of electronically excited Cr(CN)$_6{}^{3-}$.

On the basis of the scheme shown in Figure 2, the quantum yield of the Cr(CN)$_6{}^{3-}$ direct and sensitized phosphorescence can be written as

$$\Phi_d{}^{Cr} = \frac{k_{11}}{k_9 + k_{10} + k_{11}} \frac{k_{13}}{k_{12} + k_{13}} \tag{1}$$

$$\Phi_s{}^{Cr} = \frac{k_3}{k_2 + k_3} \frac{k_6[Cr]}{k_4 + k_5 + (k_6 + k_7)[Cr]} \frac{k_{13}}{k_{12} + k_{13}} \quad (2)$$

We can now define the following quantities: efficiency of the $^1CT \longrightarrow {}^3CT$ intersystem crossing of $Ru(dipy)_3^{2+}$

$$\eta_{isc}{}^{Ru} = \frac{k_3}{k_2 + k_3} \quad (3)$$

efficiency of the $^4T_{2g} \longrightarrow {}^2E_g$ intersystem crossing of $Cr(CN)_6^{3-}$

$$\eta_{isc}{}^{Cr} = \frac{k_{11}}{k_9 + k_{10} + k_{11}} \quad (4)$$

efficiency of the electronic energy transfer from $Ru(dipy)_3^{2+}$ (^3CT) to $Cr(CN)_6^{3-}$, yielding $Cr(CN)_6^{3-}$ (^2E_g)

$$\gamma = \frac{k_6}{k_6 + k_7} \quad (5)$$

Taking into account the above equations, the $\Phi_d{}^{Cr}/\Phi_s{}^{Cr}$ ratio may be written as

$$\frac{\Phi_d{}^{Cr}}{\Phi_s{}^{Cr}} = \frac{\eta_{isc}{}^{Cr}}{\eta_{isc}{}^{Ru}}\left(\frac{1}{\gamma} + \frac{k_4 + k_5}{k_6} \frac{1}{[Cr]}\right) \quad (6)$$

Considering that $\eta_{isc}{}^{Ru} = 1$,[27,32] and calling $(\Phi_s{}^{Cr})_0$ the value of $\Phi_s{}^{Cr}$ for $1/[Cr] = 0$, one obtains

$$\frac{\Phi_d{}^{Cr}}{(\Phi_s{}^{Cr})_0} = \frac{\eta_{isc}{}^{Cr}}{\gamma} \quad (7)$$

Both $\eta_{isc}{}^{Cr}$ and γ can vary between 0 and 1. Thus, eq 7 allows us to establish a new upper limiting value for $\eta_{isc}{}^{Cr}$ or for γ, depending on whether $\Phi_d{}^{Cr}/(\Phi_s{}^{Cr})_0$ is lower or higher than unity. In our case, this ratio is about 0.5 (Figure 1), so that $\eta_{isc}{}^{Cr}$ must be equal to or lower than 0.5. Such an upper limiting value is about one order of magnitude higher than the value determined for glassy solutions, using method iv[21] (see Introduction). The quantum yield of the $Cr(CN)_6^{3-}$ photosolvation, which occurs from $^4T_{2g}$,[7,11] is equal to 0.085 upon direct excitation to $^4T_{2g}$ under our experimental conditions.[11] This means that the efficiency of step 9, Figure 2, is 0.085. Since the efficiency of step 11 is ≤ 0.5, it follows that an important deactivation path for $^4T_{2g}$ is the internal conversion to $^4A_{2g}$ (step 10, $\eta_{10} > 0.4$).

The comparison of our results with those previously obtained by Binet, et al.,[33] on the benzil-$Cr(CN)_6^{3-}$ system in methanol-water at $-113°$ is very interesting. For such a system, a γ value of about 0.2 was reported on the assumption that $\eta_{isc}{}^{Cr}$ was 0.1. This means that the experimental $\eta_{isc}{}^{Cr}/\gamma$ value found by Binet, et al., was about 0.5, i.e., practically equal to that found in this paper for the $Ru(dipy)_3^{2+}-Cr(CN)_6^{3-}$ system. Since benzil and $Ru(dipy)_3^{2+}$ are very different donors from both a "chemical" and a "physical" point of view it seems that the γ values of the two systems can only be equal if each of

them is unity. In such a hypothesis, the value of $\eta_{isc}{}^{Cr}$ is definitely established as about 0.5.[34]

References and Notes

(1) (a) Istituto Chimico dell'Università, Centro di Studio sulla Fotochimica e Reattività degli Stati Eccitati dei Composti di Coordinazione del CNR, Ferrara, Italy; (b) Istituto Chimico "G. Ciamician" dell'Università, Bologna, Italy.

(2) V. Balzani and V. Carassiti, "Photochemistry of Coordination Compounds," Academic Press, London, 1970.

(3) G. B. Porter, S. N. Chen, H. L. Schläfer, and H. Gausmann, *Theoret. Chim. Acta*, **20**, 81 (1971).

(4) P. D. Fleischauer, A. W. Adamson, and G. Sartori, *Progr. Inorg. Chem.*, **17**, 1 (1972).

(5) L. S. Forster, *Transition Metal Chem.*, **5**, 1 (1969).

(6) P. D. Fleischauer and P. Fleischauer, *Chem. Rev.*, **70**, 199 (1970).

(7) N. Sabbatini and V. Balzani, *J. Amer. Chem. Soc.*, **94**, 7587 (1972); N. Sabbatini, M. A. Scandola, and V. Carassiti, *J. Phys. Chem.*, **77**, 1307 (1973).

(8) S. N. Chen and G. B. Porter, *Chem. Phys. Lett.*, **6**, 41 (1970).

(9) N. A. P. Kane-Maguire and C. H. Langford, *J. Amer. Chem Soc.*, **94**, 2125 (1972).

(10) C. H. Langford and L. Tipping, *Can. J. Chem.*, **50**, 887 (1972).

(11) H. F. Wasgestian, *J. Phys. Chem.*, **76**, 1947 (1972).

(12) R. Ballardini, G. Varani, H. F. Wasgestian, L. Moggi, and V. Balzani, *J. Phys. Chem.*, **77**, 2947 (1973).

(13) The nomenclature used in this paper conforms to the terms and definitions suggested by G. B. Porter, V. Balzani, and L. Moggi, *Advan. Photochem.*, in press.

(14) R. E. Kellogg and R. G. Bennett, *J. Chem. Phys.*, **41**, 3042 (1964).

(15) R. B. Cundall, F. J. Fletcher, and D. G. Milne, *Trans. Faraday Soc.*, **60**, 1146 (1964).

(16) A. A. Lamola and G. S. Hammond, *J. Chem. Phys.*, **43**, 2129 (1965).

(17) C. A. Parker and T. A. Joyce, *Chem. Commun.*, **108**, 234 (1966); *Photochem. Photobiol.*, **6**, 395 (1967).

(18) A. R. Horrocks, T. Medinger, and F. Wilkinson, *Chem. Commun.*, 452 (1965); T. Medinger and F. Wilkinson, *Trans. Faraday Soc.*, **61**, 620 (1965).

(19) R. F. Borkman and D. R. Kearns, *Chem. Commun.*, 446 (1966).

(20) J. N. Demas and G. A. Crosby, *J. Amer. Chem. Soc.*, **92**, 7262 (1970).

(21) K. K. Chatterjee and L. S. Forster, *Spectrochim. Acta*, **20**, 1603 (1964); **21**, 213 (1965).

(22) A. A. Lamola, "Energy Transfer and Organic Photochemistry," A. A. Lamola and N. J. Turro, Ed., Interscience, New York, N. Y., 1969, p 17.

(23) C. A. Parker, "Photoluminescence of Solutions," Elsevier, Amsterdam, 1968.

(24) F. H. Burstall, *J. Chem. Soc.*, 173 (1936).

(25) Courtesy of Dr. Bolletta, University of Bologna.

(26) A. Hutton, G. Giro, S. Dellonte, and A. Breccia, *Int. J. Radiat. Phys. Chem.*, **5**, 387 (1973).

(27) J. N. Demas and A. W. Adamson, *J. Amer. Chem. Soc.*, **93**, 1800 (1971).

(28) F. Bolletta, M. Maestri, and L. Moggi, *J. Phys. Chem.*, **77**, 861 (1973).

(29) P. Debye, *Trans. Electrochem. Soc.*, **82**, 265 (1942).

(30) H. Gausmann and H. L. Schläfer, *J. Chem. Phys.*, **48**, 4056 (1968).

(31) F. Diomedi Camassei and L. S. Forster, *J. Chem. Phys.*, **50**, 2603 (1969).

(32) J. N. Demas and G. A. Crosby, *J. Amer. Chem. Soc.*, **93**, 2841 (1971).

(33) D. J. Binet, E. L. Goldberg, and L. S. Forster, *J. Phys. Chem.*, **72**, 3017 (1968).

(34) A recent reinvestigation of the excitation spectrum of Cr^{3+} in $K_3[Co(CN)_6]$ has shown that the previously reported value[31] of $\eta_{isc}{}^{Cr}$ is in error and that this quantity is in reality much higher than 0.1 (private communication from Professor L. S. Forster).

Three-Element Reaction Coordinates. III. Barrier Curvature Effects on Intramolecular Kinetic Isotope Effects

Joseph H. Keller and Peter E. Yankwich*

Noyes Laboratory of Chemistry, University of Illinois, Urbana, Illinois 61801   (Received August 6, 1973)

A study has been made of the influence of curvature of the potential barrier on heavy-atom kinetic isotope effects calculated for reaction coordinates comprising nonzero displacements in three internal coordinates. Increase in barrier curvature may increase or decrease the isotope effect. In addition to the expected dependence on transition state bond force constants and geometry, reaction coordinate composition, and barrier curvature, the results depend in most cases on the specific selection of minor transition state force constants (required to meet the input restrictions of the method). Although chemically and physically reasonable choices of certain transition state parameters result in drastic reduction in redundancy of the output, further reduction depends on the development of criteria for assigning the barrier curvature and of rationale for selection of off-diagonal force constants.

I. Introduction

General methods have been developed[1] for forcing an arbitrary vibration of an activated complex to be a normal mode with preselected frequency. Earlier,[2] reaction coordinates were surveyed which consisted of as many as four internal coordinate displacements, subject to the condition that the associated eigenvalue λ_1 be zero; $\lambda_1 = 4\pi^2(\nu_1^*)^2$. In that study, a technique was developed which guaranteed there would be but one nonpositive transition state eigenvalue; this required certain restrictions on the signs and sizes of the elements of the associated eigenvector, *i.e.*, there were limitations on the "composition" of the reaction coordinate.

The first paper in this series[3] reported a method of broad applicability in which limitations on reaction coordinate composition were only those necessary to prevent generation of a second nongenuine vibration at the transition state. The case studied was the use of three-element reaction coordinates in calculations of the ^{13}C intramolecular kinetic isotope effect in the decomposition of oxalic acid; a flat potential barrier, $\nu_1^* = 0$, was assumed. The second report[4] dealing with reaction coordinate eigenvectors consisting of three nonzero elements was a study of the intermolecular hydrogen isotope effect on the rate of the reaction $H + Cl_2$; the transition state was nonlinear (which made displacements in *every* internal coordinate contribute to the reaction coordinate) and effects of moderate barrier curvature ($\nu_1^* = 400i$ cm^{-1}) were investigated.

This paper reports an extension of the earlier techniques to the situation where the nonzero elements of the reaction coordinate eigenvector are fewer than the number of internal coordinates defined and where both the reaction coordinate eigenvector *and* eigenvalue are treated as parameters; barrier curvature is raised to the equivalent of $\nu_1^* = 2000i$ cm^{-1}. To facilitate comparisons with the earlier extensive study,[3] calculations were carried out for three-element reaction coordinates in the ^{13}C intramolecular kinetic isotope effect in the decomposition of oxalic acid. While generally applicable to heavy-atom kinetic isotope effects, some of the conclusions fail in the case of hydrogen and other very light elements, *vide infra*.

II. Methods and Formalisms

A. The Vibration Problem. Assumptions of structures and force fields for reactant (^{0}) and transition (*) states provide the input for construction of the matrices G and F described by Wilson.[5] Where S is the matrix of internal coordinate displacements, Q the normal coordinates, L, the matrix of eigenvectors, E the identity matrix, λ the eigenvalue, and Λ the diagonal matrix of eigenvalues, we have available, after solution of the vibrational secular equation in the form

$$|GF - E\lambda| = 0 \qquad (1)$$

the relations

$$GFL = L\Lambda \qquad (2)$$

and

$$S = LQ \qquad (3)$$

Reasonable estimates may be made of the elements of G^* by analogy to G^0 for various apparently related structures. Because geometric effects on kinetic isotope effects are small, G^* is often made the same as G^0 (and such identity will be assumed here).

A variety of techniques has been employed in the construction of F^*. Its relationship to F^0 (whose elements F_{ij}^0 are usually known or estimated with relative ease and accuracy) depends on numerous assumptions concerning differences in bonding, the method for achieving the single nongenuine vibration characteristic of the transition state, and sometimes on related preselections of one or more eigenvalues and eigenvectors. Here, such preselection is limited to the eigenvalue, $\lambda_1 \equiv \lambda_1^*$, and eigenvector, $L_1 \equiv L_1^*$ associated with the reaction coordinate in the transition state of one of the two isotopic species. [To simplify later equations, we shall drop the superscripts (^{0}) and (*) *unless* they are required to avoid confusion. Most of our discussion will deal with transition state properties.] The technique examined in this paper uses in F^* diagonal elements F_{ii}^* identical with those of F^0; there are no nonzero off-diagonal elements in F^0, and those of F^*, the F_{ij}^*, are obtained by solution of eq 2 in the form

$$FL_1 = \lambda_1 G^{-1}L_1 \qquad (4)$$

The input for solution of eq 4 is a value of λ_1, the elements of G^{-1} (provided G^{-1} exists), an assumed eigenvector L_1, and the diagonal elements of F. The completed force field F derived is then applied to the other (') of the two isotopic versions of eq 1, 2, and 4 to obtain Λ', including λ_1', and L_1'. In the special case $\lambda_1 = 0$; $\lambda_1 = \lambda_1'$, $L_1 = L_1'$, and F^* is unique.

B. Calculations. Normal mode vibrational frequencies were computed using double precision programs based on those of Schachtschneider and Snyder.[6] Partition functions and other quantities needed for calculation of isotope rate constant ratios were obtained by the now standard methods of Wolfsberg and Stern.[7] Programs for systematic generation of F^*'s and for Calcomp plotting were developed in this laboratory. No corrections were made for quantum mechanical tunneling.

C. Three-Element Reaction Coordinates. Intuitively, one feels that the reaction coordinate eigenvector for a real chemical reaction must reflect displacements in every internal coordinate, subject to symmetry limitations. To advance our understanding of the relationships between transition state motions and reaction rates and isotope effects, we have employed earlier[2,3] and shall employ here the artificial restriction that the number of nonzero elements of L_1 be less than the number of elements in a nonredundant but complete set of internal coordinates. Specifically, we shall use as input relative values for three nonzero elements of L_1 ($L_i \equiv L_{i1}$, $L_j \equiv L_{j1}$, $L_k \equiv L_{k1}$) and construct F^* so that all other L_{m1} are zero. (When F^* is constructed as here and $\lambda_1 < 0$, $L_1' \neq L_1$; the differences are small in the case of ^{13}C substitution, but could be appreciable in H/D cases.)

Subject to this constraint, eq 4 yields solutions for three off-diagonal elements of F^* of the form

$$F_{ij} = (L_iC_i + L_jC_j - L_kC_k)/2L_iL_j \qquad (5)$$

where the C_i are defined by equations of the form

$$C_i = -F_{ii}L_i + \lambda_1(G_{ii}^{-1}L_i + G_{ij}^{-1}L_j + G_{ik}^{-1}L_k) \qquad (6)$$

When, as here, the rank of G is greater than three, additional off-diagonal elements of F^* are required; these are obtained also from eq 4 in relations such as

$$F_{mi} + F_{mj} + F_{mk} = \lambda_1(G_{mi}^{-1}L_i + G_{mj}^{-1}L_j + G_{mk}^{-1}L_k) \qquad (7)$$

where $m \neq i, j, k$. There is no unique solution to eq 7, only a parametric one.

In this paper we shall explore the effects of a particular pattern of selection of the F_{mi}, one in which all such are confined to a single row (or column) of F, the ith, jth, or kth. If the ith row is chosen, $F_{mj} = 0 = F_{mk}$, we shall call this selection "development of row i," and use the symbol Ri to refer to it. Each choice Ri, Rj, Rk, produces a different F, and many other kinds of choices could have been made. Each such choice is, in fact, an arbitrary selection of some subset of the elements of F^*. The tests of chemical and physical reasonableness which must ordinarily guide the selection and variation of the L_i and F_{mn} are yet indefinite. (For convenience, we shall sometimes refer to the three F_{ij} as *principal off-diagonal* force constants, to the F_{mi} as *secondary off-diagonal* force constants, and to the three diagonal force constants F_{ii}, F_{jj}, and F_{kk}, as *primary*.)

D. P Space. Kass and Yankwich[3] found that calculated isotope effects obtained in surveys over ranges of input
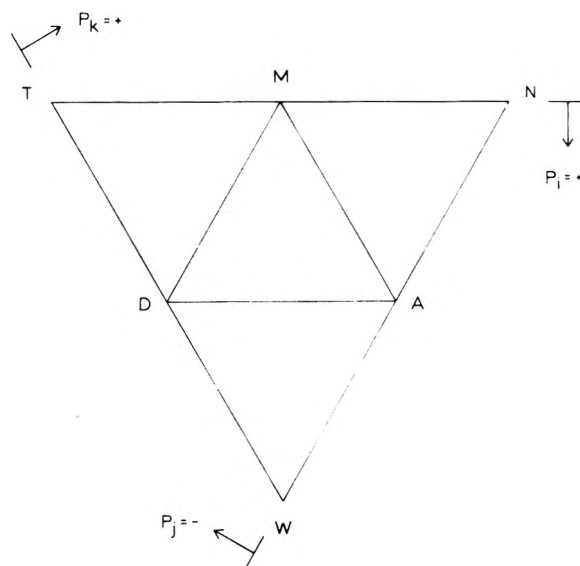
Figure 1. The P space for ($+$, $-$, $+$) relative signs of P_i, P_j, and P_k, from Figure 2 of ref 3; certain details of identification have been omitted. $P_i = 0$ along TN, reaches 0.5 at DA, and 1.0 at W; etc. Transition states are "allowed" within MAD when $\nu_1^* = 0$.

parameters L_i, L_j, and L_k were conveniently plotted as contour maps over a space P, two of those metric components, P_i, P_j, and P_k, are independent. (As if. for example, ln (k/k') were some measured property of a "three-component" system characterized by the "mole fractions" P_i, etc.) The P_i are defined by

$$P_i = L_i|(F_{ii})^{1/2}|/\Sigma|L_i(F_{ii})^{1/2}| \qquad (8)$$

subject to the mormalizing condition

$$|P_i| + |P_j| + |P_k| = 1 \qquad (9)$$

In this paper, we shall work in a region of P space in which $P_i > 0$, $P_j < 0$, and $P_k > 0$; three other similar regions correspond to the remaining distinguishable patterns of the signs of the P's. Figure 1 shows the appropriate part of Figure 2 of ref 3. Since $\lambda_1 = 0$ is a condition of such calculation, the behavior of some λ_2 is the indicator of allowedness. It is found that along the edges AD, DM, and MA, where, in turn, P_i, P_j, and P_k are 0.5, some λ_2 reaches zero; outside ADM there is no transition state within the formalism of the absolute rate theory. The area within ADM is, therefore, the *allowed* region for $\lambda_1 = 0$.

E. Allowed Region for $\lambda_1 < 0$. The assumption of curvature of the potential energy surface along the reaction coordinate at the transition state applies the constraint $\lambda_1 < 0$ over the entire region TNW. Again, $\lambda_2 = 0$ determines the boundary between allowed and forbidden regions of P space; the equation of constraint is[8]

$$|F^*| = 0 \qquad (10)$$

Convenience in mapping over P space suggests that one calculate for any particular choice Ri some function

$$X_{Ri}(P_i, P_j, P_k) = |F^*(P_i, P_j, P_k)| \qquad (11)$$

plot it, and use its zero contour to visualize the boundary of the allowed region, within which $X_{Ri} < 0$. The values of X_{Ri} and the location of the contour $X_{Ri} = 0$ will depend, here, on the choice Ri (*vide supra*).

Let

$$(F_{ij})_0 = |(F_{ii} \cdot F_{jj})^{1/2}| \qquad (12)$$
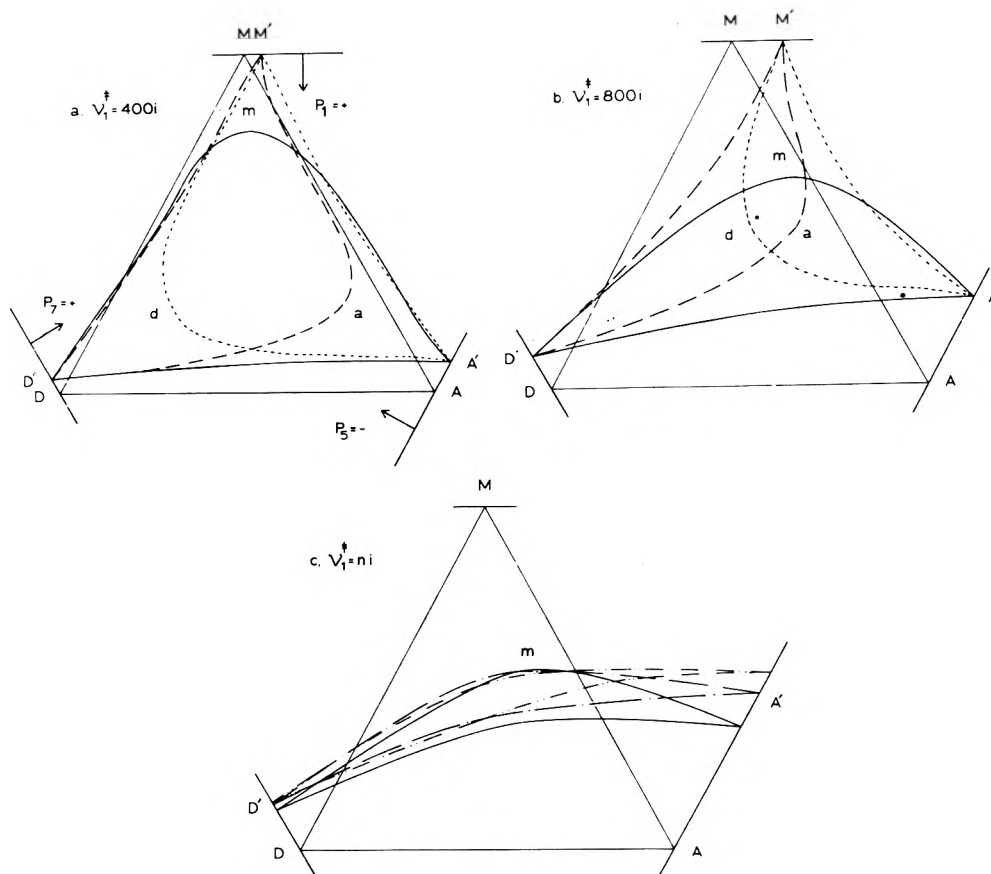
Figure 2. Allowed regions for various combinations of ν_1^* and choice (Ri) of secondary off-diagonal force constants: $R1$ (———) base points A' and D', apex m; R5 (———) base points D' and M', apex a; R7 (-----) base points M' and A', apex d; (a) $\nu_1^* = 400i$ cm^{-1}; $R1$, $R5$, $R7$; (b) $\nu_1^* = 800i$; $R1$, $R5$, $R7$; (c) $\nu_1^* = 1200i$ (————), $1600i$ (— · —), and $2000i$ (— · · —); $R1$. The heavy dot (•) in a and b is the location of the selected point for which certain results are summarized in Tables III and IV.

and

$$\alpha_{ij} = F_{ij}/(F_{ij})_0 \qquad (13)$$

Then, substitution of eq 5 and 7 into eq 11 for the choice Ri of the F_{mi} yields

$$X_{Ri} = \left(1 - \sum_m \alpha_{mi}^2\right)(\alpha_{jk}^2 - 1) - \alpha_{ij}^2(\alpha_{jk}^2 - 1) + (\alpha_{ij}\alpha_{jk} - \alpha_{ik})^2 \qquad (14)$$

where $m \neq i, j, k$. Further, let

$$\varphi_{ij} \equiv G_{ij}^{-1}/(F_{ij})_0 \qquad (15)$$

Then, the definitions of eq 8, 12, 13, and 15, substituted into eq 5 and 6 permit us to write

$$\alpha_{ij} = [-(P_i^2 + P_j^2 - P_k^2) +$$
$$\lambda_1(\varphi_{ii}P_i^2 + \varphi_{jj}P_j^2 - \varphi_{kk}P_k^2 - 2\varphi_{ij}P_iP_j)]/2P_iP_j \qquad (16)$$

and into eq 7 yield

$$\alpha_{mi} = \lambda_1(\varphi_{mi}P_i + \varphi_{mj}P_j + \varphi_{mk}P_k)/P_i \qquad (17)$$

F. The Reaction Model. The intramolecular isotope effect for oxalic acid decomposition[9-12] is the deviation from unity of k_2/k_3, in the notation of Lindsay, McElcheran, and Thode[9]

$$HOO^{13}C_1{}^{12}C_2OOH \xrightarrow{k_2} {}^{13}C_1O_2 + H^{12}COOH$$
$$\qquad (18)$$
$$HOO^{12}C_1{}^{13}C_2OOH \xrightarrow{k_3} {}^{12}C_1O_2 + H^{13}COOH$$
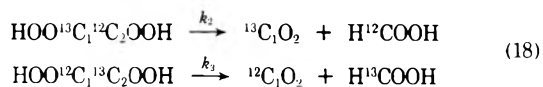
or of $L(k_2/k_3) = 100 \ln (k_2/k_3)$ from zero. We write

$$L(k_2/k_3) = L(k/k') = L(\text{TIF}) + L(\text{TDF}) = L(\text{KRAT}) \qquad (19)$$

The temperature independent factor (TIF) arises in the reaction coordinate motion and is the infinite temperature limit of k_2/k_3; depending on whether $\lambda_1 < 0$ or $\lambda_1 = 0$

$$(\text{TIF}) = (\nu_1^*/\nu_1'^*)$$
$$(\text{TIF}) = \lim_{\lambda_1 \to 0}(\nu_1^*/\nu_1'^*) \qquad (20)$$

respectively. (In actual practice, Wolfsberg and Stern's calculation[7] of TIF *via* the Redlich–Teller product rule is commonly employed.) The temperature dependent factor (TDF) arises in isotopic shifts in the genuine vibrations of the reactant and transition states.

Oxalic acid is assumed planar with carbonyl groups trans and hydroxyl hydrogens in interior orientation. Bond lengths, bond angles, and reactant force constants, obtained or adjusted from a number of sources,[2] are shown in Table I. Out-of-plane coordinates were left undefined, an omission without effect for the k/k' results presented here, but which would influence the individual calculation of k or k'; results for k/k' would be affected were such coordinates defined and any associated force constants made different between the reactant and transition states. In an intramolecular isotope effect calculation there are isotopic transition states but a single reactant state. However (using the subscripts of eq 18), $G_2^0 \neq G_3^0$ even though each comprises the same set of elements G_{ij}^0 because the mass pattern of the reactant and the internal coordinates relate to each other as determined by the definitions appropriate to the transition state. While this dis-

TABLE I: Values of Input Structural Parameters for Oxalic Acid[a]

	Bond distances, Å		Bond angles, deg
	A.	Geometry	
C–C	1.54	O=C–O	125
C–O	1.37	O=C–C	122
C=O	1.22	C–O–H	108
O–H	0.96		

Coordinate	No. i	F_{ii}
	B. Diagonal Force Field	
C_1–C_2[b]	1	4.5[c]
C_2=O	2	12.0
C_1=O	3	12.0
C_2–O	4	5.0
C_1–O	5	5.0
O_2–H	6	7.0
O_1–H	7	7.0
O=C—C	8,9	1.08
O–C–C	10,11	0.70
C–O–H	12,13	0.77

[a] Masses are in atomic mass units. [b] C_1 will appear in CO_2 product. [c] Stretching force constants in mdyn/Å; bending force constants in mdyn Å.

tinction would be obvious were the reactant and transition state geometries different, it obtains when they are the same. In this investigation, identical reactant and transition state structures are assumed; hence

$$G \equiv G_2{}^0 = G_2{}^*$$
$$G' \equiv G_3{}^0 = G_3{}^* \qquad (21)$$

The reaction coordinate investigated included displacements in internal coordinates $S_i = S_1$, C_1-C_2 stretch; $S_j = S_5$, C_1-O_1 stretch; and $S_k = S_7$, O_1-H stretch, all in the plane of the molecule. Later, reference will be made to Table II, a listing of the values for rows (or columns) 1, 5, and 7 of the elements of $(G - G')$ and G^{-1}.

III. Results and Discussion

A. *The Allowed Region.* Zero contours of X_{R1}, X_{R5}, and X_{R7} are plotted in Figure 2 at several values of $\nu_1{}^*$ between $400i$ and $2000i$ cm^{-1}. Common features of the several allowed regions are the following: (a) they are no longer confined to the triangle ADM bounded by the lines $|P_1|$, $|P_5|$, and $|P_7| = 0.5$; (b) they retain two vertices (on the perimeter of TNW) at which some $P_i = 0$, but the permitted area falls short of the expected (virtual) position of the third (*e.g.*, in $R1$: D shifts to D' A to A', but there is no actual M' vertex shifted from M; instead of $|P_1| = 0$, $|P_1|$ has some minimum value at m); (c) the shifts of the vertices increase as $\nu_1{}^*$ becomes larger (compare A – A' for $\nu_1{}^* = 1200i$, $1600i$, and $2000i$ in Figure 2c); (d) the shift of the peak of the curved segment of the boundary from the virtual third vertex increases as $\nu_1{}^*$ becomes larger. A consequence of c and d is that the area of the allowed region decreases as $|\lambda_1|$ increases.

To avoid circumlocution, let us adopt the following terminology (using the allowed region for $R1$ as an example): A'D' is a *base;* A' and D' are *base points;* the curve A'mD' is a *bow;* m is an *apex;* M' is a *virtual apex.*

B. *Conditions for Base Points and Apex.* A principal off-diagonal force constant F_{ii} exhibits complicated behavior over the region TNW; it is convenient to show this by mapping α_{ij} over the area. Figure 3 is such a map for

α_{15}, complete for $\nu_1{}^* = 0$ in part a, but only certain features are shown for nonzero values of λ_1 in parts b and c. (Table IIIA shows values of the principal off-diagonal force constants for a selected point within the allowed regions for $R1$, $R5$, and $R7$ at $\nu_1{}^*$ values of 0, $400i$, and $800i$ cm^{-1}. Of the three, only $F_{15}{}^*$ depends strongly on barrier curvature. In light of eq 6, Table II shows this to be due to the additivity of terms in $G_{11}{}^{-1}$ and $G_{55}{}^{-1}$ in $F_{15}{}^*$ and their subtractive relationship in $F_{17}{}^*$ and $F_{57}{}^*$.)

Note, in Figure 3a, that $|\alpha_{15}|$ is indeterminate at A and M, infinite elsewhere along TN and NW, finite between T and N, and finite everywhere *within* TNW. Note that the limits of the allowed region are defined by $|\alpha_{15}| = 1$.

When $\nu_1{}^* \neq 0$, Figures 3b and 3c, $|\alpha_{15}|$ is indeterminate at A' and M', infinite elsewhere along TN and NW, finite between T and N, and finite everywhere within TNW. Note that the limits of the allowed region are *not* defined by $|\alpha_{15}| = 1$; though the base is close to $\alpha_{15} = -1$, the bow is not close to $\alpha_{15} = +1$.

The behavior of a secondary off-diagonal force constant F_{mi} over TNW is more complex,[13] and the details will be skipped; but we see from eq 17 for the choice $R1$ that $|\alpha_{m1}|$ would be finite at W (where $P_1 = 1$ and $P_5 = P_7 = 0$) and within TNW, but infinite along TN, except possibly for one point. (Part B of Table III lists values at $\nu_1{}^* = 800i$ cm^{-1} of the secondary off-diagonal force constants F_{mi} at the selected point mentioned earlier. In light of eq 7, Table II shows the similarity of the several sets of force constants is due to the similarity of the $|P_i|$.)

An $\alpha_{m1} \neq 0$ couples internal coordinate S_1 to another internal coordinate S_m. At some *finite* value of F_{m1}, some λ_2 will become zero and there will be no transition state. Thus, if $\lambda_1 < 0$ and $\mathbf{F}^*$ is developed *via* $R1$, $|P_1|$ cannot itself fall to zero within the allowed region. The allowed region will therefore exhibit a *bow*-like boundary between base points and one of its original vertices will become virtual if there are more than three defined internal coordinates.

To obtain the location of a base point, we apply to eq 16 the condition that P_i or P_j be zero. For example, see Figure 2b, $P_5 = 0$ at A'. If α_{15} is to be indeterminate there, then

$$-(P_1{}^2 - P_7{}^2) + \lambda_1(\varphi_{11}P_1{}^2 - \varphi_{77}P_7{}^2) = 0 \qquad (22)$$

Application of eq 9 and rearrangement yields (still for choice $R1$)

$$P_1(A') = \left[1 + \left(\frac{1 - \lambda_1\varphi_{11}}{1 - \lambda_1\varphi_{77}} \right)^{1/2} \right]^{-1} \qquad P_5 = 0 \qquad (23)$$

Similarly at D'

$$P_1(D') = \left[1 + \left(\frac{1 - \lambda_1\varphi_{11}}{1 - \lambda_1\varphi_{55}} \right)^{1/2} \right]^{-1} \qquad P_7 = 0 \qquad (24)$$

As barrier curvature is increased, the displacements of the base points from their positions at $\lambda_1 = 0$ approach asymptotic limits such as (from eq 23)

$$\lim_{\lambda_1 \to -\infty} P_1(A') = \left[1 + \left(\frac{\varphi_{11}}{\varphi_{77}} \right)^{1/2} \right]^{-1} \qquad (25)$$

The base-plus-bow shapes of the allowed regions and of the contours of the α_{ij} tempt one to identify the latter with the zero contour of the appropriate X, here X_{Rk}. The bases M'A' for $R7$ (*i.e.*, the contours $X_{R7} = 0$ between M' and A') in Figure 2 appear to be very close to the contours of $\alpha_{15} = -1$ in Figure 3. This correspondence is always close, usually within plotting error, but it is not exact.

Joseph H. Keller and Peter E. Yankwich

TABLE II: Elements of Rows (or Columns) 1, 5, and 7 of the Matrices (G − G′) and G⁻¹

	$10^2(G_{ij} - G_{il'})$			G_{ij}^{-1}		
j	1	5	7	1	5	7
1	0.0	0.2505	0.0	22.6130	3.5526	−0.3293
2	−0.3397	0.0	0.0	4.0288	−1.2013	−0.0841
3	+0.3397	+0.3677	0.0	3.9412	2.2164	0.2504
4	−0.2505	0.0	0.0	3.6320	2.6284	−0.0319
5	+0.2505	−0.6410	0.0	3.5526	13.2896	0.1637
6	0.0	0.0	0.0	−0.3373	−0.0304	−0.0034
7	0.0	0.0	0.0	−0.3293	0.1637	0.9747
8	−0.4460	−0.3832	0.0	9.1436	1.4390	−0.3163
9	+0.4460	−0.8136	0.0	8.9574	−4.5266	−0.1895
10	−0.4307	+0.3832	0.0	10.1777	2.1216	0.0762
11	+0.4307	+0.3832	0.0	9.9386	2.6866	−0.7411
12	+0.4307	0.0	0.0	0.2998	0.2077	0.0061
13	−0.4307	0.0	0.0	0.2925	0.7802	0.0062
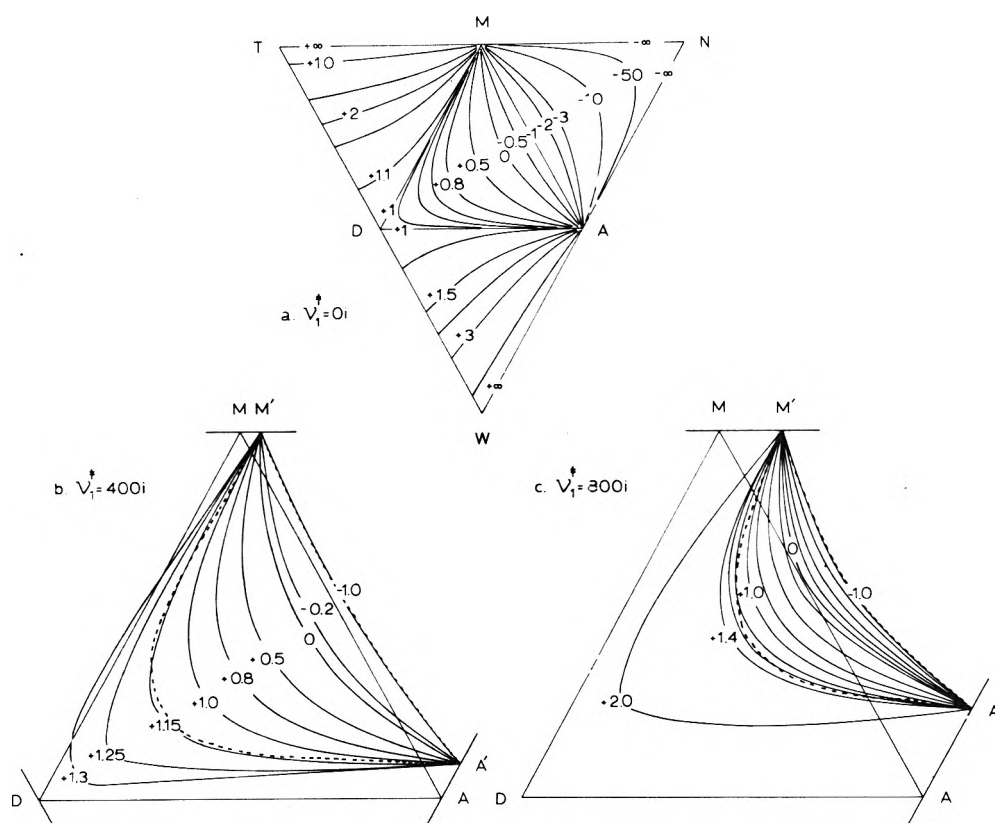
Figure 3. Contours of α_{15} at various barrier curvatures: (a) $\nu_1^* = 0$; the unlabeled contours are for $\alpha_{15} = 0.9, 0.95,$ and 0.99; (b) $\nu_1^* = 400i$; (c) $\nu_1^* = 800i$; unlabeled contours are $\alpha_{15} = -0.8, -0.5, -0.2, +0.2, +0.5, +0.8, +1.2, +1.3$. The allowed region in a coincides with the contours ± 1; in b and c the dashed curves (-----) indicate the boundary of the allowed region for $R7$.

Consider the base M′A′. While this portion of the zero contour of X_{R7} nearly matches the shape of $\alpha_{15} = -1$, the shapes of the contours of α_{17} and α_{57} will not; they are bows. For this base, eq 14 is

$$X_{R7} = (1 - \Sigma\alpha_{m7}^2)(\alpha_{15}^2 - 1) -$$
$$\alpha_{17}^2(\alpha_{15}^2 - 1) + (\alpha_{17}\alpha_{15} - \alpha_{57})^2 \quad (26)$$

If $\alpha_{15} = -1$ and $X_{R7} = 0$, then it is necessary that $|\alpha_{17}| = |\alpha_{57}|$ along M′A′; a glance at eq 5 and 6 suggests the rarity of such behavior. However, allowed region bases do closely approximate contours such as $|\alpha_{ij}| = 1$.

C. The $L(TIF) - (P_i, P_j, P_k)$ Surface as a Function of ν_1^* and Ri. Figure 4 shows $L(TIF)$ over the permitted ranges of P_1, P_5, and P_7 for $\nu_1^* = 0, 400i,$ and $800i$ cm^{-1},

and each of the choices $R1$, $R5$, and R^7 of sets F_{mi} of the secondary off-diagonal force constants.

All of the surfaces are very similar in shape, though different in extent. At $\nu_1^* = 400i$ the comparisons among the several Ri and with the $\nu_1^* = 0$ surface are quite close. The differences are,[14,15] however, proportional to λ_1 and at $\nu_1^* = 800i$ changes in position of surface features and of $L(TIF)$ value are apparent, though small. The $R1$ maps are slightly shifted from $\nu_1^* = 0$ positions, and the $R5$ surfaces are both shifted and depressed. None of these effects is of any practical significance, being small in comparison with ordinary experimental error. Very precise measurements at very high temperatures would not permit one to assign a "best" value to ν_1^* on the basis of the apparent
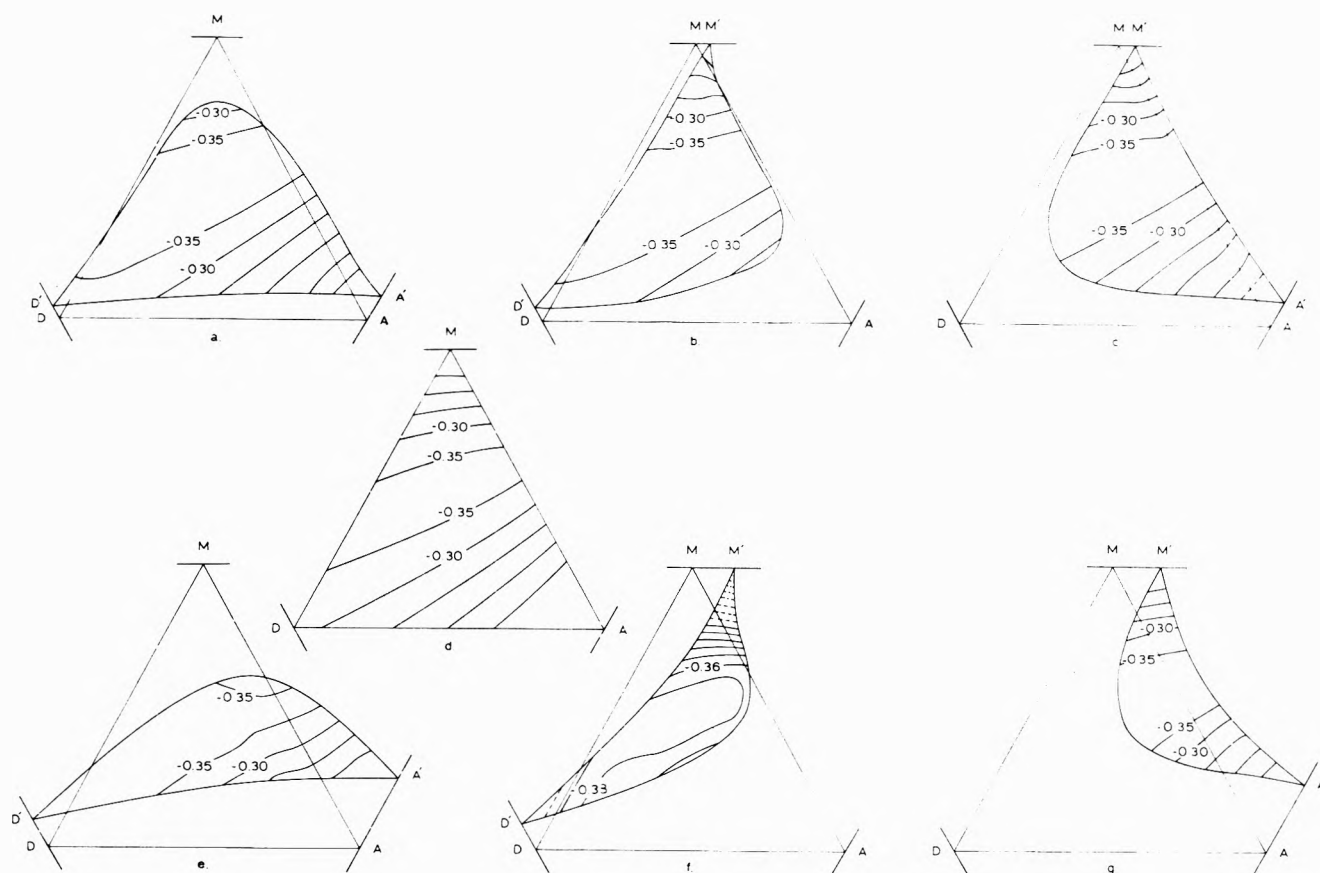
Figure 4. Contours of $L(\text{TIF})$ for various combinations of ν_1^* and choice (Ri) of secondary off-diagonal force constants: (a. b. c) $\nu_1^* =$ 400i; $R1$, $R5$, $R7$, respectively; (d) $\nu_1^* = 0$; (e, f, g) $\nu_1^* = 800i$: $R1$, $R5$, $R7$, respectively. Contour interval is 0.02L unit in f 0.05L unit elsewhere; dashed contours are estimated.

TABLE III: Selected Transition State Force Constants[a]

	ν_1, cm^{-1}		
	0	400i	800i
A. Principal Off-Diagonal Force Constants[b]			
F_{13}^*	+0.67763	+1.91957	+5.64540
F_{17}^*	−2.80624	−2.80364	−2.79584
F_{37}^*	+4.64835	+4.70021	+4.85582

m	F_{m1}^*	F_{m5}^*	F_{m7}^*
B. Secondary Off-Diagonal Force Constants, F_{mi}^*, for Each Ri at $\nu_1^* = 808i$ cm^{-1} [c,d]			
2[c]	−2.07896	+1.56530	−1.62057
3	−0.49700	+0.37418	−0.38740
4	−0.03774	−0.02842	−0.02942
6	+0.11359	−0.08552	+0.08855
8[d]	−2.57269	+1.93704	−2.00544
9	−5.54987	+4.17863	−4.32619
10	−2.81051	+2.11610	−2.19083
11	−2.04250	+1.53784	−1.59215
12	−0.01196	+0.00900	−0.00932
13	+0.27726	−0.20876	+0.21613

[a] All are for the point $P_1 = 0.24$, $P_5 = -0.35$, $P_7 = 0.40$. [b] mdyn/Å. [c] $m = 2-6$, mdyn/Å. [d] $m = 7-13$, mdyn.

value of $L(\text{TIF})$ for any allowed reaction coordinate (P_1, P_5, P_7).

The small λ_1 dependent shifts in $L(\text{TIF})$ are reflections of the appearance in $\mathbf{L}'$ of small nonzero elements L_m' in addition to the primary L_1', L_5', and L_7'; there are no

such secondary elements in $\mathbf{L}$, because it is the input with $\mathbf{G}$ and λ_1 for the construction of $\mathbf{F}^*$, eq 4. When $\mathbf{F}^*$ for $\lambda_1 \neq 0$ is used with $\mathbf{G}'$ in eq 1 to compute the $\lambda' \neq \lambda$, and this input and output used in eq 2, it is found that the output $\mathbf{L}'$ is slightly different from the input $\mathbf{L}$. In Table IV, elements of a specific input $\mathbf{L}_1$ (the selected point of Table III) are shown along with those of output $\mathbf{L}_1'$ for several combinations of ν_1^* and Ri. Values of the "contaminant" elements of $\mathbf{L}_1'$ are roughly related to those of the corresponding G_{ij}^{-1}, but the connection is a tortuous one; see eq 5–7. This is the origin of larger differences between $\mathbf{L}_1$ and $\mathbf{L}_1'$ for hydrogen isotopy. More directly, the *signs* of the secondary elements of $\mathbf{L}_1'$ reflect the simple one dimensional shift of the center of mass between the structures leading to $\mathbf{G}$ and $\mathbf{G}'$.

D. The $L(TDF)$-(P_i, P_j, P_k) Surface as a Function of ν_1^* and Ri. Figure 5 compares $L(\text{TDF})$ for $\nu_1^* = 400i$ cm^{-1} and choice $R1$ at each of three temperatures with similar results for $\nu_1^* = 0$. The retention of surface characteristics as ν_1^* increases is very great especially near the base AD, A'D'; we show below that such shape retention is not general. The following observations *are* typical of effects found also with other ν_1^* and Ri: at neither barrier curvature are there significant effects of temperature on the shape of the surface; and $|L(\text{TDF})|$ generally decreases with increasing temperature (decreasing θ). Most exceptions to this behavior are associated with the occurrence of a nodal curve for $L(\text{TDF})$ within the allowed region (*vide infra*).

Figure 6 shows $L(\text{TDF})$ at $\theta = 1000/T°K = 5$ for $\nu_1^* = 0$, 400i, and 800i cm^{-1}, and each of the choices $R1$, $R5$, $R7$

TABLE IV: Reaction Coordinate Eigenvectors at the Point $P_1 = 0.25$, $P_3 = -0.35$, $P_7 = 0.40$ for Each Ri at $\nu_1^* = 400i$ and $800i$ cm^{-1}

| | | L_i': $\nu_1^* = 400i$ | | | L_i': $\nu_1^* = 800i$ | |
		R1 401.5322i	R5 401.5307i	R7 401.5319i	R1 803.1627i	R5 803.1442i	R7 803.1956i
i	$\nu_1'^*$						
1		0.272969	0.273522	0.274044	0.268911	0.271093	0.272124
2		0.000277	0.000276	0.000268	0.001240	0.001185	0.000783
3		−0.000197	−0.000220	−0.000214	−0.000500	−0.000808	−0.000756
4		0.000445	0.000409	0.000422	0.001243	0.000976	0.000820
5		−0.373368	−0.363050	−0.364039	−0.360131	−0.359278	−0.360207
6		−0.000009	−0.000009	−0.000009	−0.000014	−0.000012	−0.000014
7		0.350696	0.350704	0.351086	0.346802	0.347082	0.341992
8		0.001337	0.001299	0.001256	0.001745	0.001749	−0.000235
9		−0.004838	−0.004686	−0.004867	−0.009125	−0.008080	−0.012067
10		0.003702	0.003536	0.003569	0.006574	0.005642	0.005657
11		−0.001927	−0.002094	−0.002085	−0.001862	−0.002749	−0.003004
12		−0.000042	−0.000051	−0.000042	−0.000843	−0.000815	−0.000496
13		0.000192	0.000138	0.000178	0.001004	0.000423	0.001837

[a] At all ν_1^*: $L_1 = +0.276931$, $L_5 = -0.367807$, $L_7 = +0.355262$ (when $\nu_1^* = 0$, $L_i' = L_i$). All L' renormalized, $\Sigma_i |L_i| = 1$.
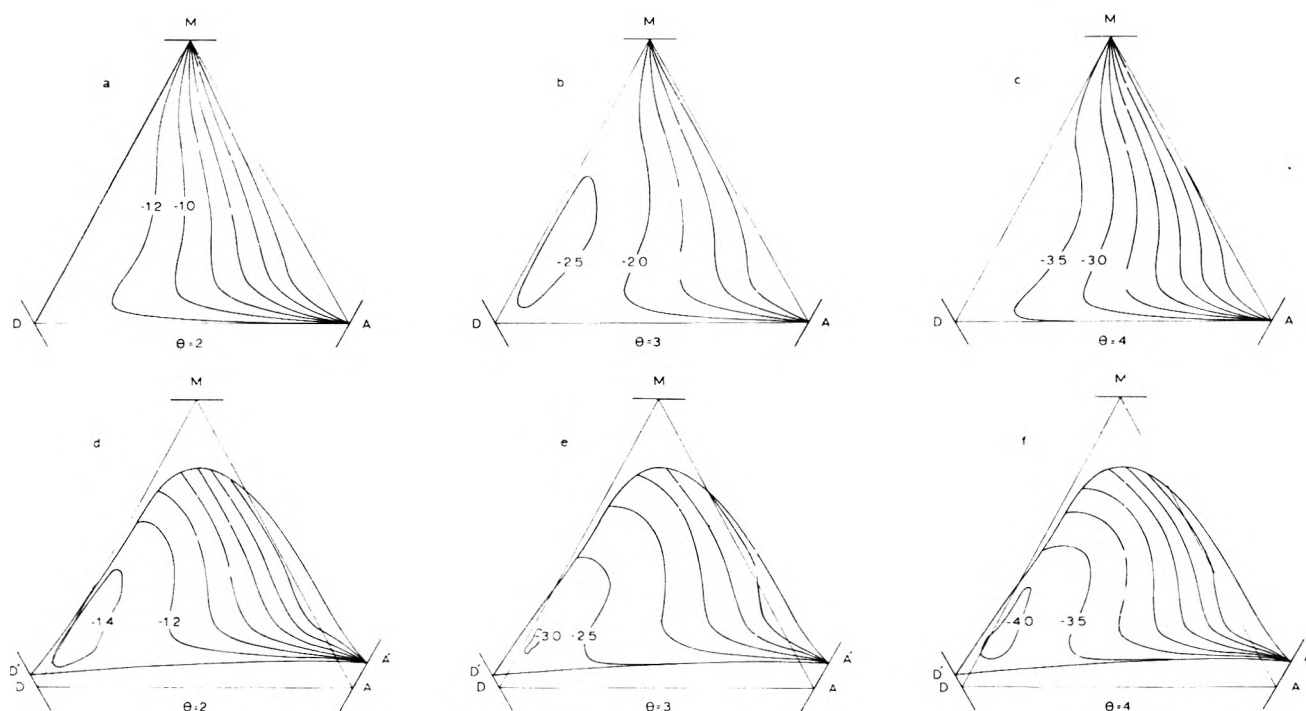
Figure 5. Temperature dependence of L(TDF): (a, b, c) $\nu_1^* = 0$; $\theta = 1000/T^\circ K = 2$, 3, and 4, respectively; (d, e, f) $\nu_1^* = 400i$; $\theta = 2$, 3, and 4, respectively. The "disappearance" of the "basin" in a and c is an artifact of the contour intervals selected. Contour interval is 0.2L unit at $\theta = 3$, 4.

of the F_{mi}. At $\nu_1^* = 0$, L(TDF) approaches a limit at each of the boundary lines AD, DM, and MA; no contours of L(TDF) would cross the boundaries if extended. (In other examples, this asymptotic behavior results in very steep slopes near the boundary. This is one of several considerations, another being the lowering under such conditions of the frequencies of one or more of the *genuine* vibrations of the transition state to values which physically are unreasonably small. To side-step such difficulties it is necessary to avoid reliance on results within 0.02–0.04 P unit of a *base*-like boundary curve.)

As remarked above, the H + Cl$_2$ reaction with nonlinear transition state was described by reaction coordinates involving all three of the internal coordinates.[14] Under such conditions, the allowed region for $\lambda_1 < 0$ is bounded by three base curves connecting three vertices lying on the

boundary of P space. The L(TDF) surface for $\nu_1^* = 400i$ cm^{-1} in that study was closely similar in shape at each temperature to that for $\nu_1^* = 0$ *when viewed relative to the boundary of the allowed region*: the distortion of the boundary from the original triangular shape is accompanied by closely related distortion of the L(TDF) surface. Comparable values of L(TDF) at different ν_1^* are to be sought not at the same points in the plane, but at points which are similarly located with respect to the boundary curves. This is an important difference from the behavior of L(TIF)–(P_i, P_j, P_k) surfaces, as described above. (The elements of an appropriate transformation between the P spaces at different ν_1^* values are not immediately obvious.) Another effect noted when $\lambda_1 < 0$ was that the distorted boundary is no longer an asymptote for L(TDF); contours of L(TDF) would cut the boundaries if extended,
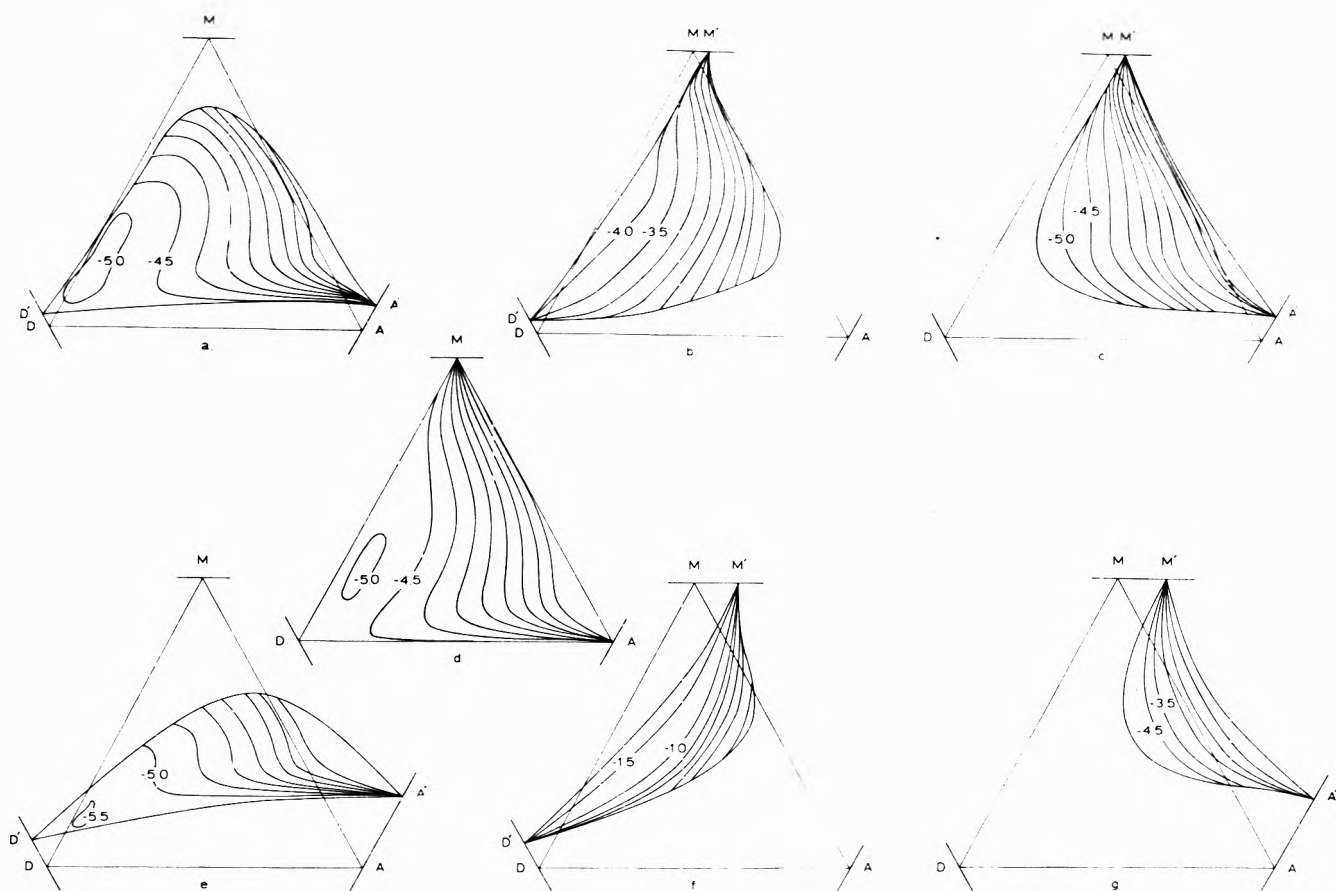
Figure 6. $L(\text{TDF})$ at $\theta = 5$ for various combinations of ν_1^* and Ri: (a, b, c) $\nu_1^* = 400i$; $R1$, $R5$, $R7$, respectively; (d) $\nu_1^* = 0$; (e, f, g) $\nu_1^* = 800i$; $R1$, $R5$, $R7$, respectively. Contour interval $0.5L$ unit.
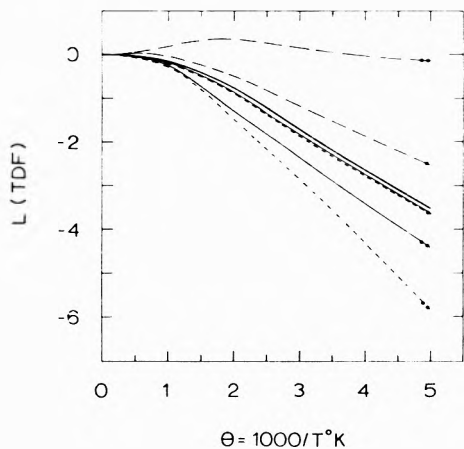
Figure 7. Temperature dependence of $L(\text{TDF})$ at the selected point (see Figure 2) $P_1 = +0.25$, $P_5 = -0.35$, $P_7 = +0.40$, at various ν_1^* and Ri: (——) $\nu_1^* = 0$; (——) $R1$; (— — —) $R5$; (— — —) $R7$. Curves for $\nu_1^* = 400i$ terminate in •, for $\nu_1^* = 800i$ in ••.

though the angles of incidence are very small. In a typical case, $L(\text{TDF})$ changes about 2% in value between base points.

The various plots in Figure 6 reveal much more complex ν_1^*-related changes when a three-element reaction coordinate is employed with an eight-atom transition state: (a) the bow is not the transformed sum of the other base-like $\nu_1^* = 0$ boundary lines; (b) instead of the allowed region *containing* a distorted-but-whole $L(\text{TDF})$ surface, the base-plus-bow boundary vignettes part of a distorted sur-

face; (c) the surfaces for a given Ri retain shape as ν_1^* increases only at a base, and often not even there; (d) surface shape retention as λ_1 becomes negative is good for the choice $R1$ of secondary off-diagonal force constants, but so poor for $R5$ and $R7$ that, at least in the case of $R5$, all resemblance to the $L(\text{TDF})$ surface for $\lambda_1 = 0$ has been lost; (e) the pattern of $L(\text{TDF})$ value changes varies with the choice Ri: value retention (relative to the base) is good for $R1$, $L(\text{F})$ falls somewhat as ν_1^* increases for $R7$, but rises rapidly in the case of $R5$. (Plots of $L(\text{TDF})$ vs. θ are shown in Figure 7 for the selected point of Table III, for each choice Ri, and at $\nu_1^* = 0$, $400i$, and $800i$ cm^{-1}. The details of Ri and ν_1^* dependences are more easily seen than in maps such as those in Figure 5.)

Properties a and b have been explained in sections IIIA and B above; together they account for the bows cutting contours of $L(\text{TDF})$ at large angles. Characteristically, bases cut $L(\text{TDF})$ contours at grazing angles.

The rather "good" behavior of the $R1$ surfaces when $\lambda_1 < 0$ is traceable to the fact that alone among the isotopic internal coordinates S_1, the C_1–C_2 stretch is unchanged between the isotopic transition states. Note in Table II that $(G_{ii} - G_{ii}') = \Delta G_{11} = 0$, and that all other ΔG_{ij}'s are positive and negative pairs. The corresponding G_{ij}^{-1} do not pair, but their differences when paired according to internal coordinates (2, 3; 4, 5; etc.) are small. Although the force constants F_{m1} may be large, their influence on $L(\text{TDF})$ is reduced markedly because of the pairing of the ΔG_{ij}'s, at least when P_1 is large. As P_1 falls (*i.e.*, as one moves from the base A'D' in the direction of apex m, there is increased distortion of the surface; see eq 7).

The different behavior of $L(\text{TDF})$ for $R5$ and $R7$ thus
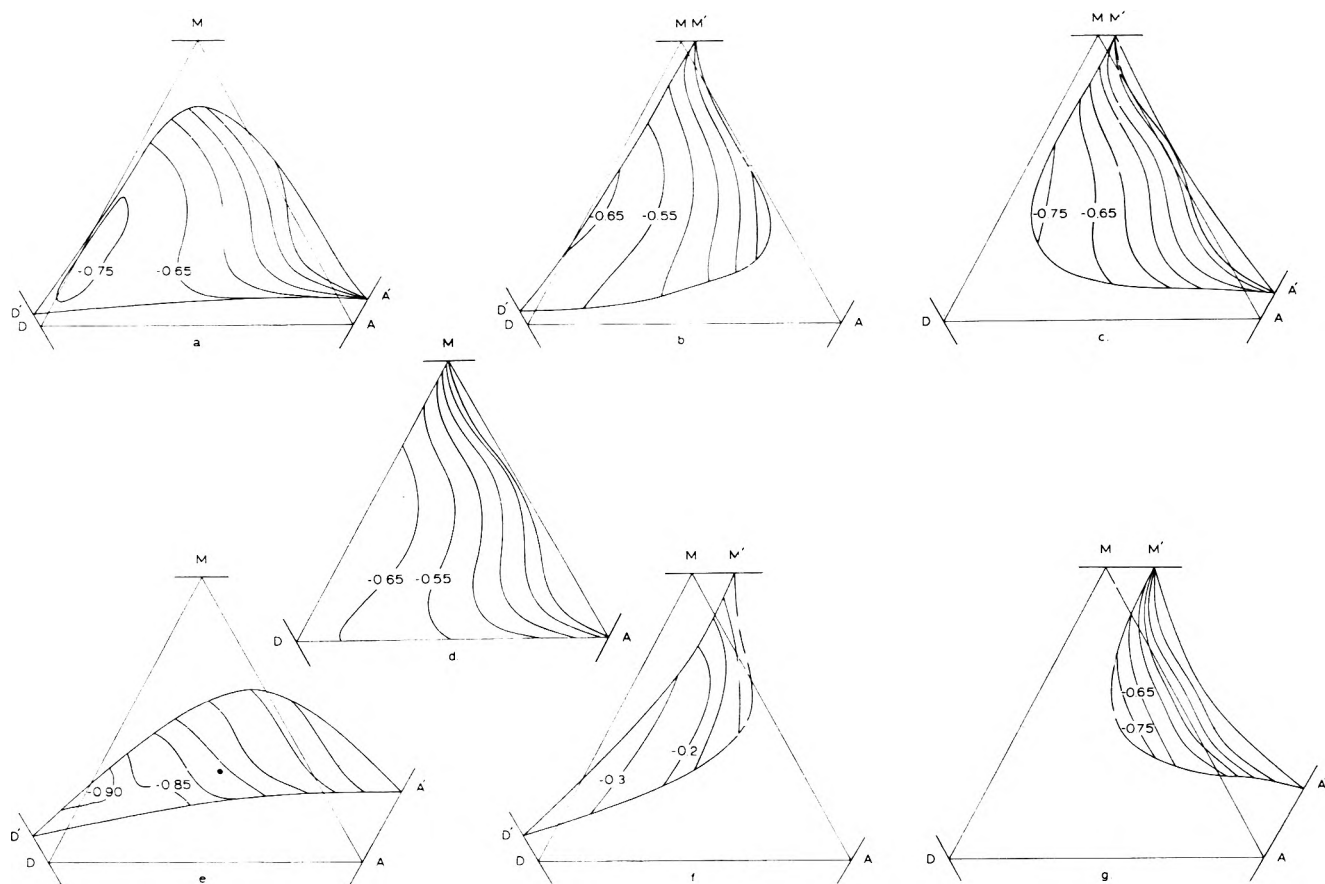
Figure 8. $L(KRAT)$ at $\theta = 1$ for various combinations of ν_1^* and Ri: (a, b, c) $\nu_1^* = 400i$; $R1$, $R5$, $R7$, respectively; (d) $\nu_1^* = 0$; (e, f, g) $\nu_1^* = 800i$; $R1$, $R5$, $R7$, respectively. Contour interval is $0.05L$ unit in e, $0.1L$ unit in the other parts of the figure.

appears to be unexceptional! Reference to Table II shows that the usually larger F_{m5}^{-1} than G_{m7}^{-1} will result in the force constants F_{m5} being larger than the F_{m7}. Since the same is true for the ΔG_{m5} in comparison to the ΔG_{m7}, the λ_1-induced changes in $L(TDF)$ should be much larger for $R5$ than for $R7$. If one looks at the general value levels for $R5$ and $R7$ and ignores the problems of shape (in comparison to the respective base regions at $\nu_1^* = 0$) the comparison is seen to be as described.

Property c above is reflected in the observations recorded as d and e, and is the most difficult to account for of the several findings. Comparison of Figures 3 and 6 shows that, at least for $R5$ and $R7$, the symmetries of the $L(TDF)$ surfaces near the bases D'M' and M'A' are very similar to those of the plots of α_{17} and α_{15}, respectively. At a first-order level of effects, but perhaps not at a higher, this correspondence is likely accidental. We believe that it is due to the kind of near matching of component effects noted in our discussion of eq 26 above.

E. The $L(KRAT)$-(P_i, P_j, P_k) Surface as a Function of ν_1^* and Ri. The $L(KRAT)$ surface, which is the sum of $L(TIF)$ and $L(TDF)$, will likely be, when techniques for its use with actual experimental measurements have been perfected, of greater utility than either of its components. $L(TIF)$ can be separated from experimental data on $L(KRAT)$ only if very precise measurements are available over a substantial range of high temperatures; Stern and his coworkers[16,17] have given persuasive demonstration of the hazards involved in attempts to evaluate $L(TIF)$ by extrapolation of moderate temperature $L(KRAT)$ data to a high-temperature limit. (However, deeper under-

standing of the origins of these factors should assist such techniques for estimation.)

At very high temperatures, the appearance of $L(KRAT)$-(P_i, P_j, P_k) should be very similar to that of the $L(TIF)$ surface, because $L(TDF)$ is expected to be very small at small values of θ. By the same token, the $L(KRAT)$ surface should resemble that for $L(TDF)$ at low temperatures, large θ. At intermediate temperatures the appearance of maps of $L(KRAT)$ will depend on the relationships among the values and gradients in value of the maps of the component functions.

Figure 8 shows maps of the $L(KRAT)$-(P_1, P_5, P_7) surfaces at 1000°K, $\theta = 1$, for the combinations of Ri and ν_1^* used in Figures 4 and 6. The resemblance of corresponding $L(TDF)$ and $L(KRAT)$ surfaces in Figures 6 and 8 is close at $\nu_1^* = 400i$, less so but still considerable at $800i$ cm^{-1}. These similarities are due to the very gentle slopes on the $L(TIF)$ surface together with the occurrence of larger gradients on the $L(TDF)$ surfaces even at a temperature as high as 1000°K. By the test suggested above, 1000°K is not a "high" temperature for these combinations of transition state parameters and properties. (Note the effects of Ri and ν_1^* on the angles of incidence of the $L(KRAT)$ contours to the base curves. These angles are smallest for $R7$ because $L(TIF)$ is a shallow trough whose axis is nearly perpendicular to M'A'.)

F. How to Use Maps in (P_i, P_j, P_k) Space. A few examples will illustrate the use of mappings such as those discussed here and in the earlier publication.[3] These employ the same geometry for reactant and transition states. We shall assume further that the investigator has been led to

a "best choice" of the three internal coordinates to be combined into the reaction coordinate, that suitable values have been selected for the transition state diagonal force constants (not necessarily those of the reactant state), and that experimental data are in hand. The variables accessible to us are the curvature of the potential barrier (choice of $\nu_1{}^*$) and the choice Ri of secondary off-diagonal force constants to achieve that curvature. The test of the model is whether the allowable and physically reasonable range of reaction coordinate compositions (i.e., ranges of P_i, P_j, and P_k, here P_1, P_5, and P_7) yield calculated $L(\text{KRAT})$ in agreement with the observed.

Example 1. Suppose that $L(\text{KRAT}) = -0.80 \pm 0.05$ at $\theta = 1$ is an experimental datum (for the model reaction, conditions, and assumptions detailed above). The span of the data for $L(\text{KRAT})$ is from -0.85 to -0.75. Examination of the several parts of Figure 8 shows that the data cannot be contained by $\nu_1{}^* = 0$ [in 8d, the contour -0.75 is outside the allowed region MAD]; $R5$ is not a useful method for curving the barrier [8b and 8f show that barrier curvature increases $L(\text{KRAT})$ for $R5$]; at $\nu_1{}^* = 400i$, the fall of the surfaces for $R1$ and $R7$ brings the upper limit of the experimental range into the allowed region [-0.75 contours in 6a and 8c]; at $\nu_1{}^* = 800i$, the whole experimental range is allowed for $R1$ [8e], but increased curvature has not improved the usefulness of $R7$ [-0.75 still near apex in 8g]. Within the compass of the variations embodied in Figure 8, we would conclude that the best models, given the restrictions listed above, corresponded to a barrier curvature near $800i$ cm^{-1} achieved through interactions between the C_1-C_2 stretch and other internal coordinates, and that acceptable reaction coordinates involved $P_7 \sim 0.3$ [locus of the contour -0.80 in 8e], P_1 in the range 0.25-0.40, and P_5 from -0.25 to -0.45. Absent other information or criteria, these P_i ranges correspond to reasonable motions.

Example 2. [As a convenience, we ignore $L(\text{TIF})$ and treat the graphs in Figure 5 as $L(\text{KRAT})$ rather than $L(\text{TDF})$.] Suppose that $L(\text{KRAT}) = -2.0 \pm 0.1$ at $\theta = 3$ and -3.0 ± 0.1 at $\theta = 4$ are experimental data. These contours in Figures 5b and 5c, respectively, are nearly coincident, and except near DA they lie close to the bisector of angle DMA; thus at $\nu_1{}^* = 0$ the input structural parameters yield the experimental results for any reaction coordinate in which $|P_5| \cong |P_7|$, so the model tells us nothing about the participation of S_1 (the C_1-C_2 stretch) in the reaction. The contours of these data in 5e and 5f are also nearly coincident, but there they weave in sigmoid fashion about the line $P_7 \cong 0.35$; thus at $\nu_1{}^* = 400i$ the models contain the data for a family of reaction coordinates such that $|P_1| + |P_5| \cong 0.65$. Additional principles are required (*vide infra*) to assist our judgement as to whether the effect of barrier curvature is an improvement in the model or not.

Example 3. Suppose the experimental data are $L(\text{KRAT}) = -2.5 \pm 0.1$ at $\theta = 3$ and -3.5 ± 0.1 at $\theta = 4$. In Figures 5b and 5c, respectively, these contours are not the same shape and their separation is far more than the combined experimental imprecision; the model cannot reproduce the experimental results if the barrier is flat. In Figure 5e and 5f, though still separated by somewhat more than the experimental imprecision, the contours are close together and their shapes similar. Curving the barrier so that $\nu_1{}^* = 400i$ has brought the properties of the model within range of the data. The nature of further refinement (*e.g.*, a more strongly curved barrier, further ad-

justment of the diagonal force constants, etc.) would depend on assessment of the chemical and physical reasonableness of the direction of change in input parameters and of the output allowable reaction coordinates.

IV. Conclusions

This study of the influence of three-element reaction coordinate eigenvector composition and of potential barrier curvature on the values of calculated ^{13}C knetic isotope effects shows that the range of compositions corresponding to an acceptable transition state is altered as barrier curvature is increased. The allowed range depends not only on $\nu_1{}^*$ but on the selection of secondary off-diagonal force constants used to maintain a simple reaction coordinate eigenvector; further, where the number of defined internal coordinates exceeds the number of nonzero elements in the reaction coordinate eigenvector, the allowed range decreases as $\nu_1{}^*$ increases in magnitude.

There are small nonzero secondary elements in the reaction coordinate eigenvector of the isotopic companion to the species whose properties are used in construction of the transition state force field; in sum, these secondary elements do not comprise a substantial perturbation of the preselected input motion. As a result the temperature independent factor (TIF) in k/k' is a function of the preselected reaction coordinate motion and almost independent of the value of $\nu_1{}^*$ and of details of the transition state force field.

The temperature dependent factor (TDF) in k/k' may depend strongly, for a given reaction coordinate eigenvector, on the barrier curvature and on the selection of minor force constants employed. The shifts from behavior when $\lambda_1 = 0$ (flat barrier) may be positive or negative, with the results that isotope effects have their signs changed and/or exhibit crossover (nodes in $L(\text{TDF})$ vs. $1/T$).

The method of restriction of reaction coordinate eigenvector and eigenvalue explored here yields neither transition states of obvious physical reasonableness nor output kinetic isotope effects unique in value and temperature dependence for a given pairing of eigenvector and eigenvalue: a three-element reaction coordinate (eigenvector) is obviously an approximation where ten other possible elements belong to the same symmetry class; and the pairing mentioned can result from many different transition state force fields each, potentially, yielding a unique isotope effect.

On the other hand, limitation of calculations to chemically and physically reasonable reaction coordinates and to similarly reasonable values for some force constants is easily achieved. This leaves as the exposed but unsolved major problems: first, establishment of the criteria of reasonableness for the barrier curvature employed (*i.e.*, for the value of λ_1 or of $\nu_1{}^*$); and, second, a rationale for the assignment of nonzero values to any off-diagonal elements in the transition state force constant matrix. Further studies of three-element reaction coordinates designed to expose the elements of solutions to these two problems are underway in our laboratories.

References and Notes

(1) W. E. Buddenbaum and P. E. Yankwich, *J. Phys. Chem.*, **71**, 3136 (1967).
(2) T. T.-S. Huang, W. J. Kass, W. E. Buddenbaum, and P. E. Yankwich, *J. Phys. Chem.*, **72**, 4431 (1968).
(3) W. J. Kass and P. E. Yankwich, *J. Phys. Chem.*, **73**, 3722 (1969).
(4) G.-J. Wei and P. E. Yankwich, *J. Chem. Phys.*, **58**, 5552 (1973).
(5) E. B. Wilson, Jr., J. C. Decius, and P. C. Cross, "Molecular Vibrations," McGraw-Hill, New York, N. Y., 1955.
(6) J. H. Schachtschneider and R. G. Snyder, *Spectrochim. Acta*, **19**, 117 (1965).
(7) M. Wolfsberg and M. J. Stern, *Pure Appl. Chem.*, **8**, 225 (1964).
(8) A. M. Katz and W. H. Saunders, Jr., *J. Amer. Chem. Soc.*, **91**, 4469 (1969).
(9) J. G. Lindsay, D. E. McElcheran, and H. G. Thode, *J. Chem. Phys.*, **17**, 589 (1949).
(10) A. Fry and M. Calvin, *J. Phys. Chem.*, **56**, 897 (1952).
(11) W. E. Buddenbaum, M. A. Haleem, and P. E. Yankwich, *J. Phys. Chem.*, **71**, 2929 (1967).
(12) G. Lapidus, D. Barton, and P. E. Yankwich, *J. Phys. Chem.*, **70**, 1575, 3135 (1966).
(13) G.-J. Wei and P. E. Yankwich, *J. Chem. Phys.*, in press.
(14) R. W. Kidd and P. E. Yankwich, *J. Chem. Phys.*, **59**, 2723 (1973).
(15) R. W. Kidd and P. E. Yankwich, *J. Chem. Phys.*, in press.
(16) M. J. Stern, W. Spindel, and E. U. Monse, *J. Chem. Phys.*, **48**, 2938 (1968).
(17) P. C. Vogel and M. J. Stern, *J. Chem. Phys.*, **54**, 779 (1971).

COMMUNICATIONS TO THE EDITOR

Intermediate of Oxygen Exchange Reaction over Illuminated Titanium Dioxide

Sir: In the past several years, three forms of oxygen, O^-, O_2^-, and O_3^-, have been observed on oxides by the esr technique,[1] but the reactivity or selectivity of these species have not been firmly characterized. The author has shown that O^- is the reactive intermediate in the catalytic oxidation of carbon monoxide over ZnO[2,3] and O_2^- is less reactive in the oxidation as well as in the isotopic exchange of oxygen between O_2^- and CO, and O_2^- and CO_2.[4] Naccache has also shown the high reactivity of O^- on MgO for O_2, CO, and C_2H_4.[5]

This communication suggests an O_3^- intermediate in the photocatalytic exchange reaction of $^{16}O_2$ and $^{18}O_2$ over illuminated TiO_2. The isotopic analysis of the gas-phase oxygen as well as the desorbed oxygen were carried out simultaneously by connecting the reactor directly to the mass spectrometer.

Rutile type TiO_2 (1.50 g of Titanox RA-10 from Titanium Pigment Corp.) was mounted in a Pyrex glass reactor, evacuated at *ca.* 410° for more than 10 hr, and cooled to room temperature *in vacuo*, after which $^{18}O_2$ of 0.6 cm pressure was first adsorbed at room temperature for 6 hr and then removed by 30 min of evacuation. $^{16}O_2$ of 1.0 cm pressure was added to the above $^{18}O_2$ preadsorbed TiO_2 for 1.5 hr at room temperature and then removed by 30 min of evacuation. The reactor was connected to the mass spectrometer for isotopic analysis of the desorbed oxygen, which has a maximum around 180° and has been identified as O_2^- by esr.

The isotopic composition of the desorbed oxygen from TiO_2 changes with increasing temperature and approaches to a uniform composition at higher temperatures as shown in Figure 1. This is the same as has been observed on ZnO,[4] suggesting the heterogeneity of the adsorption strength of O_2^-; adsorbed oxygen which will desorb at the lower temperature takes much perturbation from the gas-phase oxygen.

A mixture of $^{18}O_2$ and $^{16}O_2$, each of 1 mm pressure, was admitted to the TiO_2 on which $^{18}O_2^-$ and $^{16}O_2^-$ had been coadsorbed, and was subjected to illumination with a medium pressure mercury lamp (Toshiba H-400-P) at room temperature. The reactor was shaken during illumination so that the TiO_2 powder may be exposed to light homogeneously.

Figure 2 gives a typical result of the isotopic analysis of gas-phase oxygen and of desorbed oxygen. The isotopic exchange reaction of gas-phase oxygen is so enhanced by illumination that equilibrium has been established within 3 min of illumination. The exchange reaction over TiO_2 in the dark at room temperature is slow compared with that under illumination and illumination without TiO_2 gives no exchange. Accordingly, the rapid exchange observed in gas phase under illumination is undoubtedly a photocatalytic reaction taking place over TiO_2. After the 3 min illumination, the gas-phase oxygen was removed by evacuation and the thermal desorption was carried out. The iso-
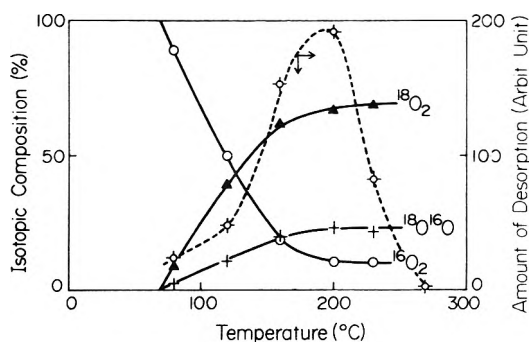
Figure 1. Isotopic composition of desorbed oxygen from TiO_2 which has been exposed to $^{18}O_2$ and then to $^{16}O_2$. The dotted line is the approximate amount of desorption.
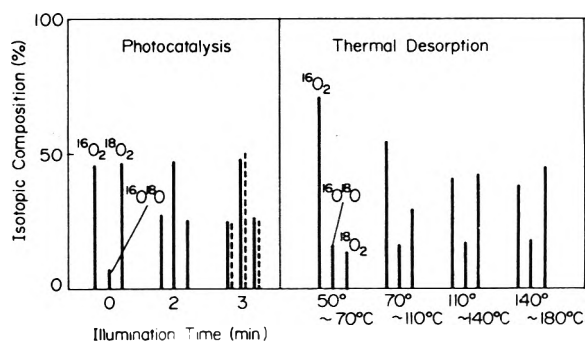
Figure 2. The change of isotopic composition of gas-phase oxygen under illumination and that of desorbed oxygen from TiO_2 after 3 min of illumination. The dotted lines show the equilibrium composition.

topic composition of the desorbed oxygen is unambigously far from the gas-phase equilibrium composition. The fraction of ^{18}O in the desorbed oxygen increases with desorption temperatures as observed in the desorption experiment shown in Figure 1. From the results of the thermal desorption, it is obvious that the oxygen with maximum desorbtion around 180°, O_2^-, has not been the intermediate species of the homomolecular oxygen exchange reaction over the illuminated TiO_2. Accordingly, either the dissociative or the associative mechanisms, such as (i) $O_2^- \rightleftarrows 2O^-$ or (ii) $O_2 + O_2^- \rightleftarrows O_4^-$, including O_2^- should be ruled out.

The O_3^- species have been directly detected by Tench and Lawson[6] and Lunsford and Wong[7] over uv irradiated MgO, and O_3^- over uv irradiated MgO appears inactive for the exchange reaction. However, Kazansky, *et al.*,[8] have suggested the O_3^- intermediate in the homomolecular oxygen exchange reaction on vanadium oxide supported on silica by reason of unstability of the O_3^- species. Accordingly, we may conclude that the homomolecular oxygen exchange reaction taking place over illuminated TiO_2 proceeds *via* weakly held O_3^- intermediates formed from O_2 and O^-, because the desorption of O^- is implausible at room temperature. This result perhaps reveals the important role of O_3^- in catalytic oxidation particularly in photocatalytic oxidation over TiO_2.

References and Notes

(1) J. H. Lunsford, *Catal. Rev.*, **8**, 135 (1973).
(2) K. Tanaka and G. Blyholder, *Chem. Commun.*, 736 (1971); *J. Phys. Chem.*, **76**, 1807 (1972).
(3) K. Tanaka and G. Blyholder, *Chem. Commun.*, 1343 (1971); *J. Phys. Chem.*, **76**, 3184 (1972).
(4) K. Tanaka and K. Miyahara, *Chem. Commun.*, 877 (1973).
(5) C. Naccache, *Chem. Phys. Lett.*, **11**, 1323 (1971).
(6) A. J. Tench and T. Lawson, *Chem. Phys. Lett.*, **7**, 459 (1970).
(7) N. B. Wong and J. H. Lunsford, *J. Chem. Phys.*, **56**, 2664 (1972).
(8) V. B. Kazansky, V. A. Skvets, M. Ya Kon, U. U. Nikisha, and B. N. Shelimov, *Proc. 5th Int. Congr. Catal.*, 104 (1972).

Research Institute for Catalysis   **Ken-ichi Tanaka**
Hokkaido University
Sapporo, Japan 060

Solvation Numbers in Nonaqueous Solvents

Sir: In a recent paper,[1] Della Monica and Senatore state that in methanol monovalent cations are more solvated than divalent cations of comparable crystallographic radii. This statement was based on the Stokes radii, as calculated from conductance data[2] by means of eq 1.[3] This con-

$$r_s = 0.82|Z|/(\lambda_+^0)\eta \qquad (1)$$

clusion is contrary to that expected on the basis of Coulombic theory[4] as well as the results found by this method for mono- and divalent cations in aqueous solutions,[5] and is, in fact, so unexpected that it casts doubt on the estimation of solvation numbers from conductance data. Because of these discrepancies and the possibility that nonaqueous solvents, or at least methanol, behave anomalously in their interactions with cations it seemed of value to reexamine this method of calculating solvation numbers for divalent cations in as many nonaqueous solvents as data were available.

In Table I are given the λ^0 values and the calculated Stokes radii for a number of mono- and dipositive ions in methanol, acetonitrile, propanol, and acetone. Also given

in this table are the corrected radii obtained from the Stokes radii by assuming that the crystallographic radii of the larger tetraalkylammonium ions represent their true radii in solution (*i.e.*, that they are unsolvated).[6] From these data, it can be seen that both the Stokes and corrected radii for the divalent ions studied are greater than those for monovalent ions in all solvents. This is in agreement with expectations of a greater degree of solvation for more highly charged species and indicates that these solvents behave no differently, in this regard at least, than water. Because the results obtained here for methanol are based on the same conductance data as those of Della Monica and Senatore, it would seem that their unusual conclusion was due to the omission of a factor of 2 (for the charge of the alkaline earth ions) in eq 1. The apparent correlation between the extent of solvation and the charge density is further substantiated by the decrease in corrected radii (and therefore in solvation) in a given solvent which is found with increasing crystallographic radii for ions of like charge.

In an attempt to compare the solvation numbers found by this method with those obtained by other methods, eq 2 was applied to the data for Mg^{2+}, using values of 0.65 Å

$$h = 4/3\pi \frac{(r_{corr}^3 - r_{cryst}^3)}{V_{solv}} \qquad (2)$$

for r_{cryst} for Mg^{2+} [7] and 50, 68, 170, and 145 Å³ for the volumes of the methanol, acetonitrile, propanol, and acetone molecules, respectively. The values of h so obtained (15, 14, 14, and 16, respectively) are remarkably similar although they are very dependent on the molecular volumes assumed. The value of 15 obtained for methanol is much greater than the value of 6 measured by means of nmr.[8] A comparable difference occurs for the hydration numbers of Mg^{2+} found from conductance ($h = 12$)[9] and nmr ($h = 6$)[10] data and is most likely due to the fact that the nmr results reflect the number of solvent molecules in the first solvation sphere alone,[11] while conductance measurements lead to the inclusion of at least one additional layer of the solvent sheath.

In conclusion, this study gives no indication that the solvation numbers obtained from conductance data for cations in nonaqueous solvents are in any way anomalous, increasing as they do with increasing charge density of the

TABLE I: Conductivities, Stokes Radii, and Corrected Radii for Ions in Different Solvents

	MeOH ($\eta = 0.00547$)			MeCN ($\eta = 0.00346$)			PrOH ($\eta = 0.01952$)			Me₂CO ($\eta = 0.00303$)		
	λ^0	r_s	r_{corr}	λ^0	r_s	r_{corr}	λ^0	r_s	r_{corr}	λ^0	r_s	r_{corr}
Li^+	39.6^a	3.78_6	4.73	79.9^c	2.96_6	4.13_7				72.8^h	3.717	4.62_5
Na^+	45.7^a	3.28_0	4.42_5	76.9^c	3.08_2	4.23_8	10.32^e	4.07_1	4.91_8	77.49^h	3.49_2	4.42
K^+	53.8^a	2.78_6	4.12_2	83.4^c	2.84_2	4.00	12.45^c	3.37_4	4.41_8	80.6^h	3.358	4.29_4
Cs^+	62.3^a	2.40_6	3.89	97.6^c	2.42_8	3.625						
Me_4N^+	66.7^b	2.24_8		94.2^d	2.51_6		14.40^f	2.917		96.63^i	2.80_1	
Et_4N^+	58.2^b	2.57_6		83.7^d	2.83_1		15.05^f	2.79_1		89.49^i	3.02_4	
Pr_4N^+	43.9^b	3.41_5		69.6^d	3.40_5		12.19^f	3.44_6		75.09^i	3.60_4	
Bu_4N^+	36.9^b	4.06_3		61.3^d	3.86_6		10.17^f	4.13_1		66.40^i	4.07_6	
Mg^{2+}	57.6^a	5.20_5	5.62	94.8^c	5.00	6.01	9.40^g	8.93_8	8.280	70.2^g	7.71_0	8.18_8
Ca^{2+}	60.0^a	5.00_0	5.50							83.6^g	6.474	7.05
Sr^{2+}	59.0^a	5.08_2	5.54									
Ba^{2+}										85.0^g	6.36_8	6.95_0
Zn^{2+}	59.6^a	5.030	5.52	94.8^c	5.00	6.01						

a Reference 2.⊚ *b* E. C. Evers and A. G. Knox, *J. Amer. Chem. Soc.*, **73**, 1739 (1951). *c* W. Libus and H. Strzelecki, *Electrochim. Acta*, **17**, 1749 (1969). *d* A. H. Harkness and H. M. Daggett, *Can. J. Chem.*, **43**, 1215 (1965). *e* T. A. Gover and P. G. Sears, *J. Phys. Chem.*, **60**, 330 (1956). *f* D. F. Evans and P. Gardam, *J. Phys. Chem.*, **72**, 3281 (1968). *g* P. Van Rysselberghe and R. M. Fristrom. *J. Amer. Chem. Soc.*, **67**, 680 (1945). *h* M. B. Reynolds and C. A. Kraus, *J. Amer. Chem. Soc.*, **73**, 3293 (1951). *i* D. F. Evans, J. Thomas, J. Nadas, and M. A. Matesich, *J. Phys. Chem.*, **75**, 1714 (1971).

ion. They are, however, appreciably larger than the solvation numbers obtained from nmr studies and comparisons of the results obtained by these methods must be made with the knowledge that they measure different quantities, although each can provide useful information about the behavior of closely related solvents[11,12] and ions.[11,13]

References and Notes

(1) M. Della Monica and L. Senatore, J. Phys. Chem., 74, 205 (1970).
(2) H. Hartley and H. R. Raikes, Trans. Faraday Soc., 23, 393 (1927).
(3) R. A. Robinson and R. H. Stokes, "Electrolyte Solutions," Butterworths, London, 1968, p 44.
(4) B. E. Douglas and D. H. McDaniel, "Concepts and Models of Inorganic Chemistry" Blaisdell, New York, N. Y., 1965, p 126.
(5) Reference 3, p 12.
(6) Reference 3, p 125.
(7) J. E. Huheey, "Inorganic Chemistry, Principles of Structure and Reactivity," Harper and Row, New York, N. Y., 1972, p 73.
(8) J. H. Swinehart and H. Taube, J. Chem. Phys., 37, 1579 (1962).
(9) Reference 3, p 62.
(10) N. A. Matwiyoff and H. Taube, J. Amer. Chem. Soc., 90, 2796 (1968).
(11) A. Fratiello in "Inorganic Reaction Mechanisms," J. O. Edwards, Ed., Interscience, New York, N. Y., 1972, p 57 ff.
(12) A. P. Zipp, J. Phys. Chem., 77, 718 (1973).
(13) P. Brunc, M. Della Monica, and E. Righetti, J. Phys. Chem., 77, 1258 (1973).

Department of Chemistry   **Arden P. Zipp**
State University College
Cortland, New York 13045

Some Comments on the Calculation of Equilibrium Constants and Extinction Coefficients for 1:1 Complexes

Sir: Several authors have reported methods for using nonlinear least-squares analysis to infer formation constants, K, and optical extinction coefficients, ϵ_{DA}, for a molecular complex, DA, existing in solution in equilibrium with free donor and acceptor molecules.[1] Standard errors in the parameters have also been computed from the shape of the error surface (the sum of squares of absorbance deviations as a function of K and ϵ_{DA}) in the vicinity of the optimum values of K and ϵ_{DA}.[1c,d] Various investigators have argued that numerical optimization methods are superior to graphical or linear least-squares methods based on the Benesi–Hildebrand (BH) equation[2] and related linear relations. What seems not to have been properly appreciated by many workers in the charge-transfer field is that use of any of the linear forms will yield answers virtually identical with those inferred from the more complicated nonlinear analyses *if* data are correctly weighted. For example, a recent paper in this journal[3] includes a discussion of the relative merit of various linear forms of the BH equation (in terms of differences in correlation coefficients of the least-squares fits) and a comparison of two nonlinear fitting methods with the linear forms. In our opinion, this type of discussion is unproductive, since all of the various linear and nonlinear forms based upon the same physical

TABLE I: Comparison of Least-Squares Fits of Spectral Data For Et$_2$O–I$_2$ in Heptane at 15°[a]

	K, M^{-1}	ϵ_{DA}, M^{-1} cm^{-1}
Nonweighted linear fit[b]	1.156 ± 0.028	5745 ± 119
Weighted linear fit[b]	1.234 ± 0.033	5556 ± 93
Nonlinear fit	1.231 ± 0.045	5559 ± 89

[a] Data taken from the Ph.D. Dissertation of J. D. Childs, The University of Oklahoma, 1971; absorbances were measured at 250 nm. Corrections have been made for the absorbance of free donor and acceptor in all three fitting methods. [b] Benesi–Hildebrand equation[2] was used.

and mathematical model must give consistent results if proper statistical methods are employed.

To illustrate this point, we consider using the BH equation in the form

$$\frac{[A]}{A} = \frac{1}{K\epsilon_{DA}[D]} + \frac{1}{\epsilon_{DA}} \tag{1}$$

where A is the absorbance per unit path length, and where we assume that the total donor concentration ($[D]$) is so much greater than the total acceptor concentration ($[A]$) that the concentration of free donor (C_D) is practically equal to $[D]$. We also ignore the effects of absorbance of donor and acceptor at the wavelength chosen for analysis, although these absorbances can be taken into account with little additional difficulty. The principle of weighted linear least squares[4] requires that we seek a minimum in the function

$$\sum_i W_i \left(\frac{[A]_i}{A_i} - \frac{1}{K\epsilon_{DA}} \frac{1}{[D]_i} - \frac{1}{\epsilon_{DA}} \right)^2 \tag{2}$$

where the summation extends over all sets of measured values of A_i, $[A]_i$, and $[D]_i$. Standard methods are readily applied to obtain least-squares values of K and ϵ_{DA} and estimates of their standard deviations, σ_K and $\sigma_{\epsilon_{DA}}$, provided the W_i values can be chosen properly. If the weights are chosen injudiciously (for example, if W_i is by default taken to be unity for all points) unreliable answers may be obtained with the BH equation; criticism in the literature of the uncritical use of the BH equation in this way is quite appropriate.[5] However, the calculation of weights is straightforward if reasonable estimates of the uncertainties in absorbances and concentrations can be made. Decisions regarding these errors should not be made thoughtlessly since the calculated parameters can depend strongly on the weights, especially when the data do not permit a precise determination of K and ϵ_{DA}.

Let us consider the case in which it is reasonable to assume that the absorbances are subject to equal absolute error at all points and that the donor and acceptor concentrations are known exactly. (These are the assumptions usually made in nonlinear analyses of spectral data.) The dependent variable ($Y_i = [A]_i/A_i$) in the linear fit of Y_i *vs.* $1/[D]_i$ will then have the weight

$$W_i = \frac{1}{\sigma_{Y_i}^2} = \frac{1}{(\partial Y_i/\partial A_i)^2 \sigma_A^2} = \frac{A_i^4}{[A]_i^2 \sigma_A^2} \tag{3}$$

where σ_A is the (constant) error in absorbance.[6] Using this weighting scheme, best values of K and ϵ_{DA}, and estimates of standard deviations in ϵ_{DA}^{-1} and $(K\epsilon_{DA})^{-1}$ result directly from the standard linear least-squares analysis. Simple propagation of errors formulas than yield σ_K and $\sigma_{\epsilon_{DA}}$.

Table I compares results of nonweighted and weighted linear least-squares treatments of a set of spectral data. The weighted linear analysis gives results which are quite similar to those obtained by using the nonlinear least-squares method of Grundnes and Christian.[1c] The latter method uses Sillen's criteria[7] for determining σ_K and $\sigma_{\epsilon_{DA}}$ from the shape of the error surface near $K^{optimum}$, $\epsilon_{DA}{}^{optimum}$. Because of the near equivalence of the weighted linear and nonlinear methods, it is a matter of preference which analysis to use. However, the simplicity of the weighted linear method should make it the preferable technique in many cases. Obviously, any of the linear forms of the BH-type should give the same values of K and ϵ_{DA} and their standard deviations.

The weighted linear least-squares method can also be applied with iteration if the complex concentration is not small compared to [D]. In this case, the term $1/K\epsilon_{DA}[D]$ is replaced by $1/K\epsilon_{DA}C_D$, and an approximate value of K is used to estimate the amount of donor in the complexed form. Several passes through the linear least-squares program will ordinarily lead to convergent values of K and ϵ_{DA}, which agree with $K^{optimum}$ and $\epsilon_{DA}{}^{optimum}$ inferred from the nonlinear method.

References and Notes

(1) (a) K. Conrow, G. D. Johnson, and R. E. Bowen, *J. Amer. Chem. Soc.*, **86**, 1025 (1964); (b) W. C. Coburn, Jr., and E. Grunwald, *ibid.*, **80**, 1318, 1322 (1958); (c) J. Grundnes and S. D. Christian, *ibid.*, **90**, 2239 (1968); (d) D. R. Rosseinsky and H. Kellawi, *J. Chem. Soc. A*, 1207 (1969).
(2) H. A. Benesi and J. H. Hildebrand, *J. Amer. Chem. Soc.*, **71**, 2703 (1949).
(3) P. G. Farrell and P. N. Ngô, *J. Phys. Chem.*, **77**, 2545 (1973).
(4) W. E. Deming, "Statistical Adjustment of Data," Wiley, New York, N. Y., 1943.
(5) R. L. Scott. *Recl. Trav. Chim. Pays-Bas*, **75**, 787 (1956); D. A. Deranleau, *J. Amer. Chem. Soc.*, **91**, 4044 (1969).
(6) In order to allow for variable absorbance and concentration errors. W_i is related to the error in the ith residual (res_i) by

$$W_i = \frac{1}{\sigma_{res_i}{}^2}$$

where

$$res_i = \frac{[A]_i}{A_i} - \frac{1}{K\epsilon_{DA}[D]_i} - \frac{1}{\epsilon_{DA}}$$

(7) L. G. Sillén, *Acta Chem. Scand.*, **18**, 1085 (1964), and references therein.

Department of Chemistry   **Sherril D. Christian***
The University of Oklahoma   **Edwin H. Lane**
Norman Oklahoma 73069   **Frank Garland**

From the borders of organic chemistry ... To the borders of theoretical physics:

Inorganic Chemistry brings you a broad range of authoritative information presenting both experimental and theoretical studies in all phases of inorganic chemistry.

Each month, this rapidly growing journal brings you the data you need on synthesis and properties of new compounds, quantitative studies regarding structure, and thermodynamics of inorganic reactions.

When you've seen the 50 or more papers offered in each issue, you'll also want to look through the Notes and Correspondence sections for their concise exchange of scientific views and ideas.

To order INORGANIC CHEMISTRY today, just complete and return the form below.

... another ACS service

Inorganic Chemistry